Adam Kraśnicki

ROTATIONAL SPECTROSCOPY OF SELECTED MOLECULES OF ASTROPHYSICAL IMPORTANCE

PH.D DISSERTATION

INSTITUTE OF PHYSICS
POLISH ACADEMY OF SCIENCES

Warszawa

July 2011

Acknowledgements

I would like to thank my supervisor Prof. Zbigniew Kisiel for his scientific support, guidance, and research ideas.

I thank everyone in the ON2.3 group at IFPAN, for all the help for various aspects of my research. Especially I would like to express my gratitude Dr. Ewa Białkowska-Jaworska for many fruitfull discussions. I am also grateful to Lech Pszczółkowski for ensuring the continuity of measurements, and Jerzy Kosarzewski for technical support.

Abstract

This dissertation presents results of the measurements and the analysis of the rotational spectra for selected molecules of astrophysical importance: cyanamide, acrylonitrile, pyruvonitrile, phenylacetylene, urethane, and propionitrile. Several different types of rotational spectrometers, operating in different, complementary frequency regions have been used for the measurements. Simultaneus access to broadband high-frequency rotational spectra and to spectra measured with the cavity Fourier Transform Microwave (FTMW) spectrometer allowed precise determination of the rotational, centrifugal and nuclear quadrupole coupling constants for the studied species. For each investigated molecule the ground state rotational transitions and some of the low-frequency excited vibrational modes have been subjected to analysis. Various interactions between rotational levels of different vibrational states have been identified and fitted to experimental accuracy with a suitable Hamiltonian. Results of this type have been obtained for cyanamide (inversion doublet $0^+ \leftrightarrow 0^-$), for acrylonitrile (g.s. $\leftrightarrow v_{11} = 1$), and for phenylacetylene ($v_{24} = 1 \leftrightarrow v_{36} = 1$). A coupled analysis of the interacting states enabled determination of the precise energy differences beetwen them and of multiple interaction constants. Special treatment was needed in the case of pyruvonitrile for which the internal rotation doublet A, E was observed for each vibrational state.

The experimental ground state rotational constants determined in this thesis for many isotopologues of cyanamide and acrylonitrile (most of them for the first time) were combined with calculated CCSD(T) quality zero-point vibrational corrections resulting in accurate semi-experimental equilibrium r_e^{SE} geometries for these molecules.

Measurements of the Stark effect at conditions of supersonic expansion with the FTMW spectrometer at IFPAN allowed determination of precise electric dipole moments for pyruvonitrile, urethane, propionitrile, and acrylonitrile. The newly determined values allow prediction of reliable intensities of rotational transitions, especially in the high-frequency spectral range. The experimental results have been confronted with previous results and with *ab initio* calculations at different theoretical levels of electron correlation corrections.

The measurements and analysis for molecules reported in this dissertation allow more precise predictions in support of astronomical observations with the new high spectral resolution radiotelescopes, such as Herschel, SOFIA, and ALMA.

Scientific activity

Publications

1. A. Kraśnicki, M. Kręglewski, H. Mäder, "Rotational spectra and structure of 1,2,3,4 - tetrafluorobenzene", *J. Mol. Struct.* **882**, 123-127 (2008).

2. M. Goubet, R. A. Motiyenko, F. Réal, L. Margulés, T. R. Huet, P. Asselin P. Soulard, A. Krasnicki, Z. Kisiel, "Influence of the geometry of a hydrogen bond on conformational stability: a theoretical and experimental study of ethyl carbamate", *Phys. Chem. Chem. Phys.* **11**, 1719-1728 (2009).

3. Z. Kisiel, A. Kraśnicki, L. Pszczółkowski, S. T. Shipman, L. Alvarez-Valtierra, B. H. Pate, "Assignment and analysis of the rotational spectrum of bromoform enabled by broadband FTMW spectroscopy", *J. Mol. Spectrosc.* **257**, 177-186 (2009).

4. A. Kraśnicki, Z. Kisiel, L. Pszczółkowski, "Analysis of the rotational spectrum of pyruvonitrile up to 324 GHz", *J. Mol. Spectrosc.* **260**, 57-65 (2010).

5. Z. Kisiel, A. Kraśnicki, "The millimetre-wave rotational spectrum of phenylacetylene", *J. Mol. Spectrosc.* **262**, 82-88 (2010).

6. A. Kraśnicki, Z. Kisiel, W. Jabs, B. P. Winnewisser, M. Winnewisser, "Analysis of the mm- and submm-wave rotational spectra of isotopic cyanamide: New isotopologues and molecular geometry", *J. Mol. Spectrosc.* **267**, 144-149 (2011).

7. A. Kraśnicki, Z. Kisiel, B. J. Drouin, J. C. Pearson, "Terahertz spectroscopy of isotopic acrylonitrile", *J. Mol. Struct.* doi:10.1016/j.molstruc.2011.05.050 (2011).

8. A. Kraśnicki, Z. Kisiel, "Electric dipole moments of acrylonitrile and of propionitrile measured in supersonic expansion", *J. Mol. Spectrosc.* **270**, 83-87 (2011).

Talks and presentations

1. Z. Kisiel, A. Kraśnicki, L. Pszczółkowski, S. T. Shipman, L. Alvarez-Valtierra, B. H. Pate, "Assignment and analysis of the rotational spectrum of bromoform enabled by broadband FTMW spectroscopy", presented at the 63rd International Symposium on Molecular Spectroscopy, Ohio State University, Columbus, USA, June, 16-20, 2008.

2. Z. Kisiel, A. Kraśnicki, B. P. Winnewisser, M. Winnewisser, "Detailed analysis of the $0^+ - 0^-$ inversion doublet", presented at the 63rd International Symposium on Molecular Spectroscopy, Ohio State University, Columbus, USA, June, 16-20, 2008.

3. A. Kraśnicki, Z. Kisiel, L. Pszczółkowski, J.-C. Guillemin, "Rotational spectroscopy and structure of the cyclic biomimetic 2-aminopyridine...water cluster", presented at the 20th International Conference on High Resolution Spectroscopy, PRAHA 2008, Prague, Czech Republic, September, 2-6, 2008.

4. A. Kraśnicki, Z. Kisiel, L. Pszczółkowski, J.-C. Guillemin, "Detailed analysis by rotational spectroscopy 2-aminopyridine...water: a cyclic biomimetic cluster", presented at the BIOSYS 2008 - The Study of Biomimetic Systems, An International French-German Summer School, Villa Clythia, Fréjus, France, September, 21-27, 2008.

5. Z. Kisiel, A. Kraśnicki, I. R. Medvedev, C. Neese, S. Fortman, M. Winnewisser, F. C. de Lucia, H. S. P. Müller "Rotational spectroscopy of ethylamine into the THz", presented at the 64th International Symposium on Molecular Spectroscopy, Ohio State University, Columbus, USA, June, 22-26, 2009.

6. A. Kraśnicki, Z. Kisiel, B. P. Winnewisser, M. Winnewisser, "Assignment of the mm- and smm-wave rotational spectra of rare isotopologues of cyanamide and the $r_m^{(1)}$ molecular geometry of NH_2CN", presented at the 64th International Symposium on Molecular Spectroscopy, Ohio State University, Columbus, USA, June, 22-26, 2009.

7. Z. Kisiel, A. Kraśnicki, "The millimetre-wave rotational spectrum of phenylacetylene", presented at the 65th International Symposium on Molecular Spectroscopy, Ohio State University, Columbus, USA, June, 21-25, 2010.

8. A. Kraśnicki, Z. Kisiel, B. J. Drouin, J. C. Pearson, "Terahertz spectroscopy of isotopic species of acrylonitrile", presented at the 21st International Symposium on Molecular Spectroscopy, Adam Mickiewicz University, Poznań, Poland, September, 7-11, 2010.

9. Z. Kisiel, A. Kraśnicki, "Improved dipole moments for acrylonitrile and propionitrile", presented at the 66th International Symposium on Molecular Spectroscopy, Ohio State University, Columbus, USA, June, 20-24, 2011.

Contents

Chapter 1

Introduction

Rotational spectroscopy studies interaction of the electromagnetic field with rotating molecules in the gas phase. The interaction corresponds to discrete absorption or emission of energy and is associated with a change of the rotational quantum numbers between two energy levels in a molecule. As a result, a rich rotational spectrum consisting of many rotational transitions can be observed. Usually, rotational transitions fall from the centimeter to the far-infrared frequency region of the electromagnetic spectrum.

The origin of rotational spectroscopy dates back to the 1940s when the use of microwaves in spectroscopy became possible due to development of microwave technology, initially used only for military purposes. Since then this field has progressed considerably, and is still one of the most valuable and powerful spectroscopic techniques. The fact that each molecule has a different rotational spectrum which is its distinct "fingerprint", has been found to be very useful in identification of particular molecules not only in the laboratory sample, but also in the interstellar medium. Hence, rotational spectroscopy plays a fundamental role in investigations of interstellar chemistry and the study of how stars and the planetary systems are born. Laboratory rotational spectroscopy provides information on the transition frequencies of a given species, and such information is then used by astrophysics in identification of interstellar molecules and in derivation of their abundance from the spectrum detected by radioastronomy. Rotational spectroscopy is a high resolution technique with precision limited by the Doppler width, and is an excellent source of reference data for new high-resolution telescope facilities operating in the THz frequency region.

Rotational spectroscopy has found great utility in revealing a wealth of detailed information on molecular structure including many details of molecular dynamics. A thorough analysis of the laboratory rotational spectrum is based on the rotational Hamiltonian and enables determination of many spectroscopic constants. The primary observables are rotational constants, which contain structural information as they are inversely proportioned to the moments of inertia. This allows rotational spectroscopy to be used for determination of molecular geometries, which are usually

an order of magnitude more precise than those from crystallography. Furthermore, the Stark effect on the rotational spectrum provides accurate information on the electric dipole moment, which is another fundamental molecular property. Since rotational spectroscopy is a high resolution technique, various higher order spectroscopic effects are also observed in the spectrum. A complete analysis of the rotational spectrum in the ground and low-lying excited vibrational states yields highly accurate information on energy differences between interacting vibrational states and also more subtle details on the relevant intramolecular interactions arising from Coriolis and Fermi resonances. Rotational data also provides information on barriers to large-amplitude internal motions of certain groups of atoms such as internal rotation of the methyl group or inversion of the amino group. In addition to this, centrifugal distortion parameters can be used to extract data on the vibrational force field of the molecule. Finally, the precise molecular properties determined from rotational spectroscopy are also a useful guide to the development of quantum chemistry methods. On the other hand, for small- and medium-size molecules the advanced quantum chemistry methods might provide "spectroscopic" quality observables, such as vibrational contributions to the ground state rotational constants, which are usually out of reach experimentally. These can be combined with experimental rotational constants and used in an evaluation of equilibrium-quality molecular structure, such as those determined for cyanamide and acrylonitrile in this dissertation.

The advances in the fields of electronics and microwave techniques always had a great impact on the instrumental development in rotational spectroscopy. A very in influential technique has proved to be the combination of pulsed supersonic expansion sources with the microwave resonator, as was implemented in the first FTMW (Fourier Transform Microwave) spectrometer designed by Balle and Flygare [1]. The low effective expansion temperature of the sample in this design, of close to 1 K, enabled studies of weakly bound intermolecular species, such as hydrogen-bonded and van der Waals complexes. The high frequency precision of the FTMW measurement (2 kHz) enables observation also of fine and hyperfine effects in rotational spectra. Further development of this type of spectrometer have recently been realized in the form of the broadband Chirped-Pulsed Fourier Transform Microwave (CP-FTMW) spectrometer [2, 3, 4], in which the application of a fast arbitrary waveform generator and 40 Gs/s digital oscilloscope dramatically increased the bandwidth of the probed spectrum. As an example, the measurement and analysis of the complex rotational spectrum of bromoform [5] have been greatly facilitated due to the use of such spectrometer. Another influential development has been the use of the Backward Wave Oscillator (BWO) tubes as highly tunable, high-frequency sources of the monochromatic radiation in broadband rotational spectrometers. The powerful BWO tubes allowed this type of spectrometer to become a fundamental instrument for recording room-temperature broadband rotational spectra of molecules including astrophysically relevant species. In recent years the BWO-tubes are being displaced by Virginia-Diodes sources based on GaAs diode multipliers. The cascade multiplication systems driven from a microwave syntesizer can now reach up to 2 THz, and significantly shortens the time of the spectral recording. This instrumental solution
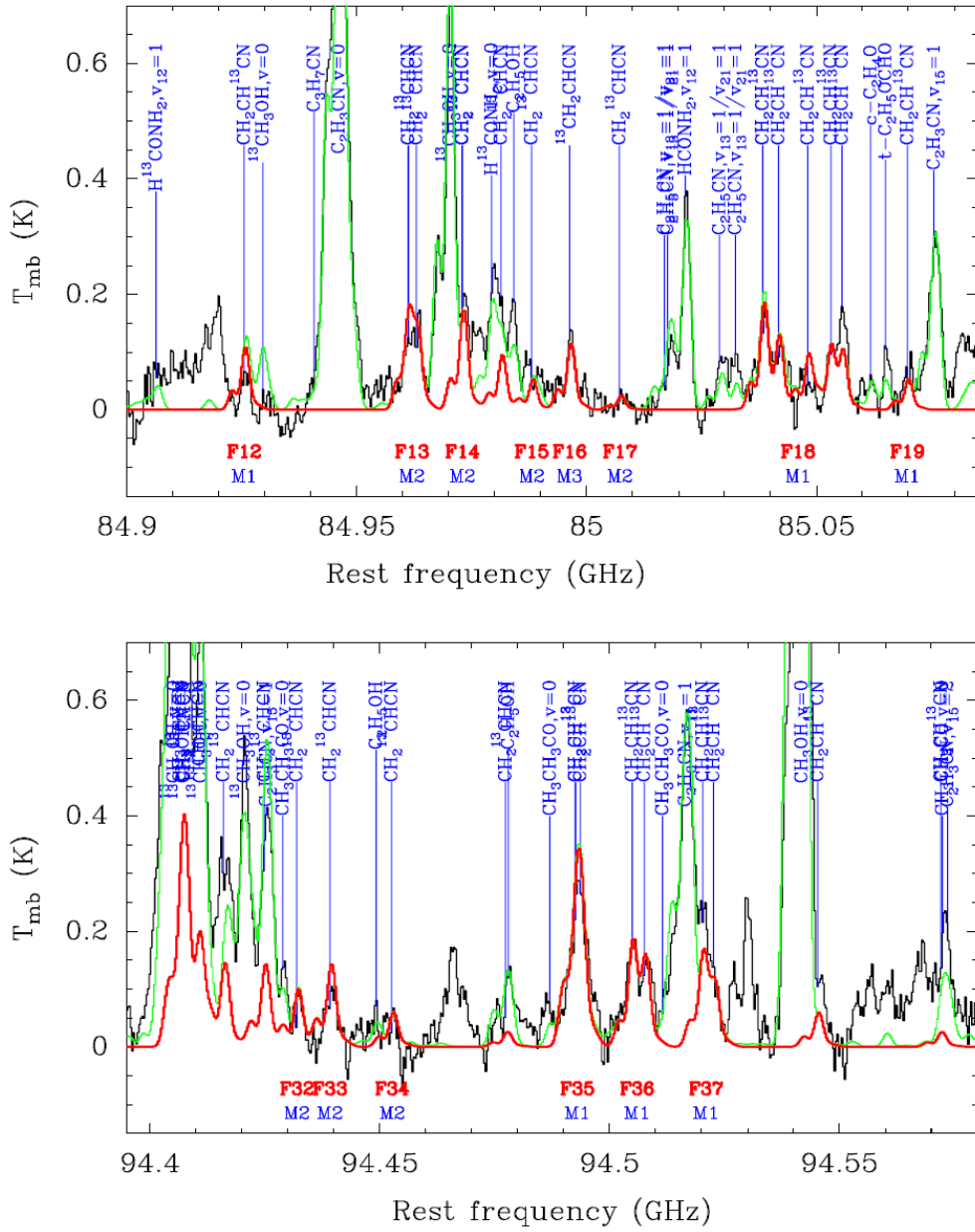
Figure 1.1: Selected transitions of the ^{13}C isotopologues of acrylonitrile detected with the IRAM 30 m telescope. In each panel, the spectrum observed toward Sgr B2(N) is shown in black, while the local thermal equillibrium (LTE) synthetic spectrum including the three ^{13}C isotopologues of vinyl cyanide is overlaid in red and the LTE model including all identified molecules in green. From [6].

is becoming the method of choice in rotational spectroscopy laboratories, especially in view of the fact that BWO tubes are no longer being produced.

The question of which species can be studied by rotational spectroscopy depends on the sample preparation. As has been mentioned above the supersonically cooled samples at temperatures close to 1 K measured in cavity FTMW spectrometers enabled studies of many molecular complexes. Furthermore, application of laser ablation made possible the vaporization of low-volatility solid state samples and measurements of their rotational spectra. This technique has the advantage over sample evaporation by heating since there is minimal sample decomposition. Hence, many species such as aminoacids [7] or metal containing molecules [8] can be studied by means of rotational spectroscopy. Laser ablation has been applied to produce species that are of particular interest for radioastronomy, for instance carbon or silicon-carbon clusters [9, 10]. The rotational spectra of many radicals important for radioastronomy have become accessible mainly by the use of the electric discharge nozzle in supersonic expansion, cavity FTMW spectrometers [11].

The progress in construction of sensitive, high resolution radioastronomy tools contributed to identification of many molecules in the interstellar medium and circumstellar envelopes. The new telescope facilities such as The Atacama Large Millimeter/submillimeter Array (ALMA), Herschel Space Observatory for the Far-Infrared, or Stratospheric Observatory for Infrared Astronomy (SOFIA) have access to the richest part of the astrophysical spectrum. Astronomical interpretation requires complete laboratory characterization of the relevant species including precise line positions, intensities, and line shapes. The combination of the laboratory and astronomical data enabled unambiguous detection of more than 140 molecules in space. Most of them are simple molecules, consisting of only a few atoms, but which have sufficiently strong rotational transitions for detection. Larger molecules are more difficult to identify because their "fingerprints" are barely visible, since their spectra are distributed over much weaker lines. A particularly large and rich region for detecting interstellar molecules is Sagittarius B2 (Sgr B2), where isotopic species substituted with ^{13}C of acrylonitrile, presented in this dissertation have been detected (see Fig. 1.1). The information on the presence of particular species in space is essential also for construction of detailed reaction pathways in the interstellar medium, and is part of the new field of astrochemistry.

The main goals of this dissertation are the comprehensive analysis of the rotational spectra of astrophysically relevant molecules, determination of their important physical properties from derived observables, and to provide accurate experimental data needed for astronomical observations.

Chapter 2

Theoretical Background

Rotational spectroscopy is one of the most powerful sources of precise information on chemical and physical properties of molecules. Advances in experimental techniques and theory, that have taken place over the last 20-30 years, have increased the power of this spectroscopic technique even further. A thorough description of theoretical methods used in rotational spectroscopy can be found in the excellent monograph of Gordy and Cook [12], as well as in the book of Papoušek and Aliev [13], which has actually been aimed at rotation-vibration spectroscopy. Noteworthy are also the older monographs of Townes and Schawlow [14], and Kroto [15] which are valuable sources of information on the early stages of the theoretical and experimental development of microwave spectroscopy. Most of the up-to-date theoretical and experimental progress in rotational spectroscopy is collected in scientific journals, such as Journal of Molecular Spectroscopy, Journal of Chemical Physics, Chemical Physics Letters, Physical Chemistry Chemical Physics, and the Review of Scientific Instruments. It is worth pointing out the PROSPE database [16, 17], which contains many of useful computer programs for rotational spectroscopy, and the ROTLINKS webpage [18] with many links of relevance to contemporary rotational spectroscopy.

The author of this dissertation does not intend to describe all available theoretical methods of rotational spectroscopy. Only the key aspects of the theory that are essential for dealing with acquired experimental data are presented.

Section 2.1 of this chapter is devoted to classical and quantum mechanical descriptions of a rotating molecule in terms of a rigid-rotor Hamiltonian. In subsequent sections several corrections to the rotational Hamiltonian are discussed, such as centrifugal distortion part of the rotational Hamiltonian, the nuclear quadrupole coupling Hamiltonian, and the Hamiltonian of the Stark effect. In section 2.8 different approaches to precise determination of molecular geometry from rotational spectra are presented. Some attention is devoted to the description of large amplitude motions, which occur in molecules studied in this work.

2.1 Rigid-Rotor Hamiltonian

2.1.1 From Classical to Quantum Mechanical Description

In order to describe the rotational spectrum of a molecule it was necessary to formulate a mathematical model from which solutions for the quantized energy levels may be obtained. The classical mechanics of a rotating rigid system of particles provides a good starting point for a detailed description of the rotating molecule. In the first approximation the molecule can be regarded as a set of atoms, each of which is taken to be a point mass m_i at coordinates x_i, y_i, z_i. When relative values of these coordinates are fixed, then the rotation of the molecule in space can be described by a $rigid - rotor$ Hamiltonian.

In classical mechanics the kinetic energy T of the rigid-rotor is given by

$$T = \frac{1}{2}\vec{\boldsymbol{\omega}}^{\dagger}\mathbf{I}\vec{\boldsymbol{\omega}}, \tag{2.1}$$

where $\vec{\boldsymbol{\omega}}$ is the angular velocity vector of the rotating body and $\mathbf{I}$ is the moment of inertia tensor.

The diagonal elements of the moment of inertia tensor in x, y, z axes are given by

$$I_{\alpha\alpha} = \sum_i m_i(\beta_i^2 + \gamma_i^2), \tag{2.2}$$

where α, β, γ is a permutation of x, y, z. The off-diagonal elements are

$$I_{\alpha\beta} = I_{\beta\alpha} = -\sum_i m_i\alpha_i\beta_i, \tag{2.3}$$

where $\alpha \neq \beta$. The origin of the Cartesian axis system x, y, z is placed at the center of mass of the molecule and the axes are chosen so that all off-diagonal elements of $\mathbf{I}$ vanish. This unique, molecule-fixed axis system is called the principal axes system. The axes are labeled a,b,c and are conventionally chosen to be in the order of increasing values of the principal moments of inertia, such that

$$I_a \leq I_b \leq I_c. \tag{2.4}$$

The values of the principal moments of inertia and hence those of rotational constants depend only on the molecular geometry (bond lengths and bond angles) and on the atomic masses. The relative values of the elements of the principal moments of inertia allow molecules to be classified into four categories:

1. *Spherical top molecules*, for which all three principal moments of inertia are equal $I_a = I_b = I_c$. Examples of spherical tops are: CH_4, SF_6.

2. *Linear molecules*, in which $I_a = 0$, $I_b = I_c$. Examples of linear tops are: CO_2, OCS, HCN, HC≡CH.

3. *Symmetric top molecules*, for which one moment of inertia is unique and two others are equal to each other.

   If the unique moment is smaller than the other two then the molecule is a *prolate symmetric top*, $I_a < I_b = I_c$. Examples of prolate symmetric tops are: CH_3D, $CH_3C\equiv CH$, $(CH_3)_3CC\equiv N$.

   Alternatively, if the unique moment is larger than the other two then the molecule is called an *oblate symmetric top*, $I_a = I_b < I_c$. Examples of oblate symmetric tops are: NH_3, benzene.

4. *Asymmetric top molecules*, for which the three moments of inertia are different from each other, $I_a < I_b < I_c$. Examples of asymmetric tops are: H_2O, NH_2D, fluorobenzene.

   Some molecules, which are strictly asymmetric tops, have two nearly equal moments of inertia. If $I_a < I_b \approx I_c$, then the molecule is a *prolate asymmetric top*, e.g. $CH_2{=}CHCN$, H_2NCN. On the other hand, if $I_a \approx I_b < I_c$ then the molecule is an *oblate asymmetric top*, e.g. $HC^{79}Br_2^{81}Br$, pyrazine.

   Asymmetric top molecules are by far the most common among molecules studied by rotational spectroscopy. In section 2.1.2 of this chapter the asymmetric top case is discussed in more detail.

In classical mechanics the angular momentum J_g of a rotating body is

$$J_g = \frac{\partial T}{\partial \omega_g}, \tag{2.5}$$

where $g = x, y, z$. Thus, the kinetic energy in Eq. 2.1 expressed in terms of angular momentum is given by

$$T = \frac{1}{2}\vec{J}^{\dagger}\boldsymbol{\mu}\vec{J}, \tag{2.6}$$

where $\boldsymbol{\mu} = \mathbf{I}^{-1}$.

Rotational energy (Eq. 2.6) in principal axes is then

$$T = \frac{1}{2}\left(\mu_{aa}J_z^2 + \mu_{bb}J_x^2 + \mu_{cc}J_y^2\right) = \frac{1}{2}\left(\frac{J_z^2}{I_a} + \frac{J_x^2}{I_b} + \frac{J_y^2}{I_c}\right), \tag{2.7}$$

where a standard identification between the general principal axes x, y, z and the conventional principal axes a, b, c has been assumed (see section 2.1.2).

Rotational energy of a molecule is quantized, so the classical angular momentum vector J_g must be replaced by its quantum-mechanical equivalent – the angular momentum operator $\hat{J}_g$. Rigid-rotor Hamiltonian (2.7), written in terms of the component angular momentum operators in the principal axes has the form

$$T = \mathcal{H}_{\mathrm{rig}} = A\hat{J}_z^2 + B\hat{J}_x^2 + C\hat{J}_y^2, \tag{2.8}$$

where *A, B, C* are rotational constants defined by

$$B = \frac{h}{8\pi I_b} \text{ etc}, \tag{2.9}$$

and the operators for momentum about the specific principal axes are related to the total angular momentum of the system by $\hat{J}^2 = \hat{J}_x^2 + \hat{J}_y^2 + \hat{J}_z^2$.

Moments of inertia in rotational spectroscopy are normally expressed in units of u·Å^2, and $1\,\mathrm{u} \cdot \mathrm{Å}^2 = 1,66053873(13) \times 10^{-47}\,\mathrm{kg} \cdot \mathrm{m}^2$. The most commonly used unit for rotational constants is MHz. On using the values of the fundamental physical constants from CODATA 2006 [19], the definition of the rotational constant can be simplified to

$$B[\mathrm{MHz}] = \frac{505379,005(36)}{I_b[\mathrm{u} \cdot \mathrm{Å}^2]}. \tag{2.10}$$

The solution for the energy levels in a quantum mechanical system is obtained from the Schrödinger equation of the rigid rotor

$$\mathcal{H}_{\mathrm{rig}}\psi = E_{\mathrm{rot}}\psi, \tag{2.11}$$

$\mathcal{H}_{\mathrm{rig}}$ is the Hamiltonian operator of the rigid-rotor system (2.8), ψ is the wavefunction describing the system and E_{rot} is the rotational energy. Certain commutation relationships arising from the Heisenberg uncertainty principle between components of angular momentum $\hat{J}_g$, $g = x, y, z$, suggest that any two components of angular momentum can not be measured simultaneously. However, by finding the operator for $\hat{J}^2$ it can be shown that the square of the total angular momentum commutes with components of angular momentum in a molecule-fixed system $\hat{J}_g$, $g = x, y, z$, and in a space-fixed system $\hat{J}_G$, $G = X, Y, Z$. This means that there exist simultaneous eigenstates of these three operators defined by independent quantum numbers J, K, and M. The quantum numbers J, K, M are used to describe wavefunctions for $\hat{J}^2$, $\hat{J}_z$, and $\hat{J}_Z$, respectively. The matrix elements of these operators are

$$\left\langle J, K, M \mid \hat{J}^2 \mid J, K, M \right\rangle = J(J+1)\hbar^2, \tag{2.12}$$

$$\left\langle J, K, M \mid \hat{J}_z^2 \mid J, K, M \right\rangle = K^2\hbar^2, \tag{2.13}$$

$$\left\langle J, K, M \mid \hat{J}_Z^2 \mid J, K, M \right\rangle = M^2\hbar^2. \tag{2.14}$$

The quantum number J is proportional to the total rotational angular momentum of the molecule. It is called the principal rotational quantum number, and takes on positive integral values 0, 1, 2, ... The quantum number K is associated with angular momentum projection $\hat{J}_z$ along a molecule fixed axis with values $K = -J, -J+1, \ldots, 0, J-1, J$. In the presence of an external magnetic or electric field the quantum number M describes the component of the total angular momentum along the space-fixed axis Z, with values $M = -J, -J+1, \ldots, 0, J-1, J$.

The selection rules for allowed transitions between rotational energy levels depend on the type of rotor. For linear and symmetric tops rotational transitions are only allowed for

$$\Delta J = \pm 1, \ \Delta K = 0, \ \Delta M = 0, \pm 1. \tag{2.15}$$

The intensity of a rotational transition is governed by the matrix elements of the dipole moment, which are defined and described in detail in Chapter II of Ref. [12],

and are non-zero only for non-zero components of the permanent dipole moment of the molecule. Here it should be noted that spherical tops are not of direct interest to rotational spectroscopy, since such molecules do not have a permanent dipole moment and do not give rise to rotational spectra. Nevertheless, in some cases, such as methane CH_4 [20], centrifugal effects (discussed in section 2.2) can induce a small dipole moment so that weak rotational spectra can be observed.

2.1.2 The Asymmetric-Top Rotor

When the molecule has three unique moments of inertia then it is classified as an asymmetric top. Most polyatomic molecules belong to this category. The rigid-rotor Hamiltonian for the asymmetric top is represented by Eq. 2.8. The methods for energy level determination of the asymmetric top are more complex than for symmetric and linear tops, for which it is possible to rearrange the Hamiltonian to be composed only of two operators $\hat{J}^2$ and $\hat{J}_z^2$. Closed expressions for the resulting energy levels can therefore be derived by using Eq. 2.12 and 2.13. Natural basis functions for asymmetric tops are linear combinations of the symmetric top functions: $\mid J, K, M \rangle$. For these wavefunctions the Hamiltonian matrix of the asymmetric top is no longer diagonal, since operators $\hat{J}_x^2$ and $\hat{J}_y^2$ give rise to off-diagonal elements of the energy matrix Hamiltonian. The diagonal elements of $\hat{J}_x^2$ and $\hat{J}_y^2$ are

$$
\begin{aligned}
\langle J, K, M \mid \hat{J}_x^2 \mid J, K, M \rangle &= \langle J, K, M \mid \hat{J}_y^2 \mid J, K, M \rangle \\
&= \frac{\hbar^2}{2} \left[J(J+1) - K^2 \right],
\end{aligned}
\tag{2.16}
$$

and the off-diagonal elements are

$$
\begin{aligned}
\langle J, K, M \mid \hat{J}_x^2 \mid J, K \pm 2, M \rangle &= -\langle J, K, M \mid \hat{J}_y^2 \mid J, K \pm 2, M \rangle \\
&= -\frac{\hbar^2}{4} f_\pm(J, K),
\end{aligned}
\tag{2.17}
$$

where

$$
f_\pm(J, K) = [J(J+1) - K(K\pm1)]^{1/2}[J(J+1) - (K\pm1)(K\pm2)]^{1/2}.
\tag{2.18}
$$

It should be noted that there are six different ways of identifying the conventional principal axes a, b, c with those denoted by x, y, z. A given identification is called the representation of the rotational Hamiltonian. The most commonly used representation is I^r, for which $b \to x$, $c \to y$, $a \to z$, so that $I_z \leq I_x \leq I_y$. Analogous representation used for the oblate rotational symmetry is III^l with $b \to x$, $a \to y$, $c \to z$. A complete table containing all possible mappings with the names of representations is given on page 35 of Ref. [15]. The optimum representation allows construction of the Hamiltonian matrix (discussed below) such that the off-diagonal elements are smallest in comparison to the diagonal ones. This procedure reduces the time required for the diagonalization process. The optimum choice of the representation used to be crucial since diagonalization of the Hamiltonian matrix was

usually a significant challenge for early computers, and is still recommended for best numerical stability of calculations.

In the prolate asymmetric top case, set up in representation I^r, the energy matrix has nonvanishing elements given by

$$E_{J,K} \quad = \quad \frac{1}{2}(B+C)J(J+1) + \left[A - \frac{1}{2}(B+C)\right]K^2, \qquad (2.19)$$

$$E_{J,K\pm2} \quad = \quad -\frac{1}{4}(B-C)f_\pm(J,K). \qquad (2.20)$$

The overall energy matrix has block diagonal form. Each block corresponds to a given value of the J quantum number and is of size $(2J+1) \times (2J+1)$. Rows and columns are labelled by the K quantum number, where $K = -J, -J+1, \ldots, 0, J-1, J$. Each block in this matrix is also tridiagonal and consists of three types of elements labelled $(K, K-2)$, (K, K), and $(K, K+2)$ with values given by Eq. 2.19 and 2.20. A second important property of the energy matrix is symmetry about the main diagonal, in that $E_{K,K-2} = E_{K,K+2}$, which is a consequence of the K^2 dependence of the rotational energy. Diagonalization of this matrix gives energies of the rotational levels. A given rotational level is no longer labelled only by the J and K quantum numbers as in symmetric tops but involves using a second K quantum number. According to the King-Hainer-Cross notation a rotational level of the asymmetric top is denoted by J_{K_a,K_c}, where K_a and K_c indicate K values at the prolate and oblate symmetric limits to which the level correlates. In the absence of external fields each rotational level is $M-$fold degenerate, where $M = 2J+1$. Regardless of the choice of the representation, the symmetry properties of the Hamiltonian matrix facilitate factorization of each J block into four independent submatrices by means of a Wang transformation. Each of these submatrices may be diagonalized independently to give the rotational energies. The order of each Wang submatrix is approximately $J/2$, which used to be a very useful reduction in matrix size on diagonalization for large values of J. The factorization procedure is described in detail on pages 237-254 of Ref. [12].

The degree of asymmetry in an asymmetric top is given by the value of Ray's parameter

$$\kappa = \frac{2B - A - C}{A - C}, \qquad (2.21)$$

where $-1 \leq \kappa \leq 1$. The two limiting values, $\kappa = -1$ and $\kappa = +1$, correspond to the prolate and oblate symmetric tops, respectively. The most asymmetric top has $\kappa = 0$. The energy levels of nearly prolate ($\kappa \approx -1$) or nearly oblate ($\kappa \approx +1$) asymmetric rotors differ from the limiting symmetric-top for which the levels with a given nonzero value of K_a and K_c are always degenerate. In the asymmetric rotor the two levels corresponding to a given value of K_a or K_c are separated. When the degeneracy in the asymmetric top is removed, the separation of the K_a or K_c levels is a function of J and K. In the rotational spectrum this is observed as the so-called K-doubling. For $K = 0$ the splitting is not possible, while the largest splitting observed for a given J takes place for $K = 1$. The doubling rapidly decreases with

K and increases with J.

For a nearly prolate asymmetric top it is expected that the spectrum is similar to that of a prolate symmetric top. The separation of groups of lines for a given $J + 1 \leftarrow J$ transition is close to $B + C$. Cyanamide and acrylonitrile are examples of nearly prolate asymmetric tops.

Selection rules for asymmetric rotor transitions with respect to J are $\Delta J = 0, \pm 1$. The condition $\Delta J = 0$ gives rise to $Q-$branch, $\Delta J = -1$ to $P-$branch and $\Delta J = +1$ to $R-$branch transitions. Asymmetric rotors can have three nonzero components of the dipole moment μ_a, μ_b and μ_c giving rise to three types of transitions governed by different ΔK_a and ΔK_c rules, which are summarised on page 256 of [12].

2.2 Distortable-Rotor Hamiltonian

The rigid-rotor model is very convenient for describing the energy levels of an asymmetric rotor. However, molecules are not rigid and the centrifugal force induced by rotation causes atoms to shift away from their equilibrium positions. This effect is apparent in every rotational spectrum as deviations of rotational line positions from those predicted by the rigid-rotor model. Usually, discrepancies between the calculated and observed frequencies are small (a few MHz), but in some situations the nonrigidity effect can be significant even for low lying rotational levels. In order to account more accurately for the positions of rotational lines the rigid-rotor theory has been extended by introducing higher-order terms to the Hamiltonian. As has been mentioned above, these higher terms arise from distortion of the molecule by centrifugal forces, which lead to an effective dependence of the rotational constants on the angular momentum. The general form of the distortable-rotor Hamiltonian is written by adding various correction terms to the rigid rotor

$$\mathcal{H}_R = \mathcal{H}_{\text{rig}} + \frac{\hbar^4}{4} \sum_{\alpha\beta\gamma\delta} \tau_{\alpha\beta\gamma\delta} \hat{J}_\alpha \hat{J}_\beta \hat{J}_\gamma \hat{J}_\delta + \hbar^6 \sum_{\alpha\beta\gamma\delta\varepsilon\eta} \tau_{\alpha\beta\gamma\delta\varepsilon\eta} \hat{J}_\alpha \hat{J}_\beta \hat{J}_\gamma \hat{J}_\delta \hat{J}_\varepsilon \hat{J}_\eta, \qquad (2.22)$$

where $\mathcal{H}_{\text{rig}}$ is defined by Eq. 2.8, $\tau_{\alpha\beta\gamma\delta}$ are the fourth-order centrifugal distortion constants (quartics), and $\tau_{\alpha\beta\gamma\delta\varepsilon\eta}$ are the sixth-order centrifugal distortion constants (sextics).

α, β, γ, δ, ε, η can take on any of the values x, y and z of the molecule-fixed coordinates. The order of the centrifugal distortion constants depends on the highest power of the element of the angular momentum operator $\hat{J}_g$, where $g = x, y, z$. The fourth-order centrifugal constant is defined by

$$\tau_{\alpha\beta\gamma\delta} = -\sum_{i,j} \mu_{\alpha\beta}^{(i)} \left(f^{-1}\right)_{i,j} \mu_{\gamma\delta}^{(j)}, \qquad (2.23)$$

in which $\mu_{\alpha\beta}^{(i)}$ is the partial derivative of the $\alpha\beta$ component of the reciprocal moment of inertia tensor with respect to internal coordinate i, and $\left(f^{-1}\right)_{i,j}$ is an element of the inverse of the matrix of harmonic force constants $f_{i,j}$. The indices i, j enumerate

internal coordinates of the molecule. The sixth-order centrifugal constants consist of three terms: harmonic, Coriolis and anharmonic

$$\tau_{\alpha\beta\gamma\delta\varepsilon\eta} = \tau^{(\text{harm})} + \tau^{(\text{cor})} + \tau^{(\text{anh})}. \tag{2.24}$$

Each term can be calculated separately and the method of their calculation is given in detail on pages 153-156 of Ref. [13].

Equation 2.23 implies that there is isotopic-dependence of centrifugal constants, so that each isotopologue will have a unique set of centrifugal constants.
In the first sum of Eq. 2.22 there is a total 81 (3^4) terms and in the second sum 729 (3^6) terms. It has, however, been shown, that due to symmetry properties and commutation relationships the number of distinct τ coefficients, is significantly smaller, and only a few linear combinations of τ are determinable from the spectrum. In the case of the nonplanar asymmetric top the centrifugal procedure turned out to be a problem leading to some confusion. It was not clear which linear combinations of the τ constants could be obtained from analysis of the rotational spectrum. Finally, Watson showed [21] that there are only five determinable linear combinations of fourth-order and seven of sixth-order τ constants.

2.2.1 Reduced Hamiltonian

In order to derive the determinable centrifugal coefficients for an asymmetric top Watson [21] carried out a unitary transformation of the rotational Hamiltonian (2.22)

$$\mathcal{H}_R^{(\text{red})} = U^{-1}\mathcal{H}_R U^{\dagger}, \tag{2.25}$$

where the unitary operator ($U^{-1} = U^{\dagger}$) is defined by $U = e^{iS_3}e^{iS_5}$. S_3 and S_5 are transformation coefficients, which depend on the combinations of powers of J_x, J_y, and J_z,

$$
\begin{aligned}
S_3 &= s_{111}(J_xJ_yJ_z + J_zJ_yJ_x), & (2.26) \\
S_5 &= s_{311}(J_x^3J_yJ_z + J_zJ_yJ_x^3) + s_{131}(J_xJ_y^3J_z + J_zJ_y^3J_x) \\
&\quad + s_{113}(J_xJ_yJ_z^3 + J_z^3J_yJ_x). & (2.27)
\end{aligned}
$$

The definition of the s_{111}, s_{311}, s_{131}, and s_{113} parameters is given in [21] and their values depend on the reduction type discussed below.

The A-reduced Hamiltonian proposed by Watson assumes that

$$s_{111} = -\frac{4R_6}{B^x - B^y}, \tag{2.28}$$

where R_6 is a certain linear combination of distortion coefficients τ (definition in Table 8.7 in Ref. [12]), and B^x, B^y are rotational constants. This leads to the A

reduced-Hamiltonian. In representation I^r and up to sixth-order centrifugal constants this Hamiltonian has the form

$$
\begin{aligned}
\mathcal{H}_R^{(A)} &= \frac{1}{2}\left(B^{(A)} + C^{(A)}\right)\hat{J}^2 + \left[A^{(A)} - \frac{1}{2}\left(B^{(A)} + C^{(A)}\right)\right]\hat{J}_z^2 \\
&\quad + \frac{1}{2}\left(B^{(A)} - C^{(A)}\right)\left(\hat{J}_x^2 - \hat{J}_y^2\right) - \Delta_J\hat{J}^4 - \Delta_{JK}\hat{J}^2\hat{J}_z^2 - \Delta_K\hat{J}_z^4 \\
&\quad - 2\delta_J\hat{J}^2\left(\hat{J}_x^2 - \hat{J}_y^2\right) - \delta_K\left[\hat{J}_z^2\left(\hat{J}_x^2 - \hat{J}_y^2\right) + \left(\hat{J}_x^2 - \hat{J}_y^2\right)\hat{J}_z^2\right] \\
&\quad + \Phi_J\hat{J}^6 + \Phi_{JK}\hat{J}^4\hat{J}_z^2 + \Phi_{KJ}\hat{J}^2\hat{J}_z^4 + \Phi_K\hat{J}_z^6 + 2\phi_J\hat{J}^4\left(\hat{J}_x^2 - \hat{J}_y^2\right) \\
&\quad + \phi_{JK}\hat{J}^2\left[\hat{J}_z^2\left(\hat{J}_x^2 - \hat{J}_y^2\right) + \left(\hat{J}_x^2 - \hat{J}_y^2\right)\hat{J}_z^2\right] \\
&\quad + \phi_K\left[\hat{J}_z^4\left(\hat{J}_x^2 - \hat{J}_y^2\right) + \left(\hat{J}_x^2 - \hat{J}_y^2\right)\hat{J}_z^4\right],
\end{aligned}
\tag{2.29}
$$

where $A^{(A)}$, $B^{(A)}$, $C^{(A)}$ are rotational constants, Δ_J, Δ_{JK}, ... are reduced quartic distortion constants and Φ_J, Φ_{JK},... are reduced sextic distortion constants.
By using the angular momentum matrix elements defined in Eq. 2.12, 2.13, 2.16, and 2.17 we can obtain the following matrix elements for the A-reduced asymmetric top Hamiltonian

$$
\begin{aligned}
E_{J,K} &= A^{(A)}K^2 + \frac{1}{2}(B^{(A)} + C^{(A)})\left[J(J+1) - K^2\right] - \Delta_J J^2(J+1)^2 \\
&\quad - \Delta_{JK}J(J+1)K^2 - \Delta_K K^4 + \Phi_J J^3(J+1)^3 \\
&\quad + \Phi_{JK}J^2(J+1)^2K^2 + \Phi_{KJ}J(J+1)K^4 + \Phi_K K^6, \tag{2.30} \\
E_{J,K\pm2} &= \left\{\frac{1}{4}(C^{(A)} - B^{(A)}) + \delta_J J(J+1) + \frac{1}{2}\delta_{JK}\left[K^2 + (K\pm2)^2\right]\right. \\
&\quad - \phi_J J^2(J+1)^2 - \frac{1}{2}\phi_{JK}J(J+1)\left[K^2 + (K\pm2)^2\right] \\
&\quad \left. - \frac{1}{2}\phi_K\left[K^4 + (K\pm2)^4\right]\right\}f_\pm(J,K). \tag{2.31}
\end{aligned}
$$

The Hamiltonian matrix is still tridiagonal and is of the same form as for the rigid rotor. The energies are calculated in the same way as for the rigid rotor, and energy levels are labelled with the same notation. This Hamiltonian provides a complete description of centrifugal effects for most asymmetric tops.

In some cases, especially when the asymmetric top is very close to the symmetric top limit, and $B^x \simeq B^y$, the constant s_{111} becomes very large (see Eq. 2.28), and thus A reduction becomes inappropriate. The choice of a different representation, can make the denominator in s_{111} larger and also result in well determined centrifugal constants. It turns out that in this situation the most suitable description of centrifugal effects is by means of the so-called S-reduced Hamiltonian. In the S reduction the definition of the s_{111} parameter is different from that for the A reduction and is

$$
s_{111} = -\frac{2R_5}{2B^z - B^x - B^y}, \tag{2.32}
$$

where R_5 is some linear combination of the distortion coefficients τ (definition in Table 8.7 in Ref. [12]). The use of the s_{111} parameter in this form involves a different structure of matrix elements of the reduced Hamiltonian from that described for the A reduction. The nonzero diagonals satisfy extended rule (K, K), $(K, K \pm 2)$, $(K, K \pm 4)$, $\ldots$, $(K, K \pm n)$ for even n. This reduction has been proposed by Winnewisser [22], who showed that unusual K doubling for the DSSD molecule (nearly prolate asymmetric top, $\kappa = -0.99999934$), can be described only if off-diagonal matrix elements with the rule $(K, K \pm 4)$ and associated with quartic centrifugal distortion constants are used.

The problem of calculating and labelling of energy levels in the S reduction is similar to that described for the A reduction. The complete S-reduced Hamiltonian and matrix elements are given in detail in Ref. [21] as well as on pages 333-339 in Ref. [12].

Centrifugal distortion constants are evaluated from an empirical fit to rotational transitions, each of which is described by a given set of quantum numbers. The A and S reductions are often used exchangeably. Usually the A reduction is better for more asymmetric molecules, while the S reduction is necessary for tops with minimal asymmetry. However, as has been shown for acrylonitrile [23] ($\kappa = -0.980$), the type of the reduction does not have a significant influence on the quality of the fit, $\sigma_{\mathrm{rms}} = 1.0601$ for the A reduction and $\sigma_{\mathrm{rms}} = 1.0281$ for the S reduction.

The rotational constants and fourth-order distortion constants are determined first from rotational spectra. When sufficient experimental data is available, sixth-order and eighth-order constants can also be determined. Rotational transitions with high J and K improve the values of the higher order constants, because only rotational energy levels with high quantum numbers depend on higher order centrifugal constants. In many cases, some higher order centrifugal constants can improve the deviation of fit even though their values may be effective and have no physical meaning.

It is worth mentioning that rotational and centrifugal constants in the S reduction differ slightly from those obtained for the A reduction. In addition to this the A, B, C rotational constants determined from the fit of data with S or A reduced Hamiltonian are not pure rigid-rotor constants. Each contains a small centrifugal contribution, which depends on the type of reduction, and appropriate formulae are given in section 2.8.4 of this chapter concerning the r_m^{SE} molecular geometry.

Fitting and prediction of the rotational spectrum of asymmetric top molecules in different representations and reductions of the Hamiltonian can be perfomed with both ASFIT/ASROT [17] and SPFIT/SPCAT [24, 25] program packages. The ASFIT/ASROT package is limited to the pure rotational asymmetric top spectrum for a single vibrational state when rotational energy levels are labelled by three quantum numbers J, K_a and K_c. In the case of more complex spectra which require additional quantum numbers (see section 2.3) the SPFIT/SPCAT package should be used.

2.3 Nuclear Quadrupole Coupling

Another necessary correction to the rotational Hamiltonian $\mathcal{H}_R$ comes from nuclear quadrupole coupling. This coupling gives rise to hyperfine structure in the rotational spectra of those molecules which have at least one atom with nucleus characterised by nuclear spin I greater than $\frac{1}{2}$. Such nuclei have a nonspherical charge distribution and a nonvanishing electric quadrupole moment Q. Quadrupolar nuclei have nonzero spin angular momentum $\mathbf{I}$ given by

$$\mathbf{I} = [I(I+1)]^{1/2}\hbar^2. \tag{2.33}$$

The interaction between Q and the electric field of the molecule takes place through the electric field gradient and leads to coupling between spin $\mathbf{I}$ and rotational angular momentum, denoted by $\mathbf{J}$. The coupling is represented by the sum of vectors $\mathbf{I}$ and $\mathbf{J}$, to give the total angular momentum $\mathbf{F}$, which involves introduction of a new quantum number F. F describes energy levels of the split, hyperfine structure of a given rotational transition, and it can take the values

$$F = J + I, J + I - 1, \ldots, \mid J - 1 \mid, \tag{2.34}$$

where J is the rotational quantum number, and I is the spin nuclear momentum quantum number as already discussed above. The additional selection rule governing transitions between the hyperfine levels is

$$\Delta F = 0, \pm 1.$$

The first-order expression for the nuclear quadrupole interaction energies, which applies to all classes of molecules is given by [12]

$$E_Q = eQq_j \frac{2J+3}{J} Y(J, I, F). \tag{2.35}$$

The function $Y(J, I, F)$, is defined as

$$Y(J, I, F) = \frac{\frac{3}{4}C(C+1) - I(I+1)J(J+1)}{2(2J-1)(2J+3)I(2I-1)}, \tag{2.36}$$

where

$$C = F(F+1) - J(J+1) - I(I+1). \tag{2.37}$$

The expression for q_j depends on the rotor type. In case of an asymmetric rotor this quantity can be expressed in terms of the field gradient defined in the principal axes system as $q_{\alpha\beta} = \partial^2 V/\partial\alpha\partial\beta$, the average values of the angular momentum operators J_a, J_b, J_c, and the asymmetry parameter κ (Eq. 2.21). Details are given in Ref. [26]. The computer program ASQ1P, which embodies first-order formulae to predict hyperfine splitting in an asymmetric top with one quadrupolar nucleus is available on the PROSPE [17] website. The first-order quadrupolar Hamiltonian is based on

the approximation that this Hamiltonian is fully diagonal, since the effect of the off-diagonal elements on rotational frequencies is usually negligible. Nevertheless, for rotational spectra measured with the use of contemporary microwave spectrometers, the necessary corrections resulting from the off-diagonal elements of the Hamiltonian matrix must be treated explicitly in order to account for the hyperfine structure to experimental accuracy. The largest discrepancies from the first-order approach are observed for coupling by nuclei with large nuclear quadrupole moments such as ^{127}I ($I = \frac{5}{2}$) or for coupling by several quadrupolar nuclei. In this case the matrix elements of the quadrupolar Hamiltonian are successfully described with the use of irreducible tensor operator methods (Chapter XV of Ref. [12]). These methods give satisfactory results for prediction of hyperfine structure of the rotational transitions measured in supersonic expansion. The approach is successful even for coupling of several quadrupolar nuclei with large nuclear qudrupole moments, such as for the recently published [5] bromoform molecule $CHBr_3$ ($I = \frac{3}{2}$ for ^{79}Br, ^{81}Br).

From the analysis of the hyperfine structure in the rotational spectrum the field gradient $q_{\alpha\beta}$ for a quadrupolar nucleus can be determined. This quantity characterizes the environment of the quadrupolar nucleus for each molecule and has a unique value (see the discussion below). The actual fitted parameters of the hyperfine structure are the nuclear quadrupole splitting constants χ defined as

$$\chi_{\alpha\beta} = eq_{\alpha\beta}Q, \tag{2.38}$$

where Q is the nuclear electric quadrupole moment, and e is the value of the elementary charge. The value of Q has been determined from other experiments and for a given nucleus is a constant. In the general case the nuclear quadrupole splitting constants in the principal inertial axes are a tensor which has the form

$$\chi = \begin{pmatrix} \chi_{aa} & \chi_{ab} & \chi_{ac} \\ \chi_{ab} & \chi_{bb} & \chi_{bc} \\ \chi_{ac} & \chi_{bc} & \chi_{cc} \end{pmatrix}. \tag{2.39}$$

The diagonal constants are often satisfactorily determinable from only the first-order nuclear quadrupole splitting Hamiltonian. Owing to the Laplace condition, which restricts the potential in a charge free region, nuclear quadrupole splitting constants are in relationship $\chi_{aa} + \chi_{bb} + \chi_{cc} = 0$. This condition means that there are only two independent diagonal tensor elements, which can be determined from the analysis of the hyperfine structure of the rotational spectrum.

For convenience, it is possible to define the principal quadrupolar axes x, y, z, obtained by diagonalization of the inertial χ tensor in Eq. 2.39. The diagonalization procedure corresponds to an axis system rotation and gives the angles between the principal inertial axes and the principal quadrupolar axes. This angle can give precise information on the molecular structure in the region of the quadrupolar nucleus. The deviation from the cylindrical symmetry of the electron charge around the chemical bond to the quadrupolar atom is measured by the asymmetry parameter η. In the principal quadrupolar axes system this is given by

$$\eta = \frac{\chi_{xx} - \chi_{yy}}{\chi_{zz}}. \tag{2.40}$$

For an ideally cylindrical electron charge distribution this parameter is equal to 0.

For a molecule with a quadrupolar nucleus each rotational line is split into several hyperfine components. For $\Delta J = 1$ transitions the components corresponding to $\Delta F = 1$ are the most intense, and their intensity relative to components from other selection rules increases with J. The splitting of the hyperfine structure decreases with J so that at high-J the hyperfine structure is overlapped, and often not resolved in the spectrum. The width of the hyperfine structure and the number of hyperfine components depend on three factors: the number of the nuclei with $I > \frac{1}{2}$, the value of the spin-angular momentum I of the nucleus, and the absolute value of the nuclear quadrupole moment Q. In general, the higher the I for the quadrupolar nucleus and the larger the number of quadrupolar nuclei in the molecule the more complicated the hyperfine pattern that is observed. For instance, in the centimeter wave region the hyperfine structure arising from one ^{14}N nucleus is measured only for low J values with a spectrometer with frequency measurement precision higher than 0.1 MHz. In the millimeter and submillimeter wave range the hyperfine structure is collapsed, although it might be still visible for some rotational transitions. The ^{14}N nucleus with $I = 1$ has the lowest possible value of I to produce the hyperfine splitting, and for this nucleus $Q = 0.02044(3)$ barn. For molecules containing a halogen atom the hyperfine structure is broader and more complex and may be visible even for high J values. A good example is difluoroiodomethane molecule CHF_2I [30], since for the ^{127}I nucleus $Q = -0.710(10)$ barn, which is more than two orders of magnitude greater than for ^{14}N, and I for ^{127}I equals $\frac{5}{2}$. Another example of a molecule with complex hyperfine structure is bromoform $CHBr_3$ [5]. The relatively high values of Q and I ($Q = 0.313(3)$ barn for ^{79}Br, and $I = \frac{3}{2}$), and the presence of three quadrupolar nuclei cause each rotational centimeter-wave transition to be split into many tens of hyperfine components.

The values of the χ constants for a given quadrupolar nucleus in a molecule depend on the nearest surroundings of the nucleus, e.g. for ^{14}N in CH_3CN $\chi_{aa} = -4.2244(15)$ MHz [27] whereas in CH_3NC $\chi_{aa} = 0.4894(4)$ MHz [28]. χ constants are very useful, and conclusive in assignment of spectra of existing rotamers of a molecule. Rotamers are conformational isomers which differ by rotation about only one single bond. A different spacial distribution of atom groups in each rotamer implies different rotational spectra. The example of L-threonine shows that the values of χ constants for ^{14}N in the $-NH_2$ group are very sensitive to its orientation with respect to the rest of the molecule and to the inertial axes. On the basis of χ values obtained from rotational spectra and from reasonable quality *ab initio* calculations, spectra of several lowest energy rotamers of L-threonine have been unambiguously assigned [29]. The value of χ can have another practical meaning: comparison of the field gradient of a free atom with modified field gradient of this atom in a molecule can be interpreted in terms of the character of chemical bonding and its degree of hybridization (Chapter XIV of Ref. [12]).

In Chapter 6 of the dissertation the hyperfine structure of the rotational spectrum of pyruvonitrile is studied. If we neglect hydrogen atoms of the methyl group then

pyruvonitrile can be regarded as a planar asymmetric top with one ^{14}N quadrupolar nucleus. Nuclear quadrupole splitting tensor in the principal inertial axes system, has the form

$$\begin{pmatrix} \chi_{aa} & \chi_{ab} & 0 \\ \chi_{ab} & \chi_{bb} & 0 \\ 0 & 0 & \chi_{cc} \end{pmatrix}. \tag{2.41}$$

In this case a and b axes lie in the plane of the molecule and c axis is perpendicular to this plane (see Fig. 6.2). The diagonal quadrupolar constants are sensitive to the frequency of hyperfine components of the rotational spectrum and are easy to determine. On the other hand, for planar asymmetric molecules with one ^{14}N nucleus the off-diagonal constants are measured rather rarely due to their insufficient contribution to the frequencies of the hyperfine components. For pyruvonitrile the diagonal quadrupole constants have been determined with the use of the SP-FIT/SPCAT program package [24, 25]. Owing to the Laplace relation, the constants explicitly determined from the fit are $\frac{3}{2}\chi_{aa}$ and $\frac{1}{4}(\chi_{bb} - \chi_{bb})$, while χ_{ab} can be estimated on the basis of *ab initio* calculations. Diagonalization of the experimental nuclear quadrupole splitting constant tensor in the principal inertial axes system gives three nuclear quadrupole splitting constants in the principal quadrupolar axes system χ_{xx}, χ_{yy}, and χ_{zz}. Quadrupolar axes are chosen so that χ_{zz} has the largest absolute value, and then the x axis is usually placed in the ab plane of a molecule so that zx plane is coplanar with the ab plane, and y axis is perpendicular to this plane. In general, for planar asymmetric tops for which an atom with a quadrupolar nucleus (here ^{14}N) is the terminal atom in a chemical bond, the $z-$axis is close to the axis of the N$-$X chemical bond ($\sim 1°$). From the diagonalization the precise value of the angle between the z axis of the quadrupole-fixed, and the a axis of the molecule-fixed system can be obtained. This value can be compared with the structural value of $\angle$(N$-$X$-a$).

2.4 The Stark Effect

The Stark effect in the rotational spectrum leads to frequency shifts and splitting of rotational lines due to application of an external electric field $\mathcal{E}$. The resulting effects are called Stark shifts and Stark splitting. Measurement of these phenomena allows the most accurate determination of electric dipole moments of gaseous molecules. The Stark effect in rotational spectra results from the interaction of the electric dipole moment μ of a molecule with the uniform external electric field $\mathcal{E}$. The Stark effect Hamiltonian can be expressed in the general form

$$\mathcal{H}_{\mathcal{E}} = -\hat{\mu}\mathcal{E}, \tag{2.42}$$

where $\hat{\mu}$ is the electric dipole moment operator, and $\mathcal{E}$ is the electric field. Electric dipole moment and the electric field are assumed to be constant in magnitude, and the field has to have a fixed direction in space Z. The additional Z axis connected

with the external electric field causes that the M degeneracy is partially lifted (see Eq. 2.14) and for the simplest case of the diatomic molecule $(2J+1)$ levels result for a given value of J. M labels the component of the total angular momentum along the space-fixed axis Z, and can take values $|M| = 0, J - 1, J$. The selection rules for M are governed by the relative orientation of the Stark field and the microwave radiation. The most commonly observed transitions are for $\Delta M = 0$ and take place when the vector of the external electric field is parallel to the electric vector of the microwave radiation. The $\Delta M = \pm 1$ transitions are observed when these two vectors are perpendicular.

The Stark energies for rotational transitions can be evaluated from perturbation theory by using the symmetric rotor functions $\mid J, K, M\rangle$. From first-order perturbation theory the energy correction is proportional to the first power of the electric field $\mathcal{E}$. The first-order Stark effect is most commonly observed for symmetric tops, and takes place for $K > 0$, $M > 0$ components. The Stark shift of the $K \neq 0$ lines with respect to the zero-field line is given by

$$\Delta\nu^{(1)}(\Delta M = 0) = 2\left(\frac{\mu\mathcal{E}}{h}\right)\frac{KM_J}{J(J+1)(J+2)}. \tag{2.43}$$

Dipole moment is expressed in Debye units ($1\ \text{D} = 3.33 \times 10^{-30}\ \text{C m}$), and electric field in V/cm. The largest Stark shift is observed for $K = M = J$. Stark shifts are inversely proportional to the value of J but first order Stark effect can be observed even for high J values.

For $K = 0$ or for $M = 0$ the first-order Stark effect vanishes (Eq. 2.43), which could suggest that for these transitions no Stark shift is observed. Furthermore, for linear tops, for which the K quantum number is not applicable, Stark shifts should also not be observed. However, perturbation theory shows that higher-order corrections for such rotational transitions are nonzero. In these situations the proper description of the Stark effect involves a second-order correction. Stark shift for linear or symmetric tops for the $J = 0 \rightarrow 1$ rotational transitions takes the form

$$\Delta\nu^{(2)} = \frac{8}{15}\frac{\mu^2\mathcal{E}^2}{h^2\nu_0}, \tag{2.44}$$

and for $J \neq 0$

$$\Delta\nu^{(2)}(J \rightarrow J+1) = \frac{2\mu^2\mathcal{E}^2}{h^2\nu_0}\left[\frac{3M_J^2(8J^2 + 16J + 5) - 4J(J+1)^2(J+2)}{J(J+2)(2J-1)(2J+1)(2J+3)(2J+5)}\right]. \tag{2.45}$$

From equations 2.43–2.45 it is apparent that the larger the value of effective dipole moment μ the lower the strength of the electric field that is required for a given Stark shift. The accuracy of the dipole moment determined from the Stark effect is higher when it is possible to observe large Stark shifts, thus rotational transitions with lower J values are preferable for Stark effect measurement. This results from the inverse proportionality of the shift with J for the first- and second order Stark shift.

For an asymmetric rotor there is no analytical expression describing the Stark effect. The solution of Eq. 2.42 in asymmetric rotor functions suggests that no first-order Stark effect should be observed. Usually, the Stark effect for an asymmetric rotor is second-order, and is proportional to $\mathcal{E}^2$. However, a near first-order effect for asymmetric tops may arise from near-degeneracy or degeneracy of rotational levels. For the nondegenerate case Golden and Wilson [31] gave an approximate expression for second-order shift which is proportional to M^2. For the near-degenerate case an intermediate-order Stark effect is observed, so that the second-order treatment is no longer applicable. The perturbation method developed by Van Vleck turned out to be very effective in dealing with near-degeneracies and degeneracies, and has been extensively used for analysis of Stark effect measurements in asymmetric tops. Details of this method are described in Chapter X of Ref. [12].

The presence of a nucleus with quadrupole coupling makes the Stark effect more complex. The total angular momentum quantum number is in this case the quantum number F, which arises from addition of the spin angular momentum and the rotational angular momentum described by quantum numbers I and J, respectively. The projection onto the space fixed axis as described by M_F can take on integer or half-integer values from $-F$ to F. The selection rule for M_F in a typical experimental setup is $\Delta M = 0$, but the less commonly observed $\Delta M \pm 1$ rule is also observed in the case of the perpendicular field configuration. For the molecule with a single quadrupolar nucleus three different cases can be identified. The weak field case, when $\mu\mathcal{E} \ll eqQ$, the strong field case $\mu\mathcal{E} \gg eqQ$, and the intermediate field case $\mu\mathcal{E} \approx eqQ$. Each case is described in Chapter 8 of Ref. [32]. The most commonly observed Stark effect in measurements with the pulsed, supersonic expansion Fourier transform microwave spectrometer (FTMW) (Chapter 3) is the third case when Stark splitting is comparable in magnitude to the quadrupolar splitting. At the same time this is the most difficult case for the analysis. Satisfactory results in the analysis of the Stark effect in the intermediate field regime are possible with irreducible tensor matrix methods, as described in detail in Ref. [33].

The QSTARK [34] program available from the PROSPE [17] database can be used for fitting/prediction of Stark shifts for various types of rotors with up to one quadrupolar nucleus. The energy matrix in QSTARK is set up by using irreducible tensor methods with matrix elements from [33, 35, 36]. The program enables to fit dipole moment components to the observed experimental Stark shifts by setting up and diagonalising a separate matrix for each combination of the electric field strength and the value of M_F. It is also useful for calibration of the applied electric field strength through the analysis of the Stark shifts of molecules with a well-known dipole moment such as OCS or CH_3CN. For Stark measurements with the FTMW technique the calibration of the electric field strength was performed with Stark shifts of CH_3CN and CH_3I [34, 37]. These two molecules have larger dipole moments and allow measurement of considerably larger Stark shifts for available electric fields than is the case for OCS.

2.5 Excited Vibrational States

In rotational spectroscopy we usually observe transitions between rotational energy levels in the ground vibrational level ($v = 0$). However, the rotational transitions in many excited vibrational states may also be observed. In spectra measured at room temperature the rotational transitions in excited vibrational states with energies of up to 500–1000 cm^{-1} usually have sufficient intensity for observation. The main factor which governs the intensity of transitions in excited vibrational states is the Boltzmann distribution $e^{(-kT/\omega_i)}$, where k is the Boltzmann constant, T is the temperature, and ω_i is the vibrational wavenumber of ith excited vibrational mode. A good example of the rotational spectra for the ground and the first excited vibrational state $v_{11} = 1$ is shown in Fig. 5.2 for the parent and four singly substituted species of acrylonitrile.

Analysis of rotational behaviour in the ground and excited vibrational states allowed formulation of the dependence of the effective rotational constants B_v^ξ on vibrational quantum numbers v_i

$$B_v^\xi = B_e^\xi - \sum_i \alpha_i^\xi \left(v_i + \frac{d_i}{2} \right) + \sum_i \sum_{i \geq j} \gamma_{ij}^\xi \left(v_i + \frac{d_i}{2} \right) \left(v_j + \frac{d_j}{2} \right). \qquad (2.46)$$

The sums run over all normal modes. B_e^ξ is the relevant equilibrium rotational constant, ξ denotes the principal axis. In general, the α^ξ constants are an order of 10^{-2} of the magnitude of B^ξ. The γ^ξ constants are of the order of 10^{-2} of the α^ξ, and are rarely determined from experiment. d_i is the vibrational degeneracy and is 1 for nondegenerate vibrations and 2 for doubly degenerate vibrations. For centrifugal constants a similar dependence to 2.46 can be formulated, but usually the vibrational dependence is too small to be determined. The rotation-vibration interaction constant α_i for the asymmetric rotor is given by

$$\alpha_i^\xi = -\frac{2(B_0^\xi)^2}{\omega_i} \left[\sum_n \frac{3(a_i^{(\xi n)})^2}{4 I_n} + \sum_j \left(\zeta_{i,j}^\xi \right)^2 \frac{(3\omega_i^2 + \omega_j^2)}{\omega_i^2 - \omega_j^2} + \sum_j \phi_{iij} a_j^{(\xi\xi)} \left(\frac{\omega_i}{\omega_j^{3/2}} \right) \right],$$
$$(2.47)$$

where ω_i is the vibrational wavenumber of the ith mode, while the $a_i^{(\xi n)}$ coefficient depends on the linear transformation matrix between internal valence coordinate and normal mode coordinate Q_i, and is defined by Eq. 12 in Ref. [39]. $\zeta_{i,j}^\xi$ is the Coriolis interaction parameter between normal modes i and j, and ϕ_{iij} is anharmonic cubic potential constant. The α_i term (2.47) can be considered to be the sum of three terms

$$\alpha_i = \alpha_i^{(\text{har})} + \alpha_i^{(\text{cor})} + \alpha_i^{(\text{anh})} \qquad (2.48)$$

The harmonic term arises from the quadratic dependence of B_i^ξ on the normal coordinate Q_i, which results in the mean square displacement of Q_i causing a change in rotational constant [39]. The Coriolis term arises from second-order Coriolis interaction between the i and j normal modes. The third term arises from the anharmonicity dependence of Q_i, which for small molecules is often the sole contributor to α_i.

If the vibrational state is isolated in energy then it can be treated with the same Hamiltonian as the ground state. In practice, however, vibrational states are sufficiently close to each other for the appearance of interstate perturbations which are discussed in the next section.

2.6   Fermi and Coriolis Interactions

The positions of the rotational energy levels in the ith excited vibrational state can be considered to result from the sum of the rotational and the vibrational energies. It might occur that rotational energy levels of different vibrational states are near degenerate. This happens when vibrational wavenumbers of the normal modes are very close in energy $E_\omega^i \simeq E_\omega^j$ such as for cyanamide (Chapter 4) or phenylacetylene (Chapter 7). In addition, the degeneracy can also occur for two relatively well separated vibrational states $E_\omega^j \gg E_\omega^i$ when some of the rotational levels of the i and j states for sufficiently large values of the K and J quantum numbers become very close. Other factors which facilitate perturbations are large rotational and centrifugal distortion constants. Such phenomena are observed in the THz spectra of acrylonitrile and its isotopologues (see Chapter 5). Moreover, the perturbation identified in acrylonitrile [23] is a prototype one since it arises from the interaction of the ground state rotational levels with those in the first excited vibrational state lying sufficiently high (228 cm^{-1}) above the ground state that the two states would normally not be expected to interact.

The near degeneracy of the rotational levels in different vibrational states induces coupling between these energy levels. The coupling can be very large and can shift the line positions substantially away from the pure rotational prediction. In this case a single state fit with a set of rotational and centrifugal constants is no longer adequate. However, for small perturbations the centrifugal constants might account for the influence of the perturbation on the rotational levels, which often results in effective values of centrifugal distortion constants, especially of D_{JK}. In general, the perturbation requires a more satisfactory treatment. For two nearly degenerate states labelled i and j, the rotational energy levels must be evaluated from the 2 $\times$ 2 block matrix containing the diagonal elements of i and j describing the pure rotational Hamiltonian, and an off-diagonal coupling term. This Hamiltonian for the coupled fit of the two states has the form

$$\mathcal{H} = \begin{pmatrix} \mathcal{H}_{\mathrm{rot}}^i & \mathcal{H}_{\mathrm{int}}^{(i,j)} \\ \mathcal{H}_{\mathrm{int}}^{(i,j)} & \mathcal{H}_{\mathrm{rot}}^j + \Delta E_{i,j} \end{pmatrix}. \tag{2.49}$$

The $\mathcal{H}_{\mathrm{rot}}^i$, and $\mathcal{H}_{\mathrm{rot}}^j$ are pure rotational Watsonian terms augmented by the energy difference $\Delta E_{i,j}$ between the i and j states. From the rotational data $\Delta E_{i,j}$ is usually determined with much higher precision than from even high resolution infrared spectra. The connecting off-diagonal term $\mathcal{H}_{\mathrm{int}}^{(i,j)}$ describes the interaction between vibrational states i, j, and is discussed below.

The most commonly observed type of coupling is the Coriolis interaction. The presence of degeneracy is not sufficient to produce Coriolis interaction. It is necessary for the vibrational modes to have appropriate symmetry. On the basis of symmetry arguments Jahn formulated a general rule for predicting which normal modes might be coupled by a Coriolis perturbation [40]. Each molecule possesses the symmetry elements of one of the symmetry point groups. Each of the $3N$ degrees of freedom, 3 rotations, 3 translations, and $3N - 6$ vibrations have the symmetry of one of the irreducible representations of the point group. Coriolis coupling between two normal modes Q_i, Q_j is possible when the product of the irreducible representation is an irreducible representation of the pertinent point group which contains rotation about one of the principal axes x, y, z

$$\Gamma(Q_i) \times \Gamma(Q_j) \in \Gamma(R_z), \tag{2.50}$$

where z denotes the rotation-axis.

The Coriolis perturbation can be described by the off-diagonal term in Eq. 2.49 which, in the case of the resultant rotation about the z axis, has the form

$$
\begin{aligned}
\mathcal{H}_{\mathrm{C}}^{(i,j)} &= i \left(G_z + G_z^J \hat{J}^2 + G_z^K \hat{J}_z^2 + G_z^{JJ} \hat{J}^4 + \ldots \right) \hat{J}_z \\
&\quad + \left(F_{xy} + F_{xy}^J \hat{J}^2 + F_{xy}^K \hat{J}_z^2 + F_{xy}^{JJ} \hat{J}^4 + \ldots \right) \left(\hat{J}_x \hat{J}_y + \hat{J}_y \hat{J}_z \right)
\end{aligned} \tag{2.51}
$$

where G_z, F_{xy} are constants determined from the fit, and z, x, y are the permutation of principal axes a, b, c. This Coriolis term results from $\mathcal{H}_{21}$ and $\mathcal{H}_{22}$ parts of the vibration-rotation Hamiltonian (Chapter 17.8 of Ref. [13]). The coupling constant G_z is related to the Coriolis coefficient $\zeta_{i,j}^{\xi}$ (here $\xi = z$) connecting the i and j vibrational modes

$$G_z = B^{\xi} \zeta_{i,j}^{\xi} \left(\sqrt{\omega_i/\omega_j} + \sqrt{\omega_j/\omega_i} \right), \tag{2.52}$$

where $\zeta_{i,j}^{\xi}$ is the Coriolis interaction parameter, which defines the efficiency of coupling between normal modes Q_i and Q_j. The G_z constant is in most cases a major parameter in the fit, and reflects the magnitude of the first-order Coriolis effect $\mathcal{H}_{21}$ and also contributions from higher-order Coriolis interaction.

Additional correction to the energy matrix results from the F_{xy} constant and its definition in terms of reduced axis Hamiltonian is given in Ref. [41]. F_{xy} proved to be very successful in perturbation analysis for $S(CN)_2$ [42], and in fitting the lowest states in an inversion potential, as discussed in subsection 2.7.1 and in results for cyanamide in Chapter 4. In many cases the Coriolis interaction takes place between vibrational modes for which vibrational indices exceed the condition for appreciable harmonic coupling in that they are not differ by unity. This higher-order, anharmonic interaction type was found in the interacting triad $v_4 = 3 \leftrightarrow v_8 = 1$ and $v_4 = 3 \leftrightarrow v_9 = 1$ in $S(CN)_2$ [42].

The lengths of the centrifugal distortion-type expansions on constants G and F in Eq. 2.51 are normally established empirically. The common practical difficulty encountered in analysis of Coriolis interaction is considerable correlation between fitted

constants: B^z, G_z and F_{xy}. This problem can be partly reduced by identifying and using in the fit those rotational transitions which clearly manifest the perturbation, as well as aiming for a large data set containing transitions governed by a variety of selection rules.

The contribution to rotational constants from the Coriolis coupling can be evaluated from the ζ term of Equation 2.47. The change of the rotational constants in state i with respect to the ground state arising from the i, j interaction is given by

$$\delta(B_i^\xi - B_0^\xi) = -\delta\alpha_i^\xi = \frac{2(B^\xi)^2}{\omega_i}\left(\zeta_{i,j}^\xi\right)^2 \frac{3\omega_i^2 + \omega_j^2}{\omega_i^2 - \omega_j^2}, \qquad (2.53)$$

Coriolis resonance produces large shifts of the rotational energy levels of a given vibrational level, and may also considerably perturb transition intensities. It might occur between higher excited vibrational states (overtones) and combination modes. The coupling is also possible between more than two states [42].

The nature of the perturbation is different in the case of coupling between two modes i and j with the same symmetry when the product of the irreducible representations of Q_i and Q_j defined by Equation 2.50 is fully symmetric. This type of interaction is called Fermi resonance. Fermi resonance is described by the off-diagonal term in Eq. 2.49, which is of the form

$$\mathcal{H}_F^{(i,j)} = W_F + W_F^J \hat{J}^2 + W_F^K \hat{J}_z^2 + \left[(W_\pm + W_\pm^J \hat{J}^2 + W_\pm^K \hat{J}_z^2 + \dots), \hat{J}_{xy}^2\right]_+, \qquad (2.54)$$

where $\hat{J}_{xy}^2 = \hat{J}_x^2 - \hat{J}_y^2$ and $[A, B]_+ = AB + BA$. The $W_\pm$ terms as written above result from the general expression for such a term incorporated in SPFIT [43]

$$\frac{1}{4}W_\pm^{n,m}\left[\left[\hat{J}_+^2 + \hat{J}_-^2, \hat{J}_a^{2n}\right]_+, \hat{J}^{2m}\right]_+, \qquad (2.55)$$

where $\hat{J}_\pm^2 = \hat{J}_x^2 \pm i\hat{J}_y^2$ and thus $\hat{J}_+^2 + \hat{J}_-^2 = 2\hat{J}_{xy}^2$.
The two-state Hamiltonian with off-diagonal Fermi terms is used for acrylonitrile in Chapter 5.

Both Coriolis and Fermi terms were determined in this dissertation from fitting the experimental data with the use of the SPFIT/SPCAT program package [24, 25].

2.7 Large Amplitude Motions

For some types of molecules certain vibrational motions are sufficiently large for their displacement vectors to be of the same order of magnitude as the molecular parameters r. These types of motions are called large amplitude motions. There are several types of large amplitude motions. In particular, internal rotation of protons in the methyl group $-CH_3$, and inversion of protons on the nitrogen atom

of the amino group –NH$_2$ are by far the most commonly encountered by rotational spectroscopy.

A representative example of large amplitude motion is the inversion motion in ammonia. The equilibrium configuration of NH$_3$ is pyramidal, but as a result of the large amplitude motion the molecule tunnels through the planar configuration to the energetically equivalent, but inverted, pyramidal configuration. The two identically equivalent configurations are separated by a potential barrier which hinders interconversion between the forms. Classically, the inversion from one minimum to the other one is possible when sufficient energy is available. Quantum mechanically, it may not be necessary to overcome the barrier in order to go from one minimum to the other. The phenomenon of quantum mechanical tunnelling allows a degree of penetration of the barrier. If the barrier is sufficiently low or narrow (or both) the penetration may be so great that an interaction occurs between the identical sets of vibrational levels in the two parts of the potential curve. This interaction splits the degenerate levels into two components, the splitting being greater towards the top of the barrier where tunnelling is more effective.

The lifting of the vibrational degeneracy allows this type of motion to be studied by rotational spectroscopy. Because each vibrational sublevel gives rise to its own spectrum, the number of measured transitions increases relative to the pure rotational prediction. Usually, even the rotational lines of the ground vibrational state are strongly perturbed, and demand an appropriate Hamiltonian, which is different for the inversion motion and for the internal rotation of the methyl group.

2.7.1   Inversion

This section is devoted to the inversion motion in molecules, and its implication on the rotational spectra. As has been mentioned above for the ammonia molecule, the conversion from one pyramidal configuration to the other through the planar configuration is possible by means of the inversion motion. This type of motion is often detectable in rotational spectra of NH$_2$$-$X-type molecules, for example in cyanamide (Chapter 4), and other known astrophysical species such as methylamine CH$_3$NH$_2$, and asymmetrically deuterated ammonia NH$_2$D, ND$_2$H. Ring-puckering of cyclic molecules like cyclobutane can also be treated in terms of inversion motion [44]. The tunneling process through the potential barrier removes the degeneracy resulting in doublets of rotational transitions. Energy splitting between the vibrational substates is a function of the potential barrier height and is reflected in spacing of the observed doublets. For relatively low potential barrier the energy splitting might be so small that rotational levels in two substates 0^+ and 0^- resulting from lifting of the vibrational degeneracy in the vibrational ground state can be strongly affected by mutual interaction. The 0^+, 0^- notation assumes $E(0^-) > E(0^+)$. In the case of strong perturbation it is necessary to carry out simultaneous fit of the data, by taking account for the higher order, Coriolis-type interaction connecting these substates. For two coupled states 2×2 block Hamiltonian should be used, as

given by Equation 2.49. The interstate coupling term for inversion is expressed in the reduced axis system Hamiltonian suggested by Pickett [41]

$$\mathcal{H}_{\text{int}}^{(0^+,0^-)} = \left(F_{xy} + F_{xy}^J \hat{J}^2 + F_{xy}^K \hat{J}_z^2 + F_{xy}^{JJ} \hat{J}^4 + \dots \right) \left(\hat{J}_x \hat{J}_y + \hat{J}_y \hat{J}_z \right), \qquad (2.56)$$

which is equivalent to second-order Coriolis coupling term (second part of Equation 2.51). The x and y denote the plane between the two inverting configurations. The coupled fit of the measured rotational frequencies is possible with the SP-FIT/SPCAT program package [24, 25]. The notation of the inversion substates (0^+, 0^-, 1^+, 1^-, ...) is used in the analysis of cyanamide, but they are often simply denoted by integer numbers 0, 1, 2, 3 etc. For correct intensity prediction of rotational transitions in the inversion spectrum it is necessary to take into account the symmetry of the vibrational function, which according to the first notation is symmetric for states denoted by +, and antisymmetric for the – substates.

Double Minimum Potential

The nature of the spectra of molecules with the inversion motion is usually discussed in terms of the inversion potential, thus it is worth to highlight its properties. The inversion problem can be reduced to one coordinate ϕ (see Fig. 4.1). One of the more successfull analytical forms of the simple one-dimentional double minimum potential is the quartic-quadratic oscillator

$$V(\phi) = a\phi^4 + b\phi^2, \qquad (2.57)$$

where a and b are constants describing the potential, and ϕ is a linear displacement along the vibrational coordinate.

The Hamiltonian for one-dimensional quartic-quadratic oscillator is given by

$$\mathcal{H}(\phi) = -\frac{\hbar^2}{2\mu}\hat{p}_\phi^2 + V(\phi), \qquad (2.58)$$

where $\hat{p} = -i\hbar\partial/\partial\phi$, μ is the reduced mass related to the inversion, and $V(\phi)$ is the potential defined by Equation 2.57.

Equation 2.58 can be transformed into a reduced form using a dimensionless coordinate z instead of ϕ

$$z = \left(\frac{2\mu}{\hbar^2} \right)^{1/6} a^{1/6}\phi, \qquad (2.59)$$

and defining new potential constants A, B

$$A = \left(\frac{\hbar^2}{2\mu} \right)^{2/3} a^{1/3}, \qquad (2.60)$$

$$B = \left(\frac{2\mu}{\hbar^2} \right)^{1/3} a^{-2/3}b. \qquad (2.61)$$

Hamiltonian 2.58 can then be written as

$$\mathcal{H}(z) = A\left(\hat{p}_z^2 + z^4 + Bz^2\right),$$

(2.62)

and the reduced quartic–quadratic potential function is given by

$$V(z) = A\left(z^4 + Bz^2\right).$$

(2.63)

A and B describe the shape of the potential, and B can be negative or positive. Negative value of B introduces a quadratic hump giving rise to double minimum potential, while a positive value of B leads to a single minimum potential. For $B = 0$ the potential is a pure quartic oscillator, and for $B \to \infty$ the function approaches the harmonic oscillator. Each value of B defines a set of eigenvalues that may be computed and then scaled by the parameter A. The z coordinate of the two minima is given by $z_{\min}^2 = -B/2$, and the height of the central barrier V_0 is equal to $AB^2/4$. The barrier height determines the magnitude of the splittings between the lowest inversion substates. In the two borderline cases of oxetane and monochloroamine (NH$_2$Cl) with barrier height of 15 cm^{-1} and 4400 cm^{-1}, respectively, the splittings are substantially different. For oxetane the differences between energy levels are $\Delta E_{1,0} = 52.90$ cm^{-1}, $\Delta E_{3,2} = 104.44$ cm^{-1} [45], whereas for monochloroamine the energy levels are nearly degenerate $\Delta E_{1,0} = 0.0023$ cm^{-1} [46], and $\Delta E_{3,2} = 0.162$ cm^{-1} [47]. The double minimum potential for cyanamide and its deuterated species is given in Fig. 4.6.

The reduced mass μ for the inversion motion of the NH$_2-$X-type molecules is a complex function of structural parameters. In general, for NH$_2-$X-type molecules a valid approximation is

$$\frac{1}{\mu} \simeq \frac{1}{4m_{\mathrm{H}_1}} + \frac{1}{4m_{\mathrm{H}_2}},$$

(2.64)

where m_{H} is the hydrogen mass. Derivation of the reduced mass is discussed on p. 229 in Ref. [32], and its explicit expression for cyanamide is given in Chapter 4 of this dissertation. Isotopic substitution in the molecule with inversion motion should not alter the shape of the potential and the barrier, however it causes changes in the inversion level spacing. In general, with an increase in the reduced mass for the inversion motion the splittings are reduced by the slower rate of tunneling through the potential barrier. In particular, substitution of the inverting hydrogen atom by deuterium substantially changes the energy levels positions, e.g. for NH$_3$ $\Delta E_{1,0} = 0.7934084(24)$ cm^{-1} [48], and for NH$_2$D $\Delta E_{1,0} = 0.40592793(39)$ cm^{-1} [49].

It is worth noting that Hamiltonian 2.62 does not have an analytical solution, thus the energy matrix is set up in the anharmonic basis set, which is a linear combination of the harmonic vibrational wave functions. The eigenvalues resulting from diagonalization of the energy matrix give the anharmonic energy levels. The eigenvalues as well as expectation values of the reduced coordinate $\langle z^2 \rangle_{vv}$, $\langle z^4 \rangle_{vv}$ have been tabulated for values of B from 0 to -10 in Ref. [50]. Energies, eigenvectors and vibrational transitions for a reduced, one-dimensional anharmonic potential on the basis of known A and B constants can also be calculated with program

ANHARM, which is available from the PROSPE website [17]. The program has been recently used in determination of the energy levels of the ring-puckering mode of 1,3-benzodioxole [51].

2.7.2   Internal Rotation

For molecules which have the methyl group –CH_3, the group can rotate about the single bond with respect to the rest of the molecule, and such motion is called internal rotation. If we consider asymmetric top molecules, then internal rotation can lead to three energetically equivalent positions of the methyl group in the molecule. The tunneling effect, analogous to the inversion in ammonia, splits each torsional level into a nondegenerate A component and a doubly degenerate E component. In consequence, each rotational line is a doublet of equal intensity components, its splitting is a sensitive function of the potential barrier of the hindered rotation. If the barrier is very high then the torsional motion corresponds to harmonic oscillation and no splitting of the rotational lines is observed (A and E components are degenerate). For a very low barrier the internal motion can be regarded as a free rotation. In order to analyze rotational spectra of pyruvonitrile – CH_3COCN (Chapter 6) three different approaches implemented in three different programs have been used. The programs have been deposited by their authors on the PROSPE website [17] and their underlying methods are briefly described in the subsections below.

A good starting point for the description of the utilized methods is the model Hamiltonian for an asymmetric rotor with a single methyl internal rotor, which is given in the principal axes system by

$$\mathcal{H}_R = \mathcal{H}_R^{(\text{red})} + \mathcal{H}_\mathrm{I}, \tag{2.65}$$

where $\mathcal{H}_R^{(\text{red})}$ is a standard reduced Watson Hamiltonian (Eq. 2.29), and the $\mathcal{H}_\mathrm{I}$ term describes the internal rotation of the methyl group defined as

$$\mathcal{H}_\mathrm{I} = F(\hat{j}_\alpha - \rho^\dagger \hat{J})^2 + V(\alpha). \tag{2.66}$$

The F constant is the internal rotation constant defined by

$$F = \frac{\hbar^2}{2rI_\alpha}, \tag{2.67}$$

where I_α is the moment of inertia of the methyl top, and $r = 1 - \sum_z \lambda_z^2 I_\alpha / I_z$, λ_z ($z = a, b, c$) are direction cosines of the internal rotation axis i of the top in the principal axes system. Components of the ρ vector are given by $\rho_z = \lambda_z I_\alpha / I_z$. $\hat{j}_\alpha$ is the angular momentum operator of the internal rotation, and finally $\hat{J}$ is the total angular momentum operator.

The internal rotation potential function for methyl rotor top has a $2\pi/3$ periodicity and can be expressed by the Fourier series

$$V(\alpha) = \frac{1}{2}V_3\left(1 - \cos 3\alpha\right) + \frac{1}{2}V_6\left(1 - \cos 6\alpha\right) + \ldots, \tag{2.68}$$

where α denotes the torsional angle, V_3 is the potential barrier height, and usually $V_3 \gg V_6$.

The classification of different methods dealing with internal rotation is correlated with the choice of the coordinate systems and has been described in great detail in Ref. [52, 53].

SPFIT

The SPFIT program enables treatment of internal rotation doublets in the framework of the basic Principal Axis Method (PAM) Hamiltonian [54]. This method uses principal axes of the entire molecule as the coordinate system, and it is mostly appropriate for analysing spectra of molecules with intermediate and high barrier to internal rotation. In this approach the A and E sublevels are treated separately, since their physical behaviour is different. For the A sublevel standard semirigid Watson's Hamiltonian is sufficient to reach experimental accuracy. On the other hand the E state requires an additional term

$$
\begin{aligned}
\mathcal{H}_{\mathrm{I}}^{\mathrm{PAM}} \quad = \quad & (D_x + D_x^J \hat{J}^2 + D_x^K \hat{J}_z^2 + D_x^{JJ} \hat{J}^4 + D_x^{JK} \hat{J}^2 P_z^2 + D_x^{KK} \hat{J}_z^4 + \dots)\hat{J}_x + \\
& (D_y + D_y^J \hat{J}^2 + D_y^K \hat{J}_z^2 + \dots)\hat{J}_y.
\end{aligned}
\tag{2.69}
$$

The subscripts x, y of the coupling constants D denote the plane containing the internal rotation axis of the methyl group in the molecule. For a planar asymmetric top the plane of the internal rotation axis is in coincidence with the principal axes plane ab, so that the coupling constants D_a, D_b are determinable from a fit of the E state transitions, and $D_c = 0$. The coupling constants are defined by

$$
D_z = F\rho_z W_E^{(1)},
\tag{2.70}
$$

and $W_E^{(1)}$ coefficients have been tabulated in Ref. [55] for a given reduced barrier s defined by

$$
s = \frac{4V_3}{9F}.
\tag{2.71}
$$

The approximate values of the "true" structural rotational constants are defined by

$$
B^\xi = (B_A^\xi + 2B_E^\xi)/3.
\tag{2.72}
$$

This approximation should also be valid for centrifugal distortion constants.

The SPFIT program also allows fitting of the hyperfine structure in internal rotation spectra arising from the presence of quadrupolar nuclei. The value of the three-fold internal rotation potential barrier V_3 is determined indirectly in SPFIT from differences of rotational constants of A and E sublevels of a given vibrational state, or from D constants obtained from a fit of the E sublevel. The procedure has been summarised in Ref. [56].

The PAM approach has been recently applied to analysis of internal rotation spectrum of pyruvic acid [57] and o-chlorotoluene [56]. In this dissertation this

method is used to fit the E states of the ground and two excited vibrational states of pyruvonitrile (Chapter 6), and the results are compared with those from other methods described below.

XIAM

The XIAM program has been originally created to fit the rotational spectrum of an asymmetric molecule with up to three symmetric internal rotors and up to one nucleus leading to a weak nuclear quadrupole coupling in the spectrum. XIAM sets up the Hamiltonian in the principal axis system of the entire molecule but the internal rotor operator of each top uses the internal axes method (IAM) given by Woods [58] and modified by Vacherand *et al.* [59], which actually can be classified as "rho axis system" (RAM). Details on the coordinate axis system and numerical solution of the torsional problem applied in XIAM can be found in [60].

XIAM allows a simultaneous fit of A and E species of a given vibrational state with a single set of rotational and centrifugal constants, and a relatively small number of internal rotation parameters. For this reason this approach is much more efficient in comparison to the PAM method implemented in SPFIT. It is possible to fit centrifugal distortion constants of the overall rotation up to the sixth order in the Watson S and A reduction. Additionally, the empirical fourth-order distortion coupling constants between the internal and overall rotation are included [61], which are given by

$$
\begin{aligned}
\mathcal{H}_I^{\mathrm{RAM}} \;=\; & 2\Delta_{Jm}(\hat{j_\alpha} - \rho^\dagger \hat{J})^2 \hat{J}^2 \\
& + \Delta_{Km}\left[(\hat{j_\alpha} - \rho^\dagger \hat{J})^2 \hat{J}_z^2 + \hat{J}_z^2(\hat{j_\alpha} - \rho^\dagger \hat{J})^2\right] \\
& + \delta_m\left[(\hat{j_\alpha} - \rho^\dagger \hat{J})^2(\hat{J}_x^2 - \hat{J}_y^2) + (\hat{J}_x^2 - \hat{J}_y^2)(\hat{j_\alpha} - \rho^\dagger \hat{J})^2\right] \\
& + \delta_{c3J}\,\cos 3\alpha \hat{J}^2,
\end{aligned}
\tag{2.73}
$$

where Δ_{Jm}, Δ_{Km}, δ_m and δ_{c3J} are empirical internal rotation – overall rotation distortion constants. These constants are usually used in the fit in order to obtain a better reproduction of the observed spectrum. However, the use of only four coupling terms limits the applicability of the program to moderate-J and K transitions. For this reason XIAM has not been sufficiently verified for fitting high-J, large milimeter-wave datasets except for a recent paper on pyruvic acid [57] and in this dissertation. The neglect of some off-diagonal terms in torsional matrix elements used in XIAM is valid only in the high-barrier limit [52], which should be kept in mind when using the program. Nevertheless, the program delivers easily interpretable quantities such as potential parameters V_3, V_6, internal rotation constant F, and rho-parameters, e.g., the magnitude of the ρ vector which is in coincidency with the z axis of the RAM system, as well as Euler angles (β, γ) between the principal axes system and the rho system.

ERHAM

The ERHAM program uses an effective rotational-torsional Hamiltonian developed for a molecule with one or two internal rotors by Groner and coworkers [62, 63, 64]. The internal rotation Hamiltonian in this approach is set up in a rho-axis system, in which the reference z axis is parallel to the internal rotation vector ρ. The matrix elements of the effective Hamiltonian are expressed in the basis

$$|JKM\nu\sigma_1\rangle = |JKM\rangle|\nu\sigma_1(K)\rangle, \tag{2.74}$$

where $|JKM\rangle$ are symmetric rotor basis functions, and $|\nu\sigma_1(K)\rangle$ are torsional basis functions characterized by the vibrational quantum number v, and the torsional symmetry number σ_1 equal to 0 for the A states and ± 1 for the E states. J, K, M are rotational quantum numbers. The torsional basis functions can be expressed as a Fourier series. The matrix elements of the effective Hamiltonian [66, 67] are then given by

$$
\begin{aligned}
\langle JK'M\nu\sigma_1\,|\mathcal{H}_{\text{eff}}|\,JKM\nu\sigma_1\rangle &= \langle JK'M\nu\sigma_1\,|\mathcal{H}_{\text{eff-rot}}|\,JKM\nu\sigma_1\rangle \\
&\quad + \sum_{K_\rho} Y_{K',K}(K_\rho)\left[\epsilon_{q=0} + 2\sum_{q>0}\left(\epsilon_q \cos\alpha'_q\right)\right],
\end{aligned}
\tag{2.75}
$$

where $Y_{K',K}(K_\rho) = \langle JK'M|JK_\rho M\rangle\langle JK_\rho M|JK'M\rangle$, K_ρ is the J projection onto the rho axis system, and q is the Fourier expansion coefficient. The terms with $q > 0$ are called tunneling terms, and $\alpha = 2\pi q(\sigma_1 - \rho K_\rho)/3$. In this Hamiltonian the potential energy terms do not appear explicitly, although the tunneling coefficients of the internal rotation energy ϵ_q depend on these terms. $\mathcal{H}_{\text{eff-rot}}$ refers to the following Fourier series

$$
\begin{aligned}
\mathcal{H}_{\text{I}}^{\text{eff-rot}} &= \left(B200_{q=0} + 2\sum_{q>0}B200_q\cos\alpha_q\right)\hat{J}^2 \\
&\quad + \left(B020_{q=0} + 2\sum_{q>0}B020_q\cos\alpha_q\right)\hat{J}_z^2 \\
&\quad + \left(B002_{q=0} + 2\sum_{q>0}B002_q\cos\alpha_q\right)(\hat{J}_+^2 + \hat{J}_-^2) \\
&\quad + (\text{Centrifugal distortion terms}) + \ldots
\end{aligned}
\tag{2.76}
$$

$Bkpr_q$ are the tunneling coefficients in the effective rotational Hamiltonian analogous to the scheme in Ref. [63], and k, p, r define the powers of the associated angular momentum operators, $\hat{J}^k$, $\hat{J}_z^p$ and $\hat{J}_+^r + \hat{J}_-^r$. The tunneling coefficients $Bkpr_q$, and the tunneling energy coefficient $\epsilon_{q=0}$ are determined from fit. The $Bkpr_q$ notation has been used in this dissertation, however, recently the author of the ERHAM program modified this notatation such as in papers [65, 66, 67]. Both notatations of some

Table 2.1: Indices and names of the lowest order tunneling parameters in two notations used in ERHAM.

IQ1[a], IQ2	k	p	r	Notation 1[b]	Notation 2[c]
Energy tunnelling parameters					
$q,\ q'$	0	0	0		$\epsilon_{qq'},\ \epsilon_{10},\ \epsilon_{01},\ \epsilon_{11}$
$q,\ -q'$	0	0	0		$\epsilon_{q,-q'},\ \epsilon_{20},\ \epsilon_{02},\ \epsilon_{1,-1}$
Rotational constants					
$q,\ q'$	0	2	0	$B020_{qq'}$	$[A-(B+C)/2]_{qq'}$
$q,\ q'$	2	0	0	$B200_{qq'}$	$[B+C]/2_{qq'}$
$q,\ q'$	0	0	2	$B002_{qq'}$	$[B-C]/4_{qq'}$
Centrifugal distortion constants					
$q,\ q'$	4	0	0	$B400_{qq'}$	$[\Delta_J]_{qq'}$
$q,\ q'$	2	2	0	$B220_{qq'}$	$[\Delta_{JK}]_{qq'}$
$q,\ q'$	0	4	0	$B040_{qq'}$	$[\Delta_K]_{qq'}$
$q,\ q'$	2	0	2	$B202_{qq'}$	$[\delta_J]_{qq'}$
$q,\ q'$	0	2	2	$B022_{qq'}$	$[\delta_K]_{qq'}$
$q,\ q'$	6	0	0	$B600_{qq'}$	$[\Phi_J]_{qq'}$
$q,\ q'$	4	2	0	$B420_{qq'}$	$[\Phi_{JK}]_{qq'}$
$q,\ q'$	2	4	0	$B240_{qq'}$	$[\Phi_{KJ}]_{qq'}$
$q,\ q'$	0	6	0	$B060_{qq'}$	$[\Phi_K]_{qq'}$
$q,\ q'$	4	0	2	$B402_{qq'}$	$[\phi_K]_{qq'}$
$q,\ q'$	2	2	2	$B222_{qq'}$	$[\phi_{JK}]_{qq'}$
$q,\ q'$	0	4	2	$B042_{qq'}$	$[\phi_K]_{qq'}$
Coriolis tunneling parameters					
$q,\ q'$	0	1	0	$B010_{qq'}$	$[G_z]_{qq'}$
$q,\ q'$	0	0	1	$B001_{qq'}$	

[a]The parameters IQ1 and IQ2 indicate to which localized state a tunneling parameter is related to. For molecules with single internal rotor only one parameter IQ1 is used.

[b]The notation of the tunneling parameters $Bkpr_{qq'}$ of the effective Hamiltonian 2.76 used in Ref. [63] and in this work. k, p, r define powers of the associated angular momentum operators J, J_z, and $J_-^r + J_+^r$, respectively.

[c]The modified notation of the tunneling parameters used in Ref. [65].

important tunneling parameters have been collected in Table 2.1. The specification of the tunneling constant names used in ERHAM can also be found on the PROSPE website [17].

The program treats A and E levels together, but it can not deal with several torsional states simultaneously. ERHAM determines the magnitude of the F constant, the value of vector ρ, the Eulerian angle between the rho-axis and the principal axes system, and the torsional energy difference ΔE_{A-E}. The program uses quartic, sextic and octic centrifugal distortion constants in both S and A reduction of Hamiltonian. With the current release it is not possible to fit hyperfine structure of torsional spectra arising from quadrupolar nuclei in the molecule.

Recent investigations of torsional spectra showed that ERHAM is a very efficient tool for analysis of excited torsional states of many astrophysical species, such as acetone [68, 69], and dimethyl ether [70].

2.8   Molecular Structure

One of the main molecular properties determined by rotational spectroscopy is the molecular structure. Molecular structure is characterized by the position of each atom determined by the nature of the chemical bonds by which it is connected to its neighboring atoms. The positions of N atoms in a molecule are described by $3N$ coordinates of the Cartesian system, corresponding to $3N - 6$ independent internal parameters. Internals are composed of $N - 1$ bond lengths, $N - 2$ bond angles, and $N - 3$ non-planar angles (dihedral or torsional angles). For planar molecules (e.g. acrylonitrile) there are only $2N - 3$ independent internals.

The most unambiguous description of the geometry of a molecule is the equilibrium structure r_e. An equilibrium internuclear distance is the distance between two hypothetically vibrationless nuclei at the global minimum of the potential energy surface. The equilibrium structure has a well defined physical meaning, within the Born-Oppenheimer approximation it is isotopically invariant, and enables comparisons between molecular structures of various molecules.

The rotational constants determined from the analysis of the rotational spectrum contain structural information. The relations of rotational constants and moments of inertia to the molecular structure are given by equations 2.2, 2.3 and 2.9. It is known that even in the vibrational ground state the molecule undergoes zero-point vibrational motions. The experimentally determined rotational constants do not define the equilibrium molecular geometry but the effective structure, denoted as r_0.

Equilibrium rotational constants B_e^ξ are related to those in the vibrational ground state and excited states B_v^ξ by Equation 2.46. Usually, the second part of Eq. 2.46 is small enough to be neglected so that the relation between equilibrium and ground

state rotational constants can be simplified to

$$B_e^\xi = B_0^\xi + \sum_i \alpha_i^\xi \frac{d_i}{2}, \tag{2.77}$$

where the sum runs over all normal modes ($3N - 6$ for non-planar molecules, where N is the number of atoms in a molecule).

From the above equation it is apparent that for an N-atomic asymmetric rotor $3N - 6$ singly excited vibrational states should be studied in order to determine equilibrium rotational constants B_e^ξ. It should be noted that rotational constants of all excited vibrational states should have been properly corrected for small contributions from centrifugal constants, and larger contributions from Fermi and Coriolis resonances, which might influence the B_0^ξ constants significantly, and affect the derived equilibrium structure. For these reasons reliable experimental equilibrium constants are known mainly for diatomic and triatomic molecules. For most polyatomic molecules the determination of B_e^ξ constants is still out of reach experimentally.

In order to describe a complete molecular structure $3N-6$ independent internals must be determined. Rotational constants of the main isotopic species are insufficient for that purpose. Thus the spectrum of substituted isotopic species must also be studied in order to provide adequate data for the evaluation the structural parameters. In general, the more data on isotopologues, the better the quality of the determined structure. Thanks to high sensitivity of contemporary spectrometers many important singly substituted isotopic species can be measured in their natural abundance, e.g. ^{34}S (4.22%), ^{13}C (1.07%), ^{15}N (0.368%), ^{18}O (0.204%). However, isotopic substitution of hydrogen atoms in the form of isotopic species containing deuterium must be usually carried out by enrichment through chemical synthesis due to low isotopic abundance of ^{2}H (0.0115%).

In the subsections below several standard methods of the structure determination from only the ground-state rotational constants are described. The effective ground-state structure - r_0 is focused on first, then the simple Kraitchman's substitution method r_s is described. Next, two different techniques devised in order to obtain a near-equilibrium structure from the ground-state rotational constants are discussed: the mass-scaled r_m structure, and the semi-experimental equilibrium structure r_e^{SE}.

2.8.1 Effective Structure r_0

The structure determined directly from the B_0^ξ constants is called the effective ground-state structure - r_0. In this method structural parameters are fitted in a least squares manner in order to obtain the best reproduction of the ground state rotational constants B_0^ξ or I_0^ξ of all available isotopologues. The basic assumption in the r_0 structure is the structural invariance for different isotopic species. This assumption is valid only for the rigid equilibrium structure of the molecule. Isotopic substitution, particularly for hydrogen and any light atoms can produce a significant

Table 2.2: Effective and equilibrium bond distances for various iso-topologues of HCl.

	$r_0{}^a$/Å	$r_e{}^b$/Å	$r_m^{(1)c}$/Å	$r_m^{(L)d}$/Å
H^{35}Cl	1.28387			
H^{37}Cl	1.28386			
D^{35}Cl	1.28124			
D^{37}Cl	1.28123			
		1.27460	1.27456	1.27458

^{a}Data from Ref. [71]
^{b}Equilibrium value is the same for all isotopologues. Data from Ref. [72]
$^c c_{bb} = 0.01850$ u$^{1/2}$Å, [71]
$^d \delta_{\mathrm{H}} = 0.009192$ u$^{1/2}$Å, [71]

change in the zero-point vibrations, so that a given set of r_0 parameters cannot be expected to precisely reproduce the B_0^ξ of more than one particular isotopic species, see Table 2.2. The rotation-vibration contributions to the moments of inertia have inverse proportionality with atomic masses, so that the r_0 coordinates of the heaviest atoms are closer to the equilibrium structure r_e than those for lighter atoms.

Availability of plentiful experimental data for diatomic molecules allowed formulation of the relation between the averaged $\langle r \rangle$ and the effective structure r_0. $\langle r \rangle$ describes the average bond length associated with the average configuration of the atoms, evaluated by a partial correction for the effects of vibration, as described in Chapter XIII of Ref. [12]. The distance r_0 does not represent the averaged bond distance, but rather is defined in terms of reciprocal of the square root of the averaged inverse square bond distance

$$ r_0 = \left\langle \frac{1}{r^2} \right\rangle^{-1/2} \neq r_e. \tag{2.78} $$

For polyatomic molecules this relation is invalid because of Coriolis contributions. In general, the r_0 method gives sufficiently good results for rigid molecules, e.g. for methyldiacetylene [73] $r(\mathrm{C-H})=1.0549(3)$, $r(\mathrm{C\equiv C})=1.2091(7)$, $r(\mathrm{C-C})=1.3753(16)$ Å, while semi-experimental equilibrium r_e^{SE} parameters (see subsection 2.7.4) are 1.0613(3), 1.2085(6), and 1.3734(14) Å, respectively. The r_0 bond lengths are expected to be longer than those at equilibrium, and thus the $r_0(\mathrm{C-H})$ value is not reliable. This anomaly is reported quite often in the literature and it results not only from the rotation-vibration contributions themselves, but also from their large change between deuterium isotopologues and the parent species. It is not surprising, therefore, that the effective values of the structural parameters involved in large amplitude motions are usually in poor agreement with the equilibrium values. For the HCl$\cdots$H$_2$O dimer [71], the r_0 out-of-plane bend angle ϕ was found to be 10 degrees lower than $r_m^{(L)}$ and equilibrium ab $initio$ values. This discrepancy is associated with substantially different position of the effective and equilibrium parameters on the

potential energy surface.

The r_0 structure can be least-squares fitted with the use of the STRFIT program [71], which is available from the PROSPE database [17]. The initial molecular geometry is given in internal coordinates with explicit declaration of the optimized parameters.

2.8.2 Substitution Structure r_s

This method uses the ground state moments of inertia I_0^ξ of the main and of the substituted species. Kraitchman has shown [74] that single isotopic substitution of an atom is sufficient to determine directly the coordinates of that atom in the principal axes of the parent molecule. The structure obtained with this method is called substitution structure, and it is denoted as r_s. Very simple formulae for derivation of atomic coordinates favoured this method over r_0. Explicit expressions have been derived for linear, symmetric top, planar and nonplanar asymmetric top molecules [74], and for convenience have been built into the computer program KRA, which is available on the PROSPE website [17].

It is generally supposed that the r_s structure is a somewhat better approximation to the equilibrium structure than r_0. This expectation arises from the fact that for diatomic molecules the $\mid b \mid$ coordinate of an atom is calculated from the difference between the moment of inertia of a substituted species $I_0^{b'}$ and of the parent species, I_0^b

$$\mid b \mid = \left[\mu^{-1} \left(I_0^{b'} - I_0^b \right) \right]^{-1/2}, \tag{2.79}$$

where $\mu = M \Delta m / (M + \Delta m)$, M is the mass of the original molecule and Δm is the mass change on isotopic substitution. Rovibrational contributions ϵ^ξ to the moments of inertia can be defined as $\epsilon^\xi = I_0^\xi - I_e^\xi$, and depend on the atomic masses. The ϵ^ξ are slightly different for the parent and for the substituted species. Nevertheless, for diatomic molecules this formula allows for partial cancellation of the rovibrational effects to the ground state moments of inertia, which is an unquestionable advantage over the r_0 method. Costain has proved that for diatomic molecules the approximation

$$r_s = (r_e + r_0) / 2, \tag{2.80}$$

is always valid, resulting in the relation $r_e < r_s < r_0$. For polyatomic molecules there is no proof that the r_s structure should be closer to the equilibrium structure. Despite this, the Kraitchman's equations are based on ΔI_0^ξ, and it is anticipated that even incomplete cancellation of the rotation-vibration terms ϵ^ξ should give better results than r_0.

The error in the derived substitution coordinates is estimated from Costain's empirical rule

$$\delta z = \frac{K}{\mid z \mid}, \tag{2.81}$$

where K is generally set to 0.0015 [75]. It follows from the above equation that small coordinates are unreliable, since for $\mid z \mid < 0.15$ Å the expected error is larger than 0.01 Å. The substitution structure might also be unreliable for coordinates larger than 0.5 Å as has been shown for many cases in [76]. Another problem with the r_s structure are imaginary coordinates arising from rovibrational contributions, as found for anisole or benzaldehyde [77]. Finally, determination of a complete molecular structure with this method requires substitution of all atoms in the molecule. This is unattainable for atoms of some elements, such as fluorine which are found in nature only in one isotopic species [78].

2.8.3   The Mass-Dependence Structure r_m

The most recent version of this method of the structure determination has been proposed by Watson and coworkers [79]. It is built upon previous experiences in the use of mass-scaling to derive equilibrium-quality geometries - the earlier r_m method of Watson [80], and the r_m^ρ method from the Harmony group [81, 82, 83, 84]. In this updated method the isotopic-dependent rovibrational contribution to the moments of inertia is expressed in explicit mathematical form by two types of adjustable parameters c^ξ and d^ξ

$$\epsilon_0^\xi = c_\xi (I_m^\xi)^{1/2} + d_\xi (m_1 m_2 \cdots m_N / M)^{1/(2N-2)}, \qquad (2.82)$$

where N is the number of atoms in the molecule, M is the molecular mass, and ξ denotes inertial axes. The parameters c_ξ and d_ξ are fitted simultaneously with the r_m structural parameters for best reproduction of the observed, ground state moments of inertia I_0^ξ according to

$$I_0^\xi = I_m^\xi + \epsilon_0^\xi, \qquad (2.83)$$

where I_m^ξ is a rigid moment of inertia calculated directly from the fitted structural internals.

The first correction term c_ξ scales the moment of inertia with mass dependence. The second term d_ξ corrects for the anomalies arising from small coordinates [85], which are troublesome in the r_s method. These two terms do not have a well-defined physical meaning, as is apparent for HCl in Table 2.2, where c_{bb} as well as δ_H parameters (see below) reproduce the rovibirational contribution ϵ_0^ξ equally satisfactorily. The result in both cases is an HCl bond length very close to the equilibrium value. The c_ξ and d_ξ parameters tend also to be determined with significant standard error. The model which includes only the c_ξ terms in Eq. 2.82 is according to [79] denoted as $r_m^{(1)}$, and that with both c_ξ and d_ξ terms is called $r_m^{(2)}$.

In [79] Watson *et al.* also accounted for the small rotation of the principal axes system induced by isotopic substitution. In order to take it into account for an asymmetric rotor three diagonal and three off-diagonal c_ξ parameters in the form of a symmetric (3×3) matrix **c** are necessary. In practice the use of off-diagonal

parameters somewhat improves fit, but only when the rotation of axes upon isotopic substitution is large, such as in H_2O [79].

The substitution of hydrogen by deuterium is associated with an unusually large relative change in atomic mass causing large changes in molecular vibrations between isotopologues. This can cause anomalies in molecular structure determinations. The Laurie correction term [86] has been added to the approaches proposed in [79] in order to determine more reliable $r_m(XH)$ bond lengths which are given by

$$r_m^{\text{eff}}(XH) = r_m(XH) + \delta_H\Big[\frac{M}{m_H(M - m_H)}\Big]^{1/2}, \qquad (2.84)$$

where δ_H is an adjustable parameter. For large M the value of δ_H is relatively invariant and is assumed to be equal to 0.010 u$^{1/2}$Å [86]. The inclusion of this term is identified in notation by a letter L, as in $r_m^{(1L)}$ and $r_m^{(2L)}$. The correction amounts to a shrinkage of the C–D bond of about 0.003 Å compared to the C–H bond but it does not significantly affect the other parameters [85]. In [79] Watson *et al.* examined this method for a number of well-known di-, tri- and tetra-atomic molecules. They showed that it gives a closer approximation to the equilibrium structure, than the standard r_s and r_0 techniques. Recently in [71] Kisiel showed that this approach delivers close to equilibrium structure for several examined molecular complexes: Rg$\cdots$HX, $N_2\cdots$HX, $H_2O\cdots$HX and Ar$_2\cdots$HX. The method gave encouraging results by taking proper account for the influence of the large amplitude vibrational motions on the ground state moments of inertia. The method was also successfully applied for relatively large molecules like phenylacetylene [87]. However, the r_m structure determination of the complex of phenylacetylene with argon [88] turned out to be difficult. This is caused by specific interaction of the rare gas atom with an aromatic molecule, that can be regarded as a nearly free-rotation. This anharmonic motion strongly influences the ground state moments of inertia in a way that is not well described by simple ϵ^ξ parameters.

The standard deviation of the least-squares fit with the r_m method is substantially lower than with the r_0 method (see Table 2.3). This method requires a comparable amount of isotopic data to that used by r_s, but it can also take advantage of multiple substitution. The $r_m^{(1)}$, $r_m^{(2)}$, $r_m^{(1L)}$, and $r_m^{(2L)}$ determinations have been incorporated into the STRFIT program [17].

2.8.4   Semi-Experimental Equilibrium Structure r_e^{SE}

Contemporary *ab initio* calculations have become a very useful aid in determination of accurate molecular structures. The state of the art level of calculation can provide good quality equilibrium structures r_e that can be used to verify experimental ones. *Ab initio* calculations at lower, but still acceptable level of theory provide reasonable quality force fields. The calculated quadratic and cubic force constants can then be used to calculate the rovibrational constants α_i^ξ (see Eq. 2.47). If the force fields are sufficiently accurate then the computed α_i^ξ can be used in place of experimental

Table 2.3: Molecular structure of silyl fluoride SiH_3F.

	$r(F{-}Si)/\text{Å}$	$r(Si{-}H)/\text{Å}$	$\angle(FSiH)/\,°$	Ref.
r_0	1.5953(9)	1.4743(14)	108.13(15)	[89]
$r_m^{(1),a}$	1.5882(6)	1.4691(1)	108.304(7)	[89]
$r_e^{SE,b}$	1.59048(6)	1.46948(9)	108.304(9)	[89]
$r_e{}^c$	1.5915	1.4675	108.037	[91]

$^a c_{aa} = 0.0242(5)\mathrm{u}^{1/2}\text{Å}$, $c_{bb} = 0.0478(47)\mathrm{u}^{1/2}\text{Å}$.

^{b}Rotation-vibration constants calculated at the CCSD(T)/cc-pCVTZ level.

^{c}Experimental r_e structure obtained from two isotopologues: $^{28}SiH_3F$ and $^{28}SiD_3F$.

rotation-vibration constants to correct experimental ground state rotational constants to equilibrium (Eq. 2.77). In view of the considerable effort required for the determination of equilibrium rotational constants this approach seems to be very promising. For small molecular systems it has recently become very popular thanks to still improving capabilities of computers and *ab initio* methods. The molecular structure determined with this method is called the semi-experimental equilibrium structure, and it is denoted as r_e^{SE}.

In order to determine the r_e^{SE} structure, the rotation-vibration contribution to the rotational constants should first be calculated. A reasonable level of *ab initio* calculation is such that accounts for electron correlation at least at the MP2 or better at the more expensive levels of theory like CCSD or CCSD(T), and uses a sufficiently large basis-set. The choice of the method and of the basis set can be tuned on the basis of comparison of the calculated and of the available experimental rotation-vibration constants α^ξ for the studied molecule. It is worth noting that experimental α_i^ξ for individual modes might be determined from a coupled fit of perturbed states, while *ab initio* usually gives the effective values of α_i^ξ. Coriolis perturbation between vibrational states is always associated with a given axis ξ of the coordinate system. The perturbation can significantly change the rotational constants connected with the ξ axis. In the case of an interaction between two excited vibrational states the contributions to rotational constants are of equal magnitude but have reversed signs. Thus the sum of the effective α_i^ξ and those with perturbation contributions should be equal. Details of evaluation of the Coriolis contribution to the rotational constants are discussed in Chapter 7.

The rotation-vibration contributions are relatively small but not negligible, and their values are usually close to $\backsim 1\%$ of those of rotational constants. Rotational constants are corrected according to Eq. 2.77.

The next, much smaller correction to experimental rotational constants results from the use of the reduced Hamiltonian in determination of the ground state rotational constants. The so-called determinable constants A, B, C introduced by

Watson [21] depend on the reduction type, and for the A reduction are given by (repr. I^r)

$$
\begin{aligned}
A &= A^{(A)} + 2\Delta_J \\
B &= B^{(A)} + 2\Delta_J + \Delta_{JK} - 2\delta_J - 2\delta_K \\
C &= C^{(A)} + 2\Delta_J + \Delta_{JK} + 2\delta_J + 2\delta_K,
\end{aligned}
\tag{2.85}
$$

in case of the S reduction

$$
\begin{aligned}
A &= A^{(S)} + 2D_J + 6d_2 \\
B &= B^{(S)} + 2D_J + D_{JK} + 2d_1 + 4d_2 \\
C &= C^{(S)} + 2D_J + D_{JK} - 2d_1 + 4d_2,
\end{aligned}
\tag{2.86}
$$

where $A^{(A)}$, ... are the experimental constants in the A-reduction, $A^{(S)}$, ... are the experimental constants in the S-reduction. However, these constants are still affected by small centrifugal distortion effects. The "true" rigid constants [90] are given by

$$
A_r = A + \frac{1}{2}\left(\tau_{bbcc} + \tau_{abab} + \tau_{acac}\right) + \frac{1}{4}\tau_{bcbc}
\tag{2.87}
$$

$$
B_r = B + \frac{1}{2}\left(\tau_{ccaa} + \tau_{bcbc} + \tau_{baba}\right) + \frac{1}{4}\tau_{caca}
\tag{2.88}
$$

$$
C_r = C + \frac{1}{2}\left(\tau_{aabb} + \tau_{caca} + \tau_{cbcb}\right) + \frac{1}{4}\tau_{abab}
\tag{2.89}
$$

Another small correction to the rotational constants arises from the electron distribution around the nuclei. The electronic correction is calculated from relation

$$
B_{el}^{\xi} = \frac{B_0^{\xi}}{1 + \frac{m}{M_p}g_{\xi\xi}},
\tag{2.90}
$$

where $g_{\xi\xi}$ is an element of the molecular tensor $\mathbf{g}$ and is expressed in units of nuclear magneton, m is the electron mass, M_p is the proton mass, ξ refers to the principal axes of the molecule. The value of the $\mathbf{g}$ tensor can be determined experimentally from the analysis of the Zeeman effect on the rotational spectrum (Chapter XI of Ref. [12]) or from *ab initio* calculations. Zeeman effect on the rotational spectrum of silyl fluoride $^{28}SiH_3F$ gives $g_{aa} = -0.32$ and $g_{bb} = 0.1145$ [91]. The electronic correction for the rotational constant $A_0 = 85077.751(39)$ MHz [92] is 14.8 MHz, and for $B_0 = 14347.568984(40)$ MHz [93] is -0.9 MHz. Corrections resulting from the use of the reduced Hamiltonian for determination of A_0 and B_0 are 0.03 MHz, and 0.2 MHz, respectively, and those for the "true" rigid rotor constants are less than 0.03 MHz. When compared to rotation-vibration contributions, which are $\frac{1}{2}\sum_i \alpha_i^a = 842.1$ MHz and $\frac{1}{2}\sum_i \alpha_i^b = 80.75$ MHz [89] it is seen that the Hamiltonian and the electronic corrections are negligible. After calculating the necessary contributions to the experimental rotational constants of all available isotopologues the internals are fitted with the least-squares procedure for best reproduction of

Table 2.4: The approximate scaling behaviour [97] of computational cost, as a function of the number of basis functions N of various quantum chemistry methods.

Scaling behaviour	Methods
N^4	HF
N^5	MP2
N^6	CCSD
N^7	CCSD(T)

corrected experimental rotational constants or moments of inertia. This method gives better results than r_0 and it is expected to be more reliable than r_m, which often underestimates the bond lengths (Table 2.3). This method is limited by the number of electrons in the molecule N, since standard *ab initio* techniques scale as N^5 for MP2 or $N^6 - N^7$ for coupled cluster methods (see Table 2.4). For this reason reasonable quality r_e^{SE} structures are still obtained only for relatively small molecules (up to 10 atoms).

The r_e^{SE} method has been used for determination of molecular structures of cyanamide (Chapter 4) and acrylonitrile (Chapter 5).

2.9   Quantum Chemistry Calculations

Quantum chemistry calculations constitute a valuable and complementary source of information on molecular properties, especially on those, which cannot be determined from experiment. In this dissertation theoretical calculations are used mainly for diagnostic comparisons of experimental data with theoretical results, without going into computational details. The size of the studied molecules and the performance of the available computers do not allow to use the "state-of-the-art" calculation levels. Thus for each case the author of the dissertation uses the theoretical level, which at moderate computational cost should give reasonable results, at least for semi-quantitative comparison with experiment. However, for some molecular properties, on which experimental data is rather scarce, such as rovibrational contributions to the ground state rotational constants (Eq. 2.47) or off-diagonal nuclear quadrupole coupling constants (Eq. 2.38) the best possible theoretical level is used to achieve reasonable values.

In this section a brief overview of the practical aspects of the *ab initio* methods used in dissertation is presented. Short description of the computational levels suitable for calculation of several types of basic molecular properties with references to the "state-of-the-art" benchmarks is also given.

Calculations presented in this work were done with the use of two freely available quantum chemistry program packages: PC-GAMESS [94, 95] and CFOUR [96]. For the presently studied molecules various methods have been used which include

electron correlation corrections to the energy, such as

- MP2 – second order Møller-Plesset perturbation theory,
- CCSD – Coupled Cluster which includes Singles and Doubles excitations,
- CCSD(T) – Coupled Cluster which includes Singles and Doubles excitations and also Triples calculated with perturbation theory.

The B3LYP approximation of the DFT theory has also been used.

Typical basis sets applied in the calculations were Pople's 6-31G(d,p) basis and Dunning's correlation-consistent basis sets cc-pVζZ, where $\zeta = $ D, T or Q.

Accounting for electron correlation is a prerequisite for reliable computation of molecular properties, thus nowadays the Hartree-Fock method by itself is rather rarely used in quantum chemical calculations. The type of the electron correlation correction to the energy and the length of the basis set is always a compromise between the quality of theoretical results and the cost required for calculations. The scaling behaviour as a function of the number of basis functions N is presented in Table 2.4. On the basis of the agreement with known experimental data a quality ordering [97] of the *ab initio* methods is as follows:

$$\text{Hartree Fock} < \text{MP2} < \text{CCSD} < \text{CCSD(T)}.$$

Analysis of rotational spectra delivers precise values of basic molecular properties discussed in the preceding sections. Results of quantum-chemical calculations performed with different theoretical approaches are often subjected to comparison with experimental values. These comparisons provide valuable information on the appropriate and optimal theoretical level to be used for calculation of chosen molecular properties. The benchmarks are often made for relatively small molecules utilizing high-level theoretical methods. In order to achieve spectroscopic accuracy it is often necessary to include several important contributions to observables, such as vibrational (zero-point) corrections, and those resulting from breakdown of the Born-Oppenheimer approximation. A short description of the recommended theoretical approaches for calculation of molecular properties is presented below. References to useful benchmarks are given. The recent review of Puzzarini *et al.* [98] presents a thorough summary of the accuracy of applied methods supported by different examples and accompanied by a short theoretical introduction to rotational spectroscopy and quantum-chemical methods.

1. *Molecular geometry*
   The CCSD(T) is the prefered method for calculation a good quality equilibrium geometry, which can be compared with molecular structures determined from rotational spectroscopy. For a sufficiently large basis set it gives results close to the molecular structure determined from experiment, e.g. for bond lengths the accuracy is at 0.002 Å, and for bond angles at $0.1 - 0.2°$ [99].

   A very useful benchmark, concerning the accuracy of rotational constants predicted by quantum-chemical calculations is given by Puzzarini *et al.* [100].

The benchmark includes molecules containing first-row elements only, all of which have been extensively studied by rotational spectroscopy. The authors recommend calculations at the CCSD(T) level of electron correlation. A high-quality computed equilibrium geometry should be obtained with the use of the extrapolation techniques to the complete basis set limit cc-pV∞Z, as discussed in [101]. For accurate prediction of the spectroscopically relevant ground state rotational constants A_0, B_0, C_0 it is necessary to include significant contributions to the values from experiment, such as zero-point vibrations or electronic contributions to rotational constants. For details see the discussion in Chapter 2.8.4.

2. *Dipole moment*
A systematic investigation of the accuracy of the molecular dipole moment from quantum chemical calculations has been carried out in Ref. [102]. Despite the fact that this benchmark is made only for small molecules it is also useful in the choice of the efficient level of calculation for larger molecular systems. Augmented basis sets with diffuse functions are important for improving the basis-set convergence, but the quality of the results depends more on the correlation treatment than on the cardinal number of the Dunning's basis set [102]. It should be kept in mind that the dipole moment must be calculated in the principal inertial axes in order to be compared with experiment.

3. *Nuclear quadrupole splitting constants*
This molecular property is defined in Eq. 2.38, and is calculated on the basis of the theoretical electric field gradient at the selected nucleus, and the experimental value of the electric quadrupole moment Q for this nucleus. For molecules containing a ^{14}N atom a comprehensive investigation towards efficient method of calculation, basis set, and scaling factor has been presented in Ref. [103]. For halogen nuclei relativistic corrections are required in order to obtain experimental quality nuclear quadrupole splitting constants [104]. On the other hand the popular scaling approaches of calculated values can also lead to predictions that are of use in experimental analysis [105].

4. *Spin-rotation constants*
The weak interactions between the nuclear magnetic dipole moment and the molecular rotation give rise to additional contributions to frequencies of hyperfine components in rotational spectra and are described by spin-rotation constants. The influence of the spin-rotation effect is often negligible being close to a few kHz. It is, therefore, usually determined only from analysis of rotational spectra measured at conditions of supersonic expansion, e.g. bromoform [5], or with the Lamb-dip technique, e.g. D_2O [106]. Electron-correlation effects, basis-set convergence, and vibrational corrections in determination of accurate theoretical spin-rotation constants are discussed in [98], and in references cited therein.

5. *Harmonic Vibrational Frequencies*
This calculation deals with the internuclear vibrations in the molecule at the

level of the harmonic approximation and computes quadratic force constants and the resulting normal mode vibrational frequencies ω_i. Vibrational frequencies are computed by determining the second derivatives of the energy with respect to the Cartesian nuclear coordinates or internal coordinates, such as bond lengths, angles, and dihedral angles. The harmonic force field calculations presented in the dissertation were performed mainly with the use of the PC-GAMESS package. Theoretical harmonic force constants can be used by the VIBCA [17] program for calculation of further observables useful for rotational spectroscopy such as fourth-order centrifugal distortion constants or Coriolis coefficients.

6. *Anharmonic force field*
   The anharmonic force field procedure has been implemented in the CFOUR program. The cubic and quartic force constants are calculated by numerical differentiation of quantum-chemical analytic second derivatives of the energy along displacements in normal coordinates (Eq. 1 and 2 in Ref. [107]). For a molecule with N atoms the differentiation procedure requires $6N - 11$ calculations of analytic second derivatives, or less if symmetry properties can be exploited. The cubic and quartic force constants are subsequently used to calculate vibration-rotation interaction constants (Eq. 2.47) for each vibrational mode. Finally, anharmonic corrections to harmonic frequencies ω_i are calculated from cubic and quartic force constants and structural parameters [107, 108] resulting in computational estimates of the fundamental vibrational frequencies ν_i. This can be a very time consuming calculation, and for the larger molecules of those presented in this dissertation, such as phenylacetylene, the anharmonic force field evaluation has been limited to rather rudimentary level of calculation. For further details on the efficiency of the method and of the basis sets preferred in the calculation of anharmonic force fields see Ref. [98].

Chapter 3

Experimental Details

The wide frequency range $(0.3 - 3000 \text{ GHz})$ in which rotational spectra can be measured leads to the use in contemporary rotational spectrometers of many different methods of signal acquisition, microwave radiation sources, detection techniques, and techniques of signal processing.

Rotational spectra can be measured at room temperature with broadband spectrometers. Complementary measurements can also be made at supersonic expansion conditions at effective temperatures of below 10 K with cavity Fourier transform, chirped pulse or with free-jet, Stark-modulation spectrometers [109]. Different experimental conditions in which rotational spectra can be measured have a direct influence on their appearance as well as on which molecular properties can be determined from their analysis.

In rotational spectroscopy the frequency range is related to the different measurement technique. The centimeter-wave region spectra $(0.3 - 30 \text{ GHz})$ are usually measured at supersonic expansion conditions. The molecular signal is detected in the time domain with Fourier transform spectrometers. The frequency accuracy of a rotational transition measured in supersonic expansion is estimated to be $1 - 2$ kHz. This high accuracy enables precise determination of several essential physical and chemical molecular properties such as the dipole moment, nuclear quadrupole coupling tensor, and spin-rotation coupling tensor. The low effective expansion temperature also allows observation of hydrogen bonded molecular complexes such as $H_2O \cdots HCl$ or van der Waals adducts such as benzene$-$rare gas atom.

The millimeter-wave $(30 - 300 \text{ GHz})$ and submillimeter-wave $(300 - 3000 \text{ GHz})$ rotational spectra are most efficiently measured in the frequency domain with broadband spectrometers. The expected resolution of the rotational spectrum is determined by the Doppler limited linewidths of the absorption lines but sometimes also by the experimental technique used for detection. The frequency measurement accuracy of the rotational transition is specified by a given experimental setup, but it is usually well below 0.1 MHz. Broadband millimeter- and sub-millimeter-wave spectra usually contain many different rotational transitions from R, Q (and sometimes P) branches up to high values of J and K quantum numbers. Such transitions

are in the ground and several low lying excited vibrational states. The most popular techniques embodied in contemporary broadband spectrometers are the PLL (Phase Locked Loop) technique in BWO based spectrometers [110], the FASSST method [111] and Cascaded Frequency Multiplication [112].

Continuous improvements in the performance of microwave devices allowed a significant increase in the sensitivity of contemporary spectrometers and in the frequency accuracy of measured spectra. A good example of the recent progress in centimeter-wave rotational spectroscopy is the broadband chirped-pulse Fourier transform microwave spectrometer [2, 3, 4], which significantly accelerates scanning over a wide frequency range. Additionally, successful combination of laser ablation with Fourier transform spectroscopy [113] has opened new possibilities in rotational spectroscopy. Laser ablation is a very efficient method of evaporating low volatility organic molecules of biological relevance which until recently were out of reach for rotational spectroscopy. Examples of such work are studies of natural amino acids, e.g. L-threonine [29] or guanine [114].

In this chapter the current configurations of the two spectrometers constructed at IFPAN in Warsaw are described. The spectrometers are the pulsed, supersonic expansion Fourier transform microwave spectrometer (FTMW), and the broadband millimeter wave spectrometer (MMW). These spectrometers have been used for recording part of the spectra analysed in this dissertation. Specific experimental conditions for measured species are described in the results chapters of this dissertation.

3.1 The FTMW Spectrometer at IFPAN

The first cavity FTMW spectrometer was constructed by Balle and Flygare [1], who applied time domain microwave spectroscopy to supersonic jets created inside a confocal Fabry-Pérot resonator placed in a vacuum chamber. The FTMW spectrometer at IFPAN is based on this original design but it embodies several key modifications for ease of use and improved sensitivity.

The FTMW spectrometer at IFPAN is presented in Fig. 3.1 and its basic operational principles can be described as follows. A gas sample is introduced perpendicular to the microwave resonator axis (as in the Balle-Flygare design). A short monochromatic microwave radiation pulse excites the gas sample, and after a short delay the molecular signal is observed in the time domain. The Fourier transform of the molecular signal gives the rotational spectrum in the frequency domain. This technique produced a significant improvement in frequency resolution (comparable to the sub-Doppler regime at room temperature) and in sensitivity, so that it provides insight into many hitherto unknown molecular properties discussed in the results chapters of the dissertation. The spectrometer, unlike the Balle-Flygare design, is constructed entirely from coaxial microwave elements. A schematic diagram and a detailed description of the first design of the FTMW spectrometer at IFPAN
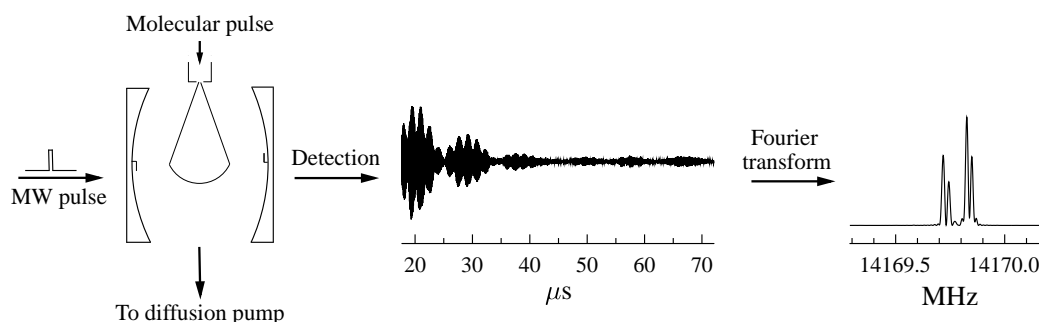
Figure 3.1: The operational principle of the pulsed supersonic expansion Fourier transform microwave spectrometer at IFPAN. The expanding molecular sample is excited by means of a short microwave pulse and the resulting molecular response signal is detected in the time-domain. The illustrated signal corresponds to two hyperfine transitions of the pyruvonitrile molecule (Chapter 6). The detected time-domain signal is averaged and subjected to a Fourier transform revealing the positions of the two rotational lines in the frequency domain. The lines at 14169.7309 MHz and 14169.8493 MHz belong to the hyperfine structure of the $2_{02} \leftarrow 1_{01}$ rotational transition in the ground state of the E species. The doubling in each line arises from the Doppler effect, and the average splitting is around 17 kHz.

are given in Ref. [115].

The increasing use of FTMW spectrometers, which took place in the 80's and 90's of the last century resulted in a number of other modifications of the original design. A popular alternative to the original Balle-Flygare is the coaxial arrangement of the microwave resonator and the gas expansion source as described in the COBRA-FTMW spectrometer [116]. This design also does not use any microwave waveguide components and has been successfully applied in many laboratories in the world.

In these measurements the investigated species are prediluted to concentrations of $0.1 - 2\%$ in a carrier gas (Ar or Ar+He), which is used at a total pressure of $0.5 - 3$ atm. The influence of the carrier gas on the intensity of the observed rotational transition is discussed in [77]. The gas mixture is pulsed into the resonator through an expansion nozzle which is an electromagnetically operated valve with a $0.3 - 0.5$ mm orifice. The duration of molecular pulses is usually from 0.8 to 1.5 ms, and the repetition rates range from 1 to 5 Hz. Gaseous substances like N_2 or HCl are usually diluted in a carrier gas and stored in a metal container. The gas mixture is transferred to the expansion nozzle through a T-type sample inlet arrangement containing two sample tubes. These are positioned just upstream of the expansion nozzle. In the case of liquid samples, the gas mixture is prepared by combining two streams of the carrier gas passed over a tube with a sample and over an empty tube. Substances with low vapour pressure such as urethane (Chapter 8.3) have been evaporated by using heated sample tubes, and a heated sample input system inclusive of the expansion nozzle. The temperature of the sample tubes and the nozzle could be varied during measurements to achieve the optimum saturation of the substance in the carrier gas.

Since the signal obtained from a single gas pulse often lies below the thermal noise, the measurement is repeated hundreds of times. Additionally, in order to

ensure undisturbed expansion of consecutive molecular pulses, an efficient high vacuum system has to be attached to the microwave resonator. The combination of a large (3000 l/s) oil diffusion pump with a fast (100 m^3/h) rotary pump continuously removes the introduced gas from the resonator and ensures background pressure at the level of 10^{-7} hPa.

An adiabatic expansion of the gas into a vacuum causes a significant decrease of the kinetic and rotational temperatures of the sample. The effective rotational temperature depends on the carrier gas [77], and the expansion parameters, but is usually close to 1 K. The high degree of rotational cooling considerably simplifies the rotational spectrum since only the low-J rotational transitions for the ground vibrational state are typically observed. For such low temperatures the maximum in the rotational absorption envelope is usually well below 20 GHz. Furthermore, due to minimized Doppler broadening effects in the pulsed supersonic expansion the linewidth is significantly reduced when compared to the room temperature static gas experiment.

The microwave resonator is a confocal Fabry-Pérot resonator formed by two aluminium mirrors of 50 cm diameter with 91 cm radius of curvature and at mirror separation of $(60 - 70$ cm). The mirrors are placed in a vacuum chamber of 60 cm diameter, which is directly attached to the pump system. One of the mirrors is kept fixed and the other is attached to a motorized translation stage, so that the distance between the mirrors can be adjusted for each polarization frequency. The stepper motor of the translation stage is controlled by the measuring computer program FTMW allowing for automatic tuning and recording of frequency scans.

The microwave power is applied to the resonator by an L-shaped antenna placed in the center of the movable mirror. The molecular signal is received by a second L-type antenna located in the fixed mirror. In order to obtain the maximum molecular signal the length L of the exciting and detecting antennas should be well-matched to the current wavelength λ. The antennas are easily changed and are chosen so that their length is in the range L $= \lambda/2 - \lambda/4$.

The pulse sequence during the single measurement cycle in the FTMW spectrometer at IFPAN is as follows. The molecular sample expanded into in the vacuum is directed between the mirrors of the microwave resonator. A short monochromatic microwave pulse of duration 1 μs is then applied to the resonator. The microwave pulse excites a range of frequencies (usually 1 MHz) around the pump frequency which may contain one of the resonant rotational transitions in molecules in the gas sample. Upon excitation the ensemble of molecules radiates a transient emission at the rotational resonance frequency, which is detected. The life time of excited states is usually short, and ranges from 50 to 150 μs so that the detection time in the FTMW spectrometer is similar. In order to avoid detection of the resonator response just after the microwave pulse a short delay of 20 μs prior to the detection of the molecular signal is necessary. The duration of the molecular pulse is relatively long in comparison to the microwave pulse and the detection time, so that typically from 10 to 20 microwave transient signals are recorded per single molecular

pulse. Before Fourier transformation, the transient signal is averaged over $50-1000$ molecular pulses. The number of the averaging cycles depends on the intensity of the measured transition as well as on other experimental conditions. The multipulse interferogram is averaged in a digital oscilloscope and then transferred to the computer only on completion of the measurement. The individual microwave segments are then coadded, and the result subjected to the fast Fourier transform procedure to yield the frequency domain spectrum. The principles of the pulse sequence in the FTMW experiment are clarified in the Flash movie available at [117].

A characteristic feature of the spectrum recorded with this type of spectrometer is a symmetric doubling of the rotational line (see Fig. 3.1). The doubling is caused by the Doppler effect, which results from conical shape of the expanding gas in the resonator leading to two dominant molecular ensembles with opposed translational vectors. The position of the center of the doublet corresponds to the molecular transition and it is invariant under changes in spectrometer operating conditions [1]. However, the magnitude of the splitting varies with experimental conditions.

The IFPAN FTMW spectrometer operates in the frequency range $2-20$ GHz. Since the molecular signal is at a very high frequency it has to be downcoverted to lower frequency, usually to the radiofrequency region before being processed by electronic devices. In the FTMW spectrometer at IFPAN there are two possible types of conversion of the detected signal. The first type is double conversion as originated in the Balle-Flygare design, and the second is the more recent single conversion. The two conversion methods are described in some detail below and the block diagram of the signal conversion process is presented in Fig. 3.2.

Double Frequency Conversion

In the first stage of the detection process the detected signal at frequency $f_{MW} - \Delta f$ is mixed with the phase-coherent signal $f_{MW} - f_{IF}$ (mixer M_1 in Fig. 3.2). Here f_{MW} denotes the pump frequency, Δf is the difference between the molecular signal frequency and the pump frequency, and $f_{IF} = 20$ MHz is the intermediate frequency defined by the electronics of the spectrometer. The signal out of this mixer is at the frequency $f_{IF} - \Delta f$, and it is the input to the second mixer M_2. The other input to this mixer is the intermediate frequency f_{IF}. The signal out of this mixer is at the frequency Δf, and then this time-domain signal Δf is recorded and averaged within a digital oscilloscope. This method provides complete demixing of the pump frequency f_{MW} from its difference from the molecular signal Δf, although the electronics used does not allow the phase (or sign) of this difference to be determined. Thus, in order to determine the absolute frequency of the molecular signal it is necessary to carry out two measurements at pumping frequencies $f_{mol} - \Delta$ and $f_{mol} + \Delta$, where Δ usually ranges from 0.2 to 0.25 MHz. The accuracy of the line center frequency, obtained with a peak finder routine from the spectrum after Fourier transformation, is estimated to be about $1-2$ kHz. The above description is related to the detailed diagram of the spectrometer presented in Fig. 1 of Ref. [115].
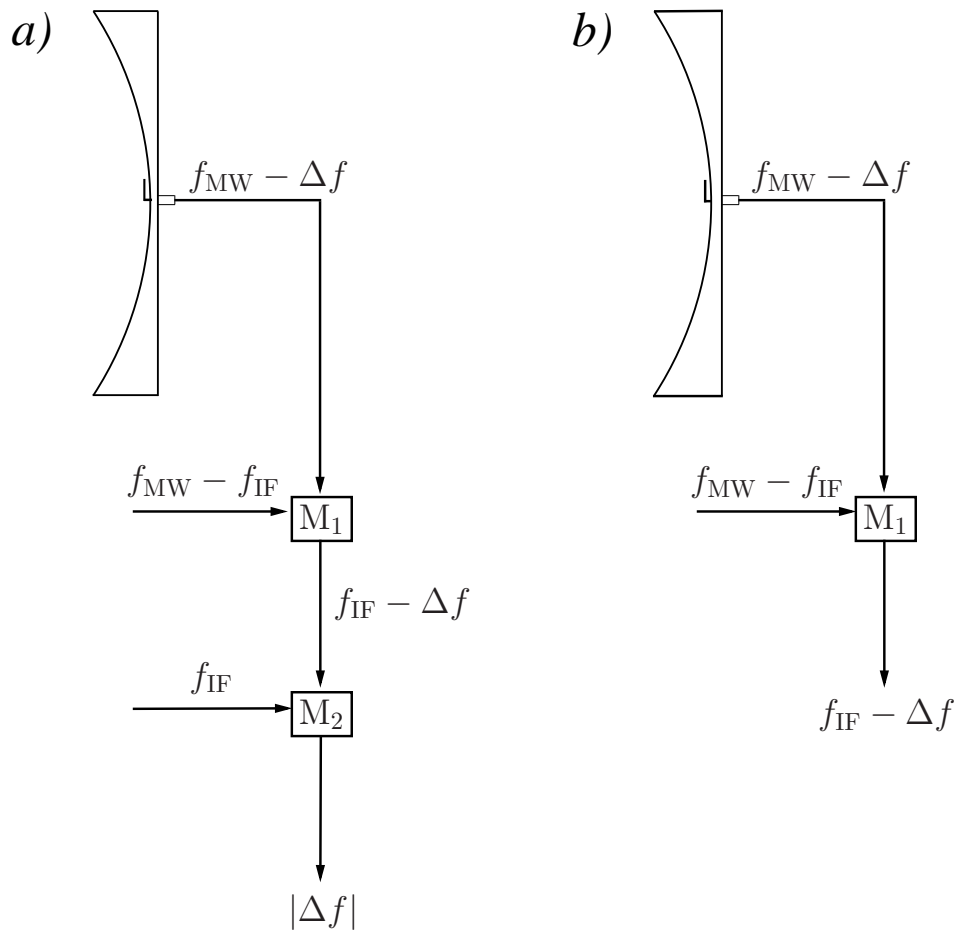
Figure 3.2: Diagrams of the signal conversion in the FTMW spectrometer at IFPAN, a) double frequency conversion, b) single frequency conversion. M_1, M_2 denote down-converting mixers, f_{MW} is the microwave pump frequency, f_{IF} is the 20 MHz intermediate frequency in these configurations, and Δf is the frequency offset of the molecular response signal f_{mol} from the pump frequency f_{MW}.

Single Frequency Conversion

In the double conversion configuration only the frequency difference of the molecular signal from the pump frequency, but not its sign, can be determined. This results in overlapping of the negative and positive frequency sidebands and requires from the user two individual measurements of a single line. Hardware solutions to the problem have been known for a long time and are based on demixing of the molecular free-induction decay to the region of some intermediate frequency f_{IF} followed directly by digitisation. There is an associated inconvenience of a strong spurious signal at the f_{IF} of choice and the established hardware solution involves pulse sequences with changing phase, such as CYCLOPS [116] or PAPS [118, 119].

In the single step conversion method applied in the FTMW spectrometer at IFPAN shown in Fig. 3.2b the $f_{IF} - \Delta f$ signal obtained from the M_1 mixer is digitized directly by the oscilloscope without additional electronic processing. The molecular

response signal is, in this case, obtained by a simple subtraction of the intermediate frequency cosine wave from the acquired time domain signal by a least squares fit of a constant amplitude signal. The intermediate signal IF is defined by

$$IF = A \cos \left(f_{IF} \cdot t + IF_{phase} \right) + IF_{shift}, \qquad (3.1)$$

where A is the amplitude of the intermediate frequency, f_{IF} is the intermediate frequency in MHz, t is time of the emitted signal, IF_{phase} is the phase of the intermediate signal, and IF_{shift} denotes a possible small shift in the signal level. There are three parameters in the fit A, IF_{phase}, and IF_{shift}. The initial values of these parameters are normally set automatically but can also be varied by the user towards better substraction of the intermediate frequency from the molecular response signal. This low cost software solution was found to work remarkably well. This method also facilitates scanning of relatively wide frequency ranges, because of easy addition of segments of the rotational spectrum into a simple synthetic spectrum. This is important in searches for rotational transitions of new molecular species, and analysis of the complex hyperfine structure in the rotational spectrum.

The IFPAN FTMW spectrometer is also equipped with a unique Stark electrode arrangement which enables measurement of the Stark effect (Chapter 2.4) at conditions of supersonic expansion. The electrodes are placed between the mirrors of a microwave resonator. The Stark electrode geometry has been developed in order to ensure a uniform electric field at the relatively large electrode separation of ~ 27 cm that is necessary in order not to perturb the microwave resonator. Detailed information on Stark effect measurement methodology and on the experimental setup developed at IFPAN has been given in [34, 37].

3.2   The MMW Spectrometer at IFPAN

The millimeter-wave spectrometer constructed at IFPAN is characterised by a number of features which have allowed access to the high-frequency, millimeter-wave region for studies of the complex rotational spectra of molecules at Doppler-limited accuracy. The spectrometer consists of the following fundamental elements: a relatively intense, monochromatic radiation source (one of several Backward Wave Oscillators or a MW-sythesizer aided with an active multiplier), a 3 m long absorption cell, and a sensitive detector (GaAs or InSb detectors). The early development of the spectrometer can be traced through published papers [120, 121], however, since the time of those reports, substantial advances in instrumental configuration have been made. Presently, there are two available modes in which the spectrometer operates: the basic PLL, BWO-based mode and the more recent one, embodying a cascaded multiplication frequency system. These two techniques are briefly described below.

The BWO-Based Mode

In this mode the spectrometer uses Istok BWOs (Backward Wave Oscillators) as radiation sources for the millimeter- and submillimeter-wave region. A set of four BWO tubes working in adjacent frequency ranges is used to cover the main operating region of the spectrometer of from 120 to 550 GHz. BWO is a relatively powerful source of monochromatic radiation $(1-50$ mW). Other very useful physical features are high inherent frequency accuracy and very broad electronic tunability which make it a suitable radiation source for spectroscopic applications. Since high resolution is a prerequisite in rotational spectroscopy, BWO tubes still need some additional frequency stabilization. In the millimeter-wave spectrometer at IFPAN the frequency stabilization to spectroscopic accuracy is achieved by means of two phase locked loops (PLLs), locking the source to a 3 GHz synthesizer. The technique of phase locking is based on mixing the source radiation frequency with harmonics of a reference frequency and monitoring of the difference signal. A detailed block diagram of the Warsaw millimeter-wave spectrometer is presented in Fig. 4 of Ref. [110] with schematic indication of the two PLLs. Signal detection is possible with the use of several different room-temperature diode detectors, such as WR3.4 and WR5.1 zero bias detectors from Virginia Diodes for higher frequency and Germanium based D-407 or GaAs Schottky based FARRAN SD-013 detectors at low mm-wave frequencies. In order to improve the sensitivity of the spectrometer a source modulation technique is used with suitable modulation applied in one of the phase locked loops. Lock-in detection at the second harmonic of the modulation frequency is employed and this leads to lines in the spectrum having a second derivative profile. A more detailed description as well as a comprehensive comparison of the PLL with FASSST techniques of recording rotational spectra is available in Ref. [110].

The Cascaded Multiplication Mode

Frequency up-conversion is a technique that has been used in rotational spectroscopy since its early days. However, the use of standard frequency multipliers resulted in the well-known problem of simultaneous observation of transitions at frequencies corresponding to different harmonics of the pump frequency. This was initially a desirable feature but it made studies of more complex spectra difficult. The impressive progress in communication technology in the 90's resulted in development of much improved microwave and millimeter-wave devices, including improved frequency multipliers. As described by Drouin *et al.* [112], the use of contemporary multipliers and chains of multipliers can be successfully implemented in rotational spectrometers to cover broad frequency ranges up to above 2 THz. The radiation generated in this way has all the desired criteria for spectroscopic applications, such as high spectral resolution, purity, large scanning range, and sufficient power.

As a first step in the implementation of the advances in millimeter-wave technology the broadband spectrometer at IFPAN has been upgraded with a millimeter-wave generator, detector and harmonic multipliers purchased from Virginia Diodes
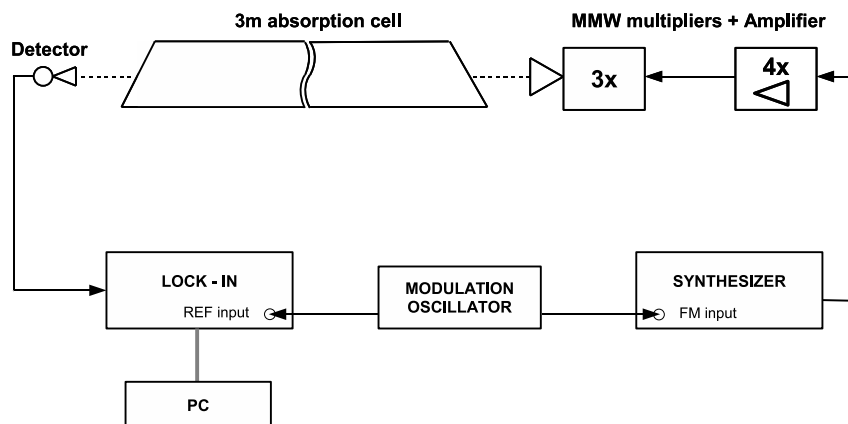
Figure 3.3: Schematic diagram of the cascaded multiplication frequency mode of the millimeter-wave spectrometer at IFPAN. The spectrometer uses a Systron Donner microwave synthesizer as a radiation source. The possible driving frequency input to the active amplifier multiplier chain system (VDI-AMC-S203) ranges from 7.5 to 11.66 GHz, with power less then 8.5 dBm. The total multiplication factor is 12 and the output frequency range is $90-140$ GHz at a power level of several mW. Computer control of the synthesizer, and the lock-in detection is provided by a measurement program utilizing standard GPIB protocols.

Inc. The millimeter-wave generator operates in the frequency range 90–140 GHz, and utilizes the technique of cascaded frequency multiplication. A harmonic multiplication source, which generates the 12th harmonic of the driving frequency from a microwave synthesizer allows coverage of the frequency region 90–140 GHz, which has hitherto been difficult to access with this spectrometer. Schematic diagram of this spectrometer configuration is presented in Fig. 3.3, and it is notable that no PLL loops external to the synthesizer are necessary.

3.3   Computer Programs

The majority of computer programs used in the analysis of spectroscopic data in this dissertation are collected on the PROSPE [16, 17] website. The programs range from simple useful tools such as PLANM for planar moment calculations or QDIAG for diagonalization of the quadrupole coupling constant tensor to more advanced, dedicated solutions to specific problems. All programs are freely available. The PROSPE page includes for each program a thorough description with examples of input and output data, a precompiled executable, and in most cases also the source code. In this section a more detailed discussion is given of the AABS package written by Kisiel and Pickett's SPFIT/SPCAT programs. These two program packages were the basic tools used in analyses of all rotational spectra, which are the subject of the dissertation.
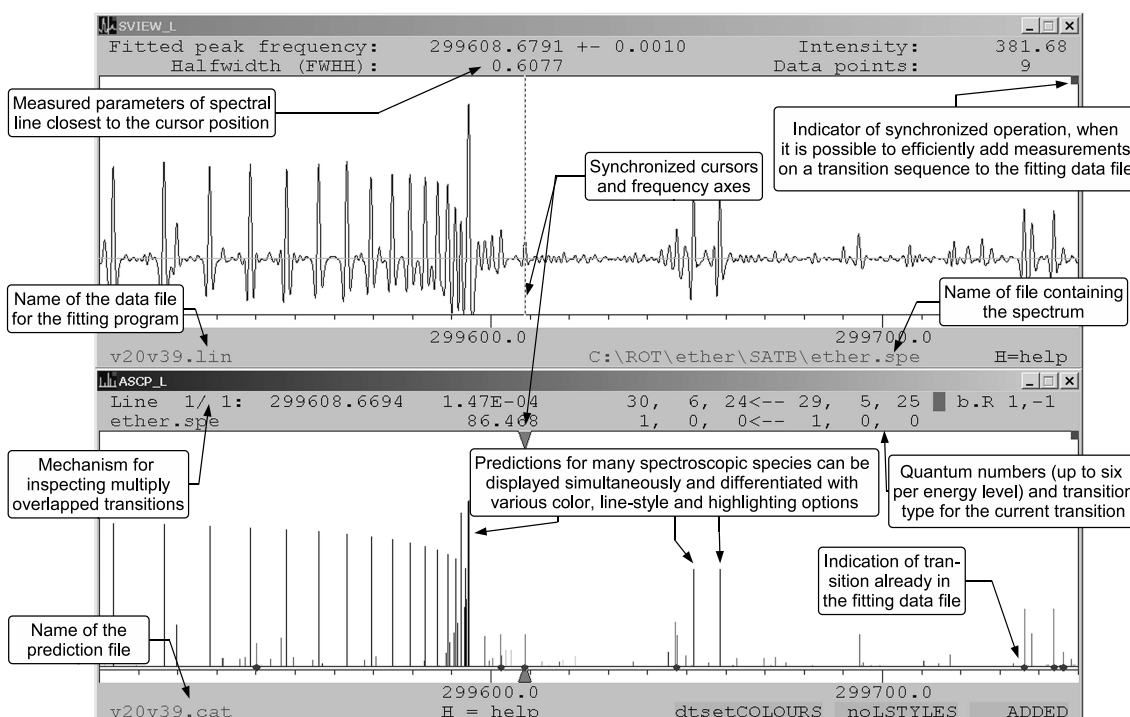
Figure 3.4: A greyscale approximation of the main display of the AABS scheme consisting of the spectral display window (program SVIEW_L) and of the predictions window (program ASCP_L). The two programs can be used separately, but in the AABS scheme their frequency axes are synchronized. The environment provides efficient facilities for reduction of broadband spectra resulting from transitions in multiple vibrational, isotopic or molecular species. Adapted from Ref. [127].

The AABS Package

The package called AABS, which is an abbreviation from "Assignment and Analysis of Broadband Spectra" is based on a pair of two computer programs, ASCP - a graphical program to display spectral predictions from ASROT [17] and from Pickett's program SPCAT, and SVIEW - a viewer for frequency domain spectra. These programs have been used extensively in the IFPAN laboratory and new versions called ASCP_L and SVIEW_L have been developed to deal with broadband spectra. In the AABS package these two programs have been synchronized in order to simultaneously display a measured spectrum in one window, and the current predictions in a second window. It is possible to display at the same time predictions for the various spectroscopic species, which are observed in a given spectrum. Synchronized control of the frequency axes of predictions and of the spectrum is provided, and standard zooming, scrolling and many other display modification commands are programmed in the package.

One of the most important features of the package is a special highlighting option of a predicted transition sequence of interest, by 'cloning' the current line. Frequency regions around successive transitions in this sequence can then be easily inspected

in turn, and if there are suitable lines in the spectrum those can be measured. The entry for the measured rotational line consisting of quantum numbers from prediction, the measured frequency and measurement error is automatically added to a specified datafile for one of several fitting programs. The next step is to fit spectroscopic constants and to make a new prediction from improved constants. The user can visually verify the compatibility of lines added to the fit by a simple refresh option of the prediction window. Subsequently, other sequences of lines that do not deviate too much from prediction can be easily added to the fitting data file. The whole procedure is performed until all measured transitions for a given spectroscopic species are included in the fit. This graphical process significantly facilitates and accelerates spectral assignment.

An alternative mode of operation is to draw a Loomis-Wood (LW) type plot of strips of the experimental spectrum centred on the frequencies of successive highlighted lines. This option is especially valuable in the earlier stages of assignment. Measurements and addition of data to the fitting file can be made in a very economic way in both the main display mode and in the LW mode. Examples of LW plots are presented in the results chapters of this dissertation, such as Fig. 5.3 and in Fig. 6.6.

The AABS package has been used in studies of many complex spectra, most recently those of acrylonitrile [23], bromoform [5], $S(CN)_2$ [42], pyruvic acid [57], and $ClONO_2$ [122, 123, 124]. This package is also successfully used for spectral assignment in other laboratories in the world, such as in the University of Bologna in Italy [125], or in the University of North Texas in the USA [126].

More detailed information on the AABS package is available in [127], and on the PROSPE website [17].

The SPFIT/SPCAT Package

The SPFIT/SPCAT program package has been written by H. M. Pickett [24, 25] of Jet Propulsion Laboratory. SPFIT is used for fitting the values of constants in a selected Hamiltonian to frequencies of measured transitions, and SPCAT calculates energies and intensities for different transitions. The extensive use of this package by the spectroscopic community results from the extended possibilities for definition of the molecular Hamiltonian required for a particular problem. The package allows declaration of spectroscopic parameters for all types of rotors. The fitted parameters can be rotational constants, centrifugal distortion constants in different reductions and representations of the rotational Hamiltonian, nuclear quadrupole coupling constants, spin-spin, and spin-rotation constants. It is also possible to fit linear combinations of these constants. Coriolis and Fermi coupling parameters between different vibrational levels and energy differences between such levels can also be simultaneously fitted. The fitting program produces an input file with improved spectroscopic constants for use by the predictive program. Spectra calculated with SPCAT can be displayed by the ASCP_L program. Some of the details of the

SPFIT/SPCAT package are described in [24], and it is freely available from [25].

A family of several postprocessing programs to deal with output and data associated with Pickett's SPFIT/SPCAT, written by Kisiel are available on the PROSPE website [17]. Program PIFORM is used to reformat the *.fit* output from SPFIT into a form closer to the requirements for publishing. Program PISLIN can perform two different types of operations on *.lin* files used by SPFIT: checking for line duplication, and sorting of the *.lin* file according to desired criteria.

The file $Crib - sheet$ [128], which is a quick-reference guide to SPFIT/SPCAT arising from experience gained on using these programs in the IFPAN laboratory is also available on the PROSPE website.

Chapter 4

Cyanamide

4.1 Introduction

Cyanamide, H_2NCN, is a nitrile substituted derivative of ammonia. Like the ammonia molecule NH_3, it has been a prototype system for the study of the inversion motion at the nitrogen atom, in this case in the framework of a highly prolate asymmetric top. Cyanamide is an astrophysically relevant molecule, with the first reported detection in Sgr B2 dating back to more than 35 years ago [129]. This molecule has not yet been subjected to a systematic astrophysical investigation, however predicted lines of cyanamide are regularly noted in astrophysical surveys. According to the NIST database [130] there are 29 detected rotational transitions that are consistent with frequencies of transitions of cyanamide. Most of those lines have been detected in Sgr B2 [131, 132]. Several lines have also been observed in the massive young star forming region Orion Molecular Cloud 1 [133] and in the IRc2 region of Orion [134]. Many discussions have been devoted to the role of cyanamide and its lowest energy tautomeric form - carbodiimide HNCNH in chemical evolution [135]-[139]. The formation of cyanamide in the interstellar medium (ISM) is postulated to be possible under the "primitive Earth conditions" (e.g., ultraviolet irradiation of HCN solutions, ionizing irradiation of CH_4-NH_3-H_2O mixtures) that are known to form biologically relevant compounds [135]. Its origin in the ISM has also been postulated as due to the ultraviolet photolysis of hexamethylenetetramine (if present in ISM) trapped in water ice [138]. Hexamethylenetetramine is the heterocyclic organic compound easily formed by the reaction of two known astrophysical species, formaldehyde and ammonia. Recent matrix isolation study [139] showed that carbodiimide can be formed from cyanamide at similar conditions to those present in the interstellar clouds. In the gas phase carbodiimide is in equilibrium with cyanamide with abundance ratio of 1:115(14) at 380 K [140]. Thus, it seems possible that this tautomeric form of cyanamide might also be a significant component of interstellar gas in those sources where cyanamide was found [141].
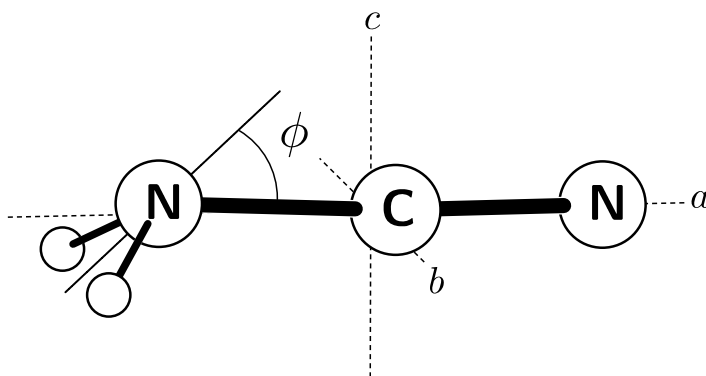
Figure 4.1: The orientation of the cyanamide molecule in the principal inertial axes. The molecule has been rotated around the c axis to show the two symmetry equivalent hydrogen atoms, which in the ac projection would be overlapped. The inversion angle ϕ has been marked.

The rotational spectrum of cyanamide has been studied on numerous occasions [142]-[151], as was its rotationally resolved infrared spectrum [152]-[155]. The rotational constants of cyanamide are rather high ($A \cong 10$ cm^{-1} for H_2NCN) so that the first studies of its rotational spectrum were limited to the lowest-J rotational transitions in the cm-wave region [142]-[145]. Extension of these studies to the mm-wave region was made in [146]-[150], although the most extensive set of spectroscopic constants for the parent H_2NCN species has been determined in the study of its far infrared spectrum [154]. In the most recent paper concerning cyanamide [155], the authors presented an analysis of the FTIR spectrum of cyanamide between 25 and 980 cm^{-1}. That work extends the quantum number coverage up to $K_a = 11$ in the first excited inversion state (1^+ and 1^- substates). Nonetheless, the reported analysis is purely effective since each sequence of rotational transitions is fitted separately using an appropriate power series expansion, and can not be subjected to a straightforward comparison with the results presented in this dissertation and with other works. Moreover, the available information on the deuterated isotopologues of cyanamide is limited to transitions measured at frequencies of less, or much less, than 60 GHz.

In the present work a comprehensive millimeter-wave and far infrared study of the deuterated species is presented. The analysis is based on a $118-650$ GHz spectrum of D_2NCN and $HDNCN$ recorded with microwave techniques, and an $8-360$ cm^{-1} spectrum of D_2NCN recorded with the Bruker IFS 120HR interferometer at resolution of 0.0018 cm^{-1}. These spectra have been measured in the investigation of the carbodiimide molecule [153]. The millimeter and submillimeter-wave spectra have turned out to be endowed with a sufficiently high signal-to-noise ratio to allow assignment of five new isotopic species in natural abundance: $D_2N^{13}CN$, $HDN^{13}CN$, $HD^{15}NCN$, $HDNC^{15}N$, and $H_2N^{13}CN$. Another new species was assigned in the spectrum of an enriched $H_2^{15}NC^{15}N$ sample. Some rotational transitions were measured with the use of enriched sample of $H_2N^{13}CN$. The data for four other species, $D_2^{15}NCN$, $D_2NC^{15}N$, $H_2^{15}NCN$, and $H_2NC^{15}N$ have been considerably extended in comparison

to previous reports.

The inversion barrier in cyanamide is considerably lower than in ammonia so that the splitting between the two lowest 0^+ and 0^- inversion substates in H_2NCN is much higher, at 49.567772(5) cm^{-1} [154] when compared with 0.7934084(24) cm^{-1} [48] in ammonia. The rotational constants of cyanamide are still sufficiently large to lead to strong perturbations between 0^+ and 0^- states so that the coupled state analysis is mandatory for studies beyond the lowest values of rotational quantum numbers. These problems become more acute on deuteration of cyanamide since the inversion splitting drops considerably. In this work the measured transition frequencies were fitted to within experimental accuracy with a unified scheme for fitting the inversion doublet transitions for all 13 isotopic species of cyanamide. Precise energy separation between the 0^+ and 0^- levels obtained from coupled state fits extended the knowledge on the inversion potential of this molecule. The newly determined precise values of rotational constants for all of the studied isotopic species of cyanamide have been combined with results of *ab initio* anharmonic force field calculations in a determination of a new molecular geometry of this molecule. The present work also provides sufficiently precise laboratory information for a radioastronomical search of deuterated species of cyanamide and for a determination of the H/D ratio in interstellar gaseous sources.

4.2   Experimental Details

The spectra used in this work were recorded by Wolfgang Jabs of Giessen University. Three different commercially available samples of cyanamide were used: the parent species and isotopically enriched $H_2N^{13}CN$ and $H_2^{15}NC^{15}N$ at a cited enrichment of 99% [153, 156]. D_2NCN was prepared by repeated deuteration of H_2NCN with D_2O according to a recipe given in [157], although millimeter-wave spectroscopy revealed that it was incompletely deuterated, and contained D_2NCN, HDNCN, and H_2NCN in approximate ratios of 1:1:0.15, respectively. This, in fact, turned out to be an advantage for the purpose of the present study, especially for the structure determination, since most of the isotopic species of interest could be measured from a single spectrum. For the far infrared measurements a sample of completely deuterated cyanamide D_2NCN was used.

The millimeter-wave rotational spectra were recorded on two different spectrometers as described in detail in [153, 156]. One of the spectrometers was the BWO-based spectrometer developed by the Analytic & Meßtechnik GmbH of Chemnitz and operated in the Giessen laboratory [158]. The second spectrometer was the Cologne millimetre/submillimetre wave/terahertz spectrometer, also based on BWO's, but operating up to much higher frequencies. The most extensive recorded spectrum was that of the nominally D_2NCN sample, and it consisted of three segments: 118-179 GHz, 202-221.4 GHz, and 570.85-649.65 GHz. In addition, a spectrum of the $H_2N^{13}CN$ sample was recorded at 118-171.5 GHz, and that of $H_2^{15}NC^{15}N$ at 119.6-172.0 GHz. All of the spectra were recorded at room temperature under a
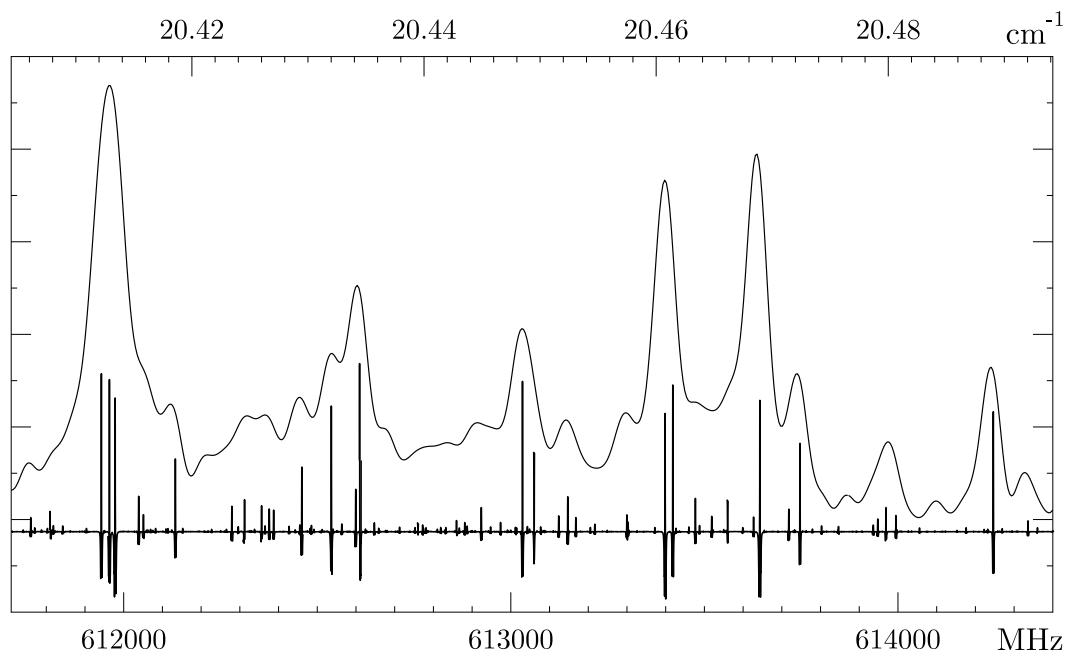
Figure 4.2: Comparison of the resolution of the microwave and the interferometer based spectrometers used in this work as illustrated on the ^aR branch of the rotational spectrum of D_2NCN. The lower trace is the spectrum obtained with the broadband millimeter wave spectrometer in Cologne, and the upper trace is the absorption spectrum measured using the FTIR Bruker spectrometer at 0.0018 cm^{-1} resolution.

continuous flow and sample pressure of cyanamide of around 15 mTorr. The estimated frequency accuracy of these measurements was 0.05 MHz. The far infrared pure rotational and rotation-inversion spectrum has been measured at a resolution of 0.0018 cm^{-1} [153] with a Bruker IFS 120 HR Fourier Transform (FT) spectrometer in the 8-360 cm^{-1} region. The sensitivity and the resolution of this spectrometer is very high for FTIR techniques but is still substantially lower than those characterising the millimeter-wave spectrometers, as illustrated in Fig. 4.2. Nonetheless, the FIR spectrum gives access to frequencies not covered by millimeter/submillimeter-wave spectrometers. The FTIR spectrum of D_2NCN contains many rotation-inversion transitions between 0^+ and 0^- states mainly in the form of dense ^cQ branches of lines, which complement the information available from the mm- and submm-wave spectra.

The mm- and submm-wave rotational spectra of the D_2NCN sample were combined into a single spectrum and subjected to analysis with the use of the AABS package already described in Chapter 3.3. The package provides a synchronised display of the spectrum and of merged predictions for all spectroscopic species of interest in a given problem. The AABS package was also used for line assignments from the FTIR spectrum. All fits and predictions were carried out by using the SPFIT/SPCAT package of Pickett [24, 25].
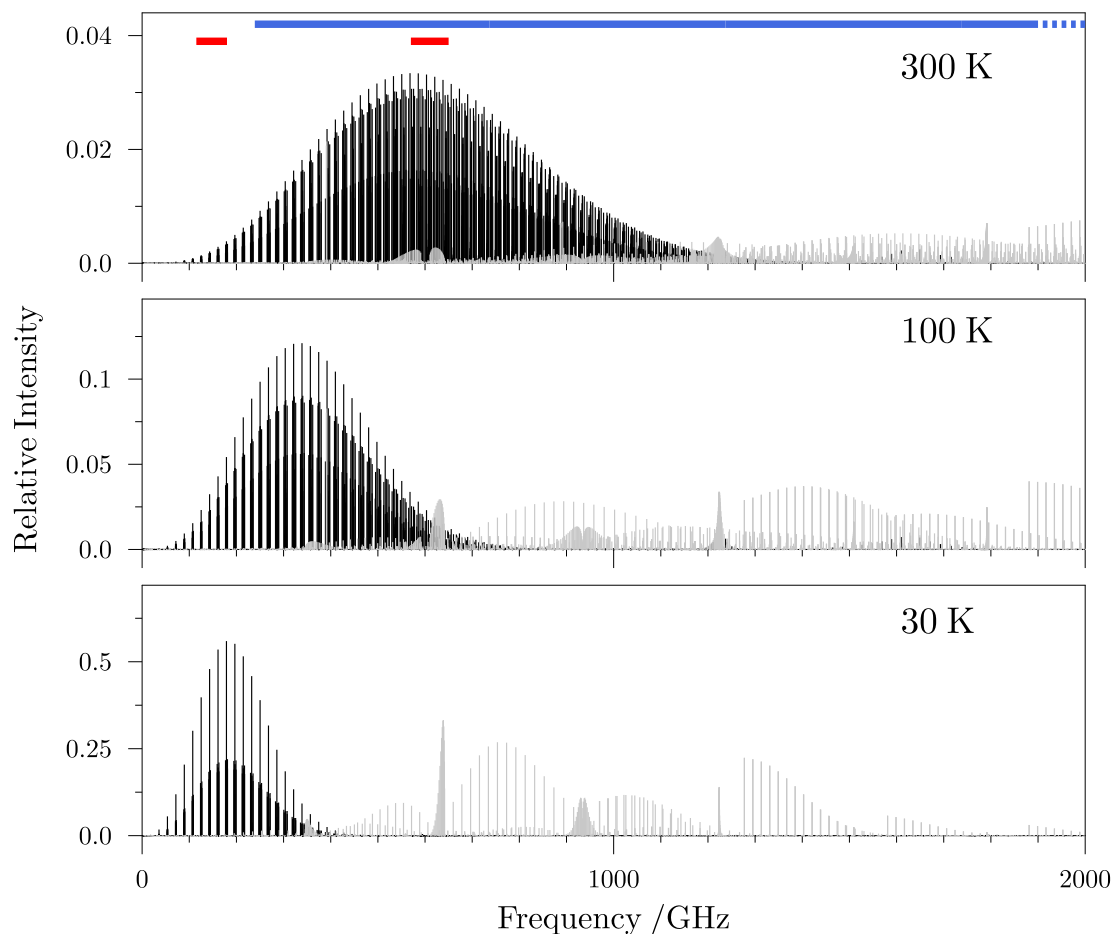
Figure 4.3: The temperature dependence of the ground state inversion spectrum of D_2NCN cyanamide. The a-type transitions in the 0^+ and 0^- states (darker) are stronger in intensity at lower frequencies than the c-type $0^+ \leftrightarrow 0^-$ interstate transitions (lighter). Dipole moments from Read et $al.$ [150] were used to calculate the intensities. The regions of the spectrum measured with mm- and submm-wave spectrometers are marked by red lines at the top of the diagram, and the frequency range recorded with the Bruker spectrometer by the blue line.

4.3   Spectral Assignment

4.3.1   Rotation and Rotation-Inversion Spectrum

The ground state rotational spectrum of cyanamide is typical of a near prolate rotor ($\kappa < -0.99$) with the presence of a doublet of 0^+, and 0^- substates arising from the inversion motion of the H_2N- group in the molecule. The spectrum of cyanamide consists of two types of transitions. The large a component of the dipole moment $\mu_a = 4.319(4)$ D gives rise to pure rotational transitions and a smaller interstate dipole moment $\langle 0^+|\mu_c|0^-\rangle = -0.956(13)$ D [150] makes observation of rotation-inversion transitions possible. The intensity envelope of the rotational spectrum at laboratory and astrophysically relevant temperatures is shown in Fig. 4.3, and it can
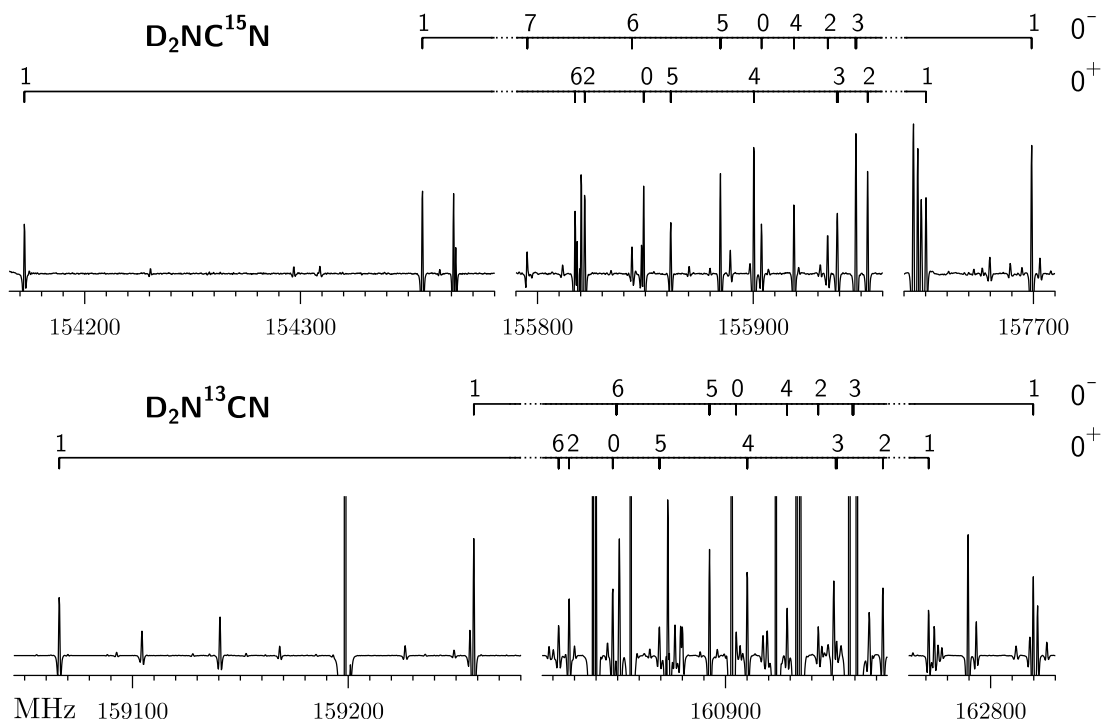
Figure 4.4: The $J = 9 \leftarrow 8$ rotational transition of $D_2NC^{15}N$ and $D_2N^{13}CN$ observed in natural abundance of ^{15}N and ^{13}C in a sample of enriched D_2NCN. There is ample signal to noise available in this spectrum and challenges to assignment are mainly posed by overlaps of transition patterns for different isotopic and vibrational species. The values of K_a are marked and the associated transition intensities are subject to 2:1 nuclear spin statistical weights, which reverse between the 0^+ and 0^- substates.

be seen that at high frequencies the rotation-inversion transitions due to the smaller interstate μ_c dipole moment component are more relevant than the pure rotation a-type ones. The nearly prolate nature of cyanamide causes the $K_a = 1$ transitions to be far removed from the pattern arising from transitions for remaining values of K_a, making the $K_a = 1$'s somewhat easier to assign. In addition, K_a doubling is observed only for low K_a values, mostly up to $K_a = 3$, and for low values of J as characteristic, equal intensity doublets separated by several MHz.

Due to the presence of two ^{14}N nuclei in cyanamide which have nuclear spin $I = 1$ a partially resolved hyperfine structure was observed for some inversion-rotation transitions in the mm-wave spectrum. The quadrupole splitting has the form of quartets or doublets. For quartets the frequency was taken as a simple average over two strongest hyperfine components. In the case of doublets the intensity weighted average of two components was taken as the central frequency for the fit.

Figure 4.4 illustrates some of the issues affecting the assignment of the rotational transitions in the millimeter-wave spectrum of deuterated cyanamide in rare isotopic species resulting from the natural abundances of carbon and nitrogen. It is seen that the signal-to-noise does not pose any problems for measurement even of the

Table 4.1: Nuclear spin statistical weights for rotational levels in cyanamide.

	0^+		0^-	
	K_a = even	K_a = odd	K_a = even	K_a = odd
H_2NCN	1	3	3	1
D_2NCN	2	1	1	2

^{15}N species at the 0.37% nominal natural abundance of this nucleus. Overlaps between transition patterns of various isotopic species and excited vibrational states are a more serious difficulty. It can be seen that while the pattern for $D_2NC^{15}N$ is subject to relatively few interlopers, the central part of the pattern for $D_2N^{13}CN$ is heavily overlapped with much stronger lines which belong to D_2NCN. This is the consequence of the small principal a-coordinate of the carbon atom, so that there are relatively small isotopic changes in rotational constants on ^{13}C substitution. Even in the $D_2NC^{15}N$ spectrum in Fig. 4.4 the $K_a = 1$ transition in the 0^+ substate at 157650 MHz is close to being blended with a triplet of lines just to low frequency, that is now known to belong to $D_2^{15}NCN$. The use of the graphical Loomis-Wood type techniques turned out to be instrumental in taking apart this spectrum. The lines were measured only if the Loomis-Wood display for a given transition sequence showed a clear series of lines at similar intensity.

4.3.2 Statistical Weights

The most distinctive, and also very helpful feature in analysis of the spectra is the presence of the differing nuclear spin statistical weights for rotational levels. These statistical weights arise from the presence of a pair of symmetry equivalent hydrogen atoms in cyanamide, and lead to intensity alternation of the line pattern. The underlying cause of the effect is the need to preserve the symmetry of the total wave function of the molecule. For nuclei with a spin of zero or an integer (Bose particles, e.g. deuterium atoms), the overall function needs to be symmetric, and for nuclei with half-integer spin (Fermi particles, e.g. hydrogen atoms) the overall function has to be antisymmetric with regard to the operation that exchanges the identical particles. In the Born-Oppenheimer approximation the symmetry of the complete wave function in the electronic ground state is the product of the symmetry of the vibrational, rotational, and nuclear spin wave functions. The vibrational wave function is symmetric for 0^+ substate and antisymmetric for 0^-. The rotational wave function is symmetric for even values of the K_a quantum number, and antisymmetric for odd values of K_a. The statistical weight for energy levels described by the symmetric nuclear spin wave function is given by

$$g^s = \frac{1}{2}\left[1 + \frac{1}{(2I+1)^n}\right], \tag{4.1}$$

and for those described by the antisymmetric spin wave function by

$$g^a = \frac{1}{2}\left[1 - \frac{1}{(2I+1)^n}\right],$$

(4.2)

where I is the nuclear spin and n is the number of equivalent pairs of hydrogen atoms. For H_2NCN which has a single pair of equivalent hydrogens we have $n = 1$ and $I = \frac{1}{2}$ and the statistical weight ratio g^s/g^a is 3/1. For D_2NCN with a pair of deuterium atoms ($I = 1$) the ratio g^s/g^a is 2/1. As a result, for the same even value of the K_a quantum number the intensity ratio between 0^+ and 0^- levels for H_2NCN is 1:3, and for D_2NCN 2:1, and for a given odd value of K_a the intensity ratio between 0^+ and 0^- levels is 3:1 for H_2NCN, and 1:2 for D_2NCN. For D_2NCN this is most clearly seen for $K_a = 1$ transitions as shown in Fig. 4.4. All possible combinations of the symmetry of vibrational, rotational wave functions, and the statistical weights for H_2NCN and D_2NCN are given in Table. 4.1. There is, of course, a lack of such weights for the HDNCN species.

4.3.3 Hamiltonian

The measured transition frequencies for the 0^+ and 0^- inversion substates were fitted simultaneously in a two-state coupled fit based on Pickett's Reduced Axis Hamiltonian (see discussion in Chapter 2.7.1), analogously to [150]. The Hamiltonian is in 2×2 block-diagonal form

$$\mathcal{H} = \begin{pmatrix} \mathcal{H}_{\mathrm{rot}}^{(0^+)} & \mathcal{H}_{\mathrm{c}}^{(0^+,0^-)} \\ \mathcal{H}_{\mathrm{c}}^{(0^+,0^-)} & \mathcal{H}_{\mathrm{rot}}^{(0^-)} + \Delta E \end{pmatrix},$$

(4.3)

containing on the diagonal the $\mathcal{H}_{\mathrm{rot}}^{(0^+)}$ and $\mathcal{H}_{\mathrm{rot}}^{(0^-)}$ single-state Watson's reduced asymmetric rotor terms in representation I^r [21] augmented by the vibrational energy difference $\Delta E = E(0^-) - E(0^+)$. The off-diagonal interstate coupling term $\mathcal{H}_{\mathrm{c}}^{(0^+,0^-)}$ is equivalent to a second order Coriolis coupling term defined by Eq. 2.56. Since inversion in cyanamide takes place through a motion about the b-principal axis (see Fig. 4.1) this term has the form

$$\mathcal{H}_{\mathrm{c}}^{(0^+,0^-)} = (F_{ac} + F_{ac}^J \hat{J}^2 + F_{ac}^K \hat{J}_z^{\,2} + \dots)(\hat{J}_a\hat{J}_c + \hat{J}_c\hat{J}_a).$$

(4.4)

The F_{ac}^J and F_{ac}^K terms in the empirical centrifugal distortion expansion of the F_{ac} coupling constant were found to be necessary for fitting the large data sets obtained for D_2NCN, H_2NCN, and HDNCN. In the HDNCN isotopologue and its substituents the inversion axis is rotated slightly in the ab-principal plane so that the term in Eq. 4.4 needs to be complemented by an analogous, smaller magnitude term in F_{bc} so that

$$\begin{aligned} \mathcal{H}_{\mathrm{c}}^{(0^+,0^-)} &= (F_{ac} + F_{ac}^J \hat{J}^2 + F_{ac}^K \hat{J}_z^{\,2} + \dots)(\hat{J}_a\hat{J}_c + \hat{J}_c\hat{J}_a) \\ &\quad + (F_{bc} + F_{bc}^J \hat{J}^2 + F_{bc}^K \hat{J}_z^{\,2})(\hat{J}_b\hat{J}_c + \hat{J}_c\hat{J}_b). \end{aligned}$$

(4.5)
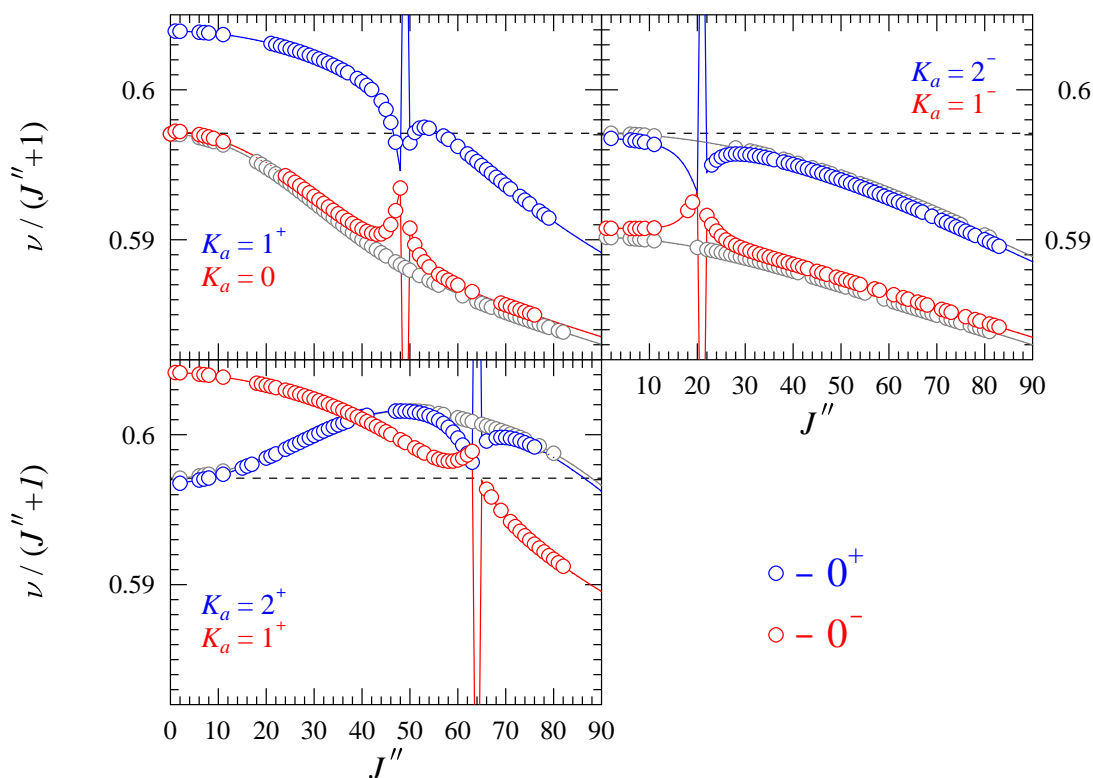
Figure 4.5: Illustration of some of the many possible level-crossing type perturbations taking place between rotational levels of 0^+ (blue) and 0^- (red) substates in D_2NCN. The plot is of the energy of the rotational levels in cm^{-1} scaled by $J'' + 1$. Scaling of the term values ensures a near horizontal baseline for these plots, and the linear-top limit $(B + C)$ is plotted by grey dotted lines for guidance. The rotational levels for a given value of K_a and $K_a + K_c = J$ are denoted by $-$ in the superscript, and those for $K_a + K_c = J + 1$ by $+$. The unperturbed rotational levels with similar K_a values are plotted for comparison. The circles mark assigned lines and the continuous lines are for frequencies calculated from the final fit.

Specific perturbations between 0^+, and 0^- states appear at low values of K_a as illustrated in Fig. 4.5 and are fitted to experimental accuracy with the use of this model. Such perturbations are manifested in many inversion-rotation Q-type transitions observed in the IR spectrum of D_2NCN, and were also reported for H_2NCN [140]. In order to maintain a unified scheme of the derived spectroscopic constants for all known isotopologues of cyanamide, the above theoretical model has also been applied to the mm-wave and IR ground state data for the parent species H_2NCN from Ref. [140]. The scheme is more reasonable than in [140] which is also difficult to reproduce due to several misprints in Table I of Ref. [140]. Additionally, more than 100 new rotational transitions for H_2NCN have been measured from the current spectra and included in the data set. Since cyanamide is a prolate molecule the S-reduction of the asymmetric rotor Hamiltonian would normally be used as the method of choice. Nonetheless, in this case the A-reduction was used because it offered greater numerical stability and somewhat smaller residuals. Similar behaviour has been found for acrylonitrile (see Chapter 5, and Ref. [23]).

It was found that inclusion of the higher order constants reduces residuals for the highest K_a transitions, however these parameters gave little to understanding of the physics of the inversion motion. In order to fit transitions within the experimental accuracy the value of the K_a had to be limited to 6, 10 and 15 for H_2NCN, HDNCN, and D_2NCN, respectively. The discrepancies between observed and calculated high K_a transitions can be rationalised when the possible interactions of the ground vibrational state levels (0^+, 0^+) with the lowest lying excited vibrational levels are also taken into account. Usually, the low-lying vibrationally excited states are treated as isolated from the ground state levels. For cyanamide the large value of the A rotational constant of close to 10 cm^{-1} allows interactions between levels with high values of K_a for the ground state and those of the excited states (e.g. the NCN out-of-plane skeletal bending mode $\nu_9 = 430$ cm^{-1}, and the NCN in-plane mode $\nu_6 = 532$ cm^{-1} for H_2NCN [159]). The interaction pattern is additionally complicated by (0^+, 0^-) inversion splitting in each vibrational satellite, and the presence of the first excited inversion doublet (1^+, 1^-). Several attempts to assign and achieve effective fits for vibrational satellites in the $v_9 = 1$, $v_6 = 1$ and the first excited inversion state were made. Unfortunately, the two state model turned out to fail for each case. Additional evidence for the presence of such interactions follows from the fact that the A rotational constant for D_2NCN is smaller by a factor of 2 than that for H_2NCN, and the perturbations for D_2NCN are manifested at higher K_a than for H_2NCN. The results of fits for the parent and for the deuterated species are listed in Table. 4.2.

For rare isotopologues measured in their natural abundance from the mm/submm-wave spectra the measured lines were limited only to a-type transitions. Although these transitions are ideal for precise determination of B and C constants, the A constant is rather difficult to fit. For two species: $H_2^{15}NCN$, $H_2NC^{15}N$, for which the numbers of measured transitions were the lowest, the A constants had to be fixed at the values for the parent species. The smaller data sets for all rare isotopologues also could not allow determination of sixth- and eighth-order centrifugal distortion constants, so that their values were fixed at the corresponding values for the parent species. For three of the previously assigned isotopic species: $D_2^{15}NCN$, $D_2NC^{15}N$ [145], and $H_2NC^{15}N$ [149], it was found that one of the $J = 2 \leftarrow 1$ transitions appeared to be misassigned; it deviated from the final fit by a frequency difference of from 2.5 to 11 MHz. In all cases this concerned the $2_{11} \leftarrow 2_{10}$ transition in either the 0^+ or the 0^- state. This is not that surprising since such transitions are positioned at the high frequency end of the pattern for a given $J + 1 \leftarrow J$ transition and are thus subject to overlap with transitions of lighter isotopic species. The results of fits for ten different isotopologues of cyanamide are collected in Tables 4.3-4.5. The assignment of the various isotopic species and the validity of the performed fits are confirmed by the relative invariance of the spectroscopic constants for the series of isotopologues in each table.

Table 4.2: Spectroscopic constants determined from the global fit of the 0^+ and the 0^- inversion states for cyanamide and its deuterated isotopologues.

		H$_2$NCN		HDNCN		D$_2$NCN	
		0^+	0^-	0^+	0^-	0^+	0^-
A	/MHz	312141.992(69)[a]	304453.63(10)	214257.080(35)	210531.83(14)	157660.4088(55)	156091.326(12)
B	/MHz	10130.35604(35)	10113.07668(30)	9605.4591(39)	9597.89063(76)	9156.53450(39)	9153.40678(52)
C	/MHz	9865.32454(35)	9866.23663(30)	9256.4123(39)	9263.28752(72)	8742.99646(36)	8751.59313(61)
Δ_J	/kHz	3.80627(26)	3.82216(24)	3.4522(11)	3.4652(10)	3.09286(19)	3.08250(20)
Δ_{JK}	/kHz	395.665(60)	359.408(77)	256.947(63)	255.305(90)	218.486(10)	221.634(20)
Δ_K	/kHz	44150.9(45)	27930.6(83)	23996.2(91)	17090.(14)	9114.06(30)	6932.06(40)
δ_J	/kHz	0.140754(33)	0.119763(38)	0.15697(15)	0.15142(10)	0.120643(52)	0.12917(12)
δ_K	/kHz	299.562(57)	211.569(85)	247.8(19)	173.59(22)	202.80(11)	159.58(26)
Φ_J	/Hz	−0.001079(99)	−0.00071(10)	0.00100(41)	0.00099(38)	0.001222(46)	0.000646(86)
Φ_{JK}	/Hz	1.681(19)	1.027(27)	1.418(36)	1.645(68)	3.477(21)	1.866(56)
Φ_{KJ}	/Hz	−339.7(38)	−191.4(41)	−139.9(12)	78.9(28)	−69.27(24)	−4.11(77)
Φ_K	/Hz	18616.(98)	4273.(174)	[10436.][b]	[2426.]	2256.3(33)	578.8(40)
ϕ_{JK}	/Hz					1.574(38)	1.02(11)
ϕ_K	/Hz					1067.(10)	243.(31)
L_{KJ}	/mHz	13.73(64)	12.08(63)	6.33(37)	2.70(41)		
L_{KKJ}	/mHz	−4071.(72)	−3241.(87)	−679.(12)	−1423.9(63)	−130.9(14)	−278.2(27)
L_K	/mHz					−337.(10)	362.(11)
ΔE	/MHz	1486004.36(18)		962009.210(94)		494551.996(25)	
ΔE	/cm^{-1}	49.5677700(60)		32.0891732(31)		16.49647891(83)	
F_{ca}	/MHz	346.870(33)		281.972(44)		267.5995(18)	
F_{ca}^J	/MHz	0.001397(12)		0.0007325(42)		[0.]	
F_{ca}^K	/MHz	−1.5150(55)		−1.7945(95)		−0.97587(71)	
F_{ca}^{JJ}	/kHz	0.00000001177(61)				[0.]	
F_{ca}^{JK}	/kHz	−0.0000559(21)				0.00000188(32)	
F_{ca}^{KK}	/kHz			9.32(38)		0.001675(74)	
F_{ca}^{KKK}	/kHz					0.00001158(25)	
F_{bc}	/MHz			8.134(87)			
F_{bc}^J	/MHz			−0.0000688(41)			
F_{bc}^K	/MHz			−0.309(34)			
$J_{\max}, K_{\max}$		70, 6		47, 10		83, 15	
σ_{w}		1.573		1.316		1.189	
N_{lines}		2436 (377, 2059)[c]		334		3096 (480, 2616)	

[a]The quantities in round parentheses are standard errors in units of the least significant digit of the value of the constant.

[b]Values in square brackets have been assumed to be equal to the average of those in H$_2$NCN and in D$_2$NCN .

[c]First number refers to mm-wave, and the second to ir data.

Table 4.3: Spectroscopic constants determined from the global fit of the 0^+ and the 0^- inversion states for the rare isotopologues of cyanamide derived from D_2NCN.

		$D_2N^{13}CN$		$D_2^{15}NCN$		$D_2NC^{15}N$	
		0^+	0^-	0^+	0^-	0^+	0^-
A	/MHz	$157657.1(12)^a$	$156084.8(15)$	$157321.3(13)$	$155770.3(19)$	$157651.8(19)$	$156081.3(22)$
B	/MHz	$9148.6717(22)$	$9145.5492(23)$	$8956.3001(23)$	$8952.6629(22)$	$8857.6043(27)$	$8854.7416(29)$
C	/MHz	$8735.7935(21)$	$8744.3841(23)$	$8561.3958(21)$	$8568.9008(23)$	$8470.0250(27)$	$8478.1575(30)$
Δ_J	/kHz	$3.09299(37)$	$3.08301(40)$	$2.96066(34)$	$2.95173(39)$	$2.87690(47)$	$2.86971(63)$
Δ_{JK}	/kHz	$216.849(45)$	$220.206(42)$	$214.088(41)$	$216.382(41)$	$206.795(41)$	$210.088(66)$
Δ_K	/kHz	$[9114.]^b$	$[6932.]$	$[9114.]$	$[6932.]$	$[9114.]$	$[6932.]$
δ_J	/kHz	$0.12053(41)$	$0.12903(46)$	$0.11954(41)$	$0.12391(43)$	$0.10911(47)$	$0.11633(52)$
δ_K	/kHz	$202.43(44)$	$160.08(46)$	$198.93(37)$	$155.12(44)$	$192.11(64)$	$152.86(69)$
Φ_{JK}	/Hz	$3.463(16)$	$1.855(14)$	$3.277(12)$	$1.712(13)$	$3.248(12)$	$1.734(17)$
Φ_{KJ}	/Hz	$-77.36(68)$	$-7.74(59)$	$-64.30(65)$	$1.81(61)$	$-68.52(47)$	$-2.1(10)$
ΔE	/MHz	$495213.1(54)$		$475573.6(65)$		$494225.5(82)$	
ΔE	/cm^{-1}	$16.51853(18)$		$15.86343(22)$		$16.48559(27)$	
F_{ca}	/MHz	$267.077(14)$		$268.635(18)$		$259.977(23)$	
J_{max}, K_{max}		$36, 7$		$37, 7$		$38, 8$	
σ_w		0.970		1.003		1.206	
N_{lines}		171		192		165	

[a]The quantities in round parentheses are standard errors in units of the least significant digit of the value of the constant.

[b]Values in square brackets have been assumed to be equal to those in D_2NCN, see text.

Table 4.4: Spectroscopic constants determined from the global fit of the 0^+ and the 0^- inversion states for the rare isotopologues of cyanamide derived from HDNCN.

		HDN^{13}CN		HD^{15}NCN		HDNC^{15}N	
		0^+	0^-	0^+	0^-	0^+	0^-
A	/MHz	214229.6(32)	210509.8(39)	213632.0(48)	209905.8(57)	214219.9(41)	210487.9(54)
B	/MHz	9599.4434(33)	9591.8702(29)	9372.3483(48)	9364.1345(40)	9293.7135(43)	9286.6139(39)
C	/MHz	9250.7649(31)	9257.6217(28)	9039.8135(45)	9045.3617(41)	8966.4646(40)	8972.9204(39)
Δ_J	/kHz	3.45128(59)	3.46486(52)	3.29666(81)	3.30801(68)	3.21324(63)	3.22637(63)
Δ_{JK}	/kHz	254.956(54)	253.650(54)	254.946(81)	251.616(75)	242.659(68)	241.526(63)
Δ_K	/kHz	[23996.]^a	[17142.]	[23996.]	[17090.]	[23996.]	[17090.]
δ_J	/kHz	0.15793(48)	0.15199(48)	0.15042(61)	0.14335(66)	0.14160(63)	0.13689(63)
δ_K	/kHz	246.3(12)	173.88(96)	240.9(18)	166.6(13)	238.1(15)	165.5(12)
Φ_{JK}	/Hz	1.427(23)	1.590(22)	1.294(32)	1.520(29)	1.276(27)	1.525(27)
Φ_{KJ}	/Hz	$-153.16(81)$	73.38(71)	$-122.3(11)$	90.8(12)	$-133.2(10)$	80.12(91)
ΔE	/MHz	962847.(32)		938762.(51)		961809.(40)	
ΔE	/cm^{-1}	32.1171(11)		31.3137(17)		32.0825(13)	
F_{ca}	/MHz	281.504(19)		280.234(44)		273.841(38)	
F_{ca}^J	/MHz	[0.0007325]		0.000835(17)		0.000676(14)	
F_{bc}	/MHz	8.1078(48)		7.9510(51)		7.6818(57)	
$J_{\max}, K_{\max}$		34, 7		35, 7		35, 7	
σ_{w}		0.887		1.195		0.999	
N_{lines}		135		133		122	

^{a}Values in square brackets have been assumed to be equal to those in HDNCN, see text.

Table 4.5: Spectroscopic constants determined from the global fit of the 0^+ and the 0^- inversion states for the rare isotopologues of cyanamide derived from H_2NCN.

		$H_2N^{13}CN$		$H_2^{15}NCN$		$H_2NC^{15}N$		$H_2^{15}NC^{15}N$	
		0^+	0^-	0^+	0^-	0^+	0^-	0^+	0^-
A	/MHz	312098.(20)	304496.(16)	$[312142.]^a$	[304454.]	[312142.]	[304454.]	311855.(577)	305096.(684)
B	/MHz	10126.2428(68)	10108.9156(69)	9854.4593(33)	9836.7827(42)	9803.2495(69)	9786.8732(78)	9531.6401(40)	9514.8899(42)
C	/MHz	9861.3964(62)	9862.2956(67)	9603.8794(33)	9603.4803(36)	9554.7270(57)	9555.4432(66)	9296.8985(39)	9296.3497(40)
Δ_J	/kHz	3.80725(85)	3.82192(78)	3.651(20)	3.662(23)	3.523(31)	3.570(26)	3.407(21)	3.420(21)
Δ_{JK}	/kHz	393.96(20)	357.97(11)	386.235(95)	348.73(14)	375.05(13)	340.81(22)	367.02(54)	329.77(51)
Δ_K	/kHz	[44151.]	[27931.]	[44151.]	[27931.]	[44151.]	[27931.]	[44151.]	[27931.]
δ_J	/kHz	0.14048(84)	0.12001(93)	[0.140754]	[0.119763]	[0.140754]	[0.119763]	[0.14075]	[0.11976]
δ_K	/kHz	300.6(29)	201.1(29)	[299.562]	[211.569]	[299.562]	[211.569]	[299.56]	[211.57]
Φ_{JK}	/Hz	1.706(58)	1.121(40)	[1.681]	[1.027]	[1.681]	[1.027]	[1.681]	[1.027]
Φ_{KJ}	/Hz	$-372.3(61)$	$-228.7(21)$	$[-339.7]$	$[-191.4]$	$[-339.7]$	$[-191.4]$	$-304.3(54)$	$-186.0(54)$
ΔE	/MHz	1486407.(183)		1462496.(78)		1486032.(124)		1457785.(5235)	
ΔE	/cm^{-1}	49.581(6)		48.784(3)		49.569(4)		48.63(17)	
F_{ca}	/MHz	346.441(42)		343.24(16)		336.18(38)		331.8(10)	
$J_{\max}, K_{\max}$		32, 6		9, 5		9, 5		9, 7	
σ_{w}		0.974		0.644		0.788		0.829	
N_{lines}		102		42		34		57	

^{a}Values in square brackets have been assumed to be equal to those in H_2NCN, see text.
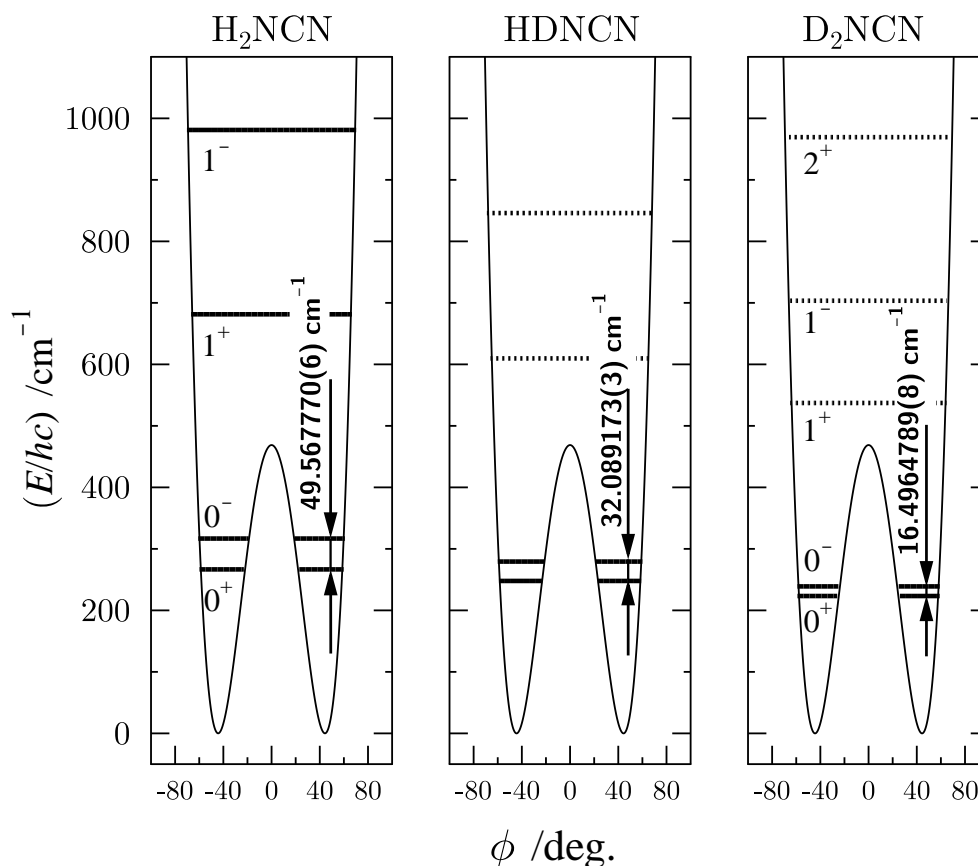
Figure 4.6:   The potential function for the inversion motion and the positions of the inversion energy levels for three isotopologues of cyanamide: H_2NCN, HDNCN, and D_2NCN. The experimentally determined energy splittings have been marked by continous lines and energies only known from calculation have been marked by dotted lines. The experimental value of the energy splitting between 0^+ and 0^- levels determined in this work has been indicated for each isotopologue.

4.4   Potential Function

The double minimum inversion potential responsible for inversion-rotation spectra is often approximated by means of the reduced quartic-quadratic potential function $V(z) = A(z^4 + Bz^2)$, which is described in Chapter 2.7.1. For cyanamide the parameters $A = 113.57$ cm^{-1} and $B = -4.0634$ in this potential were chosen to reproduce the relative energies of the 0^+, 0^-, 1^+ and 1^- levels for H_2NCN determined in [155]. The height of the central barrier for this potential is given by the relation $AB^2/4$ and equals 468.7 cm^{-1}. In general, this potential should remain invariant on isotopic substitution, but the inversion splittings and energy level spacings should be reduced with an increase in the mass of the inverting atoms. This has been confirmed for cyanamide by the experimental values of $\Delta E = E(0^-) - E(0^+)$ and is illustrated on Fig. 4.6. Conversion to the reduced potential for a different isotopic species was carried out by employing the reduced mass μ for the inversion motion
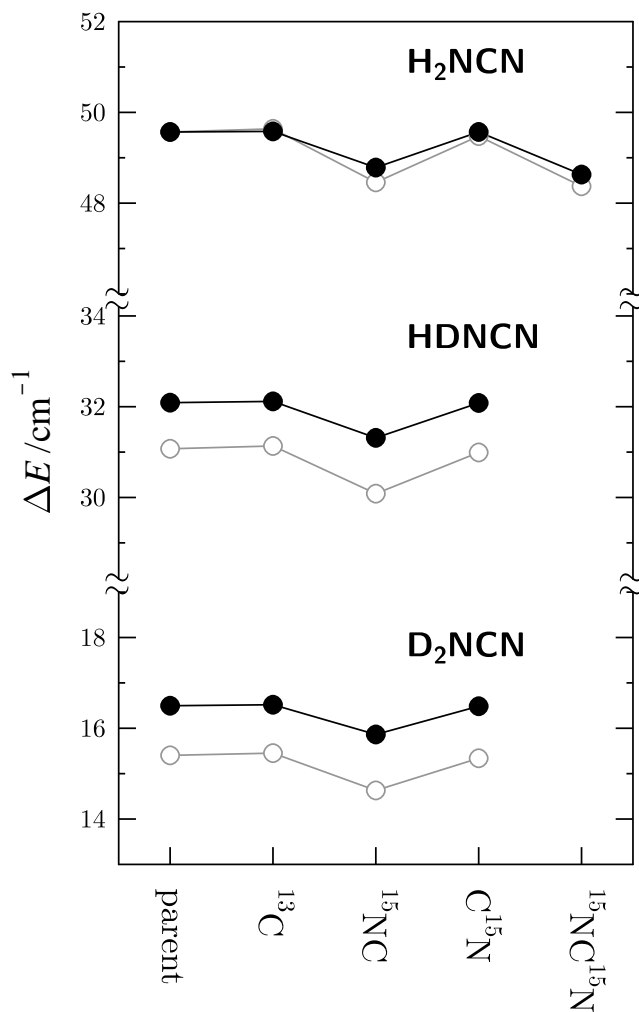
Figure 4.7: Comparison of the 0^+, 0^- inversion splittings determined from the coupled fits for the various isotopic species of cyanamide (full circles) with values calculated from the reduced quartic-quadratic double minimum potential (empty circles).

from Ref. [145]

$$
\frac{1}{\mu} = \frac{1}{m_x}\left[\frac{r_{\mathrm{H}}\cos\theta}{r_x}\right]^2 + \frac{1}{4m_{\mathrm{H}_1}} + \frac{1}{4m_{\mathrm{H}_2}}
$$
$$
+ \frac{1}{m_{\mathrm{N}}}\left[\left(\frac{r_{\mathrm{H}}\cos\theta}{r_x}\right)^2 + \frac{2r_{\mathrm{H}}\cos\theta\cos\phi}{r_x} + 1\right], \qquad (4.6)
$$

where m_x is equal to the mass of the cyanide group –CN, r_{H} is the N–H bond length, r_x is the distance of the amino nitrogen atom from the center of mass of the cyanide group, m_{N} is the mass of the amino nitrogen, ϕ is the inversion angle, and $2\theta = \angle(\mathrm{HNH})$. The structural parameters were taken from the newly determined molecular structure of cyanamide (see section below). The changes of the A and B

Table 4.6: The reduced mass μ and A, B parameters in the reduced quartic-quadratic potential for cyanamide.

	H_2NCN	HDNCN	D_2NCN
μ /u	1.6504	2.0747	2.7928
A /cm^{-1}	113.5700	97.5014	79.9749
B	-4.0634	-4.3855	-4.8422

parameters upon isotopic substitution [160] were obtained from

$$A_D = \left(\frac{\mu_H}{\mu_D}\right)^{2/3} A_H$$

$$B_D = \left(\frac{\mu_H}{\mu_D}\right)^{-1/3} B_H, \tag{4.7}$$

where subscript D refers to the parameter for the substituted species, and subscript H refers to the parameter for the parent species (see Table 4.6). Finally, the energy levels in the potential were calculated with program ANHARM available from [17]. The experimental values of $\Delta E = E(0^-) - E(0^+)$ for rare isotopologues of cyanamide have been confronted with prediction obtained as described above. Even though this simple potential is in error by 1 cm^{-1} in predicting ΔE for D_2NCN and HDNCN, it can be seen that the observed and the calculated dependence of ΔE on carbon and nitrogen isotopic substitution are practically identical. This evidence is collected in Fig. 4.7 which compares the fitted inversion splittings with values calculated from the reduced quartic-quadratic potential.

4.5 Molecular Structure

The present assignment of rotational transitions for six new isotopic species of cyanamide results in a factor of 2 increase in the number of rotational constants available for structure determination. For a relatively small molecule such as cyanamide the optimum geometry that can currently be determined is the semi-experimental equilibrium geometry, r_e^{SE} already discussed in Chapter 2.8.4. In this type of geometry the ground state rotational constants are corrected to equilibrium by means of vibration-rotation contributions for all normal modes of the molecule obtained from anharmonic force field calculations. The CFOUR package [96] was used for calculation of such vibrational changes in rotational constants, and the STRFIT program [71] was used to carry out the structural fits. The results are listed in Table 4.7 and the preferred presently determined geometry of cyanamide is also drawn in Fig. 4.8. The highest practicable level of anharmonic force field calculation turned out in this case to be the CCSD(T)/cc-pVQZ level. Since the vibrational calculation does not take account of the large amplitude motion for the fits the average values of
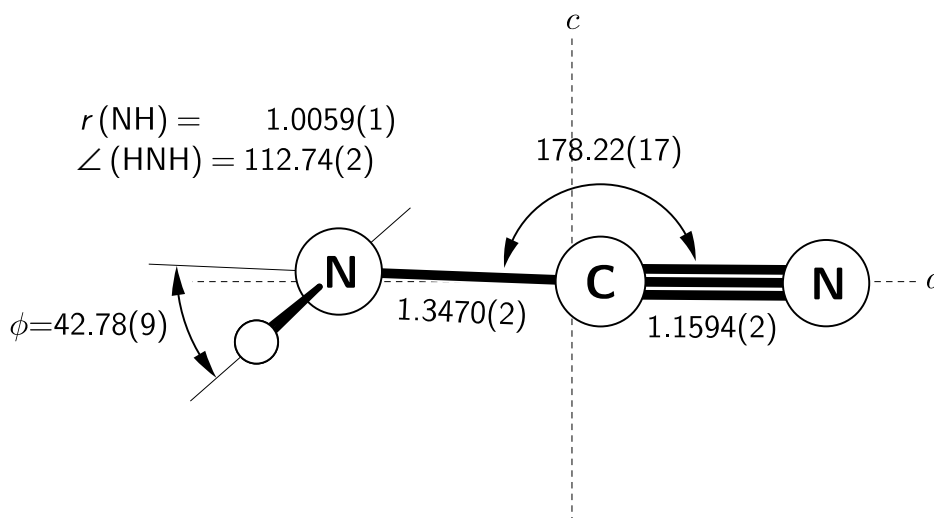
Figure 4.8: The preferred r_e^{SE} geometry for cyanamide (Å and degrees) determined by using 36 experimental rotational constants and vibration-rotation corrections evaluated at the CCSD(T)/cc-pVQZ level. Only the foreground hydrogen is visible in this orthogonal projection onto the *ac*-inertial plane, which is made from the final Cartesian coordinates. Further numerical details on this structural fit are given in Table A.1 at the end of this dissertation.

rotational constants for the 0^+ and 0^- states was used, in analogy to the procedure applied in the presence of internal rotation [162]. The difference is that in the three-fold internal rotation case the unperturbed ground state constants are given by a relation described by Eq. 2.72, which takes account of the statistical weights of the A- and the E-symmetry states. In the present case of a double minimum potential it is necessary to use a simple average.

Two different r_e^{SE} determinations are listed in Table 4.7. It has been suspected since early *ab initio* calculations that the N$-$C$\equiv$N spine in cyanamide is slightly bent from linearity in the direction away from the hydrogens [149]. Initially $\angle$(NCN) was fixed at the value from the best *ab initio* estimate (see below), obtaining a fit of very high quality. It turned out at that stage that the data actually allow the value of $\angle$(NCN) to be determined, lowering the deviation of the fit by a factor of two. This fit does not contain any structural assumptions and for this reason it is the preferred result. More details on this structural fit are given in Table A.1 of the Appendix.

The fitted geometries are compared with the best *ab initio* estimate made on the basis of a series of CCSD(T)/cc-pVnZ calculations up to $n = 4$. All structural parameters showed monotonic changes in this series so that it was possible to extrapolate to the complete basis size limit with some confidence. This was carried out with the robust cubic type extrapolation [101]

$$r(n) = r_\infty + A'n^{-3}, \tag{4.8}$$

where $r(n)$ is the structural parameter obtained at the CCSD(T)/cc-pVnZ level, r_∞ is the structural parameter extrapolated to the complete basis set CCSD(T)/cc-pV∞Z, and A' is the parameter obtained from the solution of the simultaneous

Table 4.7: Summary of the structural parameters (Å and degree) determined for cyanamide.

	Ref. [145]	Ref. [149]	This work					
	r_s	semi-rigid	r_0	$r_m^{(1)}$	$r_m^{(1\mathrm{L})}$	r_e^{SE}, I[a,b]	r_e^{SE}, II[a]	calc.[c]
$r(\mathrm{H-N})$	1.001(15)	[0.9994][d]	1.0041(7)	1.0104(14)	1.0065(11)	1.0063(1)	1.0059(1)	1.0054
$r(\mathrm{N-C})$	1.346(5)	1.3301(5)	1.3470(35)	1.3430(15)	1.3450(8)	1.3475(4)	1.3470(2)	1.3465
$r(\mathrm{C{\equiv}N})$	1.160(5)	[1.1645]	1.1620(37)	1.1614(11)	1.1620(8)	1.1594(4)	1.1594(2)	1.1576
$\angle(\mathrm{HNH})$	113.5(20)	120.8(5)	115.65(14)	113.25(15)	112.62(14)	112.69(2)	112.74(2)	112.33
ϕ^e	38.0(10)	45.03(20)	37.55(17)	40.63(29)	42.64(32)	43.35(2)	42.78(9)	43.85
$\angle(\mathrm{NCN})$	[180.0]	[174.8]	[180.0]	[180.0]	[180.0]	[176.96]	178.22(17)	176.96
c_a /u$^{1/2}$Å				−0.0175(56)	−0.1111(128)			
c_b /u$^{1/2}$Å				0.0204(74)	−0.0048(10)			
c_c /u$^{1/2}$Å				0.0321(75)	[0.0]			
δ_{H} /u$^{1/2}$Å				[0.0]	0.0381(50)			
$\sigma_{\mathrm{fit}}{}^f$ /uÅ^2			0.00965	0.00273	0.00201	0.00111	0.00055	

[a]Determined by using the computed $(B_e - B_0)$ corrections evaluated at the CCSD(T)/cc-pVQZ level.

[b]$\angle$(CCN) constrained to the *ab initio* estimate.

[c]Extrapolation to complete basis set made from the CCSD(T)/cc-pVTZ and CCSD(T)/cc-pVQZ calculations, see text.

[d]Square brackets enclose assumed values.

[e]The angle between the N−C bond and the $\angle$(HNH) bisector.

[f]Deviation of fit to moments of inertia derived from 36 experimental rotational constants averaged over the 0^+ and 0^- inversion states.

equation to the computed $r(n)$ values. For this two-point extrapolation scheme the two highest available levels of calculations for $n = 3$ and $n = 4$ were used. The estimated values are listed in Table 4.7. The experiment and calculation are seen to be in good agreement, although state of the art computations might still be desirable for a more reliable comparison. For example, the computed value for $r(\mathrm{C}\equiv\mathrm{N})$, which is shorter by 0.0018 Å relative to experiment, is most likely the result of a systematic effect. This discrepancy is found to be very similar to that for HCN, for which the complete basis set limit value evaluated in the same way (Eq. 4.8) as for cyanamide is 1.1515 Å, being 0.0017 Å shorter than the experimental equilibrium value of 1.15324(2) [163].

4.6   Conclusion

A comprehensive analysis of the mm-/submm-wave and IR spectra of cyanamide and its deuterated species has been performed for the ground state 0^+, 0^- inversion doublet within the framework of a uniform Hamiltonian model. For all singly substituted $^{13}\mathrm{C}$ and $^{15}\mathrm{N}$ isotopologues in all three H/D versions of the cyanamide about 100 rotational transitions have been assigned, for six of them for the first time. Many perturbations between 0^+, 0^- substates have been identified and fitted to within experimental accuracy. In addition, extensive experimental data for $\mathrm{H_2NCN}$, HDNCN, and for $\mathrm{D_2NCN}$ allowed tentative identification of various perturbations between the ground state inversion doublet and lowest excited vibrational states, which could not be reproduced by the current model. Nonetheless, substantially improved spectroscopic constants which reproduce the vast majority of the ground state pure rotation and rotation-inversion transitions can now be used in astronomical searches for isotopic species of cyanamide in the interstellar medium. Precise values of the energy splittings for 13 isotopologues have been determined and verified against those obtained from the reduced double-minimum potential.

The assignment of rotational spectra in six new isotopic species of cyanamide combined with improved determination of spectroscopic constants for the other isotopologues, and with advances in structural analysis allowed determination of the hitherto most precise molecular geometry of the cyanamide molecule. The preferred r_e^{SE} geometry is compared in Table 4.7 with two established literature determinations and with several other types of structural fits to the presently determined rotational constants. All those determinations required making some assumptions, starting from augmentation of substitution coordinates with the first-moment condition, as was made in [145]. In those structural fits it was also not possible to determine $\angle(\mathrm{NCN})$ with significance. The least-squares fit r_0 geometry determined from the present constants shows the expected changes relative to the equilibrium results. The r_0 pyramidal angle ϕ is smaller, as discussed for the structurally similar $\mathrm{H_2O}\cdots\mathrm{HCl}$ species [71, 164], and $\angle(\mathrm{HNH})$ is larger. The modified r_m geometries (see Chapter 2.8.3) showed considerable promise in being able to deliver equilibrium quality parameters from ground state constants, by using a very limited set of addi-

tional adjustable parameters. Two such determinations are listed in Table 4.7 and both offer a substantially better quality of fit than the r_0 geometry. The straight-forward $r_m^{(1)}$ determination is seen to be inferior to the $r_m^{(1L)}$ geometry, because the latter takes advantage of the use of the Laurie parameter δ_H to account more effectively for changes on deuteration of the NH bonds. It can be seen that the $r_m^{(1L)}$ geometry does indeed recover equilibrium quality angles, although $r(\text{C}\equiv\text{N})$ appears to be closer to r_0 quality. This determination is also not free from assumptions, concerning the indeterminable c_c constant, and the linear spine.

In conclusion, the preferred r_e^{SE} geometry is associated with both the smallest residuals of fit and is in best agreement with the computational estimate. It was found that this type of geometry determination was very successful in view of the complications arising from the presence of the large amplitude inversion motion, the small principal a-coordinate of the carbon atom, the tiny c-coordinates of all heavy atoms and that it was able to deliver a complete set of structural parameters for cyanamide.

Chapter 5

Acrylonitrile

5.1   Introduction

Acrylonitrile (vinyl cyanide $H_2C{=}CHCN$) is an important molecule in star forming regions. Its first detection in Sagittarius B2 (Sgr B2) was reported by Gardner *et al.* in 1975 [165] on the basis of low frequency hyperfine components of the $2_{11} \leftarrow 2_{12}$ rotational transition. The N region of Sgr B2 is relatively dense and hot, thus even the transitions for the lowest lying excited vibrational states $v_{11} = 1$, $v_{15} = 1$, and $v_{11} = 2$ have been identified there [132]. The ground state rotational transitions have also been detected in the Taurus Molecular Cloud [166, 167] and in the KL region of the Orion Molecular Cloud [168, 169]. In addition, the combination of relatively high abundance and sizable dipole moment of this molecule (see Chapter 8) enabled detection in Sgr B2 of all singly substituted ^{13}C species [6], (see Fig. 1.1). For these reasons acrylonitrile has been classified as an important *weed* molecule, since precise understanding of its rotational spectrum up to THz frequencies is crucial to the analysis of results from cutting edge tools of contemporary radioastronomy, such as Herschel, ALMA, and SOFIA.

The laboratory rotational spectrum of acrylonitrile has already been studied on numerous occasions (see Refs. [170]-[178], and also [23, 6]). The spectrum arises from nonzero values of the dipole moment components $\mu_a = 3.8208(40)$ D and $\mu_a = 0.6866(81)$ D (see Fig. 5.1 and Chapter 8). The rotational constants of acrylonitrile are relatively large so that this molecule is expected to be a plentiful contributor to THz-region spectra. This expectation provided the stimulus for the most recent study [23], in which the knowledge of the rotational spectrum of acrylonitrile was extended for the first time into the THz region, up to 1.67 THz. The experimental data set for the ground state of acrylonitrile was increased in size by more than a factor of 5 to number more than 3000 lines. The foray into the THz region also revealed the presence of a prototype perturbation between the ground state transitions and those in the lowest excited vibrational state, $v_{11} = 1$ at 228 cm^{-1}. A vibrational energy difference as large as this is normally expected to ensure that the
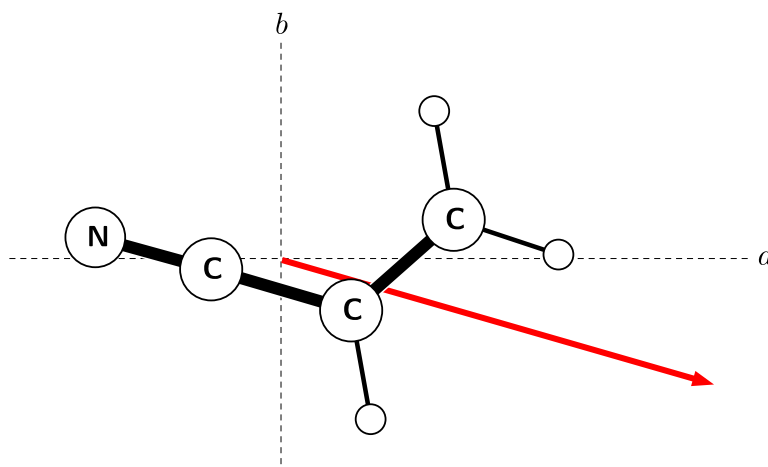
Figure 5.1: The orientation of the acrylonitrile molecule and of its electric dipole in the principal inertial axes.

pertinent energy levels are isolated from each other. In acrylonitrile the large value of the A rotational constant (1.66 cm^{-1}) allows some rotational energy levels of the ground state to interact with those in $v_{11} = 1$. The same reason allows observation of many perturbations of the ground state transitions at higher values of K_a of the inversion doublet 0^+, 0^- in cyanamide, as already discussed in Chapter 4. In the case of acrylonitrile spectroscopic manifestations of such effects are at values of J in the region of 100 or at high values of K_a so that they were not accessible at the lower frequencies of studies preceding that in [23].

The signal to noise ratio in the spectra of the natural abundance sample recorded in [23] was also sufficient for an appreciable improvement of the laboratory data sets for the singly substituted ^{13}C and ^{15}N isotopologues of acrylonitrile. Nonetheless, that data was still limited to relatively low values of J and K_a quantum numbers and was treated in terms of an effective fit of the ground state transitions. In order to extend the understanding of the spectra of the isotopic species of acrylonitrile to the level attained for the parent species the broadband rotational spectra of isotopically enriched ^{13}CH$_2$=CHCN, CH$_2$=CH^{13}CN, CH$_2$=CHC^{15}N, and CH$_2$=CDCN samples were recorded up to 1.2 THz, and their analyses are presented in this chapter. The high frequency spectra revealed the presence of characteristic perturbations between the ground state and the $v_{11} = 1$ excited vibrational state, similar to that identified in the parent molecule [23]. The broadband spectra allowed assignment also of several isotopic species with double isotopic substitution of the heavy atoms, and their spectroscopic constants provided valuable data for determination of a new, precise geometry of the acrylonitrile molecule. The extended knowledge of the THz spectra of the investigated isotopic species, and especially of the b-type transitions which are more relevant at higher frequencies can be used for further searches of these species by radioastronomy.

Table 5.1: Summary of the isotopic species of acrylonitrile studied in this work.

Main species[a]	Doubly substituted species[b]		
$^{13}CH_2{=}CHCN$	$^{13}CH_2{=}^{13}CHCN$		
$CH_2{=}CH^{13}CN$	$CH_2{=}^{13}CH^{13}CN$	$^{13}CH_2{=}CH^{13}CN$	
$CH_2{=}CHC^{15}N$	$^{13}CH_2{=}CHC^{15}N$	$CH_2{=}^{13}CHC^{15}N$	$CH_2{=}CH^{13}C^{15}N$
$CH_2{=}CDCN$			

[a]Spectra measured for isotopically enriched samples.
[b]Spectra assigned in their natural abundance from the isotopically enriched spectra of the singly substituted species.

5.2 Experimental details

For the measurements four commercially available isotopically enriched samples of acrylonitrile: $^{13}CH_2{=}CHCN$, $CH_2{=}CH^{13}CN$, $CH_2{=}CHC^{15}N$, and $CH_2{=}CDCN$ of $97-99\%$ cited enrichment were used. Broadband submillimeter and THz spectra were recorded at Jet Propulsion Laboratory, USA by using the cascaded harmonic multiplication spectrometer described in detail in Ref. [112]. This technique is also used in the broadband MMW spectrometer at IFPAN as shortly described in Chapter 3.2. The measured spectra covered $520 - 608$, $850 - 930$, $950 - 1060$, and $1060 - 1205$ GHz, and were obtained by using harmonic multiplication of frequency from the $11 - 18$ GHz driving synthesizer by factors ranging from $36 = 6 \times 2 \times 3$ at 510 GHz, to $72 = 6 \times 2 \times 2 \times 3$ at 1.2 THz. Only the experimental data for $^{13}CH_2{=}CHCN$ was missing the $850 - 930$ GHz segment since the sample was exhausted prior to this measurement. The radiation was detected after a single pass through a 3 metre length free-space absorption cell. Detection was made with room temperature zero-bias Schottky diode detectors from Virginia Diodes Inc., which were used at all of the studied frequencies. All measurements were carried out at room temperature and the pressure in the absorption cell was close to 10 mTorr. All spectra for a given sample were combined into a single spectrum, and subjected to analysis with the AABS package, already described in Chapter 3.3. The package allows the use of Loomis-Wood type graphical techniques for identifying and assigning the sequences of lines, which was found to be invaluable for all species, and particularly for assigning new ones. All fits and predictions were carried out with Pickett's SPFIT/SPCAT program package [24, 25].

Experimental uncertainties for the newly measured transition frequencies were assigned in proportion to increasing multiplication harmonic and line width. An uncertainty of 0.05 MHz was used for the $520 - 608$ GHz region and 0.15 MHz for the remaining transitions, at $850 - 1205$ GHz. The present measurements were combined with previous data sets for the ground states of the singly substituted

[13]C and ^{15}N isotopic species from Ref. [23], and those already subsumed the results from preceding work. For H_2C=CDCN the lines reported in [178] have been used. Thanks to high quality of spectra of singly substituted species it was also possible to assign the ground states of six new doubly substituted isotopologues in their natural abundance arising from either a combination of two ^{13}C atoms or a ^{13}C and a ^{15}N atom (see Table 5.1). In the case of H_2C=CDCN such species have already been identified in [178] so that the effort was concentrated on assigning the six hitherto unknown species. The transitions for the doubly substituted species were much weaker and thus more susceptible to shifts resulting from effects such as line blending so that their uncertainties were doubled relative to those used for the singly substituted species.

5.3 Rotational spectrum

The rotational spectrum of acrylonitrile at mm- and low-submmillimetre region frequencies is dominated by ^aR-type transitions, which are associated with the large $\mu_a = 3.8209(29)$ D dipole moment component. The THz-region spectra are of a different character since a-type transitions in this region are for very high-J, and are rather weak, whereas transitions associated with the much smaller $\mu_b = 0.6862(79)$ D (see Chapter 8.5) component become dominant owing to much lower J values. Both ^bR- and ^bQ-type transitions are observed, and while the former do not lead to readily discernible patters in the spectrum, the Q-type transitions group into characteristic dense bands, as visible in Fig. 5.2.

5.3.1 Single Isotopic Substitution

Analysis of the spectra for the four singly substituted isotopologues commenced with extensive measurements of ground state transitions. The ^aR-type lines were measured first, then all the intense ^bR, and ^bQ-type transitions in the higher frequency region. Finally the ^bP-type lines were measured, up to K_a ranging from 20 to 25, depending on the isotopologue. Analogously to the parent species the single-state Watsonian Hamiltonian [21] fit of the ground-state transitions showed that a significant number of lines could not be fitted to within experimental error. Due to the lack of low-frequency large amplitude motion in the molecule, such perturbations can only arise from interaction between ground-state rotational levels and those of the lowest lying excited vibrational states such as $v_{11} = 1$, and $v_{15} = 1$ at 228 cm^{-1}, and 331 cm^{-1}, respectively. As has been shown for the parent species, all of the perturbed ground-state rotational levels which contribute to transitions observed in the THz region result from their interaction with those in the $v_{11} = 1$ state. For this reason the next step in the analysis of the THz data was systematic measurement of the first excited state transitions for all four singly substituted species. The single state fits of the $v_{11} = 1$ transitions also revealed a large number of perturbed transitions. Thorough inspection of the perturbed sequences in both states showed that there
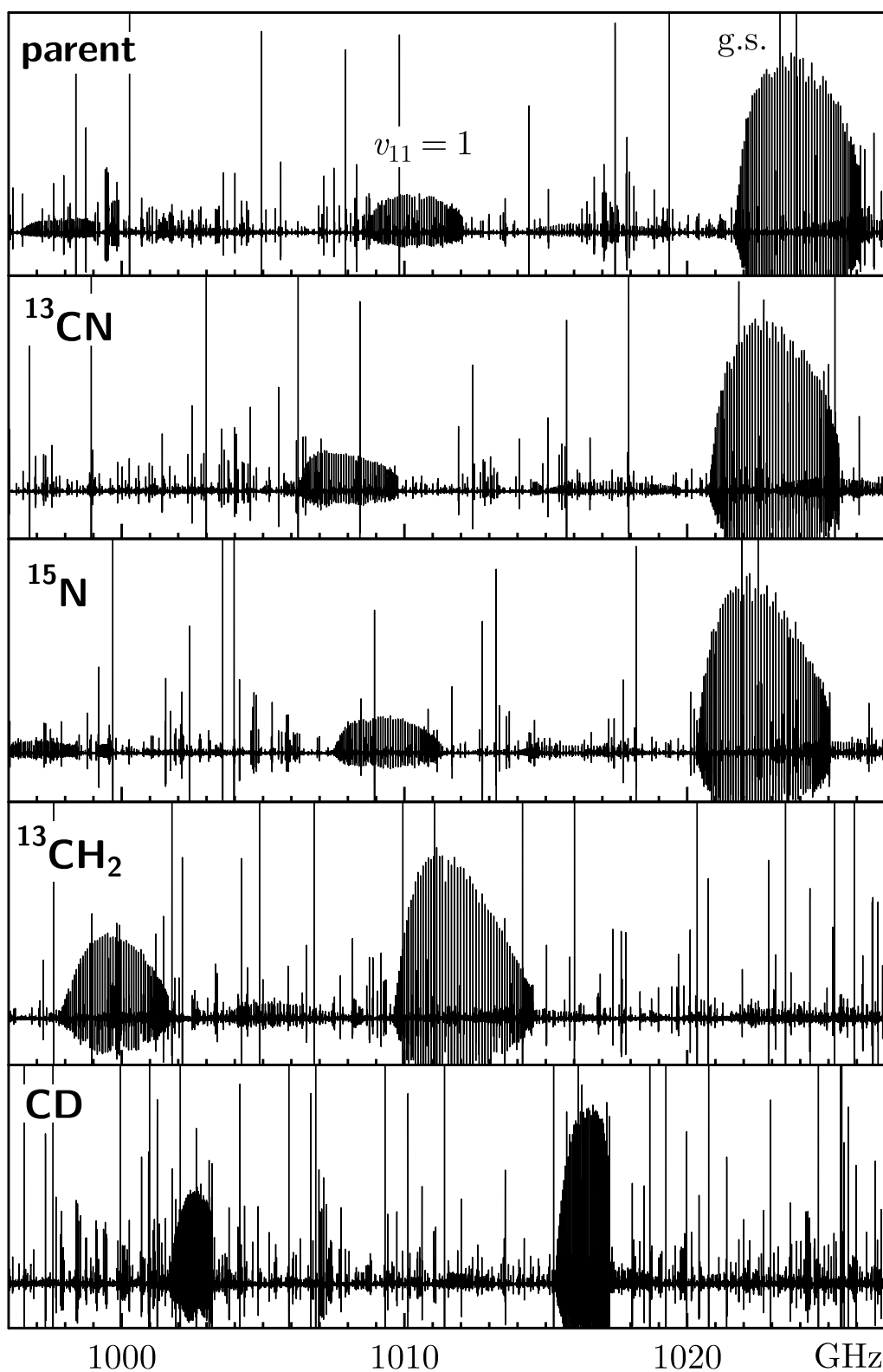
Figure 5.2: Illustration of the relative appearance of the 1 THz rotational spectra of various isotopic species of acrylonitrile. The dense bands in the four top spectra are formed by ^bQ-type transitions for $K_a = 12 \leftarrow 11$, while in the bottom spectrum the visible Q-bands are for $K_a = 15 \leftarrow 14$. The frequencies of the ground state band (right) and the band for $v_{11} = 1$ (left) provide a direct measure of the isotopic and vibrational variation in the A rotational constant.
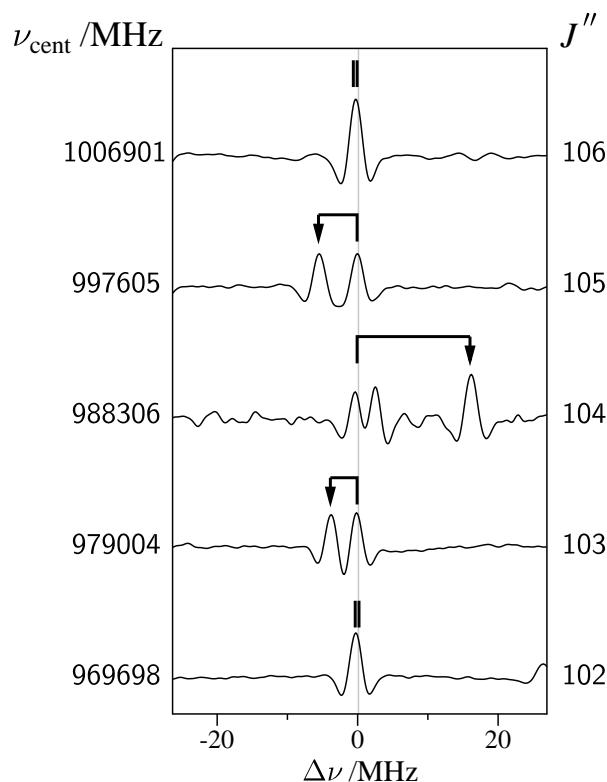
Figure 5.3: Perturbation-induced splitting in the $K_a = 12$ ground state ^aR-type transitions of $CH_2=CH^{13}CN$. The two components, $K_a + K_c = J$ and $K_a + K_c = J + 1$, would normally be degenerate, while in the experimental spectrum (centred above on the $K_a + K_c = J + 1$ sequence) the $K_a + K_c = J$ component is shifted to lower or upper frequencies as indicated by the arrows.

are several sets of interacting rotational levels involved in a g.s. $\leftrightarrow \nu_{11}$ perturbation. This manifests by deviations from single state fits which are similar in magnitude but are of reversed sign for g.s. and for ν_{11} for a given value of J but are for different values of the K_a quantum number. The changes in rotational constants between the parent and the ^{13}C and the ^{15}N species are relatively small so that the perturbations affected transitions for the same pairs of K_a values as in the parent isotopologue. At higher K_a there were rather extended, smooth changes resulting from interaction maximising at $K_a = 21, 22$ in the ground state and $K_a = 17, 18$ in $\nu_{11} = 1$, as shown in the right-hand part of Fig. 5 in Ref. [23]. There were also several accidental resonances, such as the one illustrated for $H_2C=CH^{13}CN$ in Fig. 5.3. In this case some $K_a = 12$ levels in the ground state perturb with $K_a = 2$ levels in $\nu_{11} = 1$. The maximum in this resonance is visible in the $J = 105 \leftarrow 104$ transition at 988 GHz, while a similar resonance in the parent species is maximised in the $J = 107 \leftarrow 106$ transition at 1011 GHz (see Fig 7 of Ref. [23]). The change in the rotational constant A between the parent and the $H_2C=CDCN$ species is sufficiently large (almost 10 GHz) to shift the perturbations to completely different values of quantum numbers. Thus the main high K_a perturbation is most pronounced between $K_a = 26$ in the ground state and $K_a = 22$ in $\nu_{11} = 1$. The accidental resonances are also in different places and a level crossing type sequence affecting the ground state $K_a = 15$
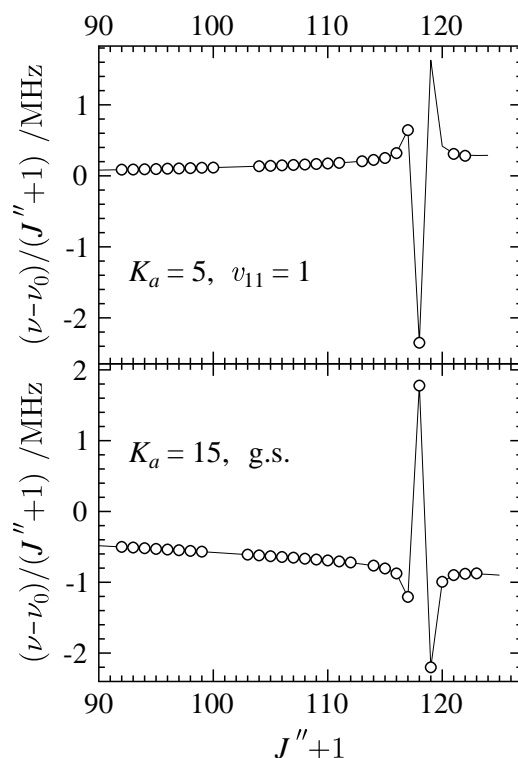
Figure 5.4: Evidence for a level-crossing type perturbation in H_2C=CDCN between the $K_a = 15$ levels of the ground state and $K_a = 5$ levels in $v_{11} = 1$. The plotted quantities are scaled differences between frequencies of ^aR-type transitions from the final coupled fit and those from single state effective fits. Continuous lines are predictions from the final fit and circles mark experimental measurements. The maximum in this perturbation is for very high J transitions with frequencies close to 1.1 THz.

transitions and $K_a = 5$ transitions of $v_{11} = 1$ is shown in Fig. 5.4. The maximum in this perturbation is for $J'' = 117$ and it is necessary to reach up to 1.1 THz in order to measure the most affected lines. A similar sequence has been identified for the parent species (left side of Fig. 5 in Ref. [23]) but in that case $K_a = 16$ rotational levels of the g.s. perturb with $K_a = 10$ levels of $v_{11} = 1$, and the maximum is at $J'' = 102$.

In view of the various perturbations the only satisfactory treatment of the extensive THz-region measurements of the ground and of the $v_{11} = 1$ states for four isotopologues was the coupled fit based on the two-state Hamiltonian (Eq. 2.49). The type of the interaction between the g.s. and $v_{11} = 1$ depends on the irreducible representations of the point group to which these states belong. For acrylonitrile both the ground and the ν_{11} state belong to the A' irreducible representation of the C_s symmetry point group, which describes the molecule. According to Eq. 2.50 these two states can interact by means of both c-axis Coriolis and Fermi interactions. The two-state Hamiltonian for the coupled fit constructed in standard 2×2 block form

for this case is given by

$$\mathcal{H} = \begin{pmatrix} \mathcal{H}_{\text{rot}}^{\text{(g.s.)}} & \mathcal{H}_{\text{C}} + \mathcal{H}_{\text{F}} \\ \mathcal{H}_{\text{C}} + \mathcal{H}_{\text{F}} & \mathcal{H}_{\text{rot}}^{(\nu_{11})} + \Delta E \end{pmatrix}. \tag{5.1}$$

The diagonal blocks consist of the rotational Hamiltonian for the pertinent states, augmented by the vibrational energy difference between $v_{11} = 1$ and the ground state, $\Delta E = E_{11} - E_0$. The off-diagonal blocks are the sum of Coriolis $\mathcal{H}_{\text{C}}$ and Fermi $\mathcal{H}_{\text{F}}$ terms defined by Eqs. 2.51, and 2.54, respectively. In similarity to the treatment used for the parent species [23] the leading terms for the Coriolis interaction for acrylonitrile are given by

$$\mathcal{H}_{\text{C}} = (F_{ab} + F_{ab}^J \hat{J}^2 + F_{ab}^K \hat{J}_z^{\,2} + \ldots)(\hat{J}_z \hat{J}_x + \hat{J}_x \hat{J}_z). \tag{5.2}$$

The second contribution off-diagonal arises from Fermi resonance (Eq. 2.54) and is of the form

$$\mathcal{H}_{\text{F}} = W_{\text{F}} + W_{\text{F}}^J \hat{J}^2 + W_{\text{F}}^K \hat{J}_z^{\,2} + \left[(W_\pm + W_\pm^J P^2 + W_\pm^K \hat{J}_z^{\,2} + \ldots), \hat{J}_{xy}^{\,2} \right]_+ \tag{5.3}$$

More detailed definition of this term is given in section 2.6 of this dissertation.

The fits revealed that the Coriolis term is a relatively minor contributor to the interaction, at least as probed by the measured transitions. For the parent species only the value of F_{ab} could be determined. For the presently studied isotopologues even this was not possible, so that the value of F_{ab} was fixed. As far as the Fermi terms are concerned, only the higher order terms in the $W_\pm$ sequence were found to be significant. The values of constants resulting from the coupled fits are listed in Tables 5.2 and 5.3, where they are also compared with the results for the parent isotopic species. It was found that the A-reduced form of Watson's asymmetric rotor Hamiltonian [21] offered somewhat better convergence and lower deviation of the coupled fit than the S-reduced form.

It is useful to clarify some specific aspects of these fits. The ground state energy levels are known to perturb with those of $v_{11} = 1$ but that state is, in turn, known to interact with the vibrational state immediately above it, namely $v_{15} = 1$ at 333 cm^{-1} [179]. In fact, a ladder of interactions connecting successively higher vibrational states of acrylonitrile has been identified [23]. Since the primary aim of this study is to provide the most reliable description of the ground state transitions it was not practicable to set up the whole chain of these interstate interactions so that the fit is limited to the two lowest states. The cutoff criterion of SPFIT was used to reject from the fit transitions of $v_{11} = 1$ that were outside the g.s. $\leftrightarrow v_{11} = 1$ interaction model. At the same time it was ensured that no transitions of the ground state were out of the fit. The success of this procedure can be assessed from Tables 5.2 and 5.3, in which a breakdown of the numbers of fitted lines and of the deviation of fit over the two states is provided. All assigned ground state lines have been fitted at a satisfactory weighted deviation of fit in the region of 1.2. For $v_{11} = 1$ the weighted deviation of fit is significantly poorer, and closer to 2, while at the

Table 5.2: Spectroscopic constants derived from the coupled fits for the two singly substituted ^{13}C isotopic species of acrylonitrile studied in this work compared with those for the parent species.

	parent		$H_2{}^{13}$C-CHC≡N		H_2C-CH^{13}C≡N	
	g.s.	$v_{11}=1$	g.s.	$v_{11}=1$	g.s.	$v_{11}=1$
A/MHz	49850.69690(73)^a	49170.4566(17)	49195.2056(23)	48582.2827(58)	49799.6210(23)	49036.2683(63)
B/MHz	4971.212477(62)	4990.77301(16)	4837.625265(73)	4856.60158(51)	4948.412910(79)	4967.36553(69)
C/MHz	4513.828478(63)	4521.96695(15)	4398.197085(64)	4406.24225(58)	4494.606874(65)	4502.44062(63)
Δ_J/kHz	2.244077(20)	2.269240(50)	2.175183(21)	2.19819(12)	2.220889(21)	2.24350(14)
Δ_{JK}/kHz	$-85.6406(29)$	$-76.5777(29)$	$-86.9335(12)$	$-78.1355(42)$	$-86.1086(10)$	$-76.3412(42)$
Δ_K/kHz	2715.446(15)	2171.438(35)	2695.957(35)	2210.398(79)	2748.907(37)	2111.844(90)
δ_J/kHz	0.4566466(46)	0.467851(16)	0.438388(13)	0.448841(31)	0.451501(12)	0.462143(42)
δ_K/kHz	24.4863(21)	27.2262(46)	22.8119(46)	25.848(23)	24.0382(39)	26.347(17)
Φ_J/Hz	0.0064398(24)	0.0064259(62)	0.0061996(37)	0.006121(15)	0.0062710(33)	0.006256(15)
Φ_{JK}/Hz	$-0.00118(53)$	0.0624(18)	$-0.02557(63)$	0.0271(35)	$-0.01310(80)$	0.0458(31)
Φ_{KJ}/Hz	$-7.7579(55)$	$-0.635(15)$	$-7.802(10)$	$-1.250(31)$	$-7.583(10)$	0.184(36)
Φ_K/Hz	384.58(13)	$-20.31(30)$	385.32(24)	40.79(63)	386.34(25)	$-125.26(71)$
ϕ_J/Hz	0.00236906(96)	0.0023851(26)	0.0022529(21)	0.0022618(57)	0.0023152(19)	0.0023351(55)
ϕ_{JK}/Hz	0.14337(55)	0.1982(13)	0.1268(11)	0.1820(48)	0.1330(10)	0.2142(33)
ϕ_K/Hz	37.364(80)	39.59(25)	34.768(82)	36.89(52)	37.48(11)	42.41(41)
L_J/mHz	$-0.00002661(10)$	$-0.00002549(27)$	$-0.00002508(16)$	$-0.00002238(61)$	$-0.00002568(14)$	$-0.00002669(58)$
L_{JJK}/mHz	$-0.001313(40)$	$-0.00290(13)$	$-0.000845(61)$	$-0.00156(24)$	$-0.000909(60)$	$-0.00308(20)$
L_{JK}/mHz	0.4537(25)	$-0.8257(81)$	0.4361(42)	$-0.896(35)$	0.1562(96)	$-1.813(21)$
L_{KKJ}/mHz	$-0.086(15)$	$-3.683(57)$	0.141(38)	$-3.11(14)$	0.761(49)	0.005(10)
L_K/mHz	$-60.46(47)$	238.3(10)	$-62.93(70)$	179.9(22)	$-60.23(74)$	348.3(24)
l_J/mHz	$-0.000011628(46)$	$-0.00001171(12)$	$-0.000010714(90)$	$-0.00001058(26)$	$-0.000011069(79)$	$-0.00001189(23)$
l_{JK}/mHz	$-0.001003(29)$	$-0.000146(76)$	$-0.000860(54)$	$-0.00041(22)$	$-0.001006(50)$	$-0.00187(15)$
l_{KJ}/mHz	$-0.1771(65)$	$-0.407(18)$	$-0.1220(90)$	$-0.257(35)$	$-0.1349(85)$	$-0.647(26)$
l_K/mHz	8.74(19)	$-10.10(93)$	7.23(39)	$-19.5(29)$	$-13.92(90)$	$-99.8(16)$
P_{KJ}/mHz	$-0.0000506(40)$	0.0001922(91)	$-0.0000792(35)$	0.0002301(67)	0.0000330(79)	$-0.000128(13)$
P_{KKJ}/mHz	$-0.0000952(70)$	0.002410(23)	$-0.000171(18)$	0.002313(85)	$-0.000256(17)$	0.00125(19)
P_K/mHz	0.00745(55)	$-0.1381(12)$	0.00938(72)	$-0.1056(27)$	0.00727(76)	$-0.2082(31)$
ΔE/MHz		6844259.15(62)		6790930.(42)		6788507.(12)
ΔE/cm^{-1}		228.29991(2)		226.5210(14)		226.4402(4)
F_{ab}/MHz		$-30.20(16)$		$[-30.2]$		$[-30.2]$
$W_\pm^K$/MHz		0.043302(68)		0.04233(12)		0.04139(12)
$W_\pm^{JK}$/MHz		$-0.0000000208(14)$		$[-0.0000000208]$		$-0.0000000718(29)$
$W_\pm^{KK}$/MHz		$-0.00002068(15)$		$[-0.00002068]$		$-0.00001345(24)$
$N_{\text{lines}}{}^b$	3145,1	1989,91	2044,0	934,49	2428,0	1258,107
$\sigma_{\text{fit}}{}^c$/MHz	0.143	0.243	0.146	0.216	0.149	0.275
$\sigma_{\text{rms}}{}^c$	1.253	2.079	1.273	1.882	1.256	2.055

^{a}Round parentheses enclose standard errors in units of the last quoted digit of the value of the constant, square parentheses enclose assumed values.

^{b}The number of distinct frequency fitted lines and the number of lines rejected at the 10σ fitting criterion of the SPFIT program.

^{c}Deviations of fit for the two vibrational subsets in each coupled fit, while σ_{rms} for the three coupled fits are, from left to right, 1.62, 1.49, and 1.58, respectively.

Table 5.3: Spectroscopic constants derived from the coupled fits for H_2C-CHC≡^{15}N and H_2C-CDC≡N compared with those for the parent isotopic species of acrylonitrile.

	parent		H_2C-CHC≡^{15}N		H_2C-CDC≡N	
	g.s.	$v_{11} = 1$	g.s.	$v_{11} = 1$	g.s.	$v_{11} = 1$
A/MHz	49850.69690(73)	49170.4566(17)	49655.3623(25)	48988.3840(78)	40196.5482(23)	39634.030(12)
B/MHz	4971.212477(62)	4990.77301(16)	4819.715497(79)	4838.78823(53)	4934.39619(22)	4953.67764(70)
C/MHz	4513.828478(63)	4521.96695(15)	4386.999238(66)	4395.08709(56)	4388.34388(22)	4395.54521(67)
Δ_J/kHz	2.244077(20)	2.269240(50)	2.106558(19)	2.13063(11)	2.034838(48)	2.05936(14)
Δ_{JK}/kHz	−85.6406(29)	−76.5777(29)	−83.1969(13)	−74.4962(39)	−44.3009(17)	−39.8033(35)
Δ_K/kHz	2715.446(15)	2171.438(35)	2724.330(38)	2191.34(11)	1300.299(20)	1003.16(14)
δ_J/kHz	0.4566466(46)	0.467851(16)	0.420764(14)	0.431558(27)	0.458760(15)	0.470098(43)
δ_K/kHz	24.4863(21)	27.2262(46)	23.6810(56)	26.647(12)	22.1313(36)	23.138(10)
Φ_J/Hz	0.0064398(24)	0.0064259(62)	0.0058938(30)	0.005836(11)	0.0054066(45)	0.005387(13)
Φ_{JK}/Hz	−0.00118(53)	0.0624(18)	−0.0141(14)	0.0697(27)	0.0803(12)	0.1055(19)
Φ_{KJ}/Hz	−7.7579(55)	−0.635(15)	−7.582(12)	−1.020(28)	−3.336(11)	−1.006(21)
Φ_K/Hz	384.58(13)	−20.31(30)	389.10(25)	−2.93(91)	115.704(82)	−55.04(80)
ϕ_J/Hz	0.00236906(96)	0.0023851(26)	0.0021312(17)	0.0021597(37)	0.0021147(19)	0.0021415(55)
ϕ_{JK}/Hz	0.14337(55)	0.1982(13)	0.1332(10)	0.1982(23)	0.13831(68)	0.1712(18)
ϕ_K/Hz	37.364(80)	39.59(25)	35.01(21)	43.66(37)	18.98(11)	19.60(16)
L_J/mHz	−0.00002661(10)	−0.00002549(27)	−0.00002370(12)	−0.00002195(40)	−0.00002105(15)	−0.00002127(49)
L_{JJK}/mHz	−0.001313(40)	−0.00290(13)	−0.000480(76)	−0.00334(16)	−0.001046(65)	−0.00202(11)
L_{JK}/mHz	0.4537(25)	−0.8257(81)	0.2398(76)	−1.211(18)	0.1377(60)	−0.761(11)
L_{KKJ}/mHz	−0.086(15)	−3.683(57)	0.480(44)	−2.919(65)	−0.170(38)	0.946(50)
L_K/mHz	−60.46(47)	238.3(10)	−62.47(70)	220.5(33)	−11.09(15)	92.4(21)
l_J/mHz	−0.000011628(46)	−0.00001171(12)	−0.000009973(65)	−0.00001064(15)	−0.000009433(72)	−0.00001021(21)
l_{JK}/mHz	−0.001003(29)	−0.000146(76)	−0.000901(47)	−0.00116(10)	−0.000924(32)	−0.001107(82)
l_{KJ}/mHz	−0.1771(65)	−0.407(18)	−0.058(11)	−0.587(22)	−0.0782(58)	−0.2265(99)
l_K/mHz	8.74(19)	−10.10(93)	−3.05(66)	−60.3(16)	−0.46(40)	−24.88(67)
P_{KJ}/mHz	−0.0000506(40)	0.0001922(91)	0.0000458(54)	−0.000144(11)	0.0000616(50)	−0.0000404(51)
P_{KKJ}/mHz	−0.0000952(70)	0.002410(23)	−0.000293(17)	0.00512(13)	−0.000029(12)	−0.000151(47)
P_K/mHz	0.00745(55)	−0.1381(12)	0.00828(70)	−0.1310(46)	0.00070(10)	−0.0398(21)
ΔE/MHz		6844259.15(62)		6770318.(17)		6763114.4(46)
ΔE/cm^{-1}		228.29991(2)		225.8335(6)		225.59321(15)
F_{ab}/MHz		−30.20(16)		[−30.2]		[−30.2]
$W_\pm^K$/MHz		0.043302(68)		0.03914(11)		0.02864(14)
$W_\pm^{JK}$/MHz		−0.0000000208(14)		−0.0000000580(21)		−0.0000000227(21)
$W_\pm^{KK}$/MHz		−0.00002068(15)		−0.00001330(22)		−0.00000421(24)
N_{lines}[a]	3145,1	1989,91	2265,0	1212,103	2379,0	1271,82
σ_{fit}[b]/MHz	0.143	0.243	0.134	0.233	0.142	0.321
σ_{rms}[b]	1.253	2.079	1.160	1.838	1.106	2.381

[a]The number of distinct frequency fitted lines and the number of lines rejected at the 10σ fitting criterion of the SPFIT program.

[b]Deviations of fit for the two vibrational subsets in each coupled fit, while σ_{rms} for the three coupled fits are, from left to right, 1.62, 1.43, and 1.67, respectively.
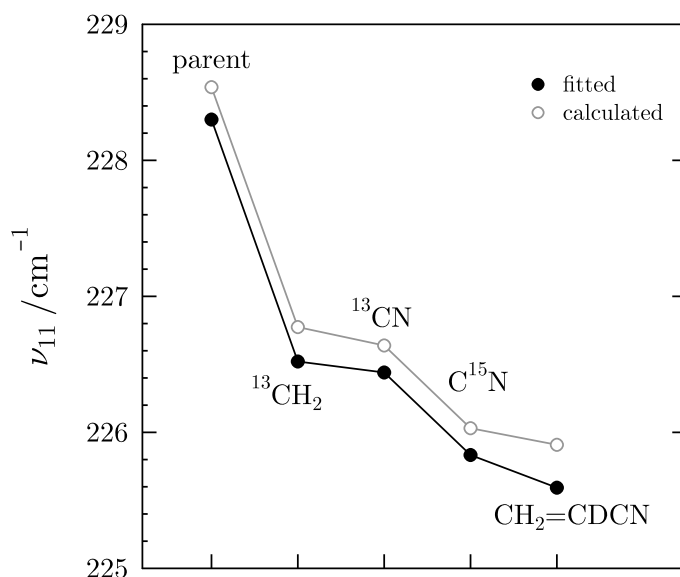
Figure 5.5: Comparison of values for ν_{11} derived from the coupled fits for the various isotopic species of acrylonitrile with those obtained from anharmonic force field calculations at the CCSD(T)/6-31G(d,p) level carried out with the CFOUR package [96].

10σ cutoff criterion there were from around 50 to over 100 lines rejected from fit, depending on the isotopic species.

The currently determined spectroscopic constants for the four singly substituted isotopic species show similar values and relative trends to those in the parent species. Only for H_2C=CDCN there are major changes in values of all K-dependent constants relative to the parent and those are associated with the large deuteration effect on the A rotational constant. The validity of the coupled state fits for the isotopic species is confirmed by the comparison with results of *ab initio* anharmonic force field calculation shown in Fig. 5.5. The observed isotopic dependence of ΔE from the fits and the calculated isotopic dependence of the fundamental frequency ν_{11} are practically identical.

5.3.2   Double Isotopic Substitution

The high isotopic enrichment of the acrylonitrile samples used in these measurements was sufficient for measurement of lines in species with double isotopic substitution. The good visibility of the spectra of the doubly substituted species is illustrated in Fig. 5.6 for lines of $H_2{}^{13}C$=CH^{13}CN in the spectrum of the enriched $H_2{}^{13}C$=CHCN sample.

The ^aR-type transitions for such species can only be assigned reliably in the lowest frequency spectral segment, at $520 - 608$ GHz. The available values of the J quantum number are thus in a relatively narrow range, typically from 55 to 68. The range of accessible J values was, however, much greater since the THz-region spectra
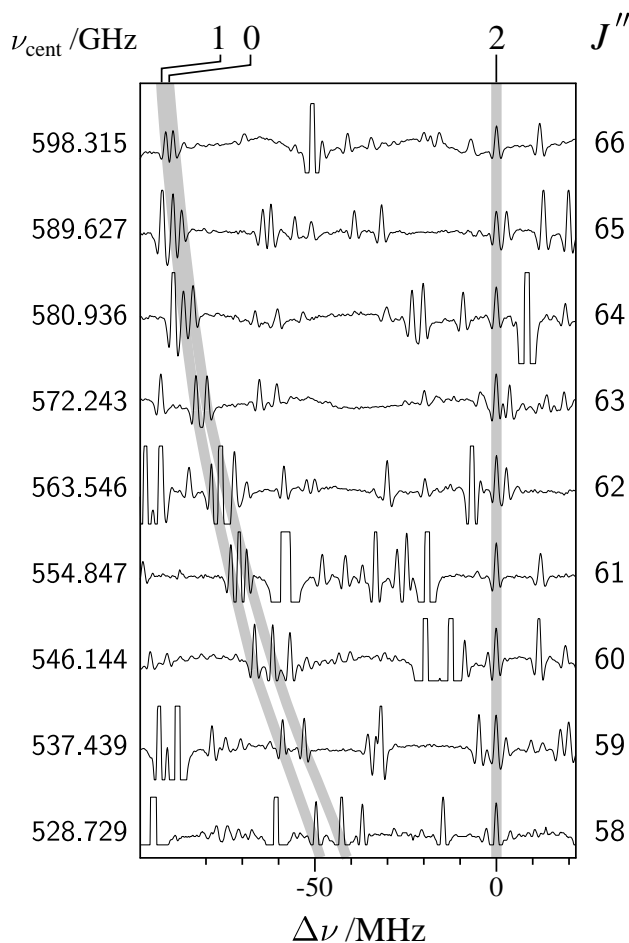
Figure 5.6: Loomis-Wood type plot illustrating the good visibility of the lines of $H_2{}^{13}C=CH^{13}CN$ in the spectrum of the isotopically enriched $H_2{}^{13}C=CHCN$ sample. Spectral strips are aligned on frequencies of successive $K_a = 2$, ^aR-type transitions of $H_2{}^{13}C=CH^{13}CN$ for the lower frequency of two possible sequences of such lines. The pertinent J'' values are listed on the right. The accidentally adjacent $K_a = 0$ and 1 line sequences for this species are also indicated by the guiding lines, but these sequences are for values of J greater by 1 from those for the $K_a = 2$ sequence.

provide access to much lower J transitions in the ^bR-type branch. These occur for intermediate values of K_a and measured transitions of this type for $H_2{}^{13}C={}^{13}CHCN$, for example, are for $J = 10 - 38$ and $K_a = 8 - 11$. It was possible to assign ^aR-type transitions up to $K_a = 20$ but since it is known from the analysis of the singly substituted species that lines for this value of K_a are already involved in perturbation with $v_{11} = 1$ the fits were restricted to $K_a = 19$.

Transitions of some isotopic species, such as $H_2{}^{13}C=CH^{13}CN$, were anticipated to occur at similar intensity in spectra of two different enriched samples, in this case in spectra of $H_2{}^{13}C=CHCN$ and $H_2C=CH^{13}CN$. This provided additional possibilities for checking the assignment and a way to measure lines that were obscured by spectral features in one but not in the other sample.

Zero order predictions of the new species were made on the basis of *ab initio* calculations, which were corrected by the difference from experiment for the assigned

Table 5.4: Spectroscopic constants for the ground states of six new isotopic species of acrylonitrile assigned in this work compared with those for the parent species.

	parent, Ref. [23]	$H_2{}^{13}C={}^{13}CHCN$	$H_2{}^{13}C=CH^{13}CN$	$H_2C={}^{13}CH^{13}CN$	$H_2{}^{13}C=CHC^{15}N$	$H_2C={}^{13}CHC^{15}N$	$H_2C=CH^{13}C^{15}N$
A^a/MHz	49850.69649(45)	$47962.983(16)^b$	49143.268(12)	48597.436(16)	48995.133(19)	48449.248(18)	49598.159(13)
B/MHz	4971.163635(39)	4818.7010(49)	4813.9503(42)	4925.5833(52)	4689.3004(72)	4796.6006(62)	4800.2635(55)
C/MHz	4513.877241(40)	4372.4772(56)	4378.2818(49)	4465.7804(60)	4273.7615(70)	4358.2478(59)	4370.5192(51)
D_J/kHz	2.182439(12)	2.0643(13)	2.0994(11)	2.0995(15)	1.9924(17)	1.9907(15)	2.0298(13)
D_{JK}/kHz	−85.01583(36)	−81.3694(51)	−86.7104(47)	−80.3217(63)	−83.8574(63)	−77.5242(62)	−83.1523(55)
D_K/kHz	2714.868(10)	2576.113(68)	2727.663(50)	2625.377(63)	2702.566(73)	2602.595(76)	2757.511(56)
d_1/kHz	−0.4565329(30)	−0.437850(68)	−0.434143(65)	−0.448720(81)	−0.40425(32)	−0.41769(31)	−0.41661(26)
d_2/kHz	−0.0308686(11)	−0.029138(19)	−0.027514(19)	−0.031108(23)	−0.026053(22)	−0.029374(22)	−0.027934(19)
H_J/Hz	0.0057393(14)	0.00548(11)	0.005693(99)	0.00541(13)	0.00528(14)	0.00515(13)	0.00500(11)
H_{JK}/Hz	−0.284122(77)	−0.25503(65)	−0.28364(59)	−0.26507(81)	−0.25989(77)	−0.24043(77)	−0.27177(69)
H_{KJ}/Hz	−6.9763(26)	−6.6776(54)	−6.8211(54)	−6.5883(64)	−6.7936(87)	−6.5949(64)	−6.7528(80)
σ_{fit}/MHz	0.1272	0.1464	0.1220	0.1694	0.1237	0.1594	0.1167
σ_{rms}	1.0281	0.8028	0.8178	0.8327	0.9175	0.9180	0.7730
N_{lines}	2852	259	301	231	229	265	266

^{a}All constants are from single state, effective fits of the S-reduced asymmetric rotor Hamiltonian.

^{b}The remaining sextic and higher order centrifugal distortion constants were fixed at values determined for the parent species, see Table 4 of Ref. [23].

species. Such predictions turned out to be accurate to within several MHz for the $K_a = 0$ transition sequences. The assignment of the relatively weak features for the doubly substituted species required careful screening for spurious coincidences and blends. For this reason lines were measured only if the Loomis-Wood display for a given transition sequence showed a clear series of lines at consistent intensity. The preceding study [23] showed that in the case when only the ground state transitions are used a somewhat better fit is obtained with the S-reduced version of the asymmetric rotor Hamiltonian. This form of the Hamiltonian was therefore used for the newly assigned species and the resulting constants are listed in Table 5.4. At the range of quantum number values represented in these data sets it is not expected to see significant perturbation effects and the deviations of fit in Table 5.4 confirm the suitability of the fitting model. The moderate scope of the data sets for the doubly substituted species allowed only constants up to H_{KJ} to be determined. Nevertheless, the small variation and the generally smaller values of centrifugal distortion constants relative to those in the parent species are also in support of the present analysis.

5.4   Molecular geometry

Several determinations of the molecular geometry of acrylonitrile have already been made, with the first published in [170], and the most recent ones in Refs. [176, 178]. The present work increases the number of available rotational constants by 45% and gives the opportunity for a considerable improvement of the geometry determination. Acrylonitrile is a relatively small molecule and therefore it is possible to determine the semi-experimental equilibrium geometry, r_e^{SE}. This method has been applied for the structure determination of cyanamide (Chapter 4), and details on this type of structure evaluation are given in Chapter 2.8.4, and in Refs. [161, 98]. In this r_e^{SE} evaluation the experimental constants are combined with *ab initio* corrections to equilibrium obtained from the anharmonic force field. It appears that a computation with the best possible accounting for electron correlation effects is a prerequisite. The length of the basis set is also important and two results are reported. The first has been obtained at the CCSD(T)/6-31G(d,p) level and the second at the CCSD(T)/cc-pVTZ, employing 75 and 162 basis functions, respectively. The *ab initio* calculations were carried out with CFOUR [96] and the structural fits were made with program STRFIT [71].

The reliability of the r_e^{SE} geometry depends largely on the accuracy of the calculation of the sum of the vibration-rotation contributions $\alpha_i/2$ over all normal modes in the molecule (see Eq. 2.77). This is rather difficult to estimate [161] although it is possible to inspect the performance of the α_i calculation for the ν_{11} mode, since rotational constants for this mode have presently determined in several isotopic species. The comparison of calculation and experiment made in Fig. 5.7 shows that the nominally inferior CCSD(T)/6-31G(d,p) calculation appears to perform appreciably better. Nevertheless, this is only a small part of the overall picture, since
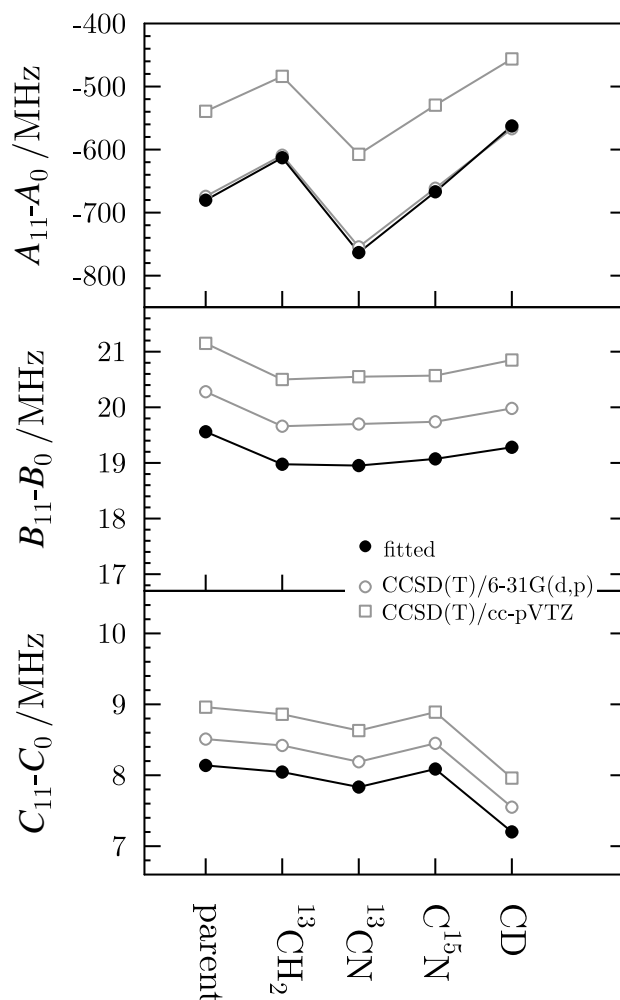
Figure 5.7: Comparison of the experimental and the calculated differences in rotational constants between $v_{11} = 1$ and the ground state for various isotopic species of acrylonitrile. The experimental values are from the coupled fits and the theoretical ones are from anharmonic force field calculations performed with CFOUR.

ν_{11} is known to be strongly coupled with the ν_{15} mode by a strong a-axis resonance [175]. The CFOUR calculation of α_i's is an effective one for each state (see Chapter 7) and is very sensitive to the energy separation of adjacent vibrational states. On the other hand the sum of a pair of α_i's for two states which may be connected by a resonance is a rather stable quantity. For the parent acrylonitrile species it was found, using also the rotational constants for $v_{15} = 1$ from [175], that the average deviation from experiment for $(\nu_{11} + \nu_{15})$ for the three rotational constants is 3.3% for CCSD(T)/6-31G(d,p) and 3.1% for the CCSD(T)/cc-pVTZ calculation. Fig. 5.7 also demonstrates that the isotopic dependence of vibration-rotation contributions to rotational constants is calculated reliably.

Geometry evaluations were carried out by using the experimental constants and the $B_e - B_0$ corrections from CFOUR for the S-reduction of the asymmetric rotor

Table 5.5: Summary of the structural parameters (Å and degree) determined for acrylonitrile.[a]

	r_0	r_s	$r_m^{(1)}$	$r_m^{(1L)}$	$\left(r_e^{\mathrm{SE}}\right)^b$	$\left(r_e^{\mathrm{SE}}\right)^c$	calc.[d]	Ref. [176][e]
$r(\mathrm{C}{=}\mathrm{C})$	1.342(2)	1.344(4)	1.3383(11)	1.3373(11)	1.3350(9)	1.3353(4)	1.3363	1.337
$r(\mathrm{C}{-}\mathrm{C})$	1.430(2)	1.429(5)	1.4271(18)	1.4322(12)	1.4315(11)	1.4314(4)	1.4302	1.432
$r(\mathrm{C}{\equiv}\mathrm{N})$	1.164(2)	1.160(5)	1.1615(13)	1.1571(15)	1.1584(11)	1.1583(4)	1.1610	1.157
$r(\mathrm{C}{-}\mathrm{H}^c)$	1.086(3)	1.093(4)	1.0884(13)	1.0749(29)	1.0800(12)	1.0797(4)	1.0776	1.081
$r(\mathrm{C}{-}\mathrm{H}^t)$	1.089(9)	1.097(17)	1.0859(42)	1.0714(47)	1.0799(36)	1.0800(13)	1.0771	1.080
$r(\mathrm{C}{-}\mathrm{H}^u)$	1.086(2)	1.085(3)	1.0865(11)	1.0717(30)	1.0800(11)	1.0798(4)	1.0768	1.082
$\angle(\mathrm{CCH}^c)$	120.6(1)	120.3(5)	120.40(6)	120.30(6)	121.36(6)	121.22(2)	121.31	121.5
$\angle(\mathrm{CCH}^t)$	119.3(14)	118.5(18)	119.81(64)	119.70(62)	120.46(58)	120.28(21)	120.42	120.3
$\angle(\mathrm{C}{=}\mathrm{CH}^u)$	122.0(1)	121.6(6)	121.76(9)	121.64(10)	121.71(8)	121.50(3)	121.35	121.4
$\angle(\mathrm{CCC})$	122.0(1)	122.0(6)	122.33(16)	122.12(16)	122.01(16)	122.03(6)	122.39	122.1
$\angle(\mathrm{CCN})$	180.4(5)	179.0(10)	179.52(32)	178.40(41)	179.13(29)	179.08(11)	178.94	179.1
c_a			−0.0097(64)	−0.0253(52)				
c_b			0.0271(85)	−0.0079(17)				
c_c			0.0381(89)	[0.0]				
δ_{H}			[0]	0.0390(73)				
$\sigma_{\mathrm{fit}}/\mathrm{u\mathring{A}}^2$	0.00409		0.00310	0.00288	0.00309	0.00112		
N_{const}	40		58	58	58	58		

[a]All fits are to constants from single state, effective fits of the S-reduced asymmetric rotor Hamiltonian.

[b]Vibration-rotation corrections evaluated at the CCSD(T)/6-31G(d,p) level.

[c]Vibration-rotation corrections evaluated at the CCSD(T)/cc-pVTZ level. Further numerical details on this structural fit are given in Table A.2 at the end of this dissertation.

[d]Ab initio equilibrium structure calculated at the CCSD(T)/cc-pVTZ level.

[e]Near-equilibrium structure (see text).
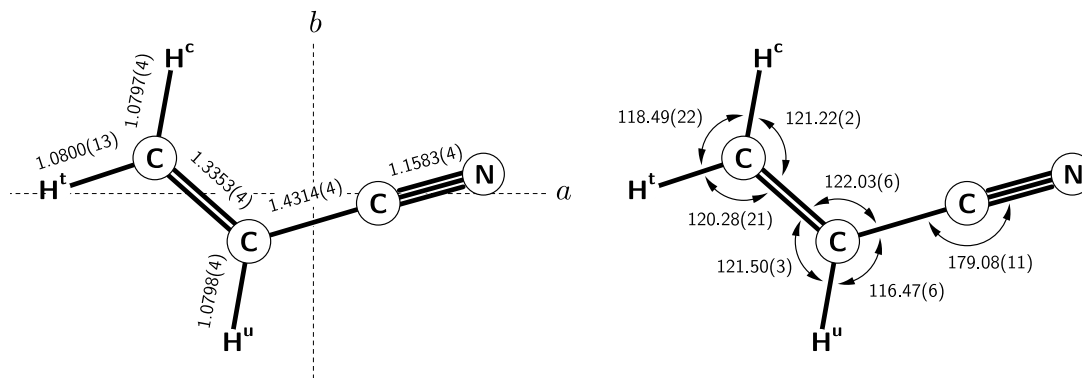
Figure 5.8: The preferred r_e^{SE} geometry for acrylonitrile (Å and degrees) determined by using 58 experimental rotational constants and vibration-rotation corrections evaluated at the CCSD(T)/cc-pVTZ level. Details on this structural fit are summarized in Table 5.5 in this Chapter, and in Table A.2 of the Appendix.

Hamiltonian. When only the A-reduced constants were available, such as from Ref. [178], those were converted to the S-reduction with the formulae from [21] and program CONVC [17]. For the four singly substituted species studied presently an effective ground state S-reduction fit was performed in the same way that was done in [23]. All known rotational constants have been used in the structural fits, except for the A rotational constant for CHD^c=CHCN from [178], which appeared to be poorly determined. The notation for the hydrogen atoms has been adopted from [178]. The results obtained from the present data are summarised in Table 5.5. It is seen that the two r_e^{SE} geometries in Table 5.5 are very similar, in that the average difference is below 0.0002 Å in bond lengths and 0.08° in bond angles (if the poorly determined parameters involving H^t are excluded). However, the geometry obtained with the CCSD(T)/cc-pVTZ corrections is associated with an almost three times smaller deviation of fit. This is preferred geometry of acrylonitrile, and it is also drawn in Fig. 5.8.

Table 5.5 lists several other geometries that are usually determined from rotational data. The r_0 and r_s geometries are simple to evaluate and are often used as a reference point for other evaluations. These geometries have been reported in [178], but they have been reevaluated since certain inconsistencies have been noted in the published values. Only the available B and C rotational constants have been used in order to circumvent the effects from the small vibrationally induced inertial defect in acrylonitrile of 0.16 uA^2. The results show, in particular, that the very small principal b-coordinate of the H^t atom (ca 0.04 Å) leads to a considerable increase in the uncertainties of $r(\text{C–H}^t)$ and $\angle(\text{CCH}^t)$. This effect has been considerably reduced in the r_e^{SE} determinations. Another, purely experimental approach to determining equilibrium quality geometries from only the ground state rotational constants has been in the form of the family of r_m geometries described in Chapter 2.8.3. Two such geometries for acrylonitrile are presented in Table 5.5. These are able to ac-

count successfully for the small inertia defect so that all rotational constants can be fitted at an acceptable deviation of fit. The $r_m^{(1L)}$ geometry is expected to be somewhat more reliable owing to a better account for the localised effects on deuterium substitution. Nevertheless, several assumptions concerning the parameters of fit were necessary in this case, and all values of $r(CH)$ are shorter relative to the r_e^{SE} structures.

5.5 Conclusions

The present measurements and analysis of the THz-region rotational spectra of isotopic acrylonitrile should allow confident prediction of transitions for these species over the whole envelope of the rotational spectrum for room-temperature and lower temperatures. Some caution would still be advised for higher-THz frequencies ($\sim$ 2 THz), since the strongest lines in that region will be due to ^bR-type transitions for values of K_a in the region of 20, which are the ones most involved in the g.s. $\leftrightarrow v_{11} = 1$ interaction. The newly determined r_e^{SE} geometry of acrylonitrile, Fig. 5.8, is found to be in good agreement with the CCSD(T)/cc-pVTZ *ab initio* geometry (Table 5.5). In particular, there is excellent agreement on the fact that the three $r(CH)$ bond lengths are practically identical and that there is around 1° deviation of the CC≡N segment from linearity towards an anti (or trans) orientation relative to the C=C bond. The present $r_e^{SE}(CN)$=1.1583(4) Å, is consistent with $r_e^{SE}(CN)$=1.1592(2) Å, determined for cyanamide (Table 4.7). Finally, the preferred r_e^{SE} geometry is in even better agreement with the near-equilibrium geometry of Ref. [176]. That evaluation is the result of extensive intercomparisons between experiment and calculation for various small molecules and for this reason it was difficult to assess its uncertainty. It is found that the differences between the near-equilibrium and r_e^{SE} geometries are at an average level of 0.0012 Å for bonds and 0.10° for bond angles.

Chapter 6

Pyruvonitrile

6.1 Introduction

Pyruvonitrile (acetyl cyanide, Fig. 6.1, and Fig. 6.2) is a small asymmetric top
nitrile molecule containing a methyl internal rotor. Pyruvonitrile is a sufficiently
small molecule that it has already been included in studies of potential carriers of
astrophysical IR transitions [180]. Pyruvonitrile is also known to be hydrolysed
to pyruvic acid in an acidic or alkaline aqueous environment, Fig. 6.1. Pyruvic
acid itself has been identified to be an important prebiotic molecule, and if present
in the interstellar medium it could initiate the formation of primitive, vesicle-like
structures through the Galaxy, as discussed in [57, 181]. In order to facilitate a
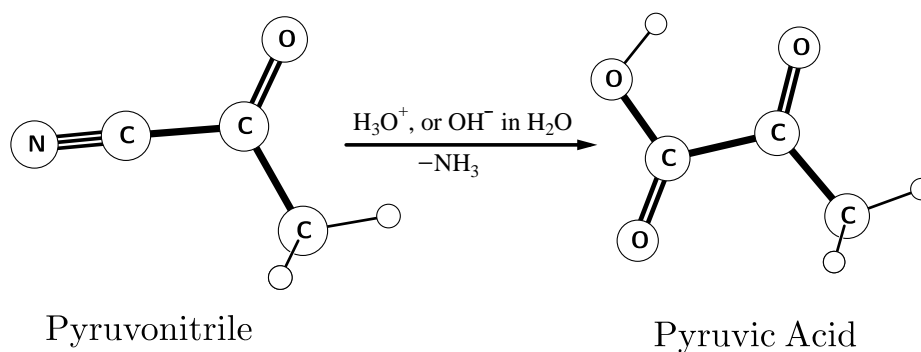
Figure 6.1: The hydrolysis of pyruvonitrile in an acidic or alkaline aqueous environment leading
to pyruvic acid.

radioastronomical search for these two compounds the recent laboratory rotational
data on pyruvic acid [57] has been augmented by analysis of the rotational spectrum
of pyruvonitrile presented in this chapter.
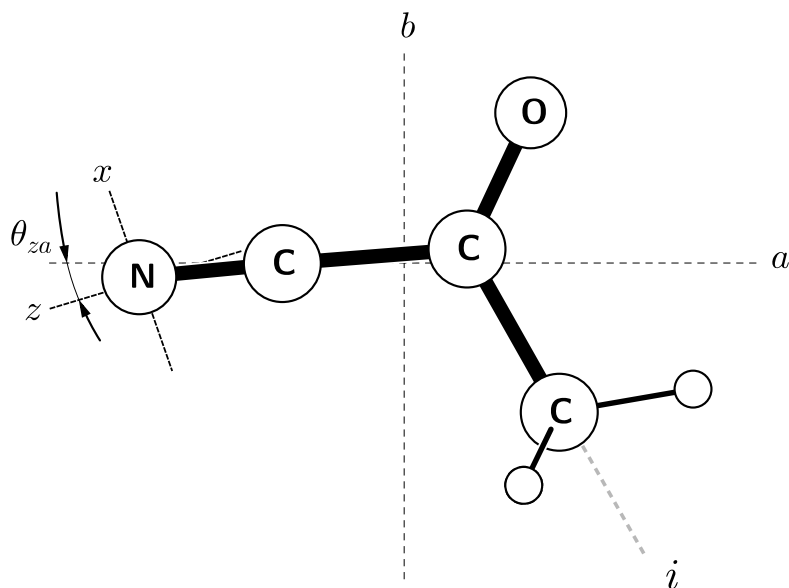
Figure 6.2: The orientation of the pyruvonitrile molecule in the principal inertial axes and the directions of the axes of the principal quadrupole tensor for the nitrogen nucleus. The discrepancy between the direction of the NC bond and the quadrupolar z axis is exaggerated for clarity. The internal rotation axis i is also indicated.

The pyruvonitrile molecule has already been studied on several occasions by rotational spectroscopy, mainly in the process of understanding the properties of the methyl torsional motion (see Chapter 2.7.2). All previous studies were, nevertheless, limited to rotational transition frequencies of less than 40 GHz. The first study was by Krisher and Wilson [182] and their analysis of centimeter-wave rotational spectra of eight isotopologues of pyruvonitrile allowed the determination of a partial molecular structure, of the barrier to internal rotation of the methyl group, and of the gas phase dipole moment. Subsequently, much work on the rotational spectrum of pyruvonitrile was done in the Kiel group [183]-[187]. The precision of all spectroscopic parameters was significantly improved and rotational transitions were also assigned in first excited states of the two lowest frequency vibrational modes: the methyl torsion, ν_{18}, and the CCN in-plane bend, ν_{12} [183, 184]. The analysis of the E-A splitting made in these works was refined further in studies of the ^{15}N isotopic species [185, 187]. Improved determination of the molecular structure was made in [186, 188] and the vibrational spectrum was analysed in [188, 189]. In [188] the frequency of 126.06 cm^{-1} for the ν_{18} torsional mode was measured directly in the far-infrared spectrum, and the frequency of the ν_{12} mode was found to be 176 cm^{-1} [189].

In this chapter the extension of measurements and of the analysis of the rotational spectrum of pyruvonitrile up to the beginning of the sub-millimeter wave region is reported. Additional measurements at conditions of supersonic expansion

were also made to determine precisely the electric dipole moment and the nuclear quadrupole coupling constants for the vibrational ground state. The present work provides sufficiently precise laboratory information for a radioastronomical search for pyruvonitrile.

6.2 Experimental details

All measurements were carried out by using the two rotational spectrometers in Warsaw already discribed in Chapter 3. The room temperature spectrum of pyruvonitrile was measured at frequencies $158 - 324$ GHz with the broadband, BWO-based, source modulation spectrometer [110] by Lech Pszczółkowski. Measurements were made on a commercial sample used without further purification, at a sample pressure of *ca* 10 mTorr.

All millimeter wave spectra were combined into a single spectrum and subjected to analysis with the use of the AABS software package for Assignment and Analysis of Broadband Spectra. The package is briefly described in Chapter 3.3, and in Ref. [127]. In order to deal with the internal rotation three different computer programs have been used: SPFIT [24, 25], XIAM [60, 61] and ERHAM [63]. Description of these programs is given in Chapter 2.7.2. The two internal rotation programs XIAM, and ERHAM, have been deposited by their authors on the PROSPE website [17] and are freely available. Integration of ERHAM with the AABS package was provided by the ERHASR program. The program converts ERHAM predictive output into the form suitable for stick display with AABS. ERHASR as well as other postprocessing programs dealing with input and output data from ERHAM are available on the PROSPE website in the internal rotation section.

Additional measurements of some A- and E-torsional sublevel lines in the vibrational ground state were also made in supersonic expansion, at $7 - 19$ GHz, with the cavity Fourier transform microwave spectrometer (FTMW) in Warsaw (see Chapter 3.1). The newly designed operational mode of the spectrometer using single frequency conversion of the signal has been applied for the measurements. Fig. 6.3 shows a scan of a rotational transition of pyruvonitrile recorded with this method. The scan has been synthesized from successive interferograms acquired at a relatively small pump-frequency step of 0.25 MHz chosen in order to improve relative intensity accuracy. The carrier gas was either Ar or a 2:1 He:Ar mixture, and the latter allowed an increase in signal strength at the cost of only a minimal increase in the Doppler doubling [77]. Pyruvonitrile concentration in the expansion mixture was estimated to be below 2%. The backing pressure was 1.1 atm and expansion was at a rate of 1 Hz through a 0.35 mm diameter orifice, by means of General Valve Corp. Series 9 nozzle. All measurements with the FTMW spectrometer have been made by the author of the dissertation.
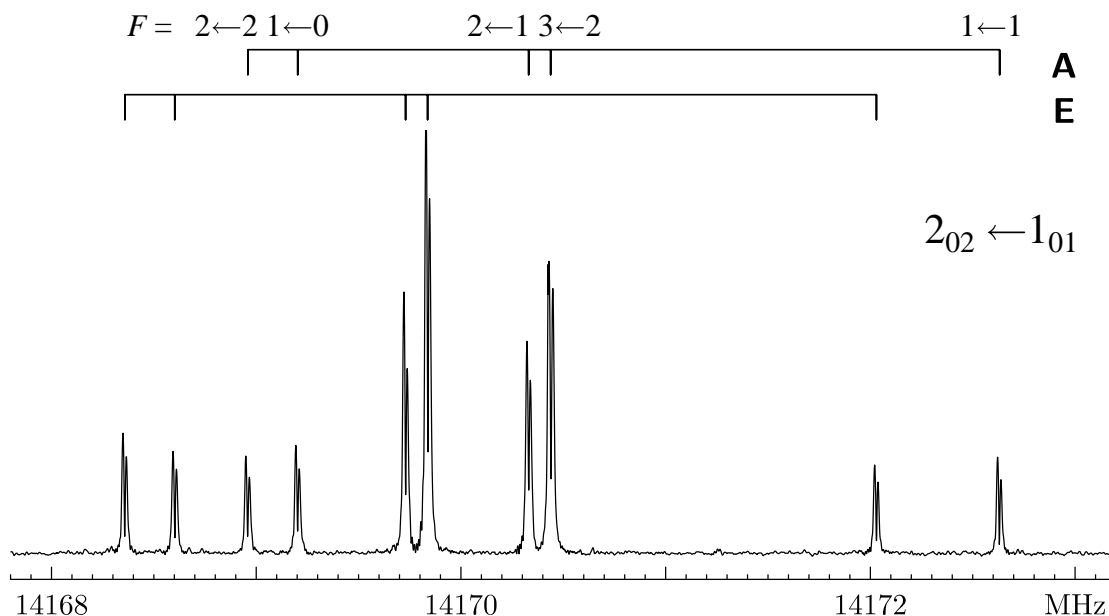
Figure 6.3: The $2_{02} \leftarrow 1_{01}$ rotational transition in the ground state of pyruvonitrile recorded in supersonic expansion in Ar carrier gas. The torsional motion of the methyl group splits the transition into two components, for the A- and E-symmetry torsional sublevels. Each of these is further split into a hyperfine multiplet by nuclear quadrupole coupling due to the ^{14}N nucleus. Finally, each hyperfine component is split by Doppler doubling, with an average splitting of around 17 kHz.

The data from previous work and from present measurements were fitted jointly. Frequency measurement uncertainties of legacy data from Ref. [183, 184] were set at 0.03 MHz, as stated for that spectrometer in [190], except that a small number of transitions were clearly incompatible with the fits and had to be excluded. In addition, for the first torsional state, the standard deviation of fit for the legacy subset was considerably higher, so that the corresponding frequency uncertainties were increased to 0.1 MHz. The current measurements were assigned frequency uncertainties of 0.05 MHz for the MMW lines, and 0.002 MHz for the FTMW lines. In cases when a given computer program was not capable of dealing with nuclear quadrupole structure the fit was made to frequencies derived by subtracting the contributions from the hyperfine structure.

6.3   Rotational spectrum

The assignment of the most prominent lines for the ground vibrational state and the first excited states of torsional and CCN in-plane bending modes was possible from predictions based on results of previous work [183, 184].

The nature of the millimeter wave rotational spectrum of pyruvonitrile is similar to that of the recently studied pyruvic acid molecule [57]. The strongest features in
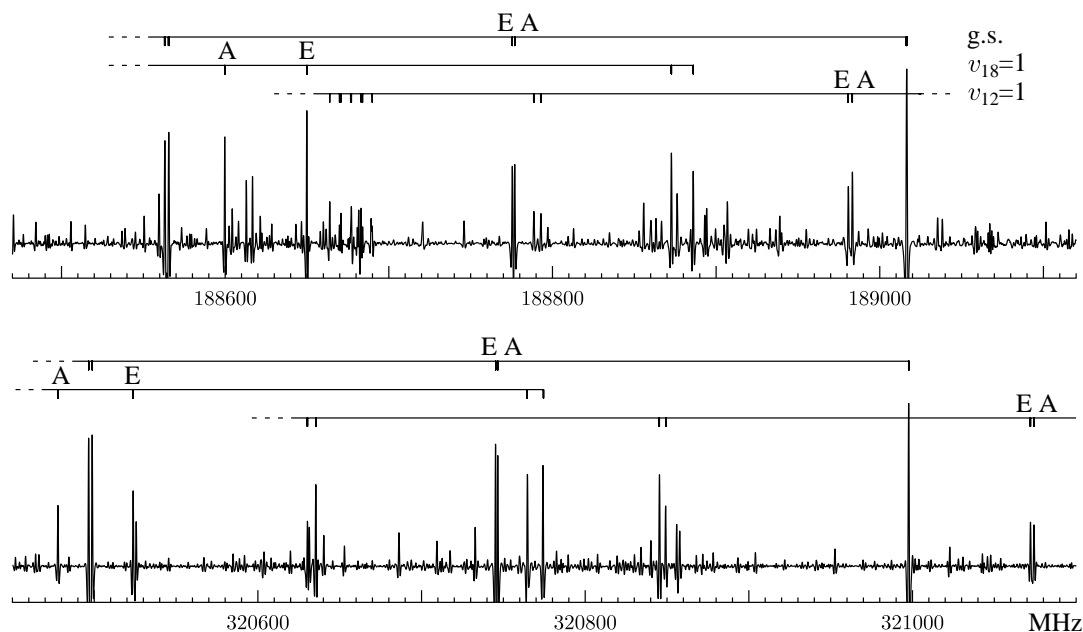
Figure 6.4: Illustration of characteristic features in the room-temperature mm-wave rotational spectrum of pyruvonitrile and of their relative invariance over a large frequency region. The type-II$^+$ R-type bands for the three studied states are marked, and the first line in each band is for J''=30 at 189 GHz, and J''=52 at 321 GHz. The A and E sublevel annotations on each band are placed on transitions between near degenerate levels with K_a=1 and 2 and illustrate the strong vibrational dependence of E-A splitting.

the spectrum are type-II$^+$ bands [120, 191], which consist of R-type transitions for lowest values of K_a. Bands of this type, illustrated in Fig. 6.4, occur in rotational spectra of planar and near-planar molecules and successive lines away from the bandhead are for increasing K_a and decreasing J. Since μ_a and μ_b dipole moment components are sizable and of similar magnitude $\mu_a = 2.42$ D, $\mu_b = 2.46$ D [182], the leading line in each band is quadruply degenerate and consists of a pair of ^aR- and a pair of ^bR-type transitions between degenerate $K_a = 0$ and $K_a = 1$ levels. The presence of the methyl torsional motion leads to observation of rotational transitions in A and E torsional sublevels for each vibrational state. The E-A splitting is strongly dependent on K_a and on vibrational state, as is visible in Fig. 6.4. The quadruple degeneracy of band transitions is lifted at higher K_a and, in combination with the E-A splitting, can lead to the formation of rather spectacular equal intensity multiplets in the rotational spectrum.

An example of such a multiplet is shown in Fig. 6.5. Finally, the analyses of transitions in E-sublevels of the studied vibrational states was aided by the loss of double degeneracy of transitions between levels with high values of K_a. The frequency difference between the two resulting high-K_a series of lines is relatively insensitive to J and K_a as shown for R-type transitions in Fig. 5 of Ref. [57]. The same type of behavior for Q-type transitions is presented in Fig. 6.6.

Figure 6.5: Octet of $J = 24 \leftarrow 23$ rotational transitions in the ground state of pyruvonitrile. The octet arises from overlap of two quartets, for the A and E torsional sublevels, each of which consists of a pair of outer ${}^bR$-type transitions, and a pair of inner ${}^aR$-type transitions. The inner and outer transitions are of similar intensity due to almost equal magnitudes of μ_a and μ_b dipole moment components (see Chapter 8).

The analysis of the spectrum was performed with the procedure used previously for pyruvic acid [57] in which fits were carried out with several different computer programs: SPFIT [24, 25], XIAM [60, 61], and ERHAM [63]. These programs have successively increasing capabilities in fitting the effects of torsional motion in the rotational spectrum. A brief description of these programs has been given in Chapter 2.7.2. For the initial stages of the analysis the use of single state effective fits made with SPFIT was the method of choice due to simplicity of use and integration with the AABS package. The A sublevel can be fitted with the standard $A-$reduced Watson's Hamiltonian in representation I^r [21], while the E sublevel can be treated by an approximation based on the perturbation treatment of internal rotation [54]. The leading terms describing the coupling between internal and overall rotation are in that case of the form $D_\alpha \hat{J}_\alpha$. The internal rotation axis of the methyl group in pyruvonitrile is in the ab inertial plane (see Fig. 6.2) so that the internal rotation Hamiltonian defined by Eq. 2.69 has the following form

$$\mathcal{H}_{\text{int}} = (D_a + D_a^J \hat{J}^2 + D_a^K \hat{J}_z{}^2 + D_a^{JJ} \hat{J}^4 + D_a^{JK} \hat{J}^2 \hat{J}_z{}^2 + D_a^{KK} \hat{J}_z{}^4 + \dots)\hat{J}_a +$$
$$(D_b + D_b^J \hat{J}^2 + D_b^K \hat{J}_z{}^2 + \dots)\hat{J}_b, \tag{6.1}$$

which can be added to Watson's rotational term. A useful summary of relations connecting the effective constants obtained in this way with the three-fold internal

Figure 6.6: Loomis-Wood type plot aligned on frequencies of successive $K_a = 17 \leftarrow 16$ ^bQ-type transitions for the A torsional sublevel in the ground state of pyruvonitrile. Each of these transitions for the A-sublevel, at the $\Delta\nu = 0$ position, is doubly degenerate. The degeneracy is lifted in the E-sublevel, giving rise to two series of transitions, identified by the two thick lines. This lifting of the high-K_a degeneracy was found to be very useful in assigning the E-sublevel transitions in all of the studied vibrational states.

rotation potential has been given in [56]. The results of effective fits made with SPFIT are summarised in Table 6.1.

These fits encompass the majority of the measured lines at close to experimental accuracy, and allow confident prediction of the strongest lines in the spectrum of pyruvonitrile. It can also be seen that significant numbers of assigned lines are excluded from the fits. In fact these fits were made to complete data sets obtained with the use of ERHAM once the predictive properties of effective fits were exhausted. For the effective fits a truncation criterion of 4 in ν(obs.-calc.)$/\delta\nu$ on inclusion of lines in the fits was used, where $\delta\nu$ is the measurement uncertainty of a given line. The lines excluded from the effective fits in this way are mostly high-K_a lines, which require a joint treatment of A and E-symmetry transitions for a given vibrational state. Such treatment is, in principle, also possible in SPFIT [192], as well as with

Table 6.1: Spectroscopic constants from effective fits made with **SPFIT** for torsional sublevels in the ground, $v_{18} = 1$, and $v_{12} = 1$ states of pyruvonitrile.

	gs, A	gs, E	$v_{18} = 1, A$	$v_{18} = 1, E$	$v_{12} = 1, A$	$v_{12} = 1, E$
A (MHz)	10185.86597(22)[a]	10185.13561(34)	10175.3382(63)	10200.1858(50)	10158.2181(10)	10157.3575(10)
B (MHz)	4157.70716(10)	4157.37176(10)	4141.8118(19)	4153.3218(20)	4176.36639(50)	4175.67666(33)
C (MHz)	3002.760177(94)	3002.76390(12)	3000.7562(10)	3000.6508(10)	3005.51749(49)	3005.52772(31)
Δ_J (kHz)	0.836735(96)	0.806930(97)	0.0990(11)	1.11150(80)	0.89226(35)	0.83503(11)
Δ_{JK} (kHz)	18.02136(52)	17.70098(39)	10.3910(63)	21.7429(60)	17.22417(94)	16.8789(10)
Δ_K (kHz)	$-6.6654(14)$	$-6.6465(14)$	$-4.938(17)$	$-6.804(13)$	$-6.4454(34)$	$-6.3029(33)$
δ_J (kHz)	0.276439(32)	0.261396(34)	$-0.08977(62)$	0.41458(43)	0.30213(11)	0.273361(52)
δ_K (kHz)	10.68129(84)	10.30320(71)	0.781(11)	13.911(11)	10.8468(20)	10.2422(22)
Φ_J (Hz)	0.001770(29)	$-0.000133(28)$	$-0.05177(40)$	[0.]	0.002800(78)	[0.]
Φ_{JK} (Hz)	0.22178(29)	0.15650(25)	$-1.4774(30)$	0.9008(42)	0.23601(93)	0.1484(11)
Φ_{KJ} (Hz)	$-0.3981(10)$	$-0.35900(81)$	1.024(12)	$-0.160(19)$	$-0.4844(30)$	$-0.3764(39)$
Φ_K (Hz)	0.2759(17)	0.2410(15)	$-0.057(18)$	[0.]	0.3012(37)	0.2702(45)
ϕ_J (Hz)	0.0008984(96)	$-0.0000788(72)$	$-0.02548(20)$	[0.]	0.001420(28)	[0.]
ϕ_{JK} (Hz)	0.12274(28)	0.07903(22)	$-1.0688(44)$	0.4213(33)	0.13343(82)	0.0704(10)
ϕ_K (Hz)	0.6295(17)	0.3555(16)	$-6.538(36)$	2.497(39)	0.7118(64)	0.3387(77)
D_a (MHz)		$-11.8910(28)$		405.331(82)		$-17.752(12)$
D_a^J (kHz)		7.3997(73)		$-248.05(14)$		10.584(15)
D_a^K (kHz)		2.903(18)		$-99.79(26)$		$-0.727(54)$
D_a^{JJ} (kHz)		$-0.0007461(24)$		0.025193(91)		$-0.0008097(55)$
D_a^{JK} (kHz)		$-0.005033(24)$		0.16298(42)		$-0.003787(54)$
D_a^{KK} (kHz)		0.002621(24)		$-0.08458(49)$		0.001204(77)
D_a^{JJK} (Hz)		0.0006565(71)		$-0.02176(24)$		
D_a^{JKK} (Hz)						0.001111(55)
D_b (MHz)		7.852(89)		278.45(19)		$-16.82(93)$
D_b^J (kHz)				$-97.04(88)$		6.0(11)
D_b^{JJ} (kHz)				0.01562(99)		
$(3/2)\chi_{aa}$ (MHz)	$-6.8574(16)$	$-6.8548(17)$	$-6.42(30)$	$-6.6(11)$	$-6.826(90)$	$-6.16(44)$
$(\chi_{bb} - \chi_{cc})/4$ (MHz)	$-0.23447(60)$	$-0.23503(59)$	$[-0.23447]$	$[-0.23447]$	$-0.363(58)$	$-0.37(12)$
K_a^{max}	28	38	25	20	30	29
N_{lines}[b]	583,42	696,18	207,186	212,84	417,24	457,17
σ_{fit} (MHz)	0.0489	0.0500	0.0854	0.0866	0.0655	0.0689
σ_{w}^c	1.086	1.096	1.704	1.732	1.343	1.393

[a]Round parentheses enclose standard errors in units of the last quoted digit of the value of the constant, square parentheses enclose assumed values.

[b]The first number is the number of fitted transitions, the second is the number of assigned transitions excluded from the fit at the criterion of ν(obs.-calc.) greater than 4 times the measurement uncertainty.

[c]Unitless deviation of the weighted fit.

BELGI [53], but it was preferred to use XIAM and ERHAM, which were already intercompared in a study of relative merits of such programs made for pyruvic acid [57]. The results of using XIAM and ERHAM are presented in Table 6.2. Both programs use the rho axis method (RAM) although XIAM (Chapter 2.7.2) is limited in the selection of minor distortion terms and for this reason it was only used for the ground state. In that case the program was also not able to deal successfully with highest-J Q-type transitions, which had to be excluded from the fit. In view of the small number of adjustable parameters the resulting fit is, nevertheless, deemed to be quite successful. The V_3 barrier (Eq. 2.68) for pyruvonitrile is currently determined at $404.87(9)$ cm^{-1}, which compares well with previous values of $423(10)$ cm^{-1} [182], $411.8(5)$ cm^{-1} [184], and 399.8 cm^{-1} [188]. The V_6 parameter was not determinable from the current ground state data set, and the reduced barrier height (Eq. 2.71), $s = 33.57$, is very similar to $s = 33.68$ from fit to only the cm-wave data [183]. It is also interesting to note that the three internal rotation-overall rotation distortion constants (see Eq. 2.73) with values $\Delta_{Jm} = 0.1302(35)$, $\Delta_{Km} = -0.505(18)$, $\delta_m = 0.0654(33)$ are currently very similar to those for pyruvic acid, $\Delta_{Jm} = 0.1524(15)$, $\Delta_{Km} = -0.4570(54)$, $\delta_m = 0.0730$, all in MHz [57], suggesting that the underlying effects in both molecules are very similar.

The best results were obtained with the effective rotational Hamiltonian embodied in ERHAM [63]. The use of this program also allowed the range of E-symmetry transitions to be significantly extended. Like SPFIT, the ERHAM program can be used within the framework of the AABS analysis package, as detailed in [17]. The results summarised in Table 6.2 for the three studied vibrational states show that it was possible to account in the fits for practically all of the confidently assigned lines in the spectrum. The deviations of fits vary, but for the ground state the fit is close to within the estimated uncertainties, as the weighted deviation of fit is close to unity. The deviations of fit are higher for the two vibrationally excited states, although this mostly results from the generally poorer deviations for the E-symmetry lines. Thus for $v_{12}=1$ the subset deviations are 0.062 and 0.086 MHz for A- and E-symmetry lines, respectively, and for the excited torsional state $v_{18}=1$ the corresponding values are 0.070 and 0.187 MHz. These fits are found to be somewhat poorer than for pyruvic acid, which was initially surprising since in that case the barrier to internal rotation is lower at $336.36(5)$ cm^{-1}, Ref. [57]. However, in the case of pyruvonitrile the rotational constants are greater, the K-dependent quartic centrifugal distortion constants are an order of magnitude greater, and many sextic constants are two orders of magnitude greater. In spite of these challenges the reported fits demonstrate a high degree of consistency of the fitted values of quartic and sextic centrifugal distortion constants among the three vibrational states. This is an excellent testimonial for the physical sensibility of the fits. The values of the quartic constants are also in very good agreement with calculation based on an *ab initio* harmonic force field, see Table 6.3. Furthermore the fitted values for the rho axis parameters ρ and β for the ground and the first excited torsional state are very close to each other. On the other hand ρ and β for the in-plane bending

Table 6.2: Spectroscopic parameters of pyruvonitrile in the ground and first excited states of the ν_{12}, and ν_{18} normal modes.

	XIAM		ERHAM		
	gs, $A+E$		gs, $A+E$	$v_{18}=1, A+E$	$v_{12}=1, A+E$
A (MHz)	10185.38569(47)		10185.37774(26)	10191.8472(22)	10157.64443(76)
B (MHz)	4157.56160(20)		4157.48341(11)	4149.5333(13)	4175.90448(37)
C (MHz)	3002.68048(20)		3002.76275(11)	3000.69275(94)	3005.52426(35)
Δ_J (kHz)	0.81491(14)		0.816733(84)	0.82116(74)	0.85288(25)
Δ_{JK} (kHz)	17.81484(51)		17.80532(26)	17.7760(28)	16.99686(63)
Δ_K (kHz)	−6.6372(18)		−6.6543(10)	−6.326(11)	−6.3501(24)
δ_J (kHz)	0.265390(43)		0.266340(26)	0.26927(38)	0.282212(89)
δ_K (kHz)	10.42615(82)		10.42700(48)	9.8403(60)	10.4415(13)
Φ_J (Hz)	0.000172(35)		0.000451(21)	0.00142(22)	0.000567(56)
Φ_{JK} (Hz)	0.17767(35)		0.17658(16)	0.1598(21)	0.17910(61)
Φ_{KJ} (Hz)	−0.3657(10)		−0.37141(51)	−0.3212(84)	−0.4144(21)
Φ_K (Hz)	0.2569(18)		0.2519(10)	0.188(19)	0.2845(27)
ϕ_J (Hz)	0.0000775(92)		0.0002183(54)	0.00056(11)	0.000253(21)
ϕ_{JK} (Hz)	0.09046(26)		0.09265(15)	0.1006(22)	0.09043(51)
ϕ_K (Hz)	0.4454(21)		0.4374(10)	0.322(18)	0.4654(43)
V_3 (cm^{-1})	404.867(90)	ϵ_1(MHz)	−100.798(98)	3571.1(15)	−219.32(28)
		$B010_1$[a] (MHz)	0.469(18)	−27.80(30)	1.604(24)
Δ_{Jm} (MHz)	0.1302(35)	$B001_1$ (MHz)		−162.188(95)	
Δ_{Km} (MHz)	−0.505(18)	$B200_1$ (kHz)	0.517(45)	23.87(45)	
δ_m (MHz)	0.0654(33)	$B020_1$ (kHz)	16.87(51)	−1061.7(91)	66.85(69)
		$B002_1$ (kHz)	0.788(29)		1.315(34)
		$B210_1$ (kHz)	−0.0611(56)	4.06(10)	−0.1367(91)
		$B201_1$ (kHz)		35.54(44)	
		$B021_1$ (kHz)		−37.8(42)	
		$B012_1$ (kHz)		1.148(69)	
		$B030_1$ (kHz)	−0.1430(73)	13.85(11)	−0.700(13)
		$B003_1$ (kHz)		17.94(47)	
		$B202_1$ (kHz)	−0.0000619(74)		
		$B220_1$ (kHz)	−0.003780(96)	0.1381(11)	−0.00998(21)
		$B022_1$ (kHz)		0.1382(48)	−0.01137(32)
		$B400_1$ (kHz)		−0.00077(12)	
		$B040_1$ (Hz)		120.0(55)	
		$B004_1$ (Hz)	−0.0774(49)		
		$B222_1$ (mHz)		−12.8(12)	
		$B024_1$ (mHz)	0.855(36)		
		ϵ_2(MHz)		13.41(14)	−1.985(38)
		$B010_2$ (kHz)			15.2(19)
		$B200_2$ (kHz)		7.43(15)	−0.495(23)
ρ	0.040791(14)		0.041280(57)	0.041534(24)	0.033956(44)
β (deg)	34.492(10)		32.583(55)	32.116(25)	39.351(58)
K_a^{max}	38(A),38(E)		38(A),38(E)	27(A),20(E)	30(A),29(E)
N_{lines}[b]	1130,90		1216,4	679,16	906,11
σ_{fit} (MHz)	0.0786		0.0528	0.1348	0.0735
σ_{w}	1.628		1.029	2.527	1.433

[a]The label $Bkpr_q$ defines tunneling parameters in the effective rotational Hamiltonian analogous to the scheme in Ref.[63], where k, p, r define the powers of the associated angular momentum operators, J^k, J_z^p and $J_+^r + J_-^r$, and q is the localised state label.

[b]The first number is the number of fitted transitions, the second is the number of assigned transitions excluded from the fit.

Table 6.3: Comparison of experimental and calculated values (kHz) of quartic centrifugal distortion constants for pyruvonitrile.

	Exp.	Calc.[a]
Δ_J^{b}	0.816733(84)	0.7538
Δ_{JK}	17.80532(26)	17.36
Δ_K	$-6.6543(10)$	-6.110
δ_J	0.266340(26)	0.2449
δ_K	10.42700(48)	10.05

[a]Calculated with the VIBCA program [17] from the unscaled B3LYP/6-31G(d,p) harmonic force field evaluated with the PC-GAMESS version [94] of the GAMESS (US) QC package [95].

[b]Centrifugal constants in A reduction and I^r representation of Watson's asymmetric rotor Hamiltonian.

satellite are appreciably different from those for the ground state. Similar behavior has been found for the ν_{10} in-plane scissor mode in acetaldehyde [193], for which $\rho=0.030903(9)$ is appreciably smaller than $\rho=0.3334654(7)$ for the stack of torsional states. It is reasonable to expect that a normal mode active in the plane containing the rotation axis of the methyl group will have an appreciable effect on the coupling of the torsional motion with rotation. The scope of the data set and the precision of fit for the ground state of pyruvonitrile are presented in the distribution plot in Fig. 6.7. R-type transitions have been confidently assigned up to $K_a = 38$, and Q-type bands up to $K_a = 25 \leftarrow 24$, for both A- and E-sublevel transitions.

6.4 Nuclear quadrupole coupling

Hyperfine structure in the ground vibrational state was measured in supersonic expansion for 16 different rotational transitions (^aR-, ^bR-, and ^bQ-type). The newly measured hyperfine components numbered 68 for the A sublevel and 67 for the E sublevel, and in the global fit their frequencies were reproduced to standard deviation of 2.3 kHz for each of these sublevels. The resulting nuclear quadrupole splitting constants, see Table 6.1, are almost identical for the two sublevels, as could have been expected from the very similar patterns apparent in the spectrum in Fig. 6.3. The various derived splitting constants are listed in Table 6.4 and an improvement in precision relative to previous work of about two orders of magnitude is visible. The nitrile group is at an angle of about 5° relative to the a inertial axis (Fig. 6.2) so that the off-diagonal splitting constant χ_{ab} is non-zero. Regrettably its value is small and it could not be determined in the fit. It was, however, possible to estimate χ_{ab} with considerable confidence on the basis of *ab initio* calculations. All levels of such calculation predicted $\chi_{ab} \approx 0.5$ MHz when their results were scaled with a single scaling factor chosen for optimum reproduction of the experimental
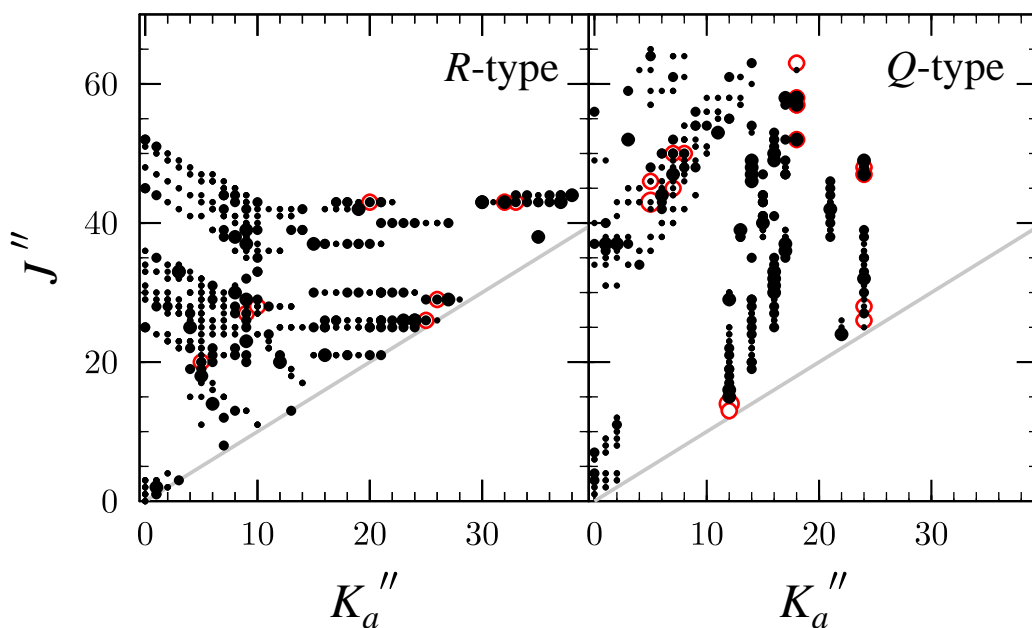
Figure 6.7:   Distribution plot of ν(obs.-calc.)$/\sigma$ for the ground state transitions of pyruvonitrile resulting from the ERHAM fit. σ is the frequency measurement uncertainty of a given line, and symbol size is proportional to the magnitude of the plotted quantity. Open circles denote ν(obs.-calc.) outside the $\pm 3\sigma$ bounds.

splitting constants. The assumed value for χ_{ab} used in Table 6.4 has been assigned an uncertainty that is about three times larger than the spread of the calculated values. The inertial quadrupole tensor can be diagonalized to yield the principal quadrupole tensor and the rotation angles between the inertial principal axes system and the quadrupole axes system. One of these angles θ_{za} is shown in Fig. 6.2. Diagonalization of the inertial quadrupole tensor results in $\theta_{za} = 4.6(9)°$, which is close to the structural angle between the nitrile group and the a-axis $\angle(\mathrm{CN}a) = 4.86°$ calculated at the B3LYP/6-31G(d,p) level. The derived values for the components $\chi_{xx}, \chi_{yy}, \chi_{zz}$ of the principal nuclear quadrupole splitting tensor and of the nuclear quadrupole asymmetry parameter η are summarised in Table 6.4.

It is notable that η in pyruvonitrile is rather large and positive. This is in contrast to the often made assumption that the field gradient around the nitrogen in the nitrile group is cylindrical, namely that $\eta = 0$. This assumption, while useful in the analysis of spectroscopic data, has rarely been tested owing to the small value of the nuclear quadrupole for the nitrogen atom. Nonetheless, it is found that for benzonitrile $\eta = -0.0802(4)$ [195] (value precise by symmetry) and for 2-chloroacrylonitrile $\eta = -0.060(2)$ [196] (determination enhanced by a suitable perturbation). The positive value of η close to 0.2 (see Tab. 6.4) seems to be characteristic of a nitrile group attached to a carbonyl group. Similar values are calculated for formyl cyanide, HC(C=O)CN, and carbonyl cyanide O=C(CN)$_2$, and are consistent with inertial nuclear quadrupole coupling constants determined for those molecules [197, 198].

Table 6.4: Nuclear quadrupole coupling constants for the ^{14}N nucleus in the A torsional sublevel of the vibrational ground state of pyruvonitrile

	Ref.[183]	This work	CCSD(T)/ 6-31G(d,p)[a]	B3PW91/ 6-311++G(3df,3pd)[b]
χ_{aa} (MHz)	−4.34(7)	−4.5716(11)	−4.595	−4.603
χ_{bb} (MHz)	2.03(31)	1.8169(13)	1.746	1.660
χ_{cc} (MHz)	2.31(31)	2.7547(13)	2.839	2.943
χ_{ab} (MHz)		[−0.52(10)]	−0.526	−0.491
χ_{zz} (MHz)	−4.37	−4.614(16)	−4.638	−4.641
χ_{xx} (MHz)	2.06	1.860(16)	1.789	1.698
χ_{yy} (MHz)	2.31	2.7547(13)	2.839	2.943
η^c	0.06	0.1942(36)	0.226	0.268
$\theta_{za}{}^d$ /deg		4.6(9)	4.71	4.46

[a]Calculated with CFOUR [96] by using $Q(^{14}$N$)=0.02044(3)$ barn [194] and further scaled with the factor 1.3177 chosen for the best average reproduction of the experimental diagonal quadrupole coupling constants.
[b]Calculated with PC-GAMESS at the r_s geometry from Ref. [188], and scaled by the calibration factor of 4.546 MHz/au determined in Ref. [103].
[c]Nuclear quadrupole asymmetry parameter, $\eta = (\chi_{xx} - \chi_{yy})/\chi_{zz}$.
[d]Rotation angle between inertial and principal nuclear quadrupole tensors.

A popular rationalisation of the values of η has been in terms of the difference between the π character for the bond to the quadrupolar atom considered along the x and y principal quadrupole axes (p. 764 of Ref. [12]). In Table 6.4 two popular approaches used in computing nuclear quadrupole splitting constants are compared. The scaled values computed at the CCSD(T) level result in the best reproduction of the experimental results. The second calculation is at one of the levels of computation that were designed to provide optimum reproduction of nuclear quadrupole coupling constants for the ^{14}N nucleus and were calibrated in Ref. [103]. The second procedure is, in principle, more satisfactory in that it is based on a calibration factor determined from a fit to experimental data for many molecules and reproduces χ_{aa} to within its cited calibration accuracy of 33 kHz. On the other hand the value calculated for η, and for the other diagonal quadrupole constants, is further from experiment than in the CCSD(T) estimate.

6.5 Conclusion

The present investigation considerably extends the coverage of the rotational spectrum of the pyruvonitrile molecule. Previous measurements for the ground vibrational state were limited to $J=12$, $K_a=3$, whereas the present data set is bounded by $J=65$, $K_a=38$. The use of the simple, effective fits made with the familiar SPFIT

Table 6.5: Comparison of values derived for the angle $\theta_{i.a}$ (degrees) between the internal rotation axis and the inertial a axis in pyruvonitrile.

	Eq.(6.2)	Eq.(6.3)	ERHAM	XIAM	calc.[a]
g.s.	58.28(29)[b]	58.94(7)	57.43(6)	59.28(1)	59.86
$v_{18} = 1$	59.35(2)	59.11(4)	57.03(3)		
$v_{12} = 1$	66.54(116)	65.33(2)	63.37(5)		

[a]The angle between the $C-CH_3$ axis and the a axis from the B3LYP/6-31G(d,p) geometry.

program satisfactorily reproduces the majority of the transitions in the spectrum, and should be more than adequate for generating linelists for astrophysically relevant rotational temperatures. Application of the more specialised programs for dealing with internal rotation encompasses a larger number of lines, although such lines are mostly at the outer limits of the data set. Even though the approaches used in the three programs tested on the data for the ground state are different, it is possible to demonstrate their essential equivalence. In the present case the internal rotation axis, i, is in the ab inertial plane (see Fig. 6.2) so that the perturbation treatment connecting the parameters of single state fits [56] leads to two simple expressions

$$\tan \theta_{i.a} = \frac{A}{B}\frac{D_b}{D_a} \tag{6.2}$$

$$\tan \theta_{i.a} = \frac{A}{B}\left(\frac{\Delta B}{\Delta A}\right)^{1/2} \tag{6.3}$$

for the orientation angle $\theta_{i.a}$. ΔA and ΔB are rotational constant differences between the A- and E-symmetry sublevels. A and B are 'true' structural rotational constants

$$A = \frac{1}{3}\left(A_A + 2A_E\right)$$
$$B = \frac{1}{3}\left(B_A + 2B_E\right) \tag{6.4}$$

calculated from the effective constants for the two sublevels (see Eq. 2.72).

The values of not only the rotational constants, but also of the major centrifugal distortion constants in Tables 6.1 and 6.2, are seen to obey the type of averaging described by the above equations satisfactorily enough. The values for $\theta_{i.a}$ determined in different ways are compared in Table 6.5 and are seen to be consistent to within a few degrees. The angles for the ground state from XIAM and ERHAM are quite similar while the ERHAM values for all states are systematically smaller than those from the effective fits.

Several other quantities derived from the internal rotation analysis made with ERHAM are also listed in Table 6.6. The ground state and first torsional excited

Table 6.6: Comparison of values derived for selected parameters resulting from the internal rotation analysis for pyruvonitrile.

	g.s.	$v_{18} = 1$	$v_{12} = 1$
$E_E - E_A{}^a$ (MHz)	302.38(30)	$-10753.7(48)$	663.94(93)
$I_\alpha{}^b$ (uÅ^2)	3.206(2)	3.2055(7)	2.915(2)
F^c (GHz)	163.746(97)	163.830(35)	178.93(13)

^{a}The energy difference between the E-symmetry and the A-symetry sublevels.

^{b}Moment of inertia of the methyl rotor, which can be compared with 3.205 uÅ^2 from the B3LYP/6-31G(d,p) geometry.

^{c}Reduced rotational constant of the methyl group defined in Eq. 2.67.

state E-A sublevel separations of 302.4(3) and $-10754(5)$ MHz, respectively, are appreciably smaller than 723.6(4) and $-21579(37)$ MHz for pyruvic acid [57], which is consistent with a higher internal rotation barrier in the present molecule.

The fitted values for the moment of inertia of the internal rotor, I_α (Chapter 2.7.2), in the ground and first excited torsional state are almost identical to that from the *ab initio* calculated geometry. On the other hand the considerable decrease in the value for the excited state of the in-plane bending mode, $v_{12} = 1$, indicates that a more refined two dimensional analysis should probably be used in further work. From the measured spectra it was possible to assign A-symmetry transitions in the first excited state of the out-of-plane CCN bending mode, $v_{17} = 1$ (at 245 cm^{-1}, Ref. [189]), and the second excited state of the torsion, $v_{18} = 2$. All of these transitions are found to be strongly perturbed and their analysis will require careful consideration of interstate interactions.

Chapter 7

Phenylacetylene

7.1 Introduction

The mid-IR astronomical spectra of sources associated with dust and gas are dominated by the emission-features which might be produced by mixtures of highly vibrationally excited polycyclic aromatic hydrocarbons (PAHs) and closely related species [199]. Phenylacetylene as a fundamental hydrocarbon derivative of benzene is implicated in chemical reaction networks associated with formation of PAHs in combustion and in the interstellar medium (ISM) [200]. Many different studies on the formation of phenylacetylene at astrophysically relevant conditions showed that it can be formed from benzene by impact shock [201] or collisions with the ethynyl radical (H−C≡C·) [200]. It can also be formed by photochemical reactions from acetylene [202], vinylacetylene [203], or 1,3-butadiene [204]. Furthermore, phenylacetylene has been formed in a mixture of gases simulating the atmosphere of Saturn's moon Titan [205], and studies of phenylacetylene in [200, 203, 204] were, in fact, also motivated by the desire to explore the rich hydrocarbon chemistry expected to be present on Titan. Phenylacetylene has a non-vanishing permanent dipole moment and is thus attractive as a potential radioastronomy marker of unsaturated, or even polyaromatic hydrocarbon chemistry, and is postulated to be relevant to the ISM [206]. The available laboratory data concerning the rotational spectrum of phenylacetylene is insufficient for radioastronomical detection applications, especially at the promising mm-wave frequencies. The work on phenylacetylene presented in this chapter aims to remedy this situation.

The rotational spectrum of phenylacetylene was first studied by Zeil $et\ al.$ [207], and their survey investigation was followed by a much more detailed study of Cox $et\ al.$ [208]. Rotational constants were obtained for seven different isotopic species leading to a determination of the molecular structure. The electric dipole moment, $\mu = \mu_a = 0.656(5)$ D, was also determined, and is appreciably higher than $0.375(10)$ D for toluene [209]. More recently, a much more extensive determination of the structure of phenylacetylene by means of FTMW rotational spectroscopy was
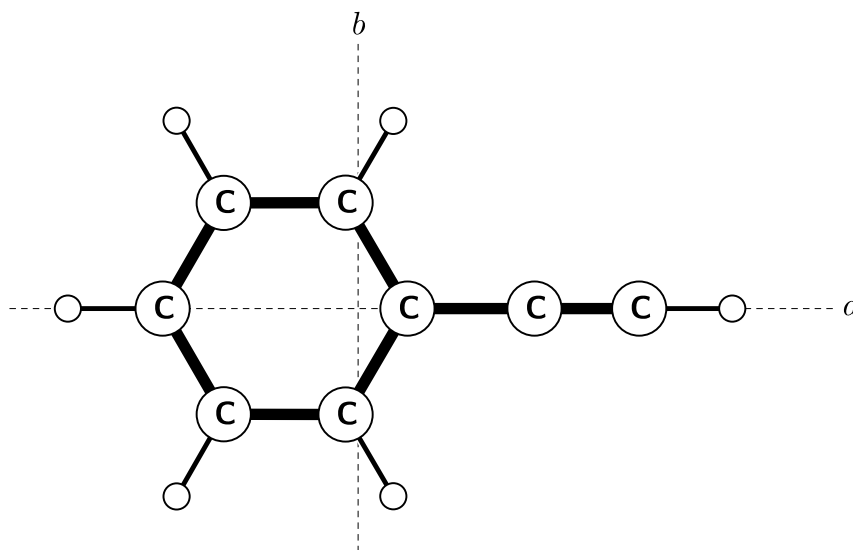
Figure 7.1: The molecular structure of phenylacetylene, and its orientation in the principal inertial axes.

carried out by Dreizler *et al.* [87] on the basis of rotational constants obtained for 39 different isotopic species. Nevertheless, the frequency coverage of all of these investigations did not extend beyond 40 GHz and no excited vibrational state transitions were assigned. In this chapter a thorough analysis of rotational transitions in the ground and two excited vibrational states at frequencies of up to 340 GHz is presented.

7.2   Experimental details

All measurements were carried out with the two rotational spectrometers in Warsaw. The room-temperature spectrum was measured at $90 - 340$ GHz with the broadband, source modulation spectrometer described in Chapter 3.2. Two Istok BWO sources, OB-24 and OB-30, were used for measurements at $175 - 340$ GHz. The region $90 - 140$ GHz was covered with a harmonic multiplication source, from Virginia Diodes Inc., which generated the 12th harmonic of the driving frequency from a microwave synthesizer. Measurements were performed on a commercial sample used without further purification and at a sample pressure of up to 10 mTorr. Additional measurements of some low-J transitions not covered in [87] were made in supersonic expansion, at $7 - 19$ GHz, with the cavity Fourier transform microwave spectrometer (FTMW) in Warsaw (Chapter 3.1). The expansion mixture was prepared by using vapour from above a liquid sample of phenylacetylene over which Ar carrier gas was passed at a backing pressure of $1.1 - 1.3$ atm. Rotational lines of phenylacetylene were observed with sufficient signal-to-noise ratio after $100 - 200$ gas pulses, depending on the strength of the rotational transitions. In these measurements there were usually 10 microwave pulses applied to a single molecular pulse.

The many individual millimeter wave spectra recorded during this work were
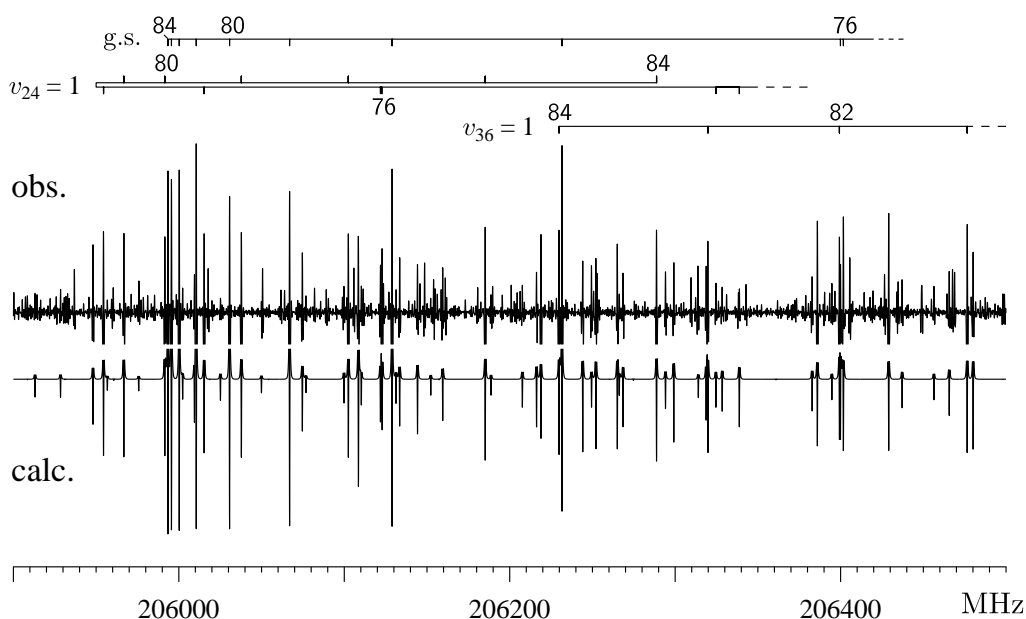
Figure 7.2: The measured (top) and the simulated (bottom) rotational spectrum of phenylacety-lene. The ground state transitions give rise to an $n=2$, type-II$^+$ band of R-type transitions, which is characteristic of planar molecules. Values of J'' are indicated on the diagram and successive transitions away from the bandhead decrease by 1 in J and increase by 1 in K_a. Similar bands for the two lowest excited vibrational states, $v_{24} = 1$ and $v_{36} = 1$, are strongly distorted by Coriolis perturbation between these states.

combined into a single spectrum and subjected to analysis with the use of the AABS software package (Chapter 3.3). The ground state data from previous work and from present measurements were fitted jointly by using the ASFIT/ASROT package [17], while the SPFIT/SPCAT package [24, 25] was used for the analysis of vibrationally excited states. Frequency measurement uncertainties of 2 and 50 kHz were assumed for supersonic expansion, and room-temperature measurements, respectively.

7.3   Rotational spectrum

The mm-wave region rotational spectrum for the ground state of phenylacetylene was predicted with accuracy sufficient for assignment by augmenting the rotational constants from previous work with quartic centrifugal distortion constants calculated from an *ab initio* harmonic force field. The high-J, ^aR-type transitions for a planar molecule are known to coalesce into strong bands, called type-II bands, with an interband frequency spacing of close to $2C$. This nomenclature has been proposed by Borchert [210] who identified the initial stage of such band formation. The properties of this type of band were investigated in more detail in the spectrum of chlorobenzene [211], and a comprehensive classification was proposed in [120, 191]. An example type-II band in the spectrum of phenylacetylene is shown in Fig. 7.2. The strongest and leading line in a band of this type consists of doubly degenerate transitions with $K_a = 0, 1$. Successive lines along the band are for values of J
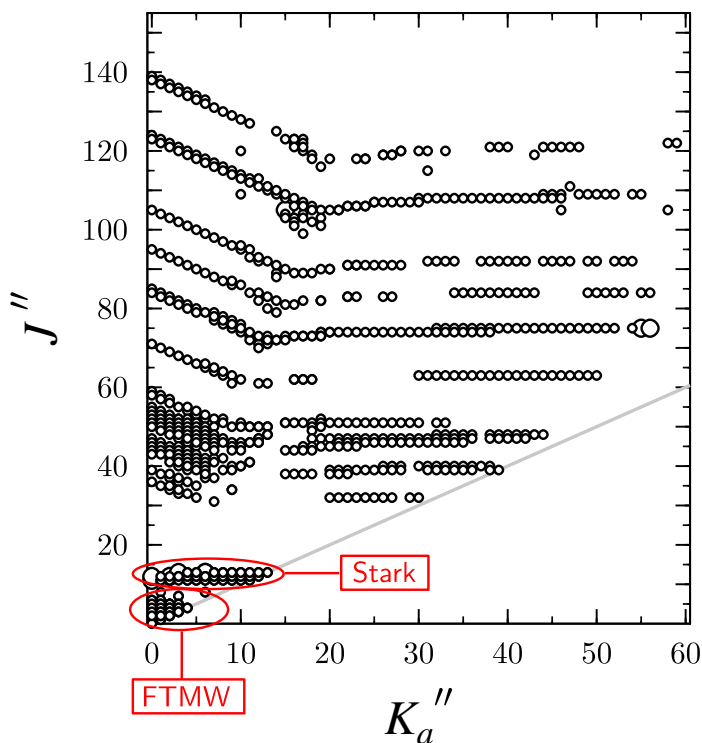
Figure 7.3: Distribution plot of values of obs.-calc. differences in the S-reduction fit for the ground state of phenylacetylene. Circle diameters are proportional to the absolute value of the difference and the largest circles correspond to values of 0.20 MHz. The data subsets for Stark spectra from Ref. [208] and supersonic expansion FTMW spectra from Ref. [87] are marked.

decreasing, and of K_a increasing in steps of 1. For positive D_{JK} the lines normally evolve from the bandhead to higher frequencies, although the line pattern is quite sensitive to the value of the inertial defect. The changes on vibrational excitation are, nevertheless, fairly moderate and normally do not prevent assignment. A typical situation is depicted for fluorobenzene in Fig. 1 of [212]. In phenylacetylene, on the other hand, while the presence of strong satellite lines in the spectrum was obvious, their assignment was not possible until a prediction was made on the basis of the expected strong Coriolis perturbation between the two lowest excited vibrational states.

7.4   Ground state

Measurements of ground state lines were extended up to 340 GHz with some care being taken to obtain a balanced coverage of the values of J and K_a quantum numbers, as shown in Fig. 7.3. For the analysis Watson's reduced asymmetric rotor Hamiltonian [21] was used, in both A- and S-reductions. The results of fit are summarised in Tables 7.1 and 7.2. The present data set allows determination of the
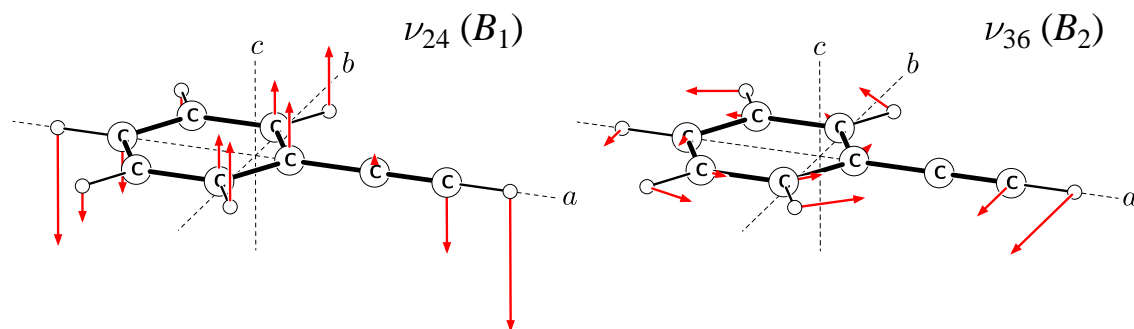
Figure 7.4: Examples of the two lowest frequency normal modes ν_{24} and ν_{36} in phenylacetylene. The vibrational motions are indicated by the red vector arrows. The vectors are unweighted eigenvectors calculated with VIBCA and VECTOR [17] from the B3LYP/6-31G(d,p) harmonic force field evaluated with the PC-GAMESS version [94] of the GAMESS package [95].

complete sextic level Hamiltonian, with the exception of H_K. The remaining two constants with only the K dependence, namely A and D_K, are also determined with smaller precision than other constants in the same order of the Hamiltonian. This is simply because phenylacetylene is a rather prolate molecule ($\kappa = -0.85$), while only ^aR-type transitions are available for measurements. A single, weak, ^aQ-type transition, $8_{1,7} \leftarrow 8_{1,8}$ was actually measured in [87] and confirmed in the present measurements. However, confident measurement of further lines of this type was not possible, probably due to insufficient microwave excitation power in the FTMW spectrometer. The overall deviation of the fit of close to 27 kHz for the ground state is very satisfactory and reflects the relatively rigid nature of the molecule. The S-reduction fit is slightly more successful, and also the values of correlation coefficients for this fit are generally lower. The quartic centrifugal distortion constants determined with both fits are in good agreement with values derived from various calculated harmonic force fields, see Table 7.3.

7.5   Vibrationally excited states

A comprehensive study of the vibrational spectrum of phenylacetylene was carried out by King and So [213], who also proposed the normal mode assignment. This was correct except for the two lowest frequency vibrational modes, which were reassigned on the basis of additional information from laser fluorescence spectra [214]. The final picture was confirmed by *ab initio* calculations [215, 216] and further normal mode analyses of phenylacetylene in comparison with related molecules [217, 218]. Phenylacetylene is a molecule of C_{2v} symmetry and it has two low frequency B-symmetry normal modes associated with distortion of the $-C\equiv CH$ group in relation to the phenyl ring, Fig. 7.4. Since there has been some confusion in the literature on the assignment of B_1 and B_2 symmetry for planar C_{2v} molecules, it is useful to recall

Table 7.1: Spectroscopic constants for phenylacetylene obtained by using the A-reduced form of the rotational Hamiltonian

	g.s.		Solution I $v_{24}=1$	Solution I $v_{36}=1$	Solution II $v_{24}=1$	Solution II $v_{36}=1$
A (MHz)	$5680.3433(19)^a$	$(A_{24}+A_{36})/2$ (MHz)	5679.62201(65)		5679.62089(65)	
		$(A_{24}-A_{36})/2$ (MHz)	$-3.60(13)$		$3.16(14)$	
B (MHz)	1529.742116(24)	B (MHz)	1531.433932(77)	1532.609669(87)	1531.433742(77)	1532.609522(92)
C (MHz)	1204.955065(21)	C (MHz)	1206.771426(61)	1205.795275(72)	1206.771561(61)	1205.795396(75)
Δ_J (kHz)	0.0422679(74)		0.0429307(29)	0.0431651(32)	0.0429290(29)	0.0431658(32)
Δ_{JK} (kHz)	0.982468(53)		0.99117(35)	0.94655(35)	0.99254(37)	0.94493(38)
Δ_K (kHz)	0.2139(43)		[0.2139]	[0.2139]	[0.2139]	[0.2139]
δ_J (kHz)	0.0101710(27)		0.0102342(18)	0.0105225(22)	0.0102324(18)	0.0105219(23)
δ_K (kHz)	0.62427(37)		0.62358(24)	0.62421(20)	0.62342(24)	0.62420(21)
Φ_J (Hz)	0.00000189(36)		[0.00000189]	[0.00000189]	[0.00000189]	[0.00000189]
Φ_{JK} (Hz)	0.001659(20)		0.001474(12)	0.001919(13)	0.001481(12)	0.001918(13)
Φ_{KJ} (Hz)	$-0.009308(72)$		$-0.006207(57)$	$-0.012610(65)$	$-0.006801(57)$	$-0.012173(58)$
Φ_K (Hz)	[0.0]		[0.0]	[0.0]	[0.0]	[0.0]
ϕ_J (Hz)	0.00000071(15)		[0.00000071]	[0.00000071]	[0.00000071]	[0.00000071]
ϕ_{JK} (Hz)	0.000822(16)		0.0008513(68)	0.0007352(69)	0.0008356(67)	0.0007489(70)
ϕ_K (Hz)	0.00760(38)		0.00773(22)	0.00997(26)	0.00804(22)	0.00972(26)
		ΔE (MHz)	461378.80(49)		461378.65(50)	
		ΔE (cm^{-1})	15.389938(16)		15.389933(17)	
		G_a (MHz)	9547.8(32)		9710.0(33)	
		G_a^J (MHz)	$-0.0048495(89)$		$-0.0047536(79)$	
		F_{bc} (MHz)	$-0.4761(26)$		$-0.3518(24)$	
		F_{bc}^K (MHz)	$-0.00000394(48)$		$-0.00000570(45)$	
$N_{\text{lines}}{}^b$	783		1006		1006	
σ_{fit} (kHz)	27.3		36.1		36.8	
$\sigma_{\text{w}}{}^c$	0.6156		0.7216		0.7367	

^{a}Round parentheses enclose standard errors in units of the last quoted digit of the value of the constant, square parentheses enclose assumed values.
^{b}The number of distinct frequency transitions used in the fit.
^{c}Unitless deviation of the weighted fit.

Table 7.2: Spectroscopic constants for phenylacetylene obtained by using the S-reduced form of the rotational Hamiltonian

	g.s.		Solution I		Solution II	
			$v_{24} = 1$	$v_{36} = 1$	$v_{24} = 1$	$v_{36} = 1$
A (MHz)	5680.3428(19)	$(A_{24} + A_{36})/2$ (MHz)	5679.61958(66)		5679.61909(67)	
		$(A_{24} - A_{36})/2$ (MHz)	$-3.16(15)$		2.69(16)	
B (MHz)	1529.740864(24)	B (MHz)	1531.42995(12)	1532.607433(91)	1531.43009(12)	1532.607195(98)
C (MHz)	1204.956302(21)	C (MHz)	1206.774758(83)	1205.797824(82)	1206.774716(88)	1205.797925(84)
D_J (kHz)	0.0305185(32)		0.031278(15)	0.031230(15)	0.031248(15)	0.031262(15)
D_{JK} (kHz)	1.053136(36)		1.0482(17)	1.0311(17)	1.0541(16)	1.0250(16)
D_K (kHz)	0.1557(43)		[0.1557]	[0.1557]	[0.1557]	[0.1557]
d_1 (kHz)	$-0.0101727(27)$		$-0.0101983(32)$	$-0.0105613(21)$	$-0.0102080(32)$	$-0.0105533(23)$
d_2 (kHz)	$-0.0058781(34)$		$-0.0057792(99)$	$-0.0059803(86)$	$-0.0058034(99)$	$-0.0059588(86)$
H_J (Hz)	$-0.00001258(14)$		$-0.00001139(48)$	$-0.00001392(48)$	$-0.00001221(46)$	$-0.00001302(46)$
H_{JK} (Hz)	0.0012034(15)		0.0009959(41)	0.0013410(41)	0.0009861(40)	0.0013523(40)
H_{KJ} (Hz)	$-0.007502(13)$		$-0.004840(58)$	$-0.009931(42)$	$-0.004949(44)$	$-0.009921(27)$
H_K (Hz)	[0.0]		[0.0]	[0.0]	[0.0]	[0.0]
h_1 (Hz)	$-0.00000050(13)$		$[-0.0000005]$	$[-0.0000005]$	$[-0.0000005]$	$[-0.0000005]$
h_2 (Hz)	0.00000737(15)		0.00000427(32)	0.00000903(30)	0.00000517(31)	0.00000819(30)
h_3 (Hz)	0.000001323(51)		0.00000009(10)	0.00000252(10)	0.00000046(10)	0.00000223(10)
		ΔE (MHz)	461374.94(53)		461375.73(55)	
		ΔE (cm^{-1})	15.389811(18)		15.389838(18)	
		G_a (MHz)	9558.6(37)		9698.9(39)	
		G_a^J (MHz)	$-0.004481(39)$		$-0.004510(38)$	
		F_{bc} (MHz)	$-0.4245(24)$		$-0.3195(37)$	
		F_{bc}^K (MHz)	$-0.00000835(21)$		$-0.00000773(19)$	
N_{lines}	783		1006		1006	
σ_{fit} (kHz)	26.9		38.2		38.4	
σ_{w}	0.6065		0.7637		0.7679	

Table 7.3: Comparison of experimental and calculated values of selected force field dependent parameters for phenylacetylene

	Exp. This work	B3LYP[a]	MP2[a]	MP2[b]	Ref.[215][c]
			Calculated		
Δ_J (kHz)	0.042268(7)	0.0396	0.0391	0.0392	0.0420
Δ_{JK} (kHz)	0.98247(5)	0.894	0.902	0.901	1.0475
Δ_K (kHz)	0.214(4)	0.265	0.239	0.244	0.1474
δ_J (kHz)	0.010171(3)	0.00954	0.00943	0.00946	0.0100
δ_K (kHz)	0.6243(4)	0.568	0.572	0.571	0.6493
$\zeta_{24,36}^a$	0.8393(3)	0.8296	0.8397	0.8381	0.84
ΔE (cm^{-1})	15.38994(2)	13.8	19.6	18.0(9.6[d])	16
$\Delta_i{}^e$ (u Å^2)	0.07875(3)	0.0939	0.0432	0.0486	

[a]From unscaled harmonic force field evaluated with the 6-31G(d,p) basis set by using PC-GAMESS.

[b]From unscaled harmonic force field evaluated with the 6-31G(d,p) basis set by using CFOUR [96].

[c]From multiscaled harmonic force field evaluated at the HF/4-21G level.

[d]Value inclusive of anharmonic corrections.

[e]Ground state inertia defect, $\Delta_i = I_c - I_a - I_b$.

a IUPAC recommendation on this matter [219]. Accordingly, the x axis is chosen to be perpendicular to the plane of the molecule, such that the $\sigma_v(xz)$ plane in the present case becomes the ac inertial plane. The in-plane and out-of-plane modes that are antisymmetric with respect to the C_2 operation are therefore assigned to be B_2 and B_1 species, respectively.

The lowest frequency normal mode in phenylacetylene is the out-of-plane, B_1 symmetry mode ν_{24}, for which only an approximate wavenumber (140 cm^{-1}) is available experimentally [214]. The next higher mode is the in-plane, B_2 symmetry mode ν_{36}, with a much more confident experimental wavenumber of 151.9 cm^{-1} [214]. The next higher modes are ν_{23} (B_1, 349 cm^{-1}), ν_{16} (A_2, 418 cm^{-1}), and ν_{13} (A_1, 465 cm^{-1}) [213], so that the most prominent excited state features in the room-temperature rotational spectrum will be due to transitions in $v_{24} = 1$ and $v_{36} = 1$. The two states are sufficiently close in energy that their mutual interaction has to be considered. The type of interaction is determined by the symmetry of the interacting modes. The ν_{24} mode belongs to the B_1 irreducible representation of the C_{2v} symmetry point, and ν_{36} to the B_2 irreducible representation. According to Eq. 2.50 we have $B_1 \otimes B_2 = A_2$ and since A_2 is the species containing the rotation about the z-axis, then Coriolis interaction about the a inertial axis will be possible. The Hamiltonian for the coupled fit of the two states is in standard 2×2 block form (see

$$v_{24} = 1 \qquad\qquad \text{g.s.} \qquad\qquad v_{36} = 1$$
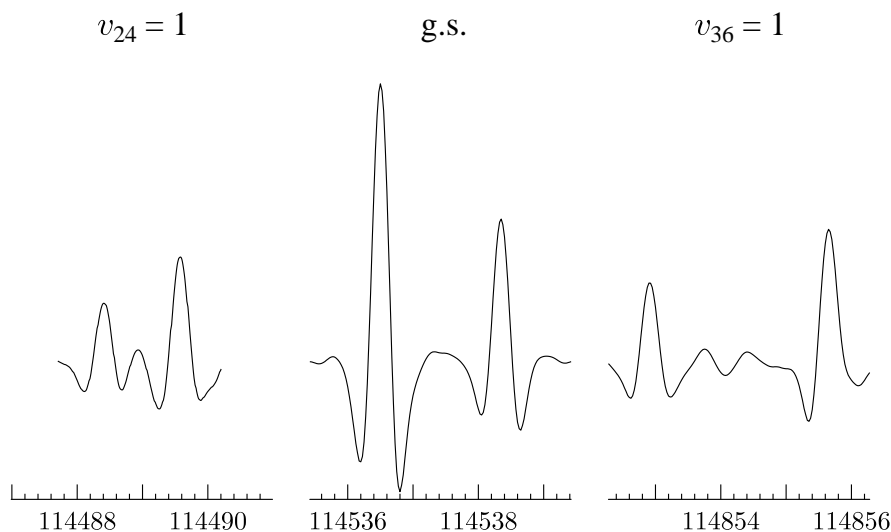
Figure 7.5: Nuclear spin statistical weights in the milimeter-wave rotational spectrum of phenylacetylene (frequency in MHz). The doublets are transitions $44_{4,41} \leftarrow 43_{4,40}$ (left component) and $44_{3,41} \leftarrow 43_{3,40}$ (right component), in a given vibrational state, which would be of similar intensity without the presence of statistical weights. For the ground state the transitions for even and odd K_a carry weights 5:3 respectively, which are reversed in B-symmetry states. The reversed weights between the ground state and the two excited states confirm that the latter are both of B-symmetry.

Eq. 2.49) and is for this case given by:

$$\mathcal{H} = \begin{pmatrix} \mathcal{H}_{\text{rot}}^{(24)} & \mathcal{H}_{\text{C}}^{(24,36)} \\ \mathcal{H}_{\text{C}}^{(24,36)} & \mathcal{H}_{\text{rot}}^{(36)} + \Delta E \end{pmatrix}, \tag{7.1}$$

and contains the pure rotational, Watsonian terms for the two vibrational states, $\mathcal{H}_{\text{rot}}^{(24)}$ and $\mathcal{H}_{\text{rot}}^{(36)}$ on the diagonal, augmented by the vibrational energy difference $\Delta E = E_{36} - E_{24}$. The connecting, off-diagonal Coriolis term (see Eq. 2.51) for the $v_{24} = 1 \leftrightarrow v_{36}$ coupling in phenylacetylene is given by

$$\begin{aligned} \mathcal{H}_{\text{C}}^{(24,36)} &= i(G_a + G_a^J \hat{J}^2 + G_a^K \hat{J}_z^{\,2} + \dots)\hat{J}_z \\ &\quad + (F_{bc} + F_{bc}^J \hat{J}^2 + F_{bc}^K \hat{J}_z^{\,2} + \dots)(\hat{J}_x \hat{J}_y + \hat{J}_y \hat{J}_x). \end{aligned} \tag{7.2}$$

The coupling constant G_a is related to the Coriolis coefficient $\zeta_{24,36}^a$ connecting the two modes by

$$G_a = A\, \zeta_{24,36}^a \left[\sqrt{(\omega_{24}/\omega_{36})} + \sqrt{(\omega_{36}/\omega_{24})} \right]. \tag{7.3}$$

Results of *ab initio* computations in [215] and of those carried out presently allowed an initial estimate of $G_a \approx 9500$ MHz to be made. Once this was incorporated into the predictions, the pattern of excited state lines, as marked in Fig. 7.2, became recognizable.

The presence of two pairs of symmetry equivalent hydrogens in the phenylacetylene molecule (Fig. 7.1) gives rise to differing nuclear statistical weights for different rotational levels. Similarly to cyanamide (Chapter 4) the rotational transitions for the same K_a quantum number for vibrational levels of different symmetry carry reversed nuclear statistical weights. Using equations 4.1, and 4.2 the statistical weight ratio g^s/g^a is 5/3, so that line intensities in the rotational spectrum carry nuclear spin statistical weights of 5:3. As a consequence a reversal in the weights between the ground state and B-symmetry excited states for the same rotational transitions is observed, and is illustrated in Fig. 7.5. This also provides confirmation of the assignment of the excited state lines to two B-symmetry vibrational states.

Once the initial assignment was made, the analysis turned out to be fairly straightforward, since the interaction between the two states was found to be very well described by only a limited number of constants in Eq. 7.2. It was possible to assign lines for a similar distribution of quantum number values to that shown in Fig. 7.3 for the ground state, except that owing to decreasing line intensity the upper limit on K_a was around 50.

The results of the final fits are also summarised in Tables 7.1, and 7.2. In contrast to the ground state the A-reduced fits are slightly more successful than the S-reduced fits, in line with similar behaviour documented for several other molecules [23, 122]. The deviations of the excited state fits are well below 40 kHz, and the relative invariance of the values of centrifugal distortion constants between the two excited sates and the ground state are evidence for the validity of the fitting model. Only Δ_K (or D_K) and some sextic level constants could not be determined with confidence and were assumed at values from the ground state.

Although these fits were ultimately successful, it was necessary to resolve several complications. First of all, there was considerable numerical instability when values of A_{24} and A_{36} were used as parameters of fit. It turned out that only their average was well determined while the difference was not. The adopted solution was to use the sum and difference of these rotational constants explicitly, as listed in Tables 7.1, 7.2. This ensured numerical stability but also revealed very limited sensitivity of the overall deviation of fit to the difference between the A rotational constants for the two excited states, as shown in Fig. 7.6. In particular, two alternative solutions, labelled I and II, could be identified and are listed in Tables 7.1, 7.2. Solution I was preferred on the basis of standard deviation, but the discrimination from solution II was minimal, at a level of less than 1 kHz in the deviation of fit. By inspecting the predictions it was found that many pairs of interacting energy levels in the two studied excited states were subject to considerable mixing. For this reason a significant number of dedicated measurements targeted at transitions between such levels have been made. From the measured spectra it was possible to identify several transitions that were described by the quantum number assignment scheme of SPFIT as transitions between the two vibrational states. In spite of this, it was still not possible to improve the discrimination between solutions I and II. It should be mentioned that there were no lines that were not accounted for in the fits, in that they were either badly shifted or missing, and the fits encompass all measurable
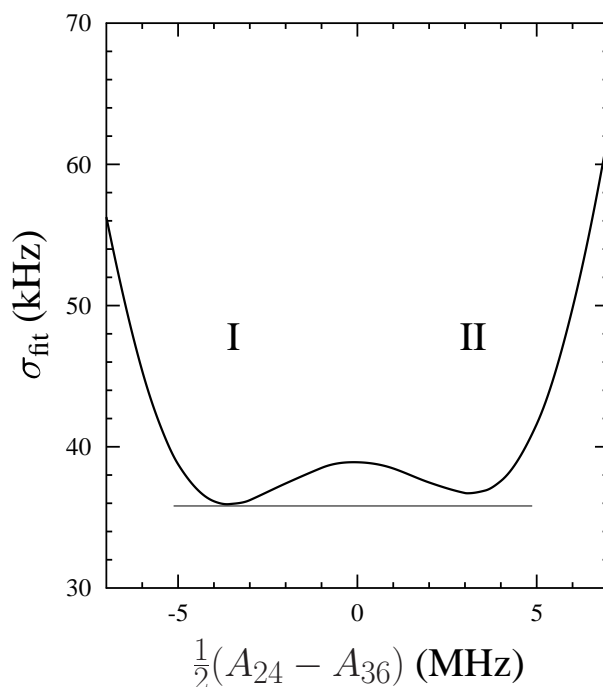
Figure 7.6: Dependence of deviation of the A-reduced coupled fit of rotational transitions in $v_{24} = 1$ and $v_{36} = 1$ vibrational states on the difference in rotational constant A between the two states. The two alternative solutions listed in Tables 7.1 and 7.2 are indicated.

transitions.

In an attempt to discriminate more confidently between solutions I and II anharmonic force field calculations were used. Although the performance of such calculations for molecules of the size of phenylacetylene has not yet been benchmarked (Chapter 2.9), there are indicators that practicable levels of calculation may already be useful [220]. The results of calculations are summarised in Table 7.4. The agreement of calculated vibrational changes for B and C rotational constants with those obtained from experiment is excellent, confirming the assignment of the lower vibrational level to $v_{24} = 1$ and of the upper to $v_{36} = 1$. The situation for the A rotational constant is more involved since CFOUR calculates vibrational changes between effective values inclusive of the effects of perturbation, as described by Eq. 2.47. The deperturbed values, in the sense of those obtained from the coupling fits made here, can be obtained by subtracting the contributions to $(A_v - A_0)$ from the $\zeta_{24,36}^a$ term as described by Eq. 2.53. For phenylacetylene such contributions are given by

$$\delta(A_{24} - A_0) = -\delta\alpha_{24}^A = \frac{2A^2}{\omega_{24}}(\zeta_{24,36}^a)^2 \frac{3\omega_{24}^2 + \omega_{36}^2}{\omega_{24}^2 - \omega_{36}^2}, \tag{7.4}$$

$$\delta(A_{36} - A_0) = -\delta\alpha_{36}^A = \frac{2A^2}{\omega_{36}}(\zeta_{24,36}^a)^2 \frac{3\omega_{36}^2 + \omega_{24}^2}{\omega_{36}^2 - \omega_{24}^2}. \tag{7.5}$$

It can be seen from Table 7.4 that application of Eq. 7.4-7.5 leads to values of $(A_v - A_0)$ which are both satisfactorily close to experiment, and also unambiguously prefer solution I, in which $A_{24} < A_{36}$.

Table 7.4: Comparison of experimental and calculated vibrational changes (MHz) in rotational constants

	Exp.[a]	Calc.[b]
$\bar{A} - A_0$[c]	$-0.7213(20)$	-0.668
$A_{24} - A_0$	$-4.32(13)$	-5.02[d]
$B_{24} - B_0$	$1.69182(8)$	1.572
$C_{24} - C_0$	$1.81846(8)$	1.716
$A_{36} - A_0$	$2.88(13)$	3.74[d]
$B_{36} - B_0$	$2.86755(9)$	2.646
$C_{36} - C_0$	$0.84021(7)$	0.752

[a]Values from A-reduction, solution I.
[b]Calculated with CFOUR [96] at the MP2/6-31G(d,p) level.
[c]$\bar{A} = (A_{24} + A_{36})/2$.
[d]Deperturbed values obtained by subtracting contributions in Eq. 7.4-7.5, from the calculated effective values $A_{24} - A_0 = -173.45$ and $A_{36} - A_0 = 172.09$ MHz.

7.6 Conclusion

The investigation presented in this chapter considerably extends the coverage of the known rotational spectrum of the phenylacetylene molecule, as is evident from Fig. 7.3. The reported spectroscopic constants should allow accurate prediction of the rotational spectrum well into the submillimeter-wave region. The analysis of the strong Coriolis coupling between the ν_{24} and the ν_{36} modes turned out to be entirely satisfactory, although selection between the two alternative numerical solutions could only be made with confidence on the basis of calculation of the vibrational changes in rotational constants. As was stated in Ref. [124], in more complex situations a given fit that is acceptable according to the criteria of satisfactory reproduction of the spectrum may not necessarily be the most meaningful solution physically.

The comparison of the various force field dependent quantities determined for phenylacetylene with the results from different calculations (Table 7.3) shows good agreement. None of the routine diagnostic-level calculations is outstandingly better than others. For example, the MP2 results are more consistent with the experimental $\zeta_{24,36}^a$, while the DFT result is better for the inertial defect. The MP2/6-31G(d,p) results illustrate the level of consistency between two independent computational packages. It was also found that there is a remarkable agreement of the current experimental results with those based on a very rudimentary HF/4-21G calculation by Csaszar *et al.* [215]. The Scaled Quantum Mechanics technique used in that work and based on a combination of results for benzene and acetylene appears to have worked very well. Finally, the use of ν_{36} from [214] and the present value of ΔE, allows an estimate of 136.5 cm^{-1} for the wavenumber of the ν_{24} fundamental.

Chapter 8

Electric Dipole Moments

8.1 Introduction

This chapter collects the results of electric dipole moment determinations carried out for four different molecules: pyruvonitrile, urethane, propionitrile, and acrylonitrile (see Fig. 8.1 for structures and dipole moment orientations). The permanent electric dipole moment of a molecule is a key physical property reflecting its ground state electron distribution. The dipole moment gives insight into the reactivity of the molecule, as it is important in determining relative molecular orientation in early stages of chemical reaction. In rotational spectroscopy precise value of the dipole moment is of particular interest because the intensities of rotational transitions are directly governed by the magnitude of the corresponding dipole moment component. Precise knowledge of this quantity is also of direct importance in quantitative determination of molecular abundances under atmospheric and astrophysical conditions probed by means of rotational spectroscopy.

The electric dipole moment is measured from rotational spectra by means of the Stark effect (Chapter 2.4). Although Stark effect measurements have been performed with almost all types of rotational spectrometers, the measurements at conditions of supersonic expansion with the FTMW spectrometers are relatively recent. The prerequisite for the measurement of the Stark-effect is the ability to apply a well characterized homogeneous, static electric field to the molecules. The FTMW spectrometer at IFPAN is equipped with a specially designed set of Stark electrodes that are able to produce a field of considerably improved uniformity in relation to standard parallel plates [34, 221]. The separation of the Stark electrodes used to measure the dipole moment has to be kept sufficiently large (27 cm in the IFPAN spectrometer) so that the modes of the microwave resonator in the FTMW spectrometer are not perturbed. This leads to the use of relatively small electric fields and for molecules with quadrupolar nuclei has the consequence that the Stark splitting is similar in magnitude to the hyperfine splitting. Hyperfine splitting is observed in the rotational spectrum of each of the studied molecules due to the
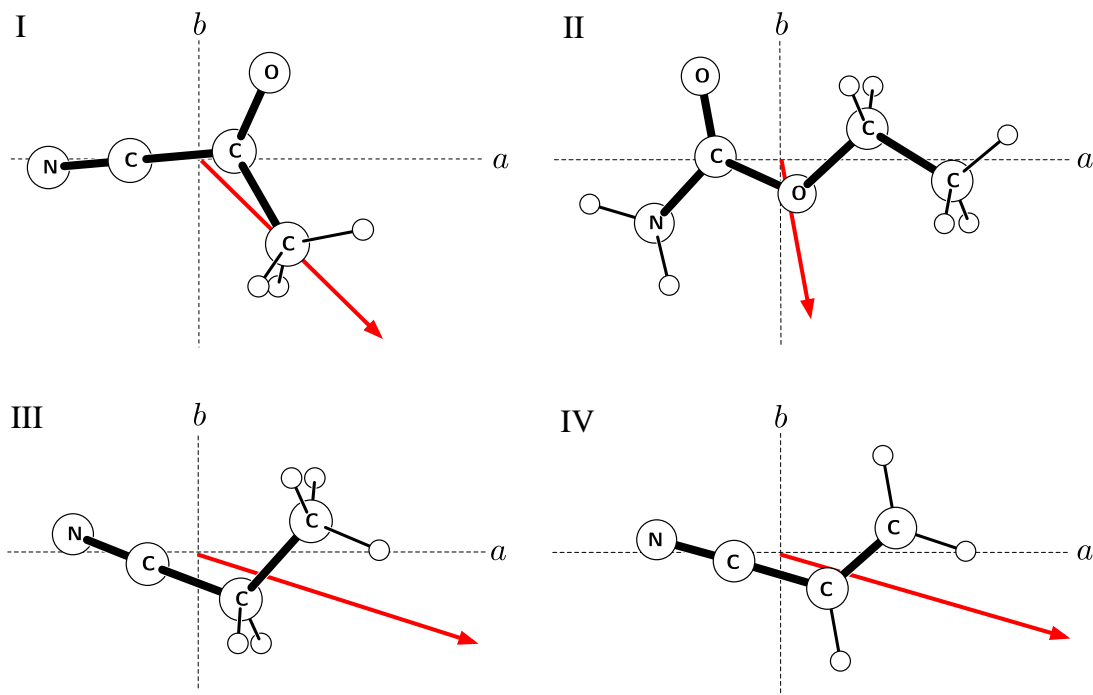
Figure 8.1: The orientation of the molecules and of their dipole moment in the inertial axes: I-pyruvonitrile, II-urethane (conformer I, see the discussion in the text), III-propionitrile, IV-acrylonitrile. The molecules I-III have been slightly rotated around the b axis to show all hydrogen atoms, since in the ab projection symmetry equivalent hydrogens are overlapped. The dipole moment arrows are drawn in the direction used for computed values, from the notional negative charge to the notional positive charge.

presence of the ^{14}N nucleus (Chapter 2.3), so that it was necessary to work in this inconvenient intermediate field regime. The only satisfactory solution is to set up and diagonalize the energy matrix separately for each value of the electric field and of the M_F quantum number. A treatment of this type is embodied in the program QSTARK [34], which was used for fitting the dipole moment components on the basis of measured Stark lobe frequencies. The QSTARK program is available from the PROSPE website [17]. The effective electrode separation has been calibrated using the procedure relying on two different calibration substances, CH_3I and CH_3CN [37]. Further details concerning the Stark electrode design and methodology of measurements are described in Refs. [34, 37, 221]. Theoretical details are given in Chapter 2.4.

All measurements have been made with the supersonic expansion FTMW spectrometer at IFPAN (Chapter 3.1). The measurements were performed on selected hyperfine components of various rotational transitions in the microwave spectrum. The experimental conditions for each studied molecule were somewhat different, thus for each case a short experimental description is given. The experimental results are discussed and compared with calculations.

Table 8.1: Comparison of experimental and calculated values of the electric dipole moment components (D) for pyruvonitrile.

	Ref.[182].	This work	Calc. μ_e^a	Calc. μ_0^b
$|\mu_a|$	2.42	2.4616(20)	2.447	2.466
$|\mu_b|$	2.46	2.4422(21)	2.464	2.450
μ_{tot}	3.45(6)	3.4675(20)	3.473	3.476
N_{lines}		44		
σ_{fit} (kHz)		3.17^c		

[a]Calculated at the CCSD/aug-cc-pVDZ level with CFOUR [96].

[b]The equilibrium CCSD/aug-cc-pVDZ dipole moment corrected to the ground state by using the zero-point vibration contributions calculated at the CCSD(T)/cc-pVDZ level.

[c]Deviation of fit to 36 Stark measurements and 8 zero-field frequencies for the measured Stark components.

8.2 Pyruvonitrile

Details concerning the FTMW measurements for pyruvonitrile have been presented in Chapter 6. The electric dipole moment for pyruvonitrile was determined from Stark measurements made on completely resolved $\Delta M=0$ Stark lobes for eight selected hyperfine components of the $1_{11} \leftarrow 0_{00}$ and $2_{02} \leftarrow 1_{01}$ rotational transitions of the A-torsional sublevel, at frequencies near 13.2 and 14.2 GHz, respectively. Electric fields of up to 185 V/cm were used and Stark shifts of up to 2.7 MHz were measured. The electric vectors of the electric field and of the polarizing microwave radiation were set to be parallel so that $\Delta M=0$ components were measured.

The results are summarised in Table 8.1 and Fig. 8.2. The rotational and quadrupole parts of the Hamiltonian were fixed by using the constants from Table 6.1 (Chapter 6), so that only the two components of the electric dipole moment constituted the parameters of fit. Fig. 8.2 shows that there is considerable mixed order Stark behaviour in the $2_{02} \leftarrow 1_{01}$ transition, in that many Stark lobes do not show a pure second order frequency shift. Nevertheless all, even the strongly curved Stark components, are fitted satisfactorily. It has been found, in contrast with the previous determination in [182], that the μ_a component is of greater magnitude than μ_b, although the differences from the earlier results are within their estimated uncertainty. Interestingly, simultaneous *ab initio* reproduction of the relative magnitude of these two components and of the total dipole moment proved to be quite challenging, and the closest computed result consistent with these two requirements is listed in Table 8.1. On the basis of CCSD(T)/cc-pVDZ anharmonic calculation it is found that zero-point correction of the equilibrium dipole moment might be important in reproducing the experimental value of the dipole moment. It reduces μ_a and increases μ_b by several 0.01 D, and reproduces the experimental relative ordering of dipole moment components $\mu_a^0 > \mu_b^0$ (see Table 8.1).
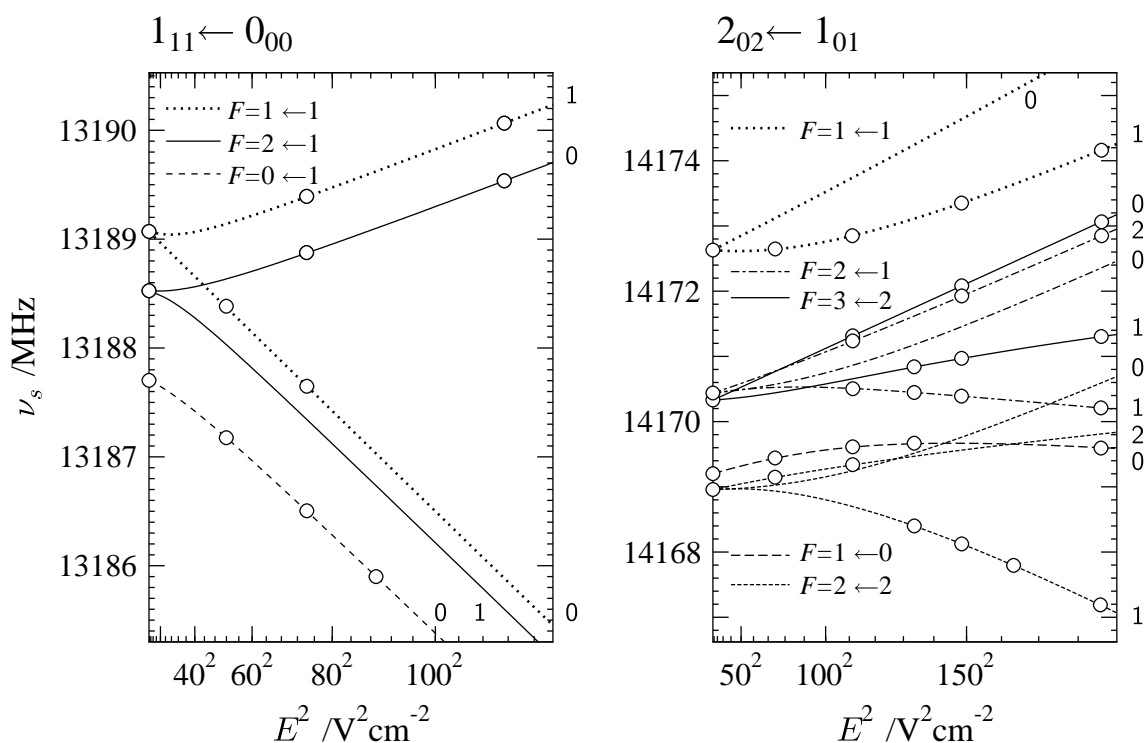
Figure 8.2: Summary of Stark shift measurements made on the $1_{11} \leftarrow 0_{00}$, (b-type), and on the $2_{02} \leftarrow 1_{01}$, (a-type) rotational transitions in the A-torsional sublevel of the ground state of pyruvonitrile. Circles denote measured Stark frequencies, continuous lines show the behaviour of the pertinent Stark components calculated on the basis of the final fit. The values of M_F are indicated next to each Stark component.

8.3   Urethane

Urethane is a white crystalline substance with a melting point of 50°C. A sample of urethane was purchased from Sigma-Aldrich and used without further purification. For the measurements the urethane sample was held in a small metal container close to the expansion nozzle, and this container and the surrounding gas handling system were heated to about 90°C. The sample was entrained in Ar carrier gas at a pressure of 1.2 atm passed through the container, and the resulting mixture was expanded into the chamber of the spectrometer at a rate of 4 Hz.

In the gas phase at room temperature urethane exists as two conformers (Fig. 8.3) both of which are visible in the millimeter-wave spectrum. However, it was found that on supersonic expansion made with Ar carrier gas only the lines of conformer I of urethane could be observed. It was not possible to measure any of the lines of conformer II, which were satisfactorily observable on the Lille FTMW spectrometer by using Ne carrier gas [222]. The greater propensity of Ar carrier for condensing the sample towards the global minimum conformation on supersonic expansion is well known [223] and allowed to establish unambiguously that conformer I is the lowest energy conformer of urethane. For further discussion on conformational stability of
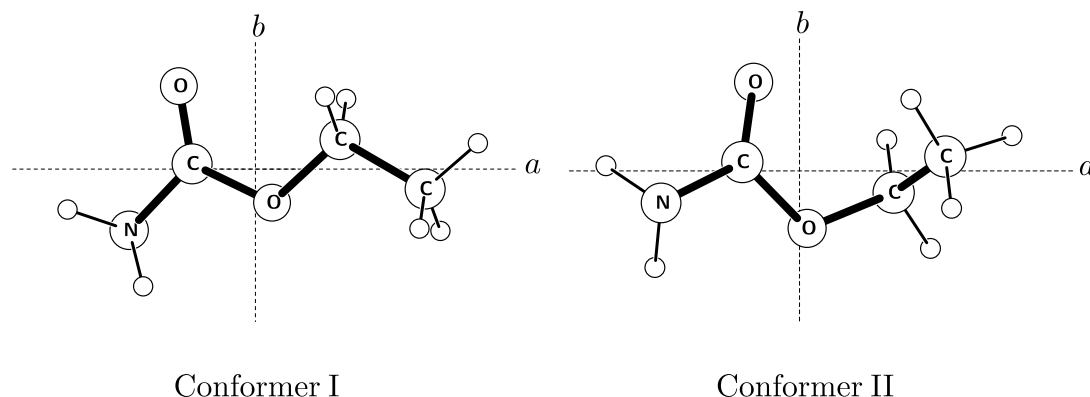
Figure 8.3: Molecular structure of the two stable conformers of urethane in their principal axes. Conformer I has been rotated around the b axis for better visibility of the out of ab plane protons. The conformers differ by the position of the $-CH_3$ group in relation to the rest of the molecule. Conformer I is the global minimum conformer, and only this species was observed with the FTMW spectrometer in Warsaw.

urethane see Ref. [222].

The dipole moment for conformer I of urethane (the global minimum conformer) was determined from Stark effect measurements on completely resolved Stark lobes of hyperfine components of the nuclear quadrupole hyperfine structure due to the ^{14}N nucleus. Two different $^bR-$type rotational transitions were used, $1_{11} \leftarrow 0_{00}$ at 10755 MHz and $2_{12} \leftarrow 1_{01}$ at 14290 MHz. Stark shifts were measured for 10 different M_F lobes of 5 different hyperfine components. The measurements are summarized graphically in Fig. 8.4, in which it is possible to discern several nonlinearities relative to simple second order Stark behaviour. Such nonlinearities are rather common in the relatively low electric field regime of measurements made with cavity FTMW spectrometers, where the magnitudes of the hyperfine splitting and the Stark splitting are comparable. This behaviour is similar to that for pyruvonitrile discussed in the previous section and shown in Fig. 8.2. Stark measurements were fitted with the program QSTARK [34] and the final results of dipole moment determination are summarised in Table 8.2. *Ab initio* calculations for conformer I predict that all three dipole moment components will be non-zero, but it was only possible to determine μ_a and μ_b from the measurements. The third component, μ_c, is calculated to be more than 0.6 D in the equilibrium configuration, and will arise almost entirely from the $-NH_2$ group. This group is subject to a low-barrier inversion motion across the ab inertial plane so it is not surprising that μ_c is effectively zero in the ground state, due to averaging over the double-minimum large-amplitude motion. A similar effect occurs in aniline [224] and in isomers of aminobenzonitrile [225]. Furthermore, although the μ_a component is rather small, there was sufficient sensitivity of Stark shifts for the rather strong b-type transitions to satisfactorily determine its value. The agreement between experiment and calculation is acceptable and only
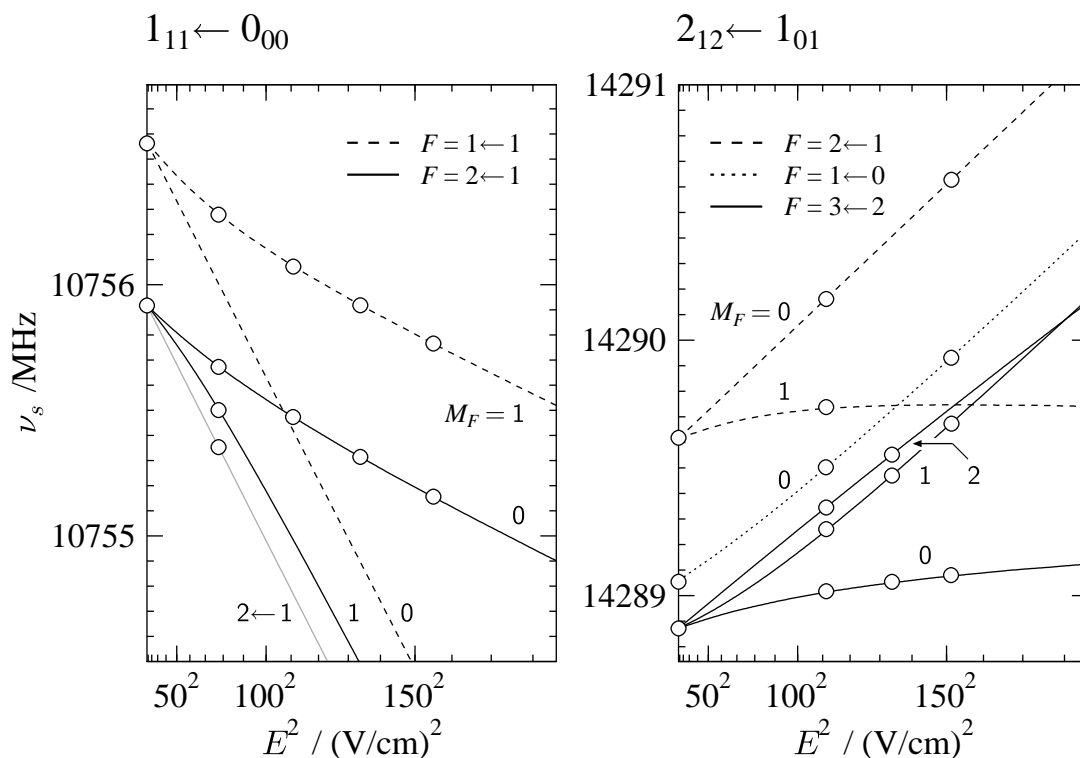
Figure 8.4: Summary of Stark shift measurements for conformer I of urethane made for two different *b*-type rotational transitions: $1_{11} \leftarrow 0_{00}$, and $2_{12} \leftarrow 1_{01}$. Circles denote measured Stark frequencies, continuous lines are predictions made on the basis of final dipole moment fit.

consistent with conformer I.

8.4   Propionitrile

Propionitrile (CH_3CH_2CN), also known as ethyl cyanide, is a well-known interstellar molecule usually associated with hot molecular cores in massive star-forming regions. Over 600 rotational transitions have been detected in astronomical observations [130]. The emission of propionitrile has been found in Sgr B2 [132], as well as in other hot cores, such as in the Orion Nebula (OMC-1) [226]. The molecule has been studied on numerous occasions by means of rotational spectroscopy. For example, the recent laboratory study of the rotational spectrum of propionitrile extending into the THz region [227] gives precise line listing of the propionitrile spectrum necessary for radioastronomical observation by high frequency tools. The present experimental work is an attempt to provide an accurate dipole moment of this molecule, which is useful in analysis of both spectroscopic and astrophysical data.

For the purpose of Stark measurements the gas mixture was prepared by combining two streams of Argon carrier gas at a pressure of 1.2 atm. One stream was

Table 8.2: Comparison of measured and calculated values of the electric dipole moment components (D) for conformers I and II of urethane.

	Conformer I		Conformer II	
	Exp.	Calc.[a]	Exp.[b]	Calc.[a]
$|\mu_a|$	0.5878(20)	0.65	–	0.01
$|\mu_b|$	2.2579(21)	2.48	–	2.25
$|\mu_c|$	$-$[c]	0.67	–	1.11
N_{lines}^{d}	23			
σ_{fit} (kHz)	2.89			

[a]Equilibrium dipole moment calculated at the MP2/aug-cc-pVTZ level.
[b]Not observed experimentally in Ar expansion.
[c]Not determinable in the ground vibrational state.
[d]The number of fitted transitions.

a minimal flow over the liquid sample and the second was in the form of a full flow over an empty sample tube. This method allowed control of gas composition and made it possible to avoid saturating the system with the propionitrile sample. The gas mixture was expanded through a valve into the vacuum chamber at a rate of 2 Hz. Typically from 10 to 15 microwave relaxation signals were recorded per single gas pulse.

Initially, the prediction of the hyperfine structure was made on the basis of quadrupole coupling constants from Ref. [228]. It turned out, however, that the accuracy of hyperfine components evaluated from those constants was insufficient for supersonic expansion measurements. In order to improve these values all available lines in the frequency region of the spectrometer were measured. The newly measured hyperfine components numbered 18, and were measured for 5 different rotational transitions. These transitions were added to lines from Refs. [227, 228] and were fitted with the use of an equivalent set of rotational and centrifugal constants to that given in Ref. [227] including diagonal quadrupole coupling constants χ_{aa}, χ_{bb}, and χ_{cc}. The fit was made with the SPFIT program [24, 25]. In similarity to pyruvonitrile (Chapter 6) the off-diagonal quadrupole coupling constant χ_{ab} could not be determined from the fit, but it was possible to estimate χ_{ab} with confidence on the basis of *ab initio* CCSD/aug-cc-pVDZ calculations made with CFOUR [96]. The results were scaled by 1.197 which provides optimum reproduction of the experimental diagonal splitting constants. The estimated value $\chi_{ab} = -2.13$ MHz was fixed and used in the global fit, resulting in the spectroscopic constants listed in Table 8.3.

In the frequency region of the FTMW spectrometer only the Stark effect of the four lowest a-type rotational transitions could be measured. The intensity of the available b-type line ($4_{04} \leftarrow 3_{13}$ at 13.9 GHz) was insufficient for precise measurement of Stark shifts. For the measurements selected hyperfine components of all four lowest-J, a-type rotational transitions have been chosen: $1_{01} \leftarrow 0_{00}$, $2_{02} \leftarrow 1_{01}$,

Table 8.3: Spectroscopic constants for the ground vibrational state of propionitrile obtained from the global fit of the $A-$reduced rotational and quadrupolar parts of the Hamiltonian to rotational transitions from Refs. [227, 228] and those measured at IFPAN.

		Ref. [228]	This work
A	(MHz)		27663.68290(46)
B	(MHz)		4714.213156(64)
C	(MHz)		4235.059478(61)
Δ_J	(kHz)		3.073451(30)
Δ_{JK}	(kHz)		$-47.65829(35)$
Δ_K	(kHz)		548.1254(28)
δ_J	(kHz)		$-0.6859876(94)$
δ_K	(kHz)		$-12.7399(13)$
Φ_J	(Hz)		0.0103705(58)
Φ_{JK}	(Hz)		$-0.02515(37)$
Φ_{KJ}	(Hz)		$-1.9066(14)$
Φ_K	(Hz)		31.6154(96)
ϕ_J	(Hz)		0.0039674(27)
ϕ_{JK}	(Hz)		0.10167(36)
ϕ_K	(Hz)		6.500(25)
L_J	(mHz)		$-0.00005110(50)$
L_{JJK}	(mHz)		$-0.000816(24)$
L_{JK}	(mHz)		$-0.1201(10)$
L_{KKJ}	(mHz)		0.3984(30)
L_K	(mHz)		$-2.386(14)$
l_J	(mHz)		$-0.00002273(28)$
l_{JK}	(mHz)		$-0.000697(23)$
l_{KJ}	(mHz)		$-0.0444(16)$
l_K	(mHz)		$-4.376(38)$
P_J	(μHz)		0.000000232(17)
P_{JK}	(μHz)		0.000923(10)
P_K	(μHz)		0.1438(69)
p_J	(μHz)		0.000000101(10)
p_K	(μHz)		$-0.0886(36)$
χ_{aa}	(MHz)	$-3.342(16)$	$-3.3572(18)$
χ_{bb}	(MHz)	1.285(21)	1.2972(35)
χ_{cc}	(MHz)	2.057(21)	2.0600(35)
χ_{ab}	(MHz)		$[-2.13]^a$
N_{lines}			3866
$\sigma_{\text{w}}{}^b$			0.994

$^a\chi_{ab}$ has been fixed at the value obtained from scaled *ab initio* CCSD/aug-cc-pVDZ calculation. The employed scaling factor of 1.197 is the average value of the $\chi_{\text{exp}}/\chi_{\text{calc}}$ ratio of diagonal quadrupole coupling constants.
^{b}Unitless deviation of the weighted fit.

Table 8.4: Comparison of experimental and calculated values of the electric dipole moment components (D) for propionitrile.

	Ref.[229]	This work	Calc. μ_e^a	Calc. μ_e^b
$|\mu_a|$	3.85(2)	3.8157(40)	3.846	3.822
$|\mu_b|$	1.23(2)	1.2359(13)	1.241	1.229
μ_{tot}	4.05(3)	4.0108(42)	4.041	4.015
N_{lines}		87		
σ_{fit} (kHz)		2.96[c]		

[a]Calculated at the CCSD/aug-cc-pVDZ level.
[b]Calculated at the CCSD(T)/aug-cc-pVDZ level.
[c]Deviation of fit to 77 Stark measurements and 10 zero-field frequencies for the measured Stark components.

$2_{12} \leftarrow 1_{11}$, and $2_{11} \leftarrow 1_{10}$ at frequencies of 8.9, 17.8, 17.4, and 18.3 GHz, respectively. The measurements were made on totally resolved $\Delta M = 0$ Stark lobes. The sensitivity of Stark shifts to values of μ_a and μ_b proved to be sufficient for accurate determination of both dipole moment components. The Stark measurements are summarised graphically in Fig. 8.5.

For the dipole moment fit the rotational and quadrupole parts of the Hamiltonian were fixed by using the constants from Table 8.3. The fit was made with QSTARK [34] to transition frequencies of 110 measured Stark components, and the results are listed in Table 8.4. The current results are in good agreement with formerly determined values at least to within the estimated uncertainty. The precision of the experimental determination has been improved by an order of magnitude and the agreement with computation is excellent.

8.5 Acrylonitrile

In the recent study of the terahertz spectrum of acrylonitrile [23] the authors began suspecting the validity of the available experimental dipole moment of acrylonitrile. The relative intensities of the a-, and b-type rotational transitions in the THz-region indicated that the literature experimental value of μ_b [174] was considerably overestimated. Despite the fact that μ_a is five times larger in magnitude than μ_b, the b-type rotational transitions dominate over the a-type ones in the terahertz spectrum by virtue of lower values of the J quantum number. This is illustrated in Fig. 1 and Fig. 3 of Ref. [23], and shows that precise knowledge of μ_a/μ_b is important in analysis of such complex terahertz spectra. In the present work an attempt was made to improve the determination of the gas phase dipole moment of acrylonitrile.

For the Stark measurements the expansion mixture consisting of approximately 1% of acrylonitrile in Ar carrier gas was expanded into the spectrometer chamber
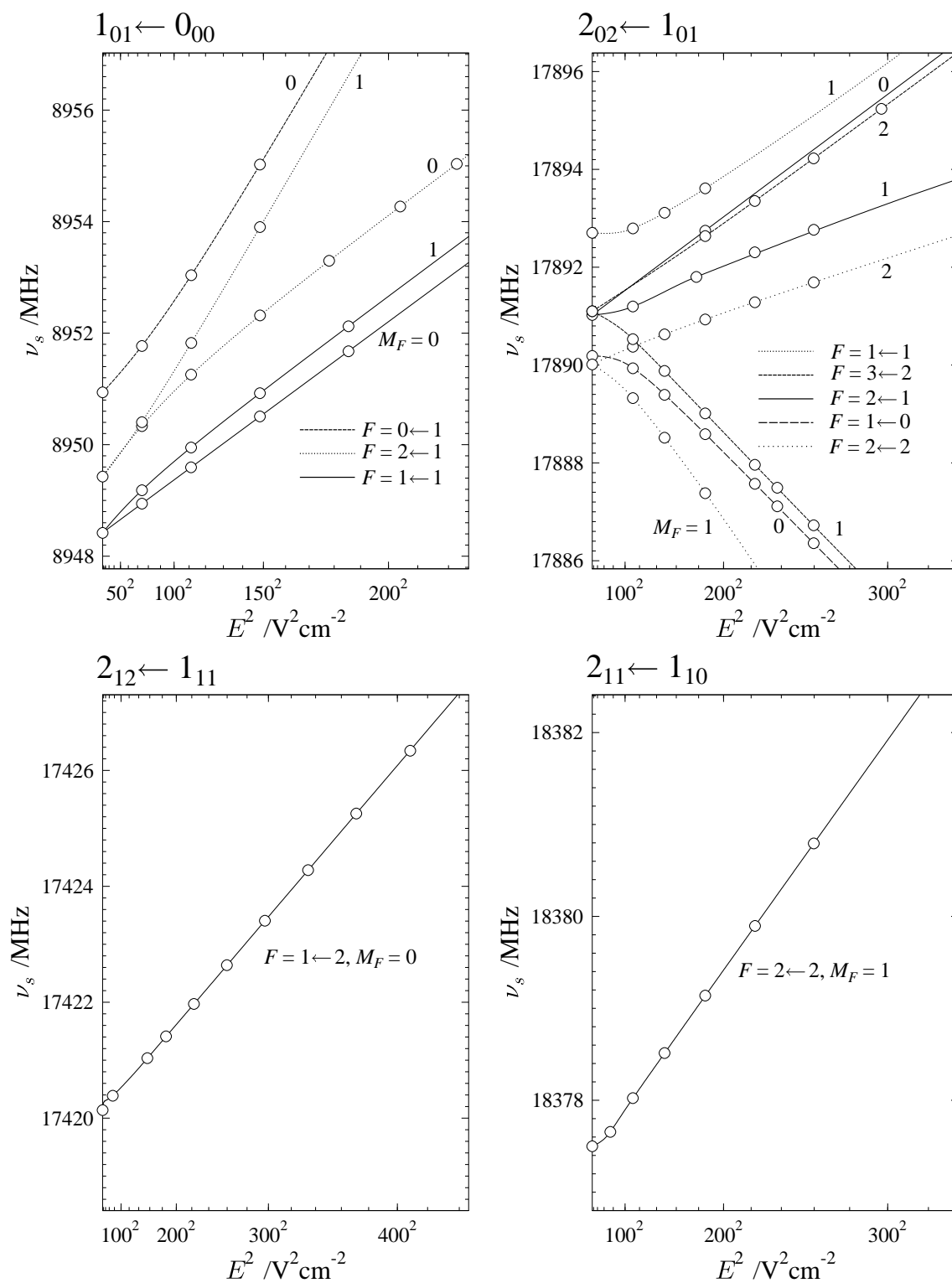
Figure 8.5: Summary of Stark shift measurements for propionitrile. Circles denote measured Stark frequencies, continuous lines are predictions made on the basis of the final dipole moment fit.

Table 8.5: Comparison of experimental and calculated values of the electric dipole moment components (D) for acrylonitrile.

	Ref.[230]	Ref.[174]	This work	Calc. μ_e^a	Calc. μ_0^b
$|\mu_a|$	3.68	3.815(12)	3.8208(40)	3.844	3.802
$|\mu_b|$	1.25	0.894(68)	0.6866(81)	0.702	0.696
μ_{tot}	3.89(8)	3.918(19)	3.8820(40)	3.907	3.865
N_{lines}			95		
σ_{fit} (kHz)			3.23^d		

[a]Equilibrium dipole moment calculated at the CCSD(T)/aug-cc-pVDZ level.

[b]Vibrationally averaged dipole moment calculated at the CCSD(T)/aug-cc-pVDZ level.

[c]Deviation of fit to 84 Stark measurements and 11 zero-field frequencies for the measured Stark components.

from a backing pressure of 1.2 atm. The sample was pulsed through a 0.35 mm diameter orifice at a rate of 2 Hz. Typically from 10 to 15 microwave relaxation signals were recorded per single gas pulse.

Electric dipole moment for acrylonitrile has been determined by performing Stark shift measurements on many different Stark components belonging to several hyperfine components. The availability of the ground state rotational transitions of acrylonitrile in the operating frequency range of the FTMW spectrometer $(2-20$ GHz$)$ is rather limited making the measurements more difficult. For the Stark effect three low K_a, ^aR-type transitions have been chosen: $1_{01} \leftarrow 0_{00}$, $2_{02} \leftarrow 1_{01}$, and $2_{11} \leftarrow 1_{10}$ near 9.5, 18.9, and 19.4 respectively, and one weak, but still measurable ^bP-type transition $2_{12} \leftarrow 3_{03}$ at 15.9 GHz. The overwhelming majority of a-type transitions made the determination of μ_a much easier than of μ_b, thus the vital issue was to choose the Stark lobes which had a significant contribution from both dipole moment components. The Stark lobes with $\Delta M = 0$ which provide information on both μ_a and μ_b are three components of the $2_{02} \leftarrow 1_{01}$ transition: $(F = 2 \leftarrow 1, M_F = 0)$, $(F = 3 \leftarrow 2, M_F = 2)$ and $(F = 2 \leftarrow 2, M_F = 1)$. Maximum frequency shifts with applied electric field of up to 9.62, 9.04 and -7.09 MHz, respectively, have been measured for these components. Such large Stark shifts relative to those normally observed with this spectrometer, could be observed mainly because of the considerable intensity of the $2_{02} \leftarrow 1_{01}$ transition. On the other hand, the Stark shift for the b-type line $2_{12} \leftarrow 3_{03}$ could be observed only up to 2 MHz, although its contribution to μ_b is comparable to that obtained from almost 10 MHz Stark shifts of the a-type line. The graphical summary of the Stark measurements is given in Fig. 8.6.

The constants in the rotational Hamiltonian (in Watson's $A-$reduced form) and quadrupole coupling constants were fixed using the values from Ref. [6], so that only the two components of the dipole moment constituted the parameters of the fit. It was found that the value of μ_b was substantially lower than those reported in
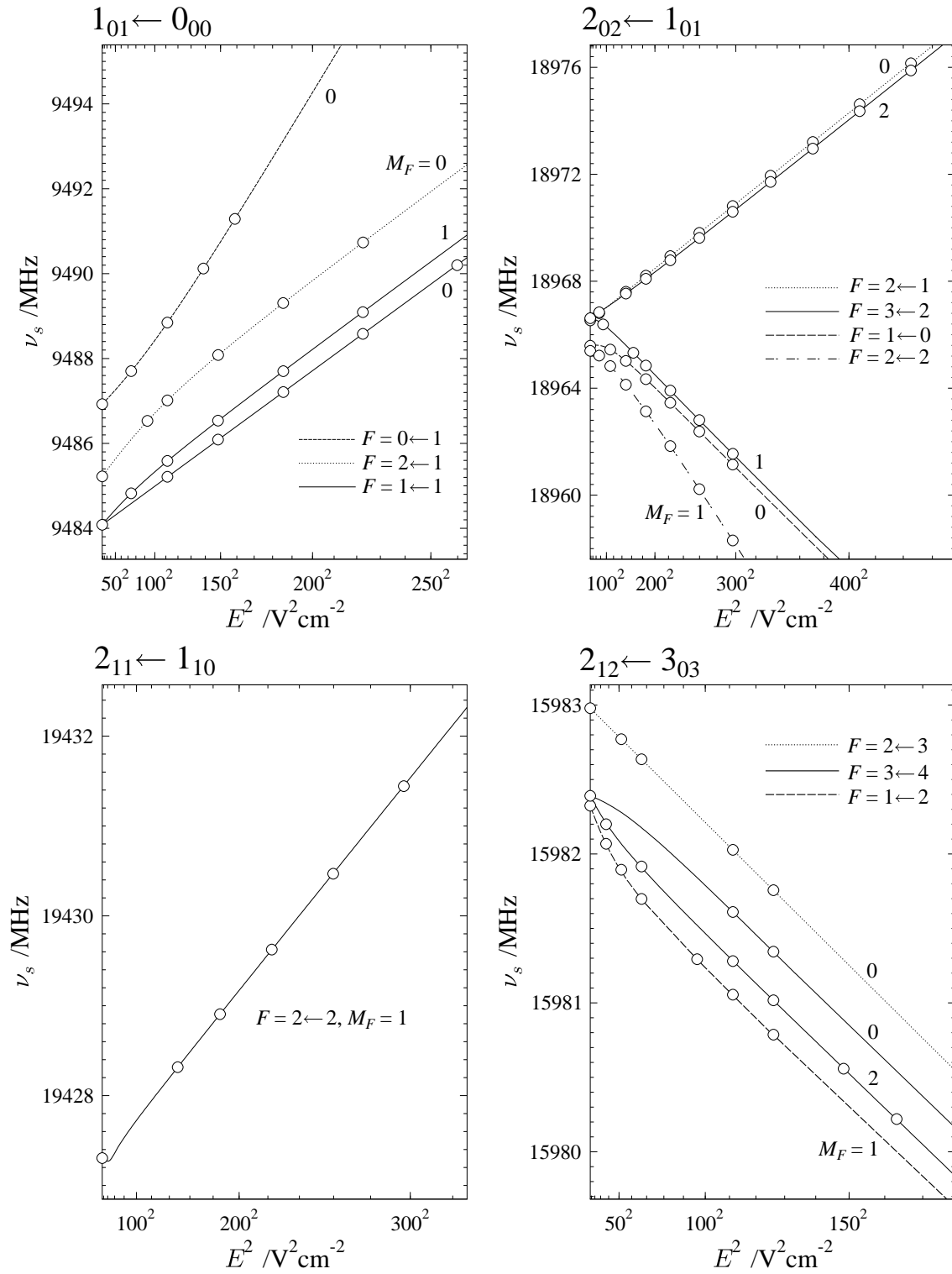
Figure 8.6: Summary of Stark shift measurements for acrylonitrile. Circles denote measured Stark frequencies, continuous lines are predictions made on the basis of the final dipole moment fit.

^{a}R $\leftrightarrow$ ^{b}R $\qquad\qquad$ ^{a}R $\leftrightarrow$ ^{b}Q $\qquad\qquad$ ^{a}R $\leftrightarrow$ ^{b}Q

$31_{24,7} \leftarrow 30_{24,6}$ $35_{1,34} \leftarrow 34_{2,33}$ $\qquad\qquad$ $27_{4,23} \leftarrow 27_{3,24}$ $\qquad$ $43_{1,42} \leftarrow 43_{0,43}$

$31_{24,8} \leftarrow 30_{24,7}$

$32_{25,7} \leftarrow 31_{25,6}$ $\qquad\qquad\qquad\qquad\qquad$ $35_{26,9} \leftarrow 34_{26,8}$

$32_{25,8} \leftarrow 31_{25,7}$ $\qquad\qquad\qquad\qquad\qquad$ $35_{26,10} \leftarrow 34_{26,9}$

MHz $\quad$ 296710 $\qquad$ 306500 $\qquad$ 306510 $\qquad$ 306520 $\quad$ 335440 $\qquad$ 335450
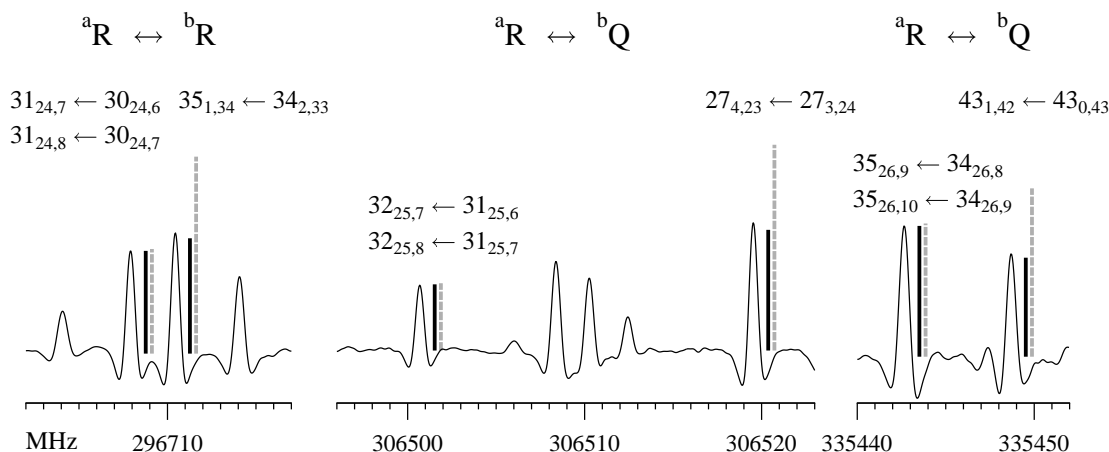
Figure 8.7: Three segments of the room-temperature millimeter-wave rotational spectrum of acrylonitrile recorded with the broadband millimeter-wave spectrometer at IFPAN (described in Chapter 3.2). The segments were chosen because of the presence of nearby of *a*- and *b*-type transitions of similar intensity. Dotted grey lines denote the intensity of transitions calculated on the basis of dipole moment components determined in Ref. [174], whereas the black lines denote the intensities calculated from dipole moment components determined in this work. The good agreement of the intensities determined from current dipole moment measurements with those observed in the spectrum confirms the validity of the current dipole moment redetermination.

previous determinations. The first reported gas phase value of μ_b was 1.25 D [230], then the value of 0.894(68) D [174] was determined. These compare to the present value of 0.6862(79) D and appear to have been significantly overestimated.

In order to confirm the new value of the dipole moment, especially of the μ_b component which is determined with a somewhat larger error, *ab initio* calculations at different theoretical levels and intensity measurements of *a*- and *b*-type rotational transitions in the millimeter-wave spectrum have been performed. In quantum-chemistry calculations the CCSD(T) level of correlation correction has been used together with a basis set augmented with the diffuse functions aug-cc-pVDZ which is suitable for more accurate calculation of dipole moments (see Chapter 2.9). In addition, zero-point vibrational corrections of the calculated equilibrium dipole moment components have been made at the same theoretical level. The results show that vibrationally averaged μ_a and μ_b are reduced in relation to equilibrium values, and are in better consistency with experiment. The experimental and theoretical results are listed in Table 8.5. The intensity of the *a*-type lines is proportional to μ_a^2 and of the *b*-types to μ_b^2. When the *b*-type transitions are concerned it is seen that using literature value of μ_b [174] and the present one the intensity prediction differs by 59%. This has been illustrated in Fig. 8.7.

Chapter 9

Summary

This dissertation presents the results of systematic studies of rotational spectra for selected molecules. All of the chosen molecules are either established astrophysical species (such as acrylonitrile and propionitrile) or potential candidates for detection by radioastronomy. For each studied molecule a short description of the current state of radioastronomical detections, or some arguments suggestive of the presence of the molecule in the interstellar medium are given. The rotational spectra analyzed in the dissertation have been recorded with three types of spectrometers: broadband, room-temperature mmw/sub-mmw spectrometers, a high-resolution infrared interferometer, and a cavity supersonic expansion FTMW spectrometer. These spectrometers operate in various frequency regions, at different resolutions, and at different experimental conditions. When more than one spectrometer could be applied to a given problem it was possible to obtain complementary information on various aspects of the rotational spectrum. Analysis of the spectra measured with these spectrometers enabled determination of many important molecular properties.

The reported assignments of the broadband rotational spectra have usually been associated with extensive measurements involving hundreds or thousands of lines. For instance, for each isotopic species of acrylonitrile more than 2000 lines have been assigned for the ground state, and around 1000 lines for the first excited vibrational state. For practical reasons the final results of the fits for each studied species have not been included in this dissertation. Most of the results presented in the thesis have already been published and others will soon be published in scientific journals. Data files containing inputs to the fitting programs, results of fits, and listings of measured lines with their experimental uncertainty for each investigation are, in most cases, deposited in the electronic repository of the related journal and are available online.

Rotational spectra. In this dissertation the most extensive rotational spectra were studied up to 1 THz by recording and analyzing several extended spectral segments spanning a total of several hundreds of GHz's. For all molecules rotational spectra were studied at least up to the lower part of the submillimeter-wave region.

The new data are sufficient to provide new or updated catalog entries for astronomical searches of the studied molecules and of their isotopic species in the ground and in some excited vibrational states. The current results are particularly valuable for the astronomical investigations with the use of more sensitive, higher frequency tools such as Herschel, ALMA or SOFIA observatories. For each studied species the frequency range, the number of the measured transitions, and the coverage of the J and K_a quantum numbers have been considerably extended in comparison to previous studies. This allowed determination of the precise values of not only rotational but also of centrifugal distortion and vibration-rotation perturbation constants of various orders. The observed perturbations have even GHz-size contributions to many transitions at higher frequencies, and their accurate values are essential for reliable prediction of the higher-frequency spectra.

For the rare isotopic species of **cyanamide** the rotation-inversion spectra have been measured in three broadband segments up to 650 GHz. The spectroscopic constants determined from their analysis should give an accurate prediction of the spectra up to 1 THz. In case of H_2NCN and D_2NCN, for which rotationally resolved infrared spectra were also analysed, accurate prediction is expected to reach wavenumbers of well above 360 cm^{-1}. The spectra of isotopic species of **acrylonitrile** have been measured up to 1.2 THz, and derived spectroscopic constants should allow reasonable prediction up to 2 THz. The rotational spectra for **pyruvonitrile** and **phenylacetylene** were measured mainly in the millimeter-wave region. Radioastronomy detection of these molecules has not yet been attempted. However, such work is now possible since the present data provide accurate line positions even up to 1 THz.

Vibration-rotation interactions. The present studies of the rotational spectra enabled investigation of various aspects of vibration-rotation interactions between rotational levels of different vibrational states. Specifically, analysis of the ground state transitions for **cyanamide** revealed the presence of strong coupling between two components of the inversion doublet: 0^+ and 0^-. A coupled two-state Hamiltonian turned out to be satisfactory in reproducing the measurements, at least in the regime of moderate values of K_a and J. The analysis of the inversion-rotation spectra of various isotopic species resulted in determination of the precise energy spacing between the 0^+ and 0^- substates, and gave additional information on the inversion potential of cyanamide. In addition, transitions with higher values of K_a which could not be described by the used Hamiltonian have been identified as involved in perturbations with other vibrationally excited states. Since the primary aim of this analysis was to obtain the most reliable description of the ground state transitions it was not practicable to set up the whole chain of these interstate interactions for cyanamide. Nonetheless, the undertaking of this task would be valuable for better understanding of the dynamics in cyanamide as manifested in rotational spectra.

The prototype interaction between the ground and the first excited vibrational state previously found for the parent species of **acrylonitrile** [23], has also been

identified for its four singly isotopically substituted species. The analysis of the measured transitions allowed precise determination of the energy difference between the interacting states, which for this case is equivalent to the vibrational wavenumber ν_{11}.

The analysis of the rotational spectrum of **pyruvonitrile** in the ground and two excited vibrational states enabled determination of spectroscopic parameters describing the coupling between internal and overall rotation. In addition, the analysis allowed derivation of many different parameters such as the height of the internal rotation barrier and of the precise energy differences between the A and E levels in the torsional potential. In order to deal with the internal rotation three different methods have been used and the results compared.

For the ground state rotational transitions of **phenylacetylene** the effective single state Hamiltonian with up to sixth-order centrifugal distortion constants was sufficient to reproduce measurements. On the other hand, in the case of the two lowest lying vibrational satellites, $v_{36} = 1$ and $v_{24} = 1$, the coupled treatment was necessary owing to the strong, a-axis Coriolis interaction between these states. The applied theoretical model allowed to fit a total of 1006 transitions for these two excited states. Additional *ab initio* calculations of the anharmonic force field turned out to be indispensable and conclusive in distinguishing between the two almost equivalent numerical solutions.

Molecular geometry. One of the most important results of this dissertation from the chemical point of view has been the precise determination of the molecular geometry of **cyanamide** and of **acrylonitrile**. Cyanamide is a molecule which undergoes large amplitude inversion motion. As a rule, equilibrium-quality molecular structure determined from the ground state rotational constants for molecule of this type is troublesome. Rotation-inversion spectra of thirteen isotopic species of cyanamide have been assigned resulting in 36 experimental rotational constants for use in structural analysis. These were combined with calculated vibration-rotation contributions to the rotational constants from the CCSD(T)/cc-pVQZ anharmonic force field and turned out to be sufficient for the complete evaluation of the semi-experimental equilibrium r_e^{SE} molecular structure of cyanamide. A similar approach applied for acrylonitrile also gave outstanding results. Deviations of these structural fits proved to be spectacularly low and the fitted parameters demonstrate high consistency with the theoretical predictions. It is expected that the determined structures will remain in the scientific literature for a long time as reference structures for these two molecules, and as a good example of the successful application of the r_e^{SE} approach, the applicability of which is still being tested.

Dipole moments. Another important result of this dissertation is the precise determination of the electric dipole moments for several molecules. The measurements were made for **pyruvonitrile**, **urethane**, **propionitrile**, and **acrylonitrile** at conditions of supersonic expansion. As discussed in Chapter 8 the dipole moment is important not only for chemical considerations, but also has a purely practical

meaning in analysis of radioastronomical spectra since intensity of rotational transitions is directly governed by the magnitude of the corresponding dipole moment component. As has been shown in Fig. 8.7 the value of μ_b for acrylonitrile is reflected by a 59% change in the calculated intensity of b-type transitions, which is confirmed by relative intensities in the mmw-wave spectrum. This high frequency spectrum of acrylonitrile is presently the subject of extensive studies by means of radioastronomy. Reliable determination of the small μ_b value for acrylonitrile seems to be a significant experimental contribution, and its determination necessitated difficult Stark shift measurements on very weak hyperfine components.

Hyperfine structure. Analysis of the hyperfine structure visible in supersonic expansion FTMW measurements allowed determination of precise nuclear quadrupole coupling constants for **pyruvonitrile** and **propionitrile**. Admittedly, these values were known from earlier studies but they turned out to be different from the current values even by 20% as is the case for χ_{cc} of ^{14}N in pyruvonitrile. The accurate values of the quadrupole coupling constants are also important in the analysis of the radioastronomical spectra. For some transitions the hyperfine structure is observed at high frequencies and additional splitting of the line confirmed by laboratory measurements might be conclusive in the assignment.

The series of investigations of selected medium-size molecules have shown how a broad range of techniques of rotational spectroscopy can be used to obtain a variety of results on molecular properties. These properties are not only useful in the field of molecular physics or chemistry but are also relevant to astronomical searches for these molecules in space. In addition, it has also been shown in this dissertation how precise experimental results can be complemented by the *ab initio* calculations in a determination of molecular structure or in distinguishing of the correct numerical solution in a fit of Hamiltonian. Furthermore, the accurate values of many experimental molecular properties determined in this thesis, such as molecular structure, dipole moment, nuclear quadrupole coupling constants, internal rotation and inversion barriers can be used as a valuable guide to the development and application of the methods of computational chemistry (*ab initio* and density functional theory).

Appendix A

Structural Fits

This Appendix summarises the primary data and the results of the preferred r_e^{SE} structural fits for cyanamide (Chapter 4) and acrylonitrile (Chapter 5). The fits have been made with the STRFIT program by the least squares procedure to moments of inertia. The experimental moments of inertia were corrected by the vibration-rotation contributions calculated with CFOUR.

Table A.1 collects the results for cyanamide. The final structure from this fit is shown in Figure 4.8.

Table A.2 collects the results for acrylonitrile. The final structure from this fit is shown in Figure 5.8.

Table A.1: Summary of the r_e^{SE} fit for cyanamide.

		$B_0\ ^a$/MHz	$(B_e - B_0)^b$/MHz	$B(\mathrm{o-c})^c$/MHz	$I(\mathrm{o-c})^c$/uÅ²
H_2NCN	A	308297.81100	−1675.27650	−231.0543	0.00124
	B	10121.71630	21.34720	0.1138	−0.00056
	C	9865.78058	42.26220	−0.0702	0.00036
HDNCN	A	212394.45500	−974.88570	22.2032	−0.00025
	B	9601.67486	23.07510	0.0288	−0.00016
	C	9259.84991	44.03130	0.0292	−0.00017
D_2NCN	A	156875.86700	−231.43540	16.6400	−0.00034
	B	9154.97064	23.07330	−0.0520	0.00031
	C	8747.29479	43.71039	0.0399	−0.00026
$D_2N^{13}CN$	A	156870.95000	−229.33190	19.3783	−0.00040
	B	9147.11045	22.95480	−0.0046	0.00003
	C	8740.08880	43.59020	0.0599	−0.00039
$D_2NC^{15}N$	A	156866.55000	−232.78190	21.1718	−0.00044
	B	8856.17295	22.27150	−0.0677	0.00043
	C	8474.09125	41.69040	−0.0056	0.00004
$D_2^{15}NCN$	A	156545.80000	−271.38020	−9.9843	0.00021
	B	8954.48150	21.72600	−0.1340	0.00084
	C	8565.14830	41.65290	0.0622	−0.00042
$HDN^{13}CN$	A	212369.70000	−975.84100	18.2215	−0.00021
	B	9595.65680	22.93510	0.0527	−0.00029
	C	9254.19330	43.89810	0.0529	−0.00031
$HDNC^{15}N$	A	212353.90000	−976.74560	17.1205	−0.00019
	B	9290.16370	22.27120	0.0200	−0.00012
	C	8969.69250	41.98000	−0.0036	0.00002
$HD^{15}NCN$	A	211768.90000	−1027.70010	−26.0833	0.00030
	B	9368.24140	21.51530	−0.0343	0.00020
	C	9042.58760	41.63800	0.0166	−0.00010
$H_2N^{13}CN$	A	308297.00000	−1675.71860	−232.2506	0.00125
	B	10117.57920	21.17190	0.1119	−0.00055
	C	9861.84600	42.11200	−0.0418	0.00022
$H_2NC^{15}N$	B	9795.06135	20.60680	0.1424	−0.00075
	C	9555.08645	40.26090	−0.1045	0.00057
$H_2^{15}NCN$	B	9845.62100	19.70840	0.0545	−0.00028
	C	9603.67985	39.63500	−0.1356	0.00074
$H_2^{15}NC^{15}N$	B	9523.26500	19.01860	0.0855	−0.00047
	C	9296.62410	37.72460	−0.1721	0.00100

[a] All rotational constants in the structural fit were taken as an average of the values for the 0^+ and 0^- substates derived from coupled fits with the A-reduced asymmetric rotor Hamiltonian.

[b] Vibration-rotation contributions $B_e - B_0^A$ calculated at the CCSD(T)/cc-pVQZ level with CFOUR [96].

[c] Differences between experimental constants corrected by the vibration-rotation contributions and calculated values from the final structure.

Table A.2: Summary of the r_e^{SE} fit for acrylonitrile.

		B_0 [a]/MHz	$(B_e - B_0)$[b]/MHz	$B(\mathrm{o-c})$[c]/MHz	$I(\mathrm{o-c})$[c]/uÅ^2
CH$_2$=CHCN [d]	A	49850.69649	134.53700	-5.0260	0.00102
	B	4971.16363	15.19900	-0.0766	0.00156
	C	4513.87724	20.30700	0.0198	-0.00049
^{13}CH$_2$=CHCN	A	49195.20200	124.82800	-4.5627	0.00095
	B	4837.57973	14.91600	-0.0654	0.00140
	C	4398.24238	19.71100	0.0284	-0.00073
CH$_2$=CD^{13}CN[e]	A	40176.32700	144.28900	-1.7429	0.00054
	B	4910.89800	14.26100	-0.0204	0.00043
	C	4369.54300	19.57300	0.0407	-0.00107
^{13}CH$_2$=CDCN[e]	A	39638.93400	136.25000	-2.3879	0.00076
	B	4805.99730	14.07000	-0.0639	0.00139
	C	4280.09280	19.11300	0.0356	-0.00097
CH$_2$=CHC^{15}N	A	49655.34310	131.18100	-5.7604	0.00117
	B	4819.66822	14.62000	-0.0487	0.00105
	C	4387.04612	19.49400	0.0315	-0.00082
CH$_2$=^{13}CHCN[d]	A	48639.64330	127.02500	-5.0329	0.00107
	B	4948.97991	14.73000	-0.0660	0.00135
	C	4485.38300	19.89400	0.0263	-0.00066
CH$_2$=CDCN	A	40196.54300	144.21600	-4.1618	0.00129
	B	4934.35201	14.29500	-0.0505	0.00104
	C	4388.38784	19.66400	0.0400	-0.00104
CH$_2$=^{13}CDCN[e]	A	39527.06000	137.28000	0.1285	-0.00004
	B	4913.06250	13.87300	-0.0271	0.00056
	C	4363.31500	19.26900	0.0108	-0.00028
CH$_2$=CH^{13}CN	A	49799.60580	133.35400	-5.7635	0.00117
	B	4948.36493	15.15300	-0.0576	0.00118
	C	4494.65455	20.20900	0.0321	-0.00080
CHD^c=CHCN[e]	B	4865.72430	12.76400	-0.0287	0.00061
	C	4349.52210	18.49200	0.0472	-0.00125
CHD^t=CHCN[e]	B	4638.59090	14.82100	-0.0335	0.00078
	C	4238.20850	18.93400	0.0391	-0.00109
CHD^c=CDCN[e]	A	34292.81000	147.17600	-3.1065	0.00132
	B	4835.17170	12.27200	-0.0301	0.00065
	C	4231.33120	18.11900	0.0335	-0.00094
CHD^t=CDCN[e]	A	40173.53000	131.70600	-3.3087	0.00103
	B	4610.25620	14.10800	-0.0338	0.00080
	C	4130.11750	18.39700	0.0492	-0.00144
CD$_2$=CDCN[e]	A	34297.03900	141.90100	-3.2738	0.00139
	B	4528.78030	12.44500	-0.0609	0.00149
	C	3995.12210	17.15600	0.0178	-0.00056

		B_0 [a]/MHz	$(B_e - B_0)$[b]/MHz	$B(o-c)$[c]/MHz	$I(o-c)$[c]/uÅ²
$^{13}CH_2=^{13}CHCN$	A	47962.98300	117.39900	−3.9587	0.00087
	B	4818.70100	14.46600	−0.0349	0.00076
	C	4372.47720	19.31900	0.0328	−0.00086
$^{13}CH_2=CH^{13}CN$	A	49143.38400	123.64200	−5.2205	0.00109
	B	4813.95540	14.86500	−0.0285	0.00062
	C	4378.28550	19.60900	0.0495	−0.00129
$CH_2=^{13}CH^{13}CN$	A	48597.43600	126.25700	−5.1965	0.00111
	B	4925.58330	14.67800	−0.0334	0.00069
	C	4465.78040	19.79000	0.0341	−0.00086
$CH_2=^{13}CHC^{15}N$	A	48449.24800	123.91600	−5.2857	0.00113
	B	4796.60060	14.16000	−0.0241	0.00053
	C	4358.24780	19.08600	0.0381	−0.00101
$^{13}CH_2=CHC^{15}N$	A	48995.13300	121.42500	−5.3873	0.00113
	B	4689.30040	14.34900	−0.0296	0.00068
	C	4273.76150	18.92100	0.0456	−0.00125
$CH_2=CH^{13}C^{15}N$	A	49598.19200	129.77800	−6.6694	0.00136
	B	4800.26410	14.57900	−0.0395	0.00086
	C	4370.51910	19.40900	0.0372	−0.00098

[a]All rotational constants obtained from the fit of the rotational transitions to the S-reduced asymmetric rotor Hamiltonian.

[b]Vibration-rotation contributions $B_e - B_0^S$ calculated at the CCSD(T)/cc-pVTZ level with CFOUR [96].

[c]Differences between experimental constants corrected by the vibration-rotation contributions and calculated values from the final structure.

[d]Rotational constants from Ref. [23].

[e]Rotational constants from Ref. [178].

Bibliography

[1] T. J. Balle, W. H. Flygare, *Rev. Sci. Instrum.* **52**, 33-45 (1981).

[2] G.G. Brown, B.C. Dian, K.O. Douglass, S.M. Geyer, B.H. Pate, *J. Mol. Spectrosc.* **238**, 200-212 (2006).

[3] G. G. Brown, B. C. Dian, K. O. Douglass, S. M. Geyer, S. T. Shipman, B. H. Pate, *Rev. Sci. Instrum.* **79**, 1-13 (2008).

[4] B. C. Dian, G. G. Brown, K. O. Douglass, B. H. Pate, *Science* **320**, 924-928 (2008).

[5] Z. Kisiel, A. Kraśnicki, L. Pszczółkowski, S. T. Shipman, L. Alvarez-Valtierra, B. H. Pate, *J. Mol. Spectrosc.* **257**, 177-186 (2009).

[6] H. S. P. Müller, A. Belloche, K. M. Menten, C. Comito, P. Schilke, *J. Mol. Spectrosc.* **251**, 319-325 (2008).

[7] L. Alonso, M. E. Sanz, J. C. López and V. Cortijo, *J. Am. Chem. Soc.* **131**, 4320-4326 (2009).

[8] A. Cooke, M. C. L. Gerry, *Phys. Chem. Chem. Phys.* **6**, 4579-4585 (2004).

[9] A. van Orden, R. A. Provencal, T. F. Giesen, R. J. Saykally, *Chem. Phys. Lett.* **237**, 77-80 (1995).

[10] A. van Orden, T. F. Giesen, R. A. Provencal, H. J. Hwang, R. J. Saykally, *J. Chem. Phys.* **101**, 10237-10241 (1994).

[11] Y. Ohshima, K. Sato, Y. Sumiyoshi, Y. Endo, *J. Am. Chem. Soc.* **127**, 1108-1109 (2005).

[12] W. Gordy, R. L. Cook, "Microwave Molecular Spectra", John Wiley & Sons, New York, (1984).

[13] D. Papoušek, M. R. Aliev, "Molecular Vibrational Rotational Spectra", Academia, Prague, (1982).

[14] C. H. Townes, A. L. Schawlow, "Microwave Spectroscopy", McGraw-Hill Publishing Company Ltd., New York, (1955).

[15] H. W. Kroto, "Molecular Rotation Spectra", Dover Publications, Inc., Mineola, New York, (1992).

[16] Z. Kisiel, in: J.Demaison *et al*. (Eds.), Spectroscopy from Space, Kluwer Academic Publishers, Dordrecht, 91-106, (2001).

[17] Z. Kisiel, PROSPE - Programs for ROtational SPEctroscopy, *available at* http://info.ifpan.edu.pl/~kisiel/prospe.htm.

[18] Z. Kisiel, ROTLINKS - Rotational Spectroscopy Links, *available at* http://info.ifpan.edu.pl/~kisiel/rotlinks.htm.

[19] P. J. Mohr, B. N. Taylor, D. B. Newell, *Rev. Mod. Phys* **80**, 633-730 (2008); *J. Phys. Chem. Ref. Data* **37**, 1187-1284 (2008); website http://physics.nist.gov/cuu/Constants/index.html.

[20] A. Rosenberg, I. Ozier, A. K. Kudian, *J. Chem. Phys.* **57**, 568-569 (1972).

[21] J. K. G. Watson, "Aspects of Quartic and Sextic Centrifugal Effects on Rotational Energy Levels", *in* "Vibrational Spectra and Structure" (J. R. Durig, red.), Vol. 6, Marcel Dekker, New York, (1977).

[22] G. Winnewisser, *J. Chem. Phys.* **56**, 2944-2954 (1972).

[23] Z. Kisiel, L. Pszczółkowski, B. J. Drouin, C. S. Brauer, S. Yu, J. C. Pearson, *J. Mol. Spectrosc.* **258**, 26-34 (2009).

[24] H. M. Pickett, *J. Mol. Spectrosc.* **148**, 371-377 (1991).

[25] H. M. Pickett, SPFIT/SPCAT package. *Available from* : http://spec.jpl.nasa.gov.

[26] J. K. Bragg, S. Golden, *Phys. Rev.* **75**, 735-738 (1949).

[27] S. G. Kukolich, D. J. Ruben, J. H. S. Wang, J. R. Williams, *J. Chem. Phys.* **58**, 3155-3159 (1973).

[28] S. G. Kukolich, *J. Chem. Phys.* **57**, 869-871 (1972).

[29] J. L. Alonso, C. Pérez, M. E. Sanz, J. C. López, S. Blanco, *Phys. Chem. Chem. Phys.* **11**, 617-627 (2009).

[30] C. T. Dewberry, Z. Kisiel, S. A. Cooke, *J. Mol. Spectrosc.* **261**, 82-86 (2010).

[31] S. Golden, E. B. Wilson, *J. Chem. Phys.* **16**, 669-685 (1948).

[32] J. E. Wollrab, "Rotational Spectra and Molecular Structure", Academic Press, New York, (1967).

[33] H. P. Benz, A. Bauder, H. H. Günthard, *J. Mol. Spectrosc.* **21**, 156-164 (1966).

[34] Z. Kisiel, J. Kosarzewski, B. A. Pietrewicz, L. Pszczółkowski, *Chem. Phys. Lett.* **325**, 523-530 (2000).

[35] M. R. Keenan, D. B. Wozniak, W. H. Flygare, *J. Chem. Phys.* **75**, 631-640 (1981).

[36] W. G. Read, W. H. Flygare, *J. Chem. Phys.* **76**, 2238-2246 (1982).

[37] O. Dorosh, Z. Kisiel, *Acta Phys. Pol. A* **112**, 95-104 (2007).

[38] S. Schlemmer, T. Giesen, F. Lewen, G. Winnewisser, "High-Resolution Laboratory Terahertz Spectroscopy and Applications to Astrophysics" in "Frontiers of Molecular Spectroscopy", Edited by J. Laane, Elsevier (2009).

[39] I. M. Mills, "Vibration–Rotation Structure in Asymmetric and Symmetric–Top Molecules" in "Molecular Spectroscopy: Modern Research", Edited by K. N. Rao and C. W. Mathews, Academic Press (1972).

[40] H. A. Jahn, *Phys. Rev.* **56**, 680-683 (1939).

[41] H. M. Pickett, *J. Chem. Phys.* **56**, 1715-1723 (1972).

[42] Z. Kisiel, O. Dorosh, M. Winnewisser, M. Behnke, I. R. Medvedev, F. C. De Lucia *J. Mol. Spectrosc.* **246**, 39-56 (2007).

[43] R. A. H. Butler, D. T. Petkie, P. Helminger, F. C. De Lucia, *J. Mol. Spectrosc.* 220 (2003) 150-152.

[44] J. Laane, "Vibrational Potential Energy Surfaces in Electronic Excited States" in "Frontiers of Molecular Spectroscopy", Edited by J. Laane, Elsevier (2009).

[45] A. Lesarri, S. Blanco, J. C. López, *J. Mol. Struct.* **354**, 237-243 (1995).

[46] G. Cazzoli, D. G. Lister, *J. Mol. Spectrosc.* **45**, 467-474 (1973).

[47] G. Hamada, S. Fujiwara, H. Buijs, *J. Mol. Spectrosc.* **129**, 354-363 (1988).

[48] Š. Urban, V. Špirko, D. Papoušek, J. Kauppinen, S. P. Belov, L. I. Gershtein, A. F. Krupnov, *J. Mol. Struct.* **88**, 274-292 (1981).

[49] L. Fusina, G. Di Lonardo, J. W. C. Johns, L. Halonen, *J. Mol. Struct.* **127**, 240-254 (1988).

[50] Z. Kisiel, PhD Thesis, University College London, p. 273-279 (1980).

[51] Z. Kisiel, L. Pszczółkowski, G. Pietraperzia, M. Becucci, W. Caminati, R. Meyer, *Phys. Chem. Chem. Phys.* **6**, 5469-5475 (2004).

[52] I. Kleiner, *J. Mol. Spectrosc.* **260**, 1-18 (2010).

[53] J. T. Hougen, I. Kleiner, M. Godefroid, *J. Mol. Spectrosc.* **163**, 559-586 (1994).

[54] C. C. Lin, J. D. Swalen, *Rev. Mod. Phys.* **31**, 841-892 (1959).

[55] D. R. Herschbach, *J. Chem. Phys.* **31**, 91-108 (1959).

[56] D. Gerhard, A. Hellweg, I. Merke, W. Stahl, M. Baudelet, D. Petitprez, G. Wlodarczak, *J. Mol. Spectrosc.* **220**, 234-241 (2003).

[57] Z. Kisiel, L. Pszczółkowski, E. Białkowska-Jaworska, S. B. Charnley, *J. Mol. Spectrosc.* **241**, 220-239 (2007).

[58] R. C. Woods, *J. Mol. Spectrosc.* **21**, 4-24 (1966).

[59] J. M. Vacherand, B. P. van Eijck, J. Burie, J. Demaison, *J. Mol. Spectrosc.* **118**, 355-362 (1986).

[60] H. Hartwig, H. Dreizler, *Z. Naturforsch.* **51a**, 923-932 (1996).

[61] H. Hansen, H. Mäder, T. Bruhn, *Molec. Phys.* **97**, 587-595 (1999).

[62] P. Groner, *J. Mol. Spectrosc.* **156**, 164-189 (1992).

[63] P. Groner, *J. Chem. Phys.* **107**, 4483-4498 (1997).

[64] P. Groner, S. Albert, E. Herbst, F. C. De Lucia, *Astrophys. J.* **156**, 1059-1063 (1998).

[65] P. Groner, S. Albert, E. Herbst, F. C. De Lucia, F. J. Lovas, B. J. Drouin, J. C. Pearson, *Astrophys. J. Suppl. Ser.* **142**, 145-151 (2002).

[66] P. Groner, M. Winnewisser, I. R. Medvedev, F. C. De Lucia, E. Herbst, K. V. L. N. Sastry, *Astrophys. J. Suppl. Ser.* **169**, 28-36 (2007).

[67] A. Maeda, I. R. Medvedev, F. C. De Lucia, E. Herbst, P. Groner, *Astrophys. J. Suppl. Ser.* **175**, 139-146 (2008).

[68] P. Groner, E. Herbst, F. C. De Lucia, B. J. Drouin, H. Mäder, *J. Mol. Struct.* **795**, 173-178 (2006).

[69] P. Groner, I. R. Medvedev, F. C. De Lucia, B. J. Drouin, *J. Mol. Spectrosc.* **251**, 180-184 (2008).

[70] C. P. Endres, B. J. Drouin, J. C. Pearson, H. S. P. Müller, F. Lewen, S. Schlemmer, T. F. Giesen, *Astron. & Astrophys.* **504**, 635-640 (2009).

[71] Z. Kisiel, *J. Mol. Spectrosc.* **218**, 58-67 (2003).

[72] F. C. De Lucia, P. Helminger, W. Gordy, *Phys. Rev. A* **3**, 1849-1857 (1971).

[73] G. Cazzoli, L. Cludi, M. Contento, C. Puzzarini, *J. Mol. Spectrosc.* **251**, 229-234 (2008).

[74] J. Kraitchman, *Am. J. Phys.* **21**, 17-24 (1953).

[75] C. C Costain, *Trans. Am. Crystallogr. Assoc.* **2**, 157-164 (1966).

[76] J. Demaison, H. D. Rudolph, *J. Mol. Struct.* **215**, 78-84 (2002).

[77] O. Desyatnyk, L. Pszczółkowski, S. Thorwith, T. M. Krygowski, Z. Kisiel, *Phys. Chem. Chem. Phys.* **7**, 1708-1715 (2005); correction *Phys. Chem. Chem. Phys.* **7**, 2080 (2005).

[78] A. Kraśnicki, M. Kręglewski, H. Mäder, *J. Mol. Struct.* **882**, 123-127 (2008).

[79] J. K. G. Watson, A. Roytburg, W. Ulrich, *J. Mol. Spectrosc.* **196**, 102-119 (1999).

[80] J. K. G. Watson, *J. Mol. Spectrosc.* **48**, 479-502 (1973).

[81] M. D. Harmony, W. H. Taylor, *J. Mol. Spectrosc.* **118**, 163-173 (1986).

[82] M. D. Harmony, R. J. Berry, W. H. Taylor, *J. Mol. Spectrosc.* **127**, 324-336 (1988).

[83] R. J. Berry, M. D. Harmony, *J. Mol. Spectrosc.* **128**, 176-194 (1988).

[84] R. J. Berry, M. D. Harmony, *Struct. Chem.* **1**, 49-59 (1989).

[85] J. Demaison, L. Margulés, H. D. Rudolph, *J. Mol. Struct.* **978**, 229-233 (2010).

[86] V. W. Laurie, *J. Chem. Phys.* **28**, 704-706 (1958).

[87] H. Dreizler, H. D. Rudolph, B. Hartke, *J. Mol. Struct.* **698**, 1-24 (2004).

[88] H. Dreizler, B. Hartke, H. D. Rudolph, *J. Mol. Struct.* **825**, 1-19 (2006).

[89] C. Puzzarini, G. Cazzoli, J. Gauss, *J. Mol. Spectrosc.* **262**, 37-41 (2010).

[90] D. Kivelson, E. B. Wilson, *J. Chem. Phys.* **20**, 1575-1579 (1952).

[91] N. Boulaftali, N. Ben Sari-Zizi, G. Graner, J. Demaison, *J. Mol. Spectrosc.* **216**, 284-291 (2006).

[92] A. Ceausu, G. Graner, H. Bürger, P. Pracna, *J. Mol. Spectrosc.* **181**, 424-434 (1997).

[93] G. Cazzoli, C. Puzzarini, J. Gauss, *J. Mol. Spectrosc.* **259**, 93-99 (2010).

[94] A. A. Granovsky, PC GAMESS version 7.1, *available at* http://classic.chem.msu.su/gran/gamess/index.html.

[95] M. W. Schmidt, K. K. Baldridge, J. A. Boatz, S. T. Elbert, M. S. Gordon, J. H. Jensen, S. Koseki, N. Matsunaga, K. A. Nguyen, S. J. Su, T. L. Windus, M. Dupuis, J. A. Montgomery, *J. Comput. Chem.* **14**, 1347-1363 (1993).

[96] CFOUR, a quantum chemical program package written by J. F. Stanton, J. Gauss, M. E. Harding, P. G. Szalay with contributions from A. A. Auer, R. J. Bartlett, U. Benedikt, C. Berger, D. E. Bernholdt, Y. J. Bomble, O. Christiansen, M. Heckert, O. Heun, C. Huber, T.-C. Jagau, D. Jonsson, J. Jusélius, K. Klein, W. J. Lauderdale, D. A. Matthews, T. Metzroth, D. P. O'Neill, D. R. Price, E. Prochnow, K. Ruud, F. Schiffmann, S. Stopkowicz, J. Vázquez, F. Wang, J. D. Watts and the integral packages MOLECULE (J. Almlöf and P. R. Taylor), PROPS (P. R. Taylor), ABACUS (T. Helgaker, H. J. Aa. Jensen, P. Jørgensen, and J. Olsen), and ECP routines by A. V. Mitin and C. van Wüllen. For the current version, see http://www.cfour.de.

[97] C. J. Cramer, "Essentials of Computional Chemistry, Second Edition - Theories and Models", John Wiley & Sons, Ltd (2008).

[98] C. Puzzarini, J. F. Stanton, J. Gauss, *Int. Rev. Phys. Chem.* **29**, 273-367 (2010).

[99] B. Hartke, "Theoretische Chemie I: Quantenchemie" - Lecture at the Institut für Physikalische Chemie, Christian-Albrechts-Universität zu Kiel (2006/2007).

[100] C. Puzzarini, M. Heckert, J. Gauss, *J. Chem. Phys.* **128**, 194108 (2008).

[101] C. Puzzarini, *J. Phys. Chem. A* **113**, 14530-14535 (2009).

[102] K. L. Bak, J. Gauss, T. Helgaker, P. Jørgensen, J. Olsen, *Chem. Phys. Lett.* **319**, 563-568 (2000).

[103] W. C. Bailey, *Chem. Phys.* **252**, 57-66 (2000).

[104] S. Stopkowicz, J. Gauss, *J. Chem. Phys.* **129**, 164119 (2008).

[105] E. Białkowska-Jaworska, Z. Kisiel, L. Pszczółkowski, *J. Mol. Spectrosc.* **238**, 72-78 (2006).

[106] G. Cazzoli, L. Dore, C. Puzzarini, J. Gauss, *Mol. Phys.* **108**, 2335-2342 (2010).

[107] J. F. Stanton, C. L. Lopreore, J. Gauss, *J. Chem. Phys.* **108**, 7190-7196 (1989).

[108] W. Schneider, W. Thiel, *Chem. Phys. Lett.* **157**, 367-373 (1989).

[109] S. Melandri, W. Caminati, L. B. Favero, A. Millemaggi, P. G. Favero, *J. Mol. Struct.* **352/353**, 253-258 (1995).

[110] I. Medvedev, M. Winnewisser, F. C. De Lucia, E. Herbst, E. Białkowska-Jaworska, L. Pszczółkowski, Z. Kisiel, *J. Mol. Spectrosc.* **228**, 314-328 (2004).

[111] D. T. Petkie, T. M. Goyette, R. P. A. Bettens, S. P. Belov, S. Albert, P. Helminger, F. C. De Lucia, *Rev. Sci. Instrum.* **68**, 1675-1683 (1997).

[112] B. J. Drouin, F. W. Maiwald, J. C. Pearson, *Rev. Sci. Instrum.* **76**, 093113-1-10 (2005).

[113] A. Lesarri, S. Mata, J. C. López, J. L. Alonso, *Rev. Sci. Instrum.* **74**, 4799-4804 (2003).

[114] J. L. Alonso, I. Peña, J. C. López, V. Vaquero, *Ang. Chem. - Int. Ed.* **11**, 4141-4144 (2009).

[115] Z. Kisiel, J. Kosarzewski, L. Pszczółkowski, *Acta Phys. Pol. A* **92**, 507-516 (1997).

[116] J.-U. Grabow, W. Stahl, H. Dreizler, *Rev. Sci. Instrum.* **67**, 4072-4084 (1996).

[117] *available at* http://www.chem.ualberta.ca/˜jaeger/research/ftmw/ftmw.htm.

[118] W. Stahl, G. Bestmann, H. Dreizler, U. Andresen, R. Schwarz, *Rev. Sci. Instrum.* **56**, 1759-1762 (1985).

[119] H. Dreizler, *Mol. Phys.* **59**, 1-28 (1986).

[120] Z. Kisiel, E. Białkowska-Jaworska, L. Pszczółkowski, *J. Mol. Spectrosc.* **177**, 240-250 (1996).

[121] Z. Kisiel, L. Pszczółkowski, *J. Mol. Spectrosc.* **181**, 48-55 (1997).

[122] R. A. H. Butler, D. T. Petkie, P. Helminger, F. C. De Lucia, Z. Kisiel, *J. Mol. Spectrosc.* **243**, 1-9 (2007).

[123] R. A. H. Butler, D. T. Petkie, P. Helminger, F. C. De Lucia, E. Białkowska-Jaworska, Z. Kisiel, *J. Mol. Spectrosc.* **244**, 113-116 (2007).

[124] Z. Kisiel, E. Białkowska-Jaworska, R. A. H. Butler, D. T. Petkie, P. Helminger, I. R. Medvedev, F. C. De Lucia, *J. Mol. Spectrosc.* **254**, 78-86 (2009).

[125] G. Cazzoli, C. Puzzarini, *J. Mol. Spectrosc.* **253**, 106-111 (2009).

[126] G. S. Grubbs II, R. A. Powoski, D. Jojola, S. A. Cooke, *J. Phys. Chem. A* **114**, 8009-8015 (2010).

[127] Z. Kisiel, L. Pszczółkowski, I. R. Medvedev, M. Winnewisser, F. C. De Lucia, E. Herbst, *J. Mol. Spectrosc.* **233**, 231-243 (2005).

[128] *available at* http://info.ifpan.edu.pl/˜kisiel/asym/pickett/crib.htm.

[129] B. E. Turner, A. G. Kislyakov, H. S. Liszt, N. Kaifu, *Astrophys. J.* **201**, L149-L152 (1975).

[130] F. J. Lovas, J. E. Bass, R. A. Dragoset, K. J. Olsen, NIST Recommended Rest Frequencies for Observed Interstellar Molecular Microwave Transitions, 2009 Revision, *available at* http://www.nist.gov/pml/data/micro/index.cfm.

[131] S. E. Cummins, R. A. Linke, P. Thaddeus, *Astrophys. J. Suppl. Ser.* **60**, 819-878 (1986).

[132] A. Nummelin, P. Bergman, Å. Hjalmarson, P. Friberg, W. M. Irvine, T. J. Millar, M. Ohishi, S. Saito, *Astrophys. J. Suppl. Ser.* **117**, 427-529 (1998).

[133] G. J. White, M. Araki, J. S. Greaves, M. Ohishi, N. S. Higginbottom, *Astron. & Astrophys.* **407**, 589-607 (2003).

[134] T. Jacq, C. M. Walmsley, C. Henkel, A. Baudry, R. Mauersberger, P. R. Jewell, *Astron. & Astrophys.* **228**, 447-470 (1990).

[135] A. Schimpl, R. M. Lemmon, M. Calvin, *Science* **147**, 149-150, (1965).

[136] J. D. Ibanez, A. P. Kimball, J. Oro, *Science* **173**, 444-446, (1971).

[137] N.G. Holm, *Orig. Life Evol. Biosph.* **22**, 1-241, (1992).

[138] M. P. Bernstein, S. A. Sandford, L. J. Allamandola, S. Chang, *J. Phys. Chem.* **98**, 12206-12210 (1994).

[139] F. Duvernay, T. Chiavassa, F. Borget, J-P. Aycard, *J. Phys. Chem. A* **109**, 603-608 (2005).

[140] M. Birk, M. Winnewisser, E. A. Cohen, *J. Mol. Spectrosc.* **136**, 402-445 (1989).

[141] B. P. Winnewisser, *Analyst* **117**, 343-349 (1992).

[142] J. K. Tyler, L. F. Thomas, J. Sheridan, *Proc. Chem. Soc.* 155-156, (1959).

[143] D. J. Millen, G. Topping, D. R. Lide, *J. Mol. Spectrosc.* **8**, 153-163 (1962).

[144] J. N. Macdonald, D. Taylor, J. K. Tyler, J. Sheridan, *J. Mol. Spectrosc.* **26**, 285-293 (1968).

[145] J. K. Tyler, J. Sheridan, C. C. Costain, *J. Mol. Spectrosc.* **43**, 248-261 (1972).

[146] A. Attanasio, A. Bauder, H. H. Günthard, *Mol. Phys.* **24**, 889-891 (1972).

[147] A. Attanasio, A. Bauder, H. H. Günthard, *Chem. Phys.* **6**, 373-381 (1974).

[148] D. R. Johnson, R. D. Suenram, W. J. Lafferty, *Astrophys. J.* **208**, 245-252 (1976).

[149] R. D. Brown, P. D. Godfrey, B. Kleibömer, *J. Mol. Spectrosc.* **114**, 257-273 (1985).

[150] W. G. Read, E. A. Cohen, H. M. Pickett, *J. Mol. Spectrosc.* **115**, 316-332 (1986).

[151] R. D. Brown, P. D. Godfrey, M. Head-Gordon, K. Wiedenmann, B. Kleibömer, *J. Mol. Spectrosc.* **130**, 213-220 (1988).

[152] M. Birk, M. Winnewisser, *Chem. Phys. Lett.* **123**, 382-385 (1986).

[153] W. Jabs, M. Winnewisser, S.P. Belov, F. Lewen, F. Maiwald, G. Winnewisser, *Mol. Phys.* **97**, 213-238 (1999).

[154] M. Birk, M. Winnewisser, E. A. Cohen, *J. Mol. Spectrosc.* **159**, 69-78 (1993).

[155] G. Moruzzi, W. Jabs, B. P. Winnewisser, M. Winnewisser, *J. Mol. Spectrosc.* **190**, 353-364 (1998).

[156] W. Jabs, Ph.D. Thesis, Justus-Liebig-Universität, Giessen (1998).

[157] W.H. Fletcher, F. B. Brown, *J. Chem. Phys.* **39**, 2478-2490 (1963).

[158] M. Winnewisser, H. Lichau, F. Wolf, *J. Mol. Spectrosc.* **202**, 155-162 (2000).

[159] K. Ichikawa, Y. Hamada, Y. Sugawara, M. Tsuboi, S. Kato, K. Morokuma, *Chem. Phys.* **72**, 301-312 (1982).

[160] Z. Kisiel, A. C. Legon, D. J. Millen, *Proc. R. Soc. Lond. A* **381**, 419-442 (1982).

[161] J. Demaison, *Molec. Phys.* **105**, 3109-3138 (2007).

[162] J. Demaison, L. Margulés, I. Kleiner, A. G. Császár, *J. Mol. Spectrosc.* **259**, 70-79 (2009).

[163] S. Carter, I. M. Mills, N. C. Handy, *J. Chem. Phys.* **97**, 1606-1607 (1992).

[164] Z. Kisiel, B. A. Pietrewicz, P. W. Fowler, A. C. Legon, E. Steiner, *J. Phys. Chem. A* **104**, 6970-6978 (2000).

[165] F. F. Gardner, G. Winnewisser, *Astrophys. J.* **195**, L127-L130 (1975).

[166] H. E. Matthews, T. J. Sears, *Astrophys. J.* **272**, 145-153 (1983).

[167] M. Ohishi, N. Kaifu, *Faraday Discuss.* **109**, 205-216 (1998).

[168] E. C. Sutton, R. Peng, W. C. Danchi, P. A. Jaminet, G. Sandell, A. P. G. Russell, *Astrophys. J. Suppl. Ser.* **97**, 455-496 (1995).

[169] L. M. Ziurys, D. McGonagle, *Astrophys. J. Suppl. Ser.* **89**, 155-187 (1993).

[170] W. S. Wilcox, J. H. Goldstein, J. W. Simmons, *J. Chem. Phys.* **22**, 516-518 (1954).

[171] C. C. Costain, B. P. Stoicheff, *J. Chem. Phys.* **30**, 777-782 (1959).

[172] M. C. L. Gerry, G. Winnewisser, *J. Mol. Spectrosc.* **48**, 1-16 (1973).

[173] M. C. L. Gerry, K. Yamada, M. Winnewisser, *J. Phys. Chem. Ref. Data* **8**, 107-123 (1979).

[174] M. Stolze, D. H. Sutter, *Z. Naturforsch.* **40a**, 998-1010 (1985).

[175] G. Cazzoli, Z. Kisiel, *J. Mol. Spectrosc.* **130**, 303-315 (1988).

[176] J. Demaison, J. Cosléou, R. Bocquet, A. G. Lesarri, *J. Mol. Spectrosc.* **167**, 400-418 (1994).

[177] O. I. Baskakov, S. F. Dyubko, V. V. Ilyushin, M. N. Efimenko, V. A. Efremov, S. V. Podnos, E. A. Alekseev, *J. Mol. Spectrosc.* **179**, 94-98 (1996).

[178] J. M. Colmont, G. Wlodarczak, D. Priem, H. S. P. Müller, E. H. Tien, R. J. Richards, M. C. L. Gerry, *J. Mol. Spectrosc.* **181**, 330-344 (1997).

[179] A. R. H. Cole, A. A. Green, *J. Mol. Spectrosc.* **48**, 246-253 (1973).

[180] M. P. Bernstein, S. A. Sanford, L. J. Allamandola, *Astrophys. J.* **476**, (1997) 932-942.

[181] Z. Kisiel, L. Pszczółkowski, E. Białkowska-Jaworska, S. B. Charnley, to appear in Bioastronomy 2007: Molecules, Microbes and Etraterrestrial Life, K. Meech *et al.* (eds.), ASP Conference Series, 2009.

[182] L. C. Krisher, E. B. Wilson Jr., *J. Chem. Phys.* **31**, 882-889 (1959) Errata: L. C. Krisher, *J. Chem. Phys.* **33**, 304 (1960).

[183] F. Scappini, H. Dreizler, *Z. Naturforsch.* **31a**, 840-846 (1976).

[184] F. Scappini, H. Mäder, H. Dreizler, *Z. Naturforsch.* **31a**, 1398-1407 (1976).

[185] G. K. Pandey, H. Dreizler, *Z. Naturforsch.* **32a**, 761-764 (1977).

[186] G. K. Pandey, M. Andolfatto, H. Dreizler, *Z. Naturforsch.* **32a**, 1301-1308 (1977).

[187] G. K. Pandey, H. Dreizler, *Z. Naturforsch.* **33a**, 204-213 (1978).

[188] S. Bell, G. A. Guirgis, J. Lin, J. R. Durig, *J. Mol. Struct.* **238**, 183-194 (1990).

[189] H. M. Heise, F. Scappini, H. Dreizler, *Z. Naturforsch.* **31a**, 1408-1412 (1976).

[190] F. Scappini, A. Guarnieri, *Z. Naturforsch.* **27a**, 1011-1014 (1972).

[191] Z. Kisiel, L. Pszczółkowski, *J. Mol. Spectrosc.* **178**, 125-137 (1996).

[192] B. J. Drouin, J. C. Pearson, A. Walters, V. Lattanzi, *J. Mol. Spectrosc.* **240**, 227-237 (2006).

[193] I. Kleiner, N. Moazzen-Ahmadi, A. R. W. McKellar, T. A. Blake, R. L. Sams, S. W. Sharpe, *J. Mol. Spectrosc.* **252**, (2008) 214-229.

[194] P. Pyykkö, *Mol. Phys.* **99**, 1617-1629 (2001); **106**, 1965-1974 (2008).

[195] K. Wolfart, M. Schnell, J.-U. Grabow, J. Küpper, *J. Mol. Spectrosc.* **247**, 119-121 (2008).

[196] Z. Kisiel, L. Pszczółkowski, *J. Mol. Spectrosc.* **184**, 215-220 (1997).

[197] M. Bogey, C. Demuynck, J. L. Destombes, Yo. Vallee, J. L. Ripoll, *J. Mol. Spectrosc.* **172**, 344-351 (1995).

[198] R.M. Lees, *Can. J. Phys.* **49**, 367-373 (1971).

[199] C. Boersma, A. L. Mattioda, C. W. Bauschlicher Jr., E. Peeters, A. G. G. M. Tielens, L. J. Allamandola, *Astrophys. J.* **690**, 1208-1221 (2009). Errata: C. Boersma *et al.*, *Astrophys. J.* **694**, 704-705 (2009).

[200] B. Jones, F. Zhang, P. Maksyutenko, A. M. Mebel, R. I. Kaiser, *J. Phys. Chem. A* (2010) **114**, 5256-5262 (2010).

[201] K. Mimura, M. Ohashi, R. Sugisaki, *Earth Planet. Sc. Lett.* **133**, 265-269 (1995).

[202] G. R. Floyd, R. H. Prince, W. W. Duley, *J. Roy. Astron. Soc. Can.* **67**, 299-305 (1973).

[203] J. A. Stearns, T. S. Zwier, E. Kraka, D. Cremer, *Phys. Chem. Chem. Phys.* **8**, 5317-5327 (2006).

[204] J. J. Newby, J. A. Stearns, C-P. Liu, T. S. Zwier, *J. Phys. Chem. A* **111**, 10914-10927 (2007).

[205] B. N. Tran, J. C. Joseph, M. Force, R. G. Briggs, V. Vuitton, J. P. Ferris, *Icarus* **177**, 106-115 (2005).

[206] Y. J. Pendleton, L. J. Allamandola, *Astrophys. J. Supl. Ser.* **138**, 75-98 (2002).

[207] W. Zeil, M. Winnewisser, H. K. Bodenseh, H. Buchert, *Z. Naturforsch.* **15a**, 1011-1013 (1960).

[208] A. P. Cox, I. C. Ewart, W. M. Stigliani, *J. Chem. Soc. Farad. Trans. II* **71**, 504-514 (1975).

[209] H. D. Rudolph, H. Dreizler, A. Jaeschke, P. Wendling, *Z. Naturforsch.* **22a**, 940-944 (1970).

[210] S. J. Borchert, *J. Mol. Spectrosc.* **57**, 312-315 (1975).

[211] Z. Kisiel, *J. Mol. Spectrosc.* **144**, 381-388 (1990).

[212] Z. Kisiel, E. Białkowska-Jaworska, L. Pszczółkowski, *J. Mol. Spectrosc.* **232**, 47-54 (2005).

[213] G. W. King, S. P. So, *J. Mol. Spectrosc.* **36**, 468-487 (1970).

[214] A. R. Bacon, J. M. Hollas, T. Ridley, *Can. J. Phys.* **62**, 1254-1263 (1984).

[215] A. G. Csaszar, G. Fogarasi, J. E. Boggs, *J. Phys. Chem.* **93**, 7644-7651 (1989).

[216] A. Shimojima, H. Takahashi, *J. Phys. Chem.* **97**, 9103-9112 (1993).

[217] G. Baranovic, L. Colombo, D. Skare, *J. Mol. Struct.* **147**, 275-300 (1986).

[218] Z. Chernia, T. Livneh, I. Pri-Bar, J. E. Koresh, *Vibr. Spectrosc.* **25**, 119-131 (2001).

[219] C. J. T. Schutte, J. E. Bertie, P. R. Bunker, J. T. Hougen, I. M. Mills, J. K. G. Watson, B. P. Winnewisser, *Pure & Appl. Chem.* **69**, 1641-1649 (1997).

[220] C. Puzzarini, G. Cazzoli, *J. Mol. Spectrosc.* **240**, 260-264 (2006).

[221] Z. Kisiel, E. Białkowska-Jaworska, B. A. Pietrewicz, O. Desyatnyk, L. Pszczółkowski, *J. Mol. Spectrosc.* **208**, 113-120 (2001).

[222] M. Goubet, R. A. Motiyenko, F. Réal, L. Margulés, T. R. Huet, P. Asselin P. Soulard, A. Krasnicki, Z. Kisiel, *Phys. Chem. Chem. Phys.* **11**, 1719-1728 (2009).

[223] T. D. Klots, R. S. Ruoff, H. S. Gutowsky, *J. Chem. Phys.* **90**, 4216-4221 (1989).

[224] T. M. Korter, D. R. Borst, C. J. Butler, D. W. Pratt, *J. Am. Chem. Soc.* **123**, 96-99 (2001).

[225] D. M. Miller, P. J. Morgan, D. W. Pratt, *J. Phys. Chem. A* **113**, 6964-6970 (2009).

[226] B. E. Turner, *Astrophys. J. Supl. Ser.* **70**, 539-622 (1989).

[227] C. S. Brauer, J. C. Pearson, B. J. Drouin, S. Yu, *Astrophys. J.* **184**, 133-137 (2009).

[228] H. Mäder, H. M. Heise, H. Dreizler, *Z. Naturforsch.* **29a**, 164-183 (1973).

[229] H. M. Heise, H. Lutz, H. Dreizler, *Z. Naturforsch.* **29a**, 1345-1355 (1974).

[230] W. S. Wilcox, J. H. Goldstein, J. W. Simmons, *J. Chem. Phys.* **22**, 516-518 (1954).